Isogeometric analysis of nonlinear eddy current problems

Isogeometric Analysis of Nonlinear Eddy Current Problems

PROEFSCHRIFT

ter verkrijging van de graad van doctor
aan de Technische Universiteit Eindhoven,
op het gezag van de rector magnificus prof.dr.ir. F.P.T. Baaijens,
voor een commissie aangewezen door het College voor Promoties,
in het openbaar te verdedigen
op vrijdag 27 november 2020 om 11:00 uur

door

Léo Arthur Jules Friedrich

geboren te Courbevoie, Frankrijk

Dit proefschrift is goedgekeurd door de promotor. De samenstelling van de promotiecommissie is als volgt:

voorzitter:	prof.dr.ir. P.H.N. de With
promotor:	prof.dr. E.A. Lomonova MSc
copromotor:	dr.ir. J.W. Jansen (Prodrive Technologies)
leden:	prof.dr. A. Buffa (EPFL)
	prof.dr. M. Kaltenbacher (TU Graz)
	prof.dr.ir. B. Koren
	dr.ir. C.V. Verhoosel
adviseur:	dr.ir. B.L.J. Gysen

Isogeometric Analysis of
Nonlinear Eddy Current Problems

L.A.J. Friedrich

Summary

Isogeometric Analysis of Nonlinear Eddy Current Problems

The demands for highly-efficient and high-force density electrical machines are ever-increasing in the transportation, manufacturing, and medical industries. To satisfy these challenging requirements, complex design topologies are researched to mitigate the performance-limiting phenomena, which include the slitting or trimming of parts. This is done for weight reduction, electrical windings junctions, mechanical interfaces, or cooling channels. Moreover, these geometrical features can lead to thermal hot-spots, which locally modify the material properties, such as electrical conductivity or magnetic remanence, and impacts the penetration depth of the electromagnetic field. It is evident that multi-physical models are needed to simulate these complex phenomena accurately while a seamless coupling from one field to another is critical. Moreover, it becomes necessary to be able to modify the topology, e.g. deform the shape or trim elements at any moment during the design stage, without impacting the model complexity dramatically. Accurate, efficient, and flexible models are therefore needed to take into account local features during the design stage and to predict their impacts on the system.

This is realized by utilizing the isogeometric paradigm, which enables the design-through-analysis of computer-aided-design models. The particularity of this class of numerical methods is the use of the same basis functions for an exact description of the geometrical shapes and the approximation of the solution of partial differential equations. These spline-based basis functions can be adaptively refined to resolve geometrical and physical singularities as well as local features. Furthermore, the construction of the high-order basis functions can be tailored to yield structure-preserving spaces that embed within their properties the characteristic behaviors expected from the physical fields, and reduce spurious modes.

In this thesis, different classes of solvers are detailed for solving low-frequency approximations of Maxwell's equations in the framework of isogeometric analysis. Concerning the evolution of the fields through time: magnetostatic, magnetoharmonic, and

transient solvers are described. Two nonlinear methods are used, namely the general Newton-Raphson method and a specific fixed-point method, to resolve the nonlinearities caused by the B-H characteristics of the soft-magnetic materials. Eddy current solvers are presented, which can predict the additional losses in electrically conducting solid regions due to time-varying fields from coil carrying current and from the motion of permanent magnet arrays. Coupled problems are introduced that include the interaction among electromagnetic and thermal fields. This multiphysics coupling is of paramount influence, since the temperature is often one of the most important constraints in the design of an electrical machine.

A specific modeling approach is proposed to simulate the steady-state solution of nonlinear eddy current problems. It uses an adaptive truncated hierarchical B-spline discretization of curl-conforming spaces in combination with the harmonic balance method to avoid the computationally expensive time-stepping approach. It yields an efficient time-frequency alternating scheme that can handle nonlinearities, motion and trimming. It solves the Fourier coefficients of the solution progressively with increasing harmonic content. This approach is also compared with a space-time discontinuous Galerkin method for solving nonlinear motional eddy current problems.

The industrial relevance and benefits of the proposed modeling approach are demonstrated on a complex multiphysics problem: computing efficiently the steady-state electromagnetic and thermal behavior of a single-sided axial-flux permanent magnet machine topology. The geometry is three-dimensional and curved. The stator core is slitted radially through multiple trimming operations along the angular direction. The motion of the permanent magnet array induces eddy current losses in the slitted core, which is both electrically conducting and magnetically permeable with nonlinear characteristics. The slits act as eddy current barriers, reducing the losses and heat generation. Both the eddy current and temperature distributions are influenced, since they are coupled through temperature-dependent material properties.

An experimental setup is manufactured to validate the developed multi-physical model, which couples magnetic, eddy current, and thermal fields pointwise in the isogeometric framework. A variable airgap is considered, which affects the magnetic flux density in the slitted core. The stronger magnetic saturation excites higher-order time harmonics, which are efficiently captured by the harmonic balance method. In addition, it increases the amount of both eddy current losses and temperature. A good agreement between the simulations and measurements is obtained with less than 10 % discrepancy for both quantities over a wide range of speeds and two different core materials.

Contents

Chapter 1

Introduction

I N the introduction chapter, the background and objectives of the research are presented. The importance of accurate and fast numerical simulation tools for the modeling of nonlinear eddy current phenomena in industrial applications is discussed. Subsequently, the challenges of the modeling and design of permanent magnet devices are described. Research objectives are formulated based on these challenges. The outline of the performed research is given at the end of this chapter.

1.1   Historical background

At the end of the 18th century, only electrostatic phenomena were known, but the invention of the electric battery by the Italian physicist Alessandro Volta in 1799 enabled research on electromagnetism across Europe. In 1820, the Danish scientist Hans Christian Ørsted discovered a new electromagnetic characteristic: a magnetized needle is perturbed from its original position when current flows through a wire, as exemplified in Fig. 1.1a. This experiment was reproduced by the French scholar François Arago later that year [152]. André-Marie Ampère, who attended the demonstration, focused immediately his research to electromagnetic interactions and developed the first electromagnetic theories after just four months of doing relentless experiments. The ideas developed by Ampère, which were already written with differential forms, led Arago to experiment on the magnetization of steel parts due to the excitation of neighboring currents, and he soon created the first electromagnet. Arago was a creative experimenter, however, he did not try to explain the phenomena he observed. It was Ampère who established the physical laws relative to his observations. He published his last report on electromagnetism in 1826 [6].

In 1825, Arago performed the first experiment that exposed *rotational magnetism*: a continuously rotating copper disk drives a magnetized needle in the same direction, as illustrated in Fig. 1.1b. This is the first observation of the eddy current phenomenon. One year later, Arago discovered that driving the needle was much less efficient if the copper disk is slitted radially, as shown in Fig. 1.2a. Arago and Ampère substituted the needle by a current-carrying coil and observed the same behavior. These experiments, however, could not be explained by the theory developed by Ampère.

(a)   (b)   (c)
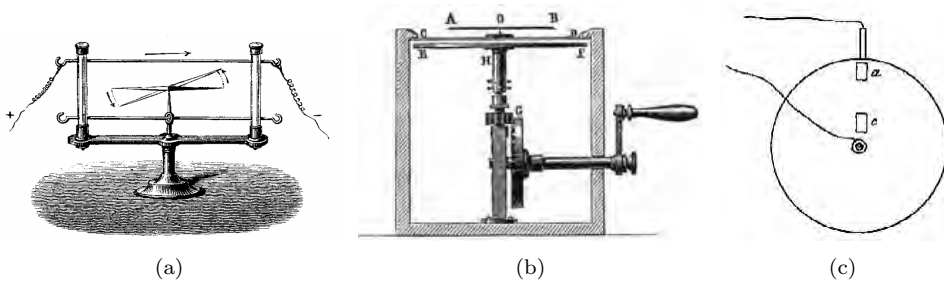
Figure 1.1: a) Ørsted's experiment: a magnetized needle rotates clockwise or anti-clockwise depending on wether the current-carrying wire is placed at the bottom or on top, b) Arago's experiment: a magnetized needle follows the rotation of a copper disk, c) Faraday's experiment: the magnetic poles (a and c) induce eddy currents in a rotating copper disk, which are harvested by a wire connected to the shaft and a brush in contact with the outer periphery of the disk [152].

(a)   (b)   (c)
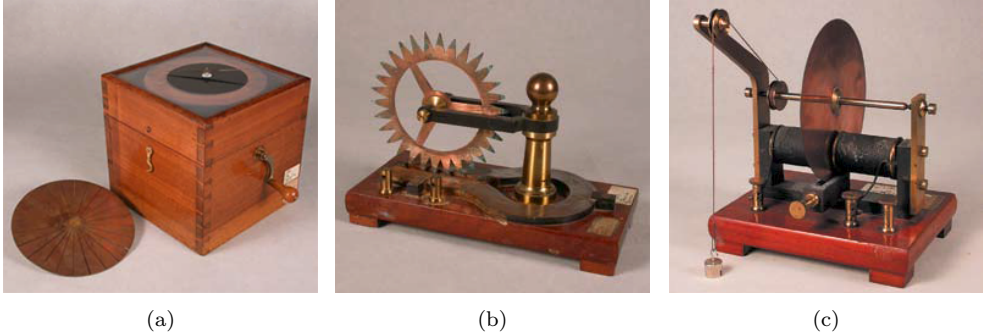
Figure 1.2: a) Arago's apparatus, b) Barlow's wheel, and c) Foucault's disk [96].

In 1831, the British physicist Michael Faraday discovered the induction phenomenon, inspired by the American scientist Joseph Henry, who, two years earlier, had developed powerful electromagnets that reverse their polarity by changing the direction of the current. Faraday used a closed magnetic circuit and induced temporarily a current in a secondary winding, after switching the current in a primary winding on or off. He also induced a temporary current by pushing a magnet inside a bobbin. He conducted the experiment shown in Fig. 1.1c, thereby creating the *magneto*, the first hand-cranked electrical generator. It is the reversed principle of Peter Barlow's star-shaped wheel shown in Fig. 1.2b. In 1822, it was presented as the first electrical motor and it utilized a mercury bath at the bottom for electrical contact with the disk. Finally, Faraday was able to explain the *rotational magnetism* observed by Arago as the manifestation of repulsive forces. He also demonstrated the existence of magnetic flux lines emerging from a permanent magnet using iron fillings. Faraday conveyed this fundamental idea to the Scottish scientist James Clerk Maxwell, who started to study his work from 1850.

Léon Foucault was interested in the eddy current damping effect and its conversion into heat [210]. In 1855, he placed a rotating copper disk belonging to his gyroscope, in between two electromagnets, as illustrated in Fig. 1.2c. He observed the rapid deceleration of the disk and the induced currents using the same method as Faraday. Foucault also imposed a continuous rotation on the disk and measured its temperature rise, highlighting the transformation from kinetic to thermal energy, which was first presented by James Prescott Joules in 1843.

Based on the previous works of Ampère and Faraday, and knowledge in fluid dynamics, Maxwell published his 20 scalar equations in 1865, which included the components of the magnetic vector potential and the scalar electric potential. Later, Oliver Heaviside and William Gibbs transformed these into the four famous vectorial-field equations, although Maxwell has been convinced, since 1873, that the correct notation for his equations is using quaternions [225].

Since Einstein introduced special relativity in 1905, Maxwell's equations are summarized using the electromagnetic four-potential. This notation is built upon the work on transformations from the Dutch physicist Hendrik Lorentz, who also left his name to the force experienced by a charged particle in an electromagnetic field.

1.2   Computational electromagnetics

More than a century after the experimental discovery of magnetism, the first electromagnetic numerical modeling methods were developed to propose a general and automated problem description beyond the reach of analytical methods.

Computational electromagnetics (CEM) refers to the procedure for modeling the interaction of electromagnetic fields with physical objects and the environment. It involves the design and analysis of numerical methods for approximating Maxwell's equations and aims for computational efficiency and accuracy. CEM is nowadays a mature topic but remains an active research and development area for a large international community and industry. Recent advances in electromagnetic field computation methods and engineering design are regularly reported during conferences, such as COMPUMAG and CEFC organized by the International Compumag Society and the IEEE Magnetics Society, respectively [205]. Four dedicated Oberwolfach workshops were organized, where a community of applied mathematicians introduced new and rigorous methods that enabled the transformation of computational electromagnetics and acoustics [110–113]. Indeed, CEM has risen in the last 30 years, as it had been lagging behind the developments made for elasticity and fluid mechanics.

The finite element method (FEM) was first developed for elasticity applications in the aircraft industry in the early 1940s. FEM was applied to magnetic problems for the first time by Winslow in 1966. The development of the Whitney forms by Bossavit [24] in the 1980s has popularized the use of edge elements, which has drastically reduced the spurious solutions, i.e. the presence of nonphysical oscillations. Bíró gathered multiple formulations for the three-dimensional magnetoquasistatic problems [21]. Differential forms and de Rham cohomology [64] have prepared a clear framework for the analysis of fields on complex geometries, much needed with the advent of computer-aided design (CAD) models. This framework led to the introduction of the isogeometric analysis (IGA) paradigm by Hughes in 2005 for structural mechanics, which relies on B-spline functions for spatial discretization and refinements [122]. This approach was further developed by Buffa [35] for the numerical analysis of partial differential equations (PDEs) arising in computational electromagnetics and fluid dynamics.

Different magnetic field modeling techniques exist that can be categorized as analytical, integral, or differential methods, each associated with their limiting geometric assumptions, limiting formulation assumptions, accuracy, and computational time.

Before the advances in computer technologies, the field modeling techniques were limited to analytical methods. The solution of the magnetic flux density radial distribution law generated by an electrical current source is named after Biot and Savart, which observed the magnetic field decreasing inversely proportional to the square of the distance, however it is actually Laplace and then Ampère who wrote the differential form, which once integrated yields the famous formulation [152]. The Fourier analysis, or harmonic modeling, originally describes electromagnetic fields in free space and has been generalized to complex geometries, such as electrical machines [2, 100, 102, 154, 242]. Geometries are, however, limited to a periodic section in Cartesian, polar, and axisymmetric coordinate systems. Geometries cannot be deformed, and are limited to orthogonal regions parallel aligned with the axis. Magnetostatic and eddy currents formulations can be developed, but are limited to linear materials characteristics [206]. Efforts have been made to enable modeling of spatially varying properties using Toeplitz matrices [54], as well as taking into account local discontinuous features beyond the traditional limitation of the Gibbs phenomenon, which occurs when approximating step functions that arise from the modeling of rectangular domains. The accuracy of the Fourier modeling approach is good when evaluated on compatible geometries, although careful scaling of the coefficient matrix may be needed to resolve possible ill-conditioning. When non-trivial geometries are considered, the resulting system of equations is small and dense. It can be inverted relatively fast with a direct solver.

To include nonlinear material characteristics in low-frequency electromechanical (EM) problems, harmonic modeling can be hybridized with magnetic equivalent circuit (MEC) theory, yielding hybrid analytical modeling (HAM). MEC, which is an integral method, introduces a network of elements that consists of magnetic flux sources, magnetomotive forces, and reluctances. Because each MEC element is localized, nonlinear material characteristic modeling in the iron regions can be realized. The coupling with a region discretized with the Fourier series is reduced to a sliding region, to model relative displacement between rotor and stator. HAM is mostly used for nonlinear multistatic simulations [43, 44].

Equivalently, for high-frequency electromagnetic problems, such as antennas or electromagnetic compatibility (EMC), partial electrical equivalent circuits (PEEC) theory can be employed for solving the arising circuit equations [190]. Inductive, resistive, and capacitive effects are included and PEEC is often combined with the modal nodal analysis (MNA). PEEC has been adapted to low-frequency problems and can take into account electrically conductive and magnetically permeable shells [162].

The boundary element method (BEM) makes use of the integral formulation of Maxwell's equations, similarly as MEC or PEEC. The principal advantage is that air and other volumic regions are not discretized, and the system is only solved at the surface interfaces between regions. BEM yields smaller but denser matrices, and therefore, needs specific tools to solve the system efficiently. In particular parallel computing using GPU-acceleration can be considered [163]. BEM is applied with low or high-order elements and is often hybridized to a volume element method to simulate local nonlinear effects in active regions. Alternatively, the method of moments (MoM) [45], which is based on volume integrals, can be used. The *moments* refer to the volume integrals in the ferromagnetic region. The distribution of these moments allows for the modeling of nonlinear magnetic materials.

The most general and widespread differential modeling technique is the finite element method (FEM) [121]. Traditionally, FEM solutions rely on a triangular or rectangular mesh, which contains first and second-order elements. This induces an inexact description of arbitrary shape geometries, or comes at the cost of a large number of elements or mesh refinement. Most established formulations are available in commercial or free software and are detailed in Section 1.5. FEM yields good accuracy,and is often considered as the reference for validating other modeling techniques, in the absence of an analytical solution. The computational effort is very attractive for two-dimensional geometries, however, it deteriorates in three dimensions, due to the difficulty of unstructured meshing and a large number of elements in the system matrix. Nonetheless, parallel processing using CPU-acceleration can be considered to speed up the simulations.

It is known that the convergence rate of a finite element solver is proportional to the polynomial order of the basis functions. This idea led to the development of spectral element methods (SEM) [37, 38], which use macro-elements of high-order polynomials (order 8 or more is common). Therefore, SEM can offer a similar accuracy to FEM at a reduced cost in terms of degrees of freedom. Since it is a spectral method, similar to the Fourier modeling approach, the refinement of the modal basis functions is therefore not localized in the physical domain. Furthermore, the geometry representation is limited to basic shapes, such as segment and arcs, that can be mapped using the transfinite interpolation method [53]. SEM leaves some room for more tailored modeling methods in terms of local approximation of the fields and geometry deformation.

The middle ground between the advantages of FEM and SEM is realized by the isogeometric analysis (IGA). It uses B-spline functions, that enable a combination of both mesh and degree refinements. The smooth basis functions with compact support yield superior approximation properties, which enable IGA to reach similar accuracy than standard FEM at a reduced computational cost [193], due to higher-order inter-element continuity. IGA is also very attractive for its exact geometry description, as

it integrates the physical analysis with the CAD models, which shape description is based on B-splines as well. This enables to operate design changes and analysis directly on the same model. A circular curved geometry is advantageously described by a single quadratic B-spline element, while more complicated shapes can be captured by raising the degree of the polynomial and modifying the control points. Adaptive local refinements can be easily produced as a result of the hierarchical structure of specific B-spline functions [122]. Trimming operations are inherently better handled by IGA than FEM [150]. IGA has gained strong popularity thanks to a community, especially in solid and fluid mechanics, that proposes many new descriptions that continuously increase the flexibility of the method. However, the application to electromagnetic problems is still relatively limited. In this thesis, the potential of IGA is explored for low-frequency electromagnetic applications, in particular, to realize the spatial discretization of the geometry and to perform the physical analysis of nonlinear eddy current problems.

To obtain the solution of nonlinear eddy current problems, electrodynamic solvers are needed to describe the temporal evolution of the eddy current phenomenon. Concerning the temporal discretization, the time-stepping approach, which is a finite difference method in time, constitutes the standard for transient finite element simulations, with for instance the so-called θ-methods [180]. However, these methods present certain limitations, such as the choice of an appropriate time step and a heavy computational effort to reach the steady-state solution. Recently, new solvers have been presented, such as the space-time Galerkin method [115, 155], which extrudes the spatial geometry along the time dimension. This enables a smooth and direct solution to dynamic systems, such as eddy current problems, using the favorable properties of the isogeometric analysis in both space and time. If the temporal excitation and response signals of the system exhibit specific characteristics, such as periodic variations, alternating time-frequency solvers like the harmonic balance method have been proposed to efficiently solve the system through its temporal Fourier coefficients [234, 235]. For motion coupling, time-stepping approaches often rely on the locked-step method, while frequency domain approaches employ sliding-surface or moving-band techniques [61, 65]. In this thesis, all three approaches for electrodynamics modeling, i.e. θ-methods, space-time Galerkin method, and harmonic balance method, are researched in the framework of IGA, on motional eddy current benchmarks, and without considering any motion coupling. Furthermore, the advantages of the harmonic balance method are investigated for nonlinear motional eddy current problems, in terms of accuracy, stability, and computational efficiency, compared to the other dynamic approaches. The convergence of the harmonic balance method has not yet been demonstrated in the literature and is therefore analyzed in detail.

1.3   Eddy currents in electrical machines

In transformers and electrical motors, the soft-magnetic core material is essential to increase the magnetic flux density and therefore, the power density. However, the soft-magnetic material introduces a nonlinear magnetic response and additional losses, which are categorized into three components: the eddy current losses, hysteresis losses, and excess losses. While the simulation of the hysteresis and excess losses is based on empirical models, bulk eddy currents are directly included in Maxwell's equations. Eddy currents are induced in electrical conductors by time-varying magnetic fields and their reaction always opposes the phenomenon that created them.

1.3.1   Applications

Induction machines rely on the induced eddy currents in the rotor to produce torque. The induction machine is the workhorse of the industry, because of its robustness and low cost. The rotor structure can be a skewed squirrel-cage, wound (slip-ring), or sleeve type. The latter is a solid-rotor induction machine, which is a cheap solution for high-speed machine applications [59, 179]. However, the highest speed range is realized with slotless permanent magnet machine topologies [126], which may include a retaining conducting sleeve [161]. Eddy current damping can also be maximized for some applications, such as eddy current braking systems [236], which can rely on permanent magnets or electromagnets. Permanent magnet-based eddy current damping concepts have been proposed as a passive fail-safe electromagnetic solution for automotive suspensions [86, 101]. Magnetic levitation is also possible through the repulsive forces caused by the eddy currents [23, 135].

Other applications directly utilize the heat generated by the eddy current losses. The most obvious example may be found in kitchens equipped with induction cooktops. Induction heating is commonly applied in foundry industries, to melt metals and to mix and stir the resulting liquid. Furthermore, because of its good controllability, eddy current induction heating can be applied to welding operations. Eddy currents are often exploited for the inspection of welds, defects, and fatigue crack propagation [89, 124]. Such nondestructive examinations are operated regularly on offshore structures, bridges, ships, submarines, and even by automotive insurance companies [1, 226]. They are crucial in nuclear or aeronautic sectors, where safety standards are very demanding. Motional eddy current testing (MET) of metal plates and pipes is widespread. Some other sensors make use of eddy currents, such as metal detectors, proximity sensors, speedometers, wattmeters, or sensors for investigating the composition and hardness of metallic structures.

In some applications, the eddy current reaction appears as a damping force, opposing the work to be performed and thus increasing the losses and producing extra heat. The heat in the magnetic permeable and electrically conducting materials leads to higher coil temperatures and increased Joule losses, furthermore, overheating decreases the lifetime of isolating materials and the structural resistance. These eddy currents should be minimized. If the topology is mostly invariant along one axis, as it is the case for transformers, and linear or rotary (radial-flux) electrical motors, lamination stacks can be adopted that segment the soft-magnetic material and reduce drastically the losses. However, each lamination is then subjected to magnetic forces that cause them to deform and vibrate. This magnetostriction phenomenon generates acoustic noise, which should be attenuated using vibro-acoustic methods, for example by dimensioning [147] or skew-welding [47].

In some other applications, where the lamination technique is not applicable, such as tubular or axial-flux motors, specific solutions exist, like the use of soft-magnetic composite materials (SMC). These isotropic materials are very efficient to reduce the losses and enable 3D magnetic field orientation. They have a lower magnetic permeability and saturation level. Due to their low losses, SMC materials are employed in higher frequency applications, such as fast-switching valve solenoids and contactless energy transfer [17, 142]. Cheaper steels are generally preferred for electrical motors production, providing that the desired level of performance is reached.

1.3.2   High-performance motors

The demands for more affordable, highly-efficient, and high-force density electrical machines are ever-increasing in the manufacturing, medical and transportation industries. The introduction of rare-earth permanent magnets, such as samarium-cobalt (SmCo) and neodymium-iron-boron (NdFeB), has helped to satisfy these challenging requirements. Furthermore, advanced design topologies have been researched to mitigate other performance-limiting phenomena. The adoption of permanent magnets increases the performances of electrical motors in terms of force density and efficiency. Ferromagnetic materials are also employed to increase the airgap flux density. To maximize the force density, the soft-magnetic materials are operated partially in saturation. The magnetic nonlinearity has different impacts depending on the regime compared to a linear material characteristic. In static situations, the saturation reduces the amplitude of the magnetic flux density and changes its distribution. In dynamic and motional situations, it generates higher-order frequency content that leads to additional losses.

Large-volume industries, such as automotive, have researched alternative designs to transition from using surface-mounted expensive and scarce rare-earth materials to developing buried ferrite-magnet motors, as they provide field-weakening capabilities
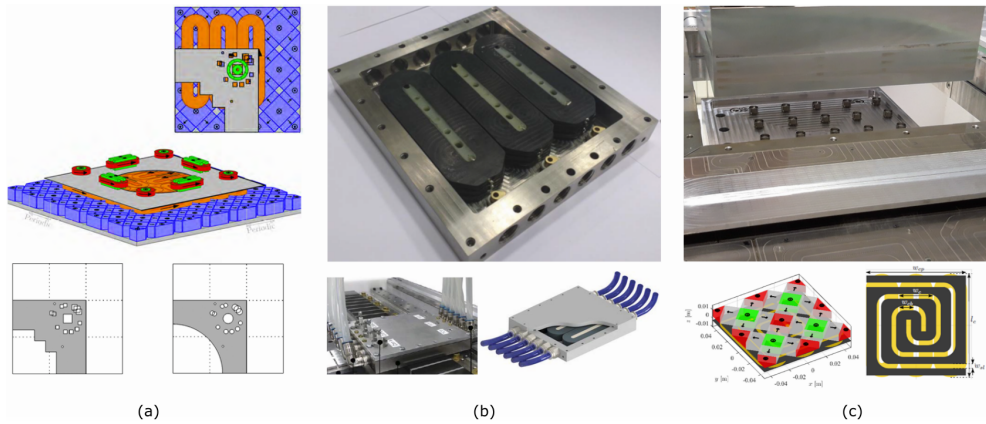
Figure 1.3: a) Magnetic shielding plate with holes for weight reduction, for cables and bolts junctions, for water and air connections [176], b) titanium enclosure with holes for cooling channels connection [216], and c) slitted titanium cooling plates [54].

which are useful at higher speeds [77]. However, it comes at the cost of new modeling challenges: for instance, complex geometrical shapes in the rotor are necessary [237], and large mechanical stresses due to centrifugal forces might arise around the magnets in the interior of the rotor that modifies locally the nonlinear material characteristics of the steel [56, 127, 233]. Flexible geometrical discretization and efficient multiphysics coupling are therefore necessary to resolve these new challenges.

High-power applications, such as submarine propulsion, MAGLEV trains, nuclear accelerators, and MRI have established the use of superconducting DC-coil motor solutions to go beyond the performances traditionally offered by permanent magnets. However, superconducting materials also behave in a highly nonlinear manner with respect to temperature and imposed magnetic field, and require advanced modeling techniques to simulate their complex behaviors.

In general, eddy currents can cause significant power losses and temperature rise, which decrease the efficiency. The time-varying fields might be due to the low-frequency motion of the mover and slotting effect, or high-frequency pulse-width-modulated inverter waveforms. To mitigate the eddy current phenomenon, thin lamination stacks in the stator are typically considered if the topology allows it, additionally, segmented permanent magnets can be used. Furthermore, electrically conducting parts of a motor can be perforated or slitted. This is done for loss and weight reduction, as well as electrical, mechanical, or cooling channels connections. Some application-specific slitting patterns are illustrated in Fig. 1.3. In particular, Fig. 1.3a represents a two-stage planar motor topology for high precision positioning in lithography application, where a magnetic shield is applied as a mean of reducing

the cross-coupling between the two stages [176]. The slitting of the shield is done for weight reduction as well as cables, bolts, water, and air connections. In Fig. 1.3b, a high-voltage coreless linear motor is presented, that achieves state-of-the-art current densities using direct liquid cooling for which connection holes to the cooling channels are drilled [216]. In Fig. 1.3c, a single-stage planar motor topology is shown, where the slitting is performed to reduce the eddy-currents in the cooling plate because they induce parasitic forces and consequently decrease the accuracy of the positioning system [54]. The geometrical features can lead to a local concentration of eddy currents and therefore thermal hotspots, which modify the properties of the materials, such as electrical conductivity or magnetic remanence, which in turn impact the penetration depth and amplitude of the electromagnetic fields. To continue pushing the development and optimization of high-performance motors, in terms of positioning accuracy and acceleration levels, the parasitic phenomena generated by the interaction of multi-physically coupled fields with complex geometries have to be resolved as efficiently and accurately as possible. To do so, state-of-the-art numerical methods like the isogeometric analysis enable to go beyond the traditional compromise between computational efficiency and accuracy, both in terms of physics and geometry.

1.3.3   Modeling challenges

Complex shapes and high aspect ratios of three-dimensional geometrical features, such as slits, need to be integrated efficiently and accurately in the model to predict their impact on the system. Adaptive isogeometric methods in two and three spatial dimensions involving hierarchical splines are adopted in this work, in order to refine the mesh and space around local features, which are cut out via the so-called trimming operations. These trimming operations can be performed after the model is built, therefore improving the flexibility during the design-through-analysis stage. Adaptive meshing also refines the basis functions locally in regions where geometrical singularities or strong field gradients occur and helps to suppress nonphysical oscillations.

Due to the nonlinearity of the soft-magnetic material characteristics and the time-varying magnetic fields, nonlinear dynamic solvers are required to incorporate the higher-order time-harmonic eddy current and iron losses. The computational effort of a time-stepping transient solver with traditional finite elements is heavy and puts a large demand on the computational power needed to perform optimization needed for the development of more-efficient industrial applications. In the framework of isogeometric analysis, the geometrical gradient with regard to the design variables is readily available and can be used to speed up the optimization process. Two alternatives to the traditional time-stepping approach are proposed to yield faster

and more accurate nonlinear steady-state solvers in both the time and frequency domain.

Multiphysics coupling including a thermal model is of crucial importance to account for the nonlinearities due to temperature-dependent parameters and cooling mechanisms. Furthermore, it is necessary to ensure that the temperatures of the coils and permanent magnets stays below critical constrained values. In this thesis, an axial-flux permanent magnet (AFPM) machine topology is chosen as an academic example combining many features of interest for the modeling, as well as presenting an industrial relevance. The AFPM machine constitutes a relatively recent class of rotating motors introduced in the late 70s [158], however, the disc-type construction can be traced back to Nikola Tesla's 1889 patent [207] or even more primitively to the Faraday's disk as shown in Fig. 1.1.

The AFPM machine presents a three-dimensional curved geometry, which cannot be captured by a two-dimensional reduced model, but is efficiently modeled using the structured mesh of IGA. AFPM topologies are often double-sided and can either be with or without stator core. For the purpose of demonstrating the nonlinear material characteristics modeling, a topology with a core is chosen, which can be reduced to a single-sided structure for analysis using an axial symmetry argument. Furthermore, using a single-sided mechanical structure enables to adapt the airgap length continuously and therefore, to change the amount of magnetic saturation, the eddy current losses, and the temperature in the core. To further complicate the model, and add small geometrical features, the slitting of the ferromagnetic stator core is investigated as a method for reducing the losses, by acting as eddy current barriers. The three-dimensional nonlinear bulk eddy current problem in the slitted core is modeled using the isogeometric framework in combination with the harmonic balance solver. The computational coupled model is analyzed and validated using an experimental setup.

1.4   Research objectives

In the previous section, challenges related to modeling nonlinear eddy current phenomena in electrical machines with complex topologies are discussed. Based on these challenges, the following research objectives are formulated:

- **The modeling of the nonlinear behavior of electromagnetic quasistatic fields for two and three-dimensional structures in the isogeometric analysis framework.**

- **The analysis in time and frequency domain of eddy current phenomena in moving-magnet devices with trimmed ferromagnetic regions exhibiting nonlinear characteristics.**

- **The development of a steady-state model with multiphysics coupling among magnetic, eddy current and thermal fields applied to the analysis of a single-sided axial-flux permanent magnet machine topology with a slitted core.**

- **The experimental validation of the coupled model for different speeds and saturation levels, in terms of global electromagnetic damping losses, as well as local quantities, such as temperature and electromagnetic time-harmonic spectra.**

1.5   Software solutions

Many simulation codes and commercial software exist for multiphysics or dedicated electromagnetics solutions. Open-source software permits users to study, adapt, and improve the flexibility as well as code capabilities by implementing new models or methods. Furthermore, they enable the reproductibility and replicability of the research. This last point might be the main disadvantage of using commercial software in public scientific research. Established commercial software programs are proposed by companies, such as *Altair, ANSYS, Autodesk, COMSOL, Siemens* or *Dassault*, their products are among the most widespread solutions. They aim for easy coupling among multiphysics simulations, CAD, integrated optimization, high-performance computing, and user support. Many research groups have developed their own simulation codes striving for flexibility, performance, and specialized research development. Some of them have emerged from industry or academic collaboration and are now recognized solutions. Examples of such simulation codes include *Elmer*, *Code_Carmel*, *Femm*, *FEMAG*, *Agros2D*, and more recently *Pyleecan*. The popular meshing solution *Gmsh* and the finite element *GetDP* are integrated in *ONELAB*. Open-source libraries, such as *Smeklib* or *Sparselizard*, have been released by graduates at the end of their PhD research. *FeniCS*, *PetIGA* and *FreeFEM* are simulation packages that use *PETSc* routines. *GeoPDEs*, *Nutils*, *G+Smo*, *NGsolve*, *CFS++* are recent numerical tools for solving PDEs. *Hypre* proposes high-performance solvers. Multiphysics coupling between different libraries can be achieved using *preCICE*. For post-processing visualization of the solution, *Paraview* is the most popular toolkit.

In the context of this thesis, the *GeoPDEs* toolbox [90, 221] has first been investigated. It is a package for isogeometric analysis in Matlab and Octave, which supports hierarchical spline and includes a versatile NURBS toolbox [202] for creating

geometries. Hierarchical properties are fundamental for performing local adaptive refinements efficiently and improve the ratio of accuracy to the number of degrees of freedom. These properties are already attractive for 2D problems, but even more advantages are expected in 3D, since the computational effort is more of a bottleneck and the differences in scales can be much stronger. In *GeoPDEs*, only the hierarchical basis functions for scalar spaces were implemented. This restricts the application of adaptive refinements to 2D electromagnetic problems and 3D thermal problems, in particular, it does not cover 3D electromagnetic problems. This is one of the reasons that another numerical toolbox, *Nutils*, has been used in the rest of the thesis, together with local development, support and collaboration. *Nutils* is a high-level Python toolbox for solving PDEs, which supports the finite element method, finite cell method, and isogeometric analysis [218]. *Nutils* supports automatic differentiation, vectorial hierarchical basis functions, and trimming operations. It allows parallel assembly and integration on Linux machines, which enables large-scale simulations. This enables to simulate complex multi-physical phenomena while locally refining the mesh and space in the vicinity of geometrical and physical features.

1.6   Thesis outline

In Chapter 2, the fundamental mathematical tools needed to construct the isogeometric framework are introduced. The different spline-based basis functions are detailed. Electromagnetism and Maxwell's equations are linked to the framework of functional spaces, which are used to solve the partial differential equations arising in this thesis.

The different magnetoquasistatic weak formulations in two and three dimensions are detailed in Chapter 3. Static, harmonic, and transient formulations are described. A steady-state thermal model, including radiation and convection, is introduced. Techniques for modeling nonlinear material characteristics, namely the Newton-Raphson and the fixed-point methods are derived. Chapter 2 and Chapter 3 address the first research objective.

In Chapter 4, a frequency-domain solver for the nonlinear eddy-current problems due to the motion of a permanent magnet array is developed in the isogeometric framework. The harmonic balance method and some of its variants are detailed in two and three dimensions. The proposed method is validated against the conventional time-stepping technique on two different two-dimensional benchmarks, in terms of accuracy, stability, and computational effort.

A time-domain solver, the space-time Galerkin approach is introduced in Chapter 5. This approach is validated against the time-stepping technique and the harmonic balance method. Furthermore, the framework for enabling trimming operations is described, and the discontinuous Galerkin method is introduced. A trimmed benchmark

is used to validate the adaptive hierarchical refinements with the harmonic balance method. The second research objective is achieved using the methods developed in Chapter 4 and Chapter 5.

In Chapter 6, the two final research objectives are realized. The complex three-dimensional academic problem with industrial relevance is introduced: the multi-physical simulation of the steady-state behavior of a single-sided axial-flux permanent magnet machine with slitted core. The electromagnetic model, which is solved using the harmonic balance method, is coupled to a thermal model in the framework of the isogeometric analysis. The multi-physical steady-state coupled model is validated using an experimental setup, where global and local quantities are measured for different rotational speeds and airgap values.

Finally, in Chapter 7, the conclusions of the work and the main contributions are summarized. Recommendations for future research are given.

Chapter 2

Isogeometric analysis of electromagnetic problems

In this chapter, the background knowledge and references needed for discretizing electromagnetic problems using the isogeometric analysis (IGA) are presented. The concepts of splines, NURBS, and hierarchical splines are defined and applied to the discretization of the computational domain. The strong formulations of Maxwell's equations are recalled and the dual potential formulations of the magnetoquasistatic problems are given. The constitutive relations between electromagnetic fields and potentials are summarized in the so-called Maxwell's house diagram. This representation indicates the links with the functional spaces and differential operators needed for their discretization. The fundamental concepts for approximating boundary value problems in the framework of isogeometric analysis are introduced.

2.1   Introduction

The concept of IGA was introduced by T.J.R. Hughes in 2005 [122]. It aims at integrating finite element analysis (FEA) within computer-aided design (CAD) models. The CAD models use non-uniform rational B-splines (NURBS) to represent complex shapes and geometries. The main idea of IGA is to use the same B-spline functions for discretizing the variational formulation of the partial differential equations (PDE) to resolve in the geometrical domain. The advantages compared to the traditional finite element method (FEM) are an exact geometrical description and a smooth solution due to the higher continuity of the basis functions.

2.2   Splines

B-splines are a family of mathematical functions of great popularity among the computer-aided design (CAD) community. B-splines, where B stands for basis, appear as a generalization of the Bézier curves. An extension of the splines family called NURBS allows to exactly represent curves, surfaces, and volumes. Multidimensional spline spaces can be easily formed through tensor products of unidimensional spline spaces. There is a wider variety of specific splines, such as T-splines (truncated), which break the tensor product, hierarchical B-splines, or HB-splines, which can be combined into THB-splines. They all aim at reducing the number of degrees of freedom and producing localized refinements.

The particularity of IGA lies into the use of the same functions, that can be B-splines or NURBS, for both the exact geometric description and the solution space discretization. This is explained in more detail in Section 2.2.4 and graphically illustrated by Fig. 2.4. Domains with irregular shapes are represented in the physical space Ω, and patched together to represent geometries with different material properties. A mapping function F, sends each patch into the parameter space, generally $\widehat{\Omega} = [0,1]^d$, which is the reference domain of dimension d. Each patch is subdivided into elements following their knots refinements in each parametric direction (η, ξ) and these elements are all mapped on the same parent space. In the parent space, interpolation points, such as Gauss points are defined and used to build and assemble the stiffness matrix, as well as to interpolate the solution or integrate quantities over surfaces and volumes.

2.2.1 B-splines

One starts to define an increasing sequence of points in $[0,1]$ to form a knot vector:

$$\Xi = \xi_1, \xi_2, ..., \xi_{n+p+1}, \tag{2.1}$$

following Cox-de-Boor's identity [57], where n is the number of B-spline functions and p is the degree of the polynomial, each knot ξ_i has the multiplicity r_i. When the knots are equally spaced, the knot vector is called uniform, otherwise it is non-uniform. The multiplicity counts the number of times a knot is repeated in the vector. When the multiplicity of a knot is exactly $r_i = p$, the basis function is C^0 continuous or interpolatory at that knot. For an open knot vector, the starting and last knots (0 and 1) are repeated $p+1$ times. In general basis functions are $\alpha_i = p - r_i$ continuous at a knot ξ_i. Starting from piecewise constant functions of degree $p = 0$:

$$B_{i,0}(\xi) = \left\{ \begin{array}{ll} 1 & \text{if } \xi_i \leq \xi \leq \xi_{i+1} \\ 0 & \text{otherwise.} \end{array} \right. \tag{2.2}$$

B-splines of higher-order can be defined recursively [57] as:

$$B_{i,p}(\xi) = \frac{\xi - \xi_i}{\xi_{i+p} - \xi_i} B_{i,p-1}(\xi) + \frac{\xi_{i+p+1} - \xi}{\xi_{i+p+1} - \xi_{i+1}} B_{i+1,p-1}(\xi). \tag{2.3}$$

B-splines are naturally extended in any dimension d, by means of the tensor product between d univariate B-splines:

$$\hat{B}_{i,p}(\hat{\mathbf{x}}) = \hat{B}_{i_1,p_1}(\hat{x}_1)\hat{B}_{i_2,p_2}(\hat{x}_2)...\hat{B}_{i_d,p_d}(\hat{x}_d). \tag{2.4}$$

Periodic B-splines of increasing degree are shown in Fig. 2.1 for an uniform knot vector. Correspondingly, periodic B-splines for a nonuniform knot vector, i.e. where the multiplicity is controlled, are shown in Fig. 2.2.

2.2.2 NURBS

To each B-spline basis function, a weight w_i is associated to form the NURBS basis functions:

$$N_{i,p}(\hat{\mathbf{x}}) = \frac{w_i \hat{B}_{i,p}(\hat{\mathbf{x}})}{\sum_j w_j \hat{B}_{j,p}(\hat{\boldsymbol{x}})}, \tag{2.5}$$

where, the index i counts the basis functions over the tensor product space. A geometry can be constructed by associating a control point $\mathbf{C}_i$ to each basis function,
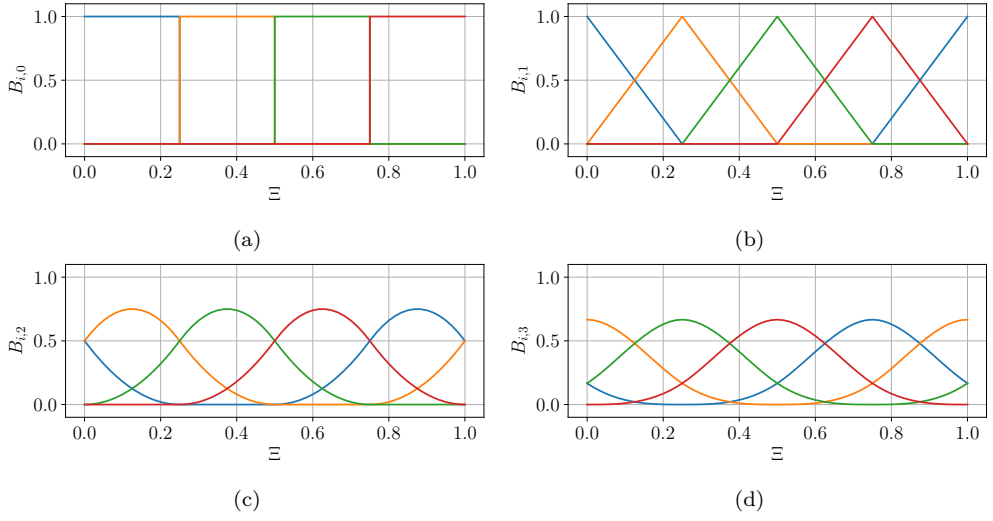
Figure 2.1: B-spline basis of degree 0, 1, 2, 3 on an open uniform knot vector: a) B-spline basis of degree 0, b) B-spline basis of degree 1, c) B-spline basis of degree 2, and d) B-spline basis of degree 3.
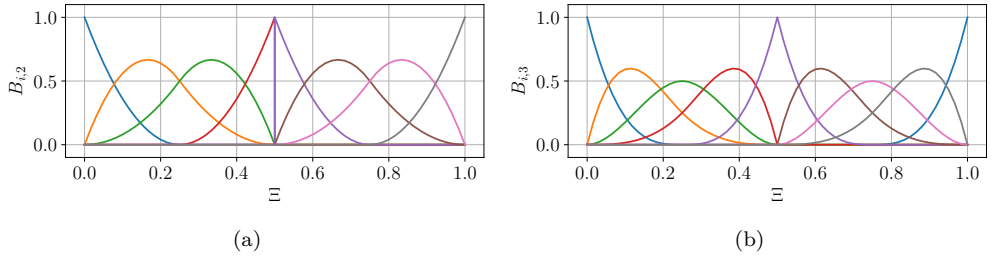
Figure 2.2: B-spline basis on an open nonuniform knot vector $\Xi = [3, 1, 3, 1, 3]$: a) B-spline basis of degree 2 and b) B-spline basis of degree 3.

therefore defining the parametrization or mapping $\mathbf{F}$:

$$\mathbf{x} = \mathbf{F}(\hat{\mathbf{x}}) = \sum_i N_{i,p}(\hat{\mathbf{x}})(\hat{\mathbf{C}}_i). \tag{2.6}$$

This defines the mapping from the parameter space $\hat{\Omega} = [0, 1]^d$ to the physical space $\Omega \in \mathbb{R}^d$. Similarly, the tensor product of knot vectors, Ξ_d, which is a Cartesian grid of the parametric space, is mapped to the physical space creating a structured grid. This grid is subdivided into patches $\Omega_k = F_k(\hat{\Omega})$, themselves subdivided into elements that represent the mesh in IGA. To represent the solution, approximation meshes and spaces for the physical fields of interest are constructed onto the geometry control net corresponding to the coarsest mesh level, which is later refined.

2.2.3 Hierarchical splines

A further generalization of the B-spline is the hierarchical (HB-) or truncated hierarchical (THB-) spline. These basis functions offer numerous advantageous properties, including a drastic reduction of the number of degrees of freedom and reduced support. The support represents the space spanned by a basis function. THB-splines offer a natural framework for adaptive refinements using *residual-based* error estimators, which are detailed in Section 3.8. Moreover, THB-splines can be used advantageously in multigrid solvers [116], since the construction of coarse and fine meshes is natural in the IGA framework.

The construction of a nested sequence of tensor product spline space $\{\mathcal{S}_l\}$, spanned by the bivariate B-spline basis $\{\mathcal{B}_l\}$ of degree p, and level l is detailed below. The basis is formed by scalar-valued B-splines:

$$\mathcal{B}_{i,l} = \{\beta_{i,l}, \ i = 1, ..., N_l\}, \tag{2.7}$$

where, N_l is the dimension of the spline space. A fundamental point is the use of the child-parent linear combination structure:

$$\beta_{i,l} = \sum_{k=1}^{N_{l+1}} c_{k,l+1}(\beta_{i,l})\beta_{k,l+1}, \quad \text{with } c_{k,l+1}(\beta_{i,l}) \geq 0. \tag{2.8}$$

This two-scale relationship can be written in a change of basis matrix that gathers the coefficients at different levels:

$$(C_l^{l+1})_{ki} = c_{k,l+1}(\beta_{i,l}). \tag{2.9}$$

The set $\boldsymbol{\Omega_n} = \{\Omega_l\}_{l=0,..,n}$ is introduced as a hierarchy of strictly contained subdomains of depth n. A simplified version of the hierarchical basis $\tilde{\mathcal{H}}$ associated with $\boldsymbol{\Omega_n}$ is constructed:

$$\tilde{\mathcal{H}}_0 = \{\beta \in \mathcal{B}_0, \ \text{supp } \beta \neq \emptyset\}, \tag{2.10}$$

$$\tilde{\mathcal{H}}_{l+1} = \{\beta \in \tilde{\mathcal{H}}_l, \ \text{supp } \beta \not\subset \Omega_{l+1}\} \cup \tag{2.11}$$

$$\bigcup_{\beta \in \tilde{\mathcal{H}}_l, \ \text{supp}\beta \subset \Omega_{l+1}} \mathcal{C}(\beta), \quad \text{for } l = 0, ..., n-2,$$

which only adds the children $\mathcal{C}(\beta)$ of the deactivated functions, and is computationally easier to select and build than its traditional counterpart [31]. To define the truncated

basis of $\beta_{i,l} \in \mathcal{B}_l$ the linear operator is introduced:

$$\text{trunc}_{l+1}(\beta_{i,l}) = \sum_{k=1}^{N_{l+1}} c_{k,l+1}^{\tau}(\beta_{i,l})\beta_{k,l+1}, \tag{2.12}$$

which coefficients are set to zero if $\beta_{k,l+1} \in \tilde{\mathcal{H}}_{l+1} \cap \mathcal{B}_{l+1}$. The construction of the simplified THB-spline basis $\tilde{\mathcal{T}}$ follows:

$$\tilde{\mathcal{T}}_0 = \{\beta \in \mathcal{B}_0, \text{ supp } \beta \neq \emptyset\}, \tag{2.13}$$
$$\tilde{\mathcal{T}}_{l+1} = \{\text{trunc}_{l+1}(\beta), \ \beta \in \tilde{\mathcal{T}}_l \wedge \text{supp}\beta \not\subset \Omega_{l+1}\} \cup \tag{2.14}$$
$$\{\beta \in \mathcal{B}_{l+1}, \text{ supp } \beta \subset \Omega_{l+1}\}, \quad l = 0, ..., n-2.$$

The matrix collecting the THB coefficients $(C_l^{l+1,\tau})$ is applied successively between consecutive levels and finally, the matrix C_l, which changes the basis from the active THB basis to $\mathcal{B}_l$, is assembled recursively:

$$C_0^{\tau} = J_0, \tag{2.15}$$
$$C_{l+1}^{\tau} = [C_l^{l+1,\tau}C_l^{\tau}, J_{l+1}], \quad l = 0, ..., n-2. \tag{2.16}$$

This matrix includes all the active level function coefficients designated by J_{l+1}. The constructed THB-spline basis restores the convex partition of unity, preserves the coefficients, and demonstrates reduced support and multilevel interactions. These basis functions are applied in Section 3.8, where the variational formulations and adaptive refinement strategies are detailed.

2.2.4   Geometry discretization

The geometry has to be discretized to be IGA compatible. Several approaches are possible depending on the shapes, complexity of the model, and the numerical implementation. Since the tensor product construction is most often employed with IGA, the reference element is $\hat{\Omega} = [0,1]^d$, where d is the dimension. In most electromagnetic applications, several materials interact within the same domain, therefore discontinuous material properties and sources arise. Two main families can be distinguished, as shown in Fig. 2.3, the conforming and nonconforming geometries, which share common interfaces or have nonoverlapping interfaces, respectively. Within the nonconforming category, conformal and nonconformal meshes can be distinguished, the nonconformal mesh exhibits hanging nodes, as shown in Fig. 2.3c.

Within the conforming geometry category, two main options are available: the single patch and multipatch approach. The single patch approach refines the knot vector and increases the knot multiplicities to decrease the level of continuity at the generated
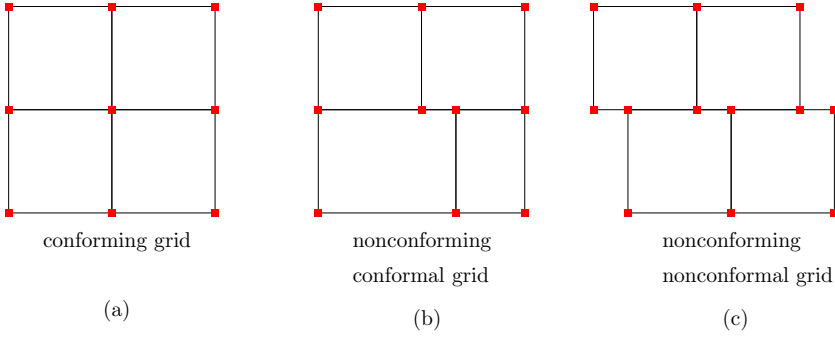
Figure 2.3: Examples of conforming and nonconforming grids or control nets.

interfaces. The multipatch approach simply glues multiple elements with a given continuity at the interfaces, most often C^0 or C^1. The multipatch approach based on NURBS offers a flexible description of the shapes of the interfaces between patches. A schematic of a multipatch discretization with IGA is represented in Fig. 2.4. The parametrizations $\mathbf{F}$ are indicated, which map each patch $\Omega_k = F_k(\widehat{\Omega})$ of the physical domain Ω to the reference element or computational domain $\widehat{\Omega}$. Algebraic methods are used in this thesis for the parametrization, in particular, Coon's patch approach [76] is used for assembling surface patches from their boundary curves. However, other methods can be applied, such as PDE-based methods, and methods based on convex quadratic cost functional minimization [107, 108]. For geometries with nonmatching boundaries, different techniques exist, such as Mortar methods [36], or discontinuous Galerkin methods (DG) [34].
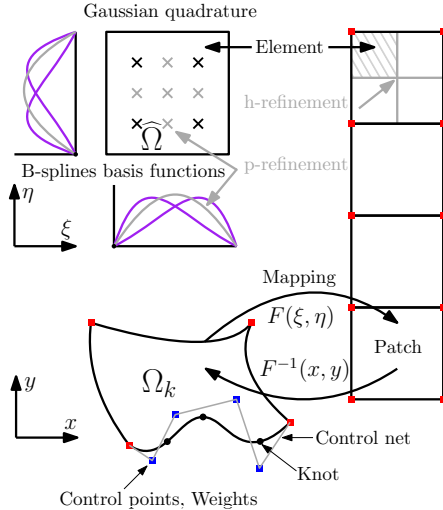
Figure 2.4: Conforming multipatch isogeometric discretization schematic.

A spline curve is defined as a linear combination of B-splines defined in (2.3) and control points:

$$\mathbf{C}(\xi) = \sum_{i=1}^{n} \mathbf{C}_i B_{i,p}(\xi), \qquad \mathbf{C}_i \in \mathbb{R}^d, \qquad d = 2, 3, \tag{2.17}$$

where, $\mathbf{C}_i$ are the control points exemplified by colored squares in Figs. 2.3 and 2.4. The control net is the gird formed by the piecewise linear curves that link all the control points. In order to be able to represent conics, additional weights $\mathbf{w}$ are introduced to form NURBS basis functions as defined in (2.5). This leads to the creation of NURBS curves by linear combination:

$$\mathbf{C}(\xi) = \sum_{i=1}^{n} \mathbf{C}_i N_{i,p}(\xi). \tag{2.18}$$

Similarly, B-splines or NURBS parametrizations of multivariate geometries are created through a tensor product of univariate curves, leading to the creation of surfaces, manifolds, and volumes. Different algorithms have been conceived to produce refinements, transformations, and deformations of these structures [57, 122, 172]. h-refinement is obtained through knot insertion and is exemplified in Fig. 2.4, p-refinement through degree elevation, and k-refinement is a degree elevation followed by knot insertion. Transformations include translations, rotations, and scalings. Concerning deformations, modifications of coordinates and weights of the control points are possible. The coordinates can be 3D Cartesian or 4D homogeneous coordinates if the weights are included.

2.3   Electromagnetism and potentials

2.3.1   Maxwell's equations and dual formulations

The strong formulations of Maxwell's equations are given as:

$$\mathbf{rot}\ \mathbf{E} = -\frac{\partial \mathbf{B}}{\partial t}, \tag{2.19}$$

$$\mathbf{rot}\ \mathbf{H} = -\frac{\partial \mathbf{D}}{\partial t} + \mathbf{J}, \tag{2.20}$$

$$\mathrm{div}\ \mathbf{B} = 0, \tag{2.21}$$

$$\mathrm{div}\ \mathbf{D} = \rho_q, \tag{2.22}$$

where, $\mathbf{E}$ is the electric field strength, $\mathbf{D}$ is the electric displacement field, $\mathbf{J}$ is the electric current density, $\mathbf{B}$ is the magnetic flux density, $\mathbf{H}$ is the magnetic field strength,

and ρ_q is the electric charge density. The set of Maxwell's equations above is called *full-wave*. For low-frequency magnetic problems, the *magnetoquasistatic* (MQS) approximation that neglects the displacement currents, $\frac{\partial \mathbf{D}}{\partial t}$, is commonly applied. The different field strengths are linked to flux densities through tensorial constitutive relations. The constitutive equations for MQS problems can be defined as:

$$\mathbf{B} = \mu \mathbf{H} + \mathbf{B}_r, \tag{2.23}$$

$$\mathbf{J} = \sigma \mathbf{E} + \mathbf{J}_s, \tag{2.24}$$

where, μ is the magnetic permeability and σ is the electric conductivity. The magnetic permeability is the product of the vacuum permeability μ_0 and the relative permeability μ_r. The constitutive laws are given by the first terms of (2.23)-(2.24), to which the permanent sources of the respective fields are added as second terms, such as the imposed electric current density $\mathbf{J}_s$ and the remanent magnetic flux density $\mathbf{B}_r = \mu_0 \mathbf{M}_r$, where $\mathbf{M}_r$ is the remanent magnetization. The electromagnetic potentials are conveniently introduced following:

$$\mathbf{B} = \mathbf{rot}\ \mathbf{A}, \tag{2.25}$$

$$\mathbf{E} = \frac{\partial \mathbf{A}}{\partial t} - \mathbf{grad}\ V, \tag{2.26}$$

$$\mathbf{J} = \mathbf{rot}\ \mathbf{T}, \tag{2.27}$$

$$\mathbf{H} = \mathbf{T} - \mathbf{grad}\ \Phi, \tag{2.28}$$

where, $\mathbf{A}$ is the magnetic vector potential, V represents the electric scalar potential, $\mathbf{T}$ is the electric vector potential, and Φ is the magnetic scalar potential. The magnetic reluctivity can be defined as $\nu = \mu^{-1}$, and similarly the electric resistivity is given as $\rho = \sigma^{-1}$. The strong forms of Maxwell's equations in the quasi-static approximation are rewritten below in terms of the introduced potentials in the general setting of three spatial dimensions for both magnetostatic and transient cases, which are the two most common regimes. The primal potential formulation $\mathbf{A} - V$, and its dual $\mathbf{T} - \Phi$, are given for:

- Magnetostatics, in terms of magnetic vector potential $\mathbf{A}$:

$$\mathbf{rot}(\nu\ \mathbf{rot}\ \mathbf{A}) = \mathbf{J}_s + \nu\ \mathbf{rot}\ \mathbf{B}_r, \tag{2.29}$$

$$\mathrm{div}\ \mathbf{A} = 0, \tag{2.30}$$

$$\mathbf{n} \times \mathbf{rot}\ \mathbf{A}|_{\Gamma_N} = 0, \tag{2.31}$$

$$\mathbf{n} \times \mathbf{A}|_{\Gamma_D} = 0, \tag{2.32}$$

where Γ_D and Γ_N represent the Dirichlet and Neumann boundaries of the domain Ω, and $\mathbf{n}$ is the normal vector to an interface.

- Magnetostatics, with magnetic scalar potential Φ and electric vector potential $\mathbf{T}$:

$$\mathbf{rot}(\rho\,\mathbf{rot}\,\mathbf{T}) = 0, \tag{2.33}$$

$$\mathrm{div}(\mathbf{T} - \mu\,\mathbf{grad}\,\Phi) = 0, \tag{2.34}$$

$$\mathbf{n} \times (\mathbf{T}|_{\Gamma_N} - \mu\,\mathbf{grad}\,\Phi|_{\Gamma_N}) = 0, \tag{2.35}$$

$$\mathbf{n} \cdot (\mathbf{T}|_{\Gamma_D} - \mu\,\mathbf{grad}\,\Phi|_{\Gamma_D}) = 0. \tag{2.36}$$

- Transient, with magnetic vector potential $\mathbf{A}$ and electric scalar potential V:

$$\mathbf{rot}(\nu\,\mathbf{rot}\,\mathbf{A}) + \sigma\left(\frac{\partial\mathbf{A}}{\partial t} + \mathbf{grad}\,V\right) = \mathbf{J}_s + \nu\,\mathbf{rot}\,\mathbf{B}_r, \tag{2.37}$$

$$\mathrm{div}\left(-\sigma\left(\frac{\partial\mathbf{A}}{\partial t} + \mathbf{grad}\,V\right)\right) = 0, \tag{2.38}$$

$$\mathbf{n} \times \mathbf{rot}\,\mathbf{A}|_{\Gamma_N} = 0, \tag{2.39}$$

$$\mathbf{n} \times \mathbf{A}|_{\Gamma_D} = 0, \tag{2.40}$$

$$\mathbf{n} \cdot \mathbf{grad}\,V|_{\Gamma_N} = 0, \tag{2.41}$$

$$V|_{\Gamma_D} = 0. \tag{2.42}$$

- Transient, with magnetic scalar potential Φ and electric vector potential $\mathbf{T}$:

$$\mathbf{rot}(\rho\,\mathbf{rot}\,\mathbf{T}) + \mu\frac{\partial}{\partial t}\left(\mathbf{T} - \mathbf{grad}\,\Phi\right) = 0, \tag{2.43}$$

$$\mathrm{div}(\mathbf{T} - \mu\,\mathbf{grad}\,\Phi) = 0, \tag{2.44}$$

$$\mathbf{n} \times (\mathbf{T}|_{\Gamma_N} - \mu\,\mathbf{grad}\,\Phi|_{\Gamma_N}) = 0, \tag{2.45}$$

$$\mathbf{n} \cdot (\mathbf{T}|_{\Gamma_D} - \mu\,\mathbf{grad}\,\Phi|_{\Gamma_D}) = 0. \tag{2.46}$$

It should be noted that, in general, the electric potentials are not defined on the whole domain Ω. In particular, the electric scalar potential V and the electric vector potential $\mathbf{T}$ are only defined in the electrically conducting regions Ω_C, i.e. where $\sigma \neq 0$. The symmetry can be noticed between the dual formulations $\mathbf{A} - V$ and $\mathbf{T} - \Phi$, each requiring both a scalar and a vector potential for the electric and magnetic quantities. Many authors have studied their characteristics in the framework of finite elements [21, 80, 143, 144, 148, 208]. Essentially, both formulations should converge towards the same value, using different numbers of degrees of freedom. For a geometry with large air volume, the $\mathbf{T} - \Phi$ formulation generates a smaller system of equations, since only a scalar potential is needed in these regions. The main drawback of this formulation is the need for generating electric cuts, usually utilizing a tree-cotree approach, for gauging the fields and linking non simply-connected elements [136, 232]. Certain techniques incorporate the gauge equation $\mathrm{div}\,\cdot = 0$, as an additional term in the formulation. Other techniques introduce a fictive potential, in terms of the
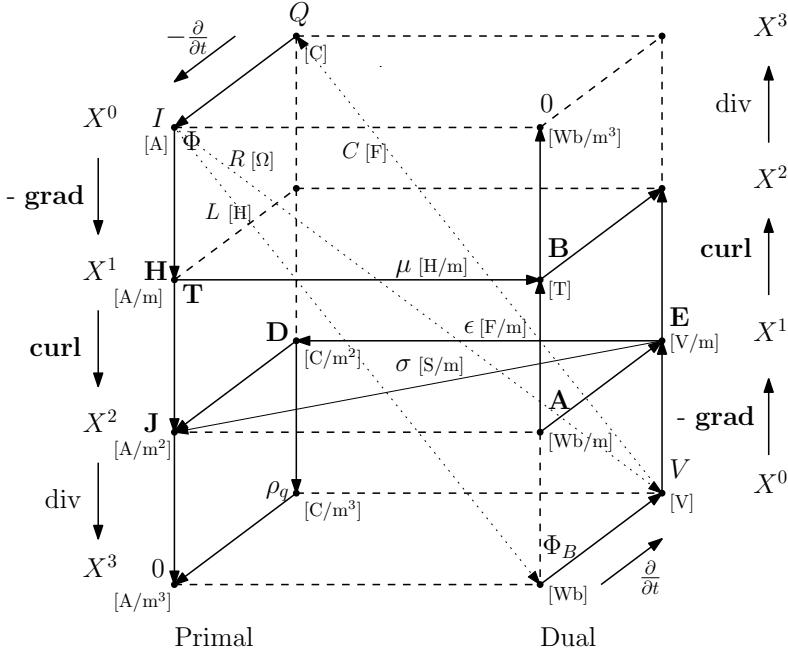
Figure 2.5: Maxwell's house.

Lagrange multipliers, in order to gauge the system. These discretization techniques are called *mixed formulations* and are detailed in Section 3.3.1.

Maxwell's equations describing the different electromagnetic interactions among potentials, fields, and their spatial and time derivatives can be represented in a general Tonti diagram [25], also called Maxwell's house [91] in the particular case of electromagnetic problems. These interaction representations can be generalized to all branches of physics by using the concept of Formal Graphs [222]. The Maxwell's house representation establishes the link between differential geometry and algebraic topology [212, 213]. In Fig. 2.5, the relations among the vectorial electromagnetic fields and potentials are represented with continuous lines, while the electrical circuit connections among scalar fields and potentials are represented with dotted lines. The fields from different levels or functional space X^i, are derived vertically from one another through the differential operators, namely the gradient, the rotational or curl, and the divergence. On the same horizontal level, the fields are linked through constitutive equations, that correspond to the Hodge transformations [10].

2.3.2   Constitutive equations

Most physical field simulations require the ability to model nonlinear material characteristics, for example, $\nu(B)$, $\sigma(E)$, $\kappa(T)$, that are the magnetic reluctivity, electric conductivity, and thermal conductivity, respectively. These nonlinear characteristics generate a nonlinear system of equations, which necessitates iterative techniques to resolve. Two techniques are introduced in Section 3.5 to resolve the nonlinear system, namely the fixed-point method (FPM), and the Newton-Raphson method (NRM). In this thesis, nonhysteretic, isotropic materials are considered. Therefore, the nonlinear relation acts on single-valued scalar values. However, in the general case, these quantities are tensors [51], and can be reinterpreted as Hodge-like operators [10].

In Fig. 2.6, the typical nonlinear relationship between B and H moduli quantities are exemplified. In the simulations, only the first quadrant of the characteristic is utilized. Furthermore, in Fig. 2.6, the effects of the nonlinear relationship on sinusoidal input signals are shown: it produces an output with different amplitude and higher-order time-harmonic content. Solving for such a behavior is the focus of Chapter 4.
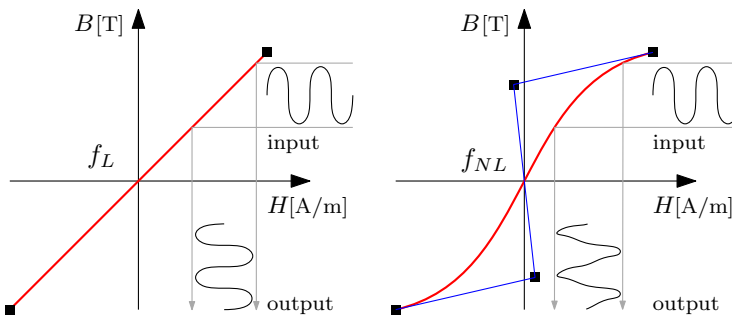
Figure 2.6: Linear and nonlinear B-H characteristic, where the black squares are control points and the blue line is the control net.

Another use of the B-spline functions can be introduced: the curve interpolation. Indeed, B-H curves are obtained using steel measurement techniques, which results in a data set. A cubic B-spline or NURBS can be fitted to this data, in order to smooth the derivative of the B-H curve and increase the convergence rate of a given nonlinear solver. Moreover, the multivariate B-splines and NURBS can advantageously represent higher-dimensional data sets, which naturally arise from hysteresis measurements, as shown in Fig. 2.7. Major loops (ML) or rather branches, first-order reversal curves (FORC), and second-order reversal curves (SORC) can be successively interpolated by NURBS curve, surface, and volume, respectively, as shown in Fig. 2.8. This interpolation can be the result of an optimization making use of skinning operations [119, 197]. The resulting light and smooth interpolant can then be used in
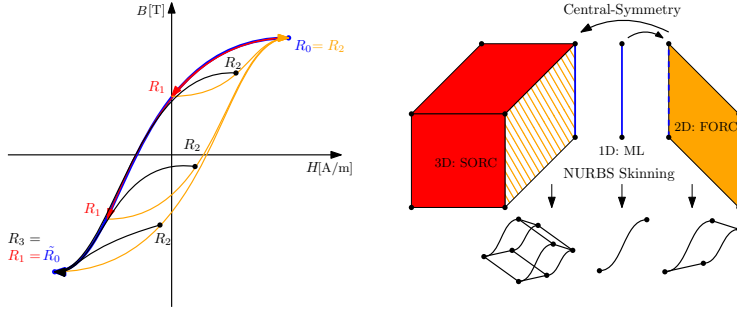
Figure 2.7: Major loops or branches (ML) in red (R_0R_1), first-order reversal curves (FORC) in orange (R_1R_2), second-order reversal curves (SORC) in black (R_2R_3), obtained by interpolating and skinning NURBS curves, surfaces and volume, respectively.
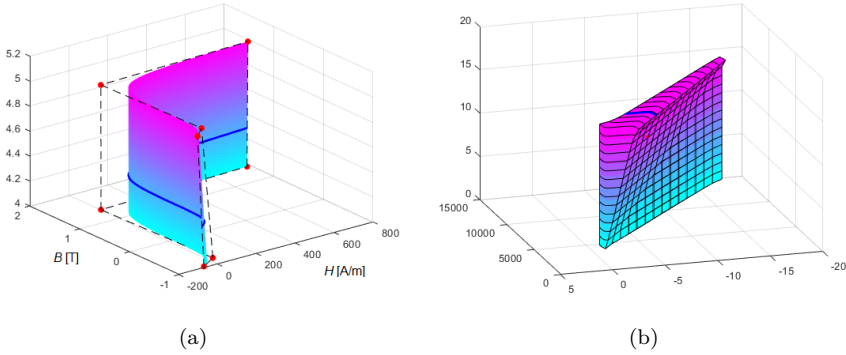
Figure 2.8: a) NURBS Surface interpolation of FORC, plotted with control net, b) NURBS Volume interpolation of SORC, plotted with knot subdivision. The axes are arbitrary, since the figure represents a collection of curves, that have to be shifted back to the origin to recover their physical meaning.

hysteresis models, such as the Preisach model or congruency-based models [239]. The hysteretic models are not used throughout the thesis.

2.4 Functional spaces

2.4.1 Functional analysis

This section introduces the spaces necessary to describe the electromagnetic problems defined in Section 2.3.1. Taking $\Omega \in \mathbb{R}^3$, a Lipschitz domain bounded by $\partial\Omega =$

$\Gamma_N \cup \Gamma_D$, a boundary where the Dirichlet and Neumann boundary conditions can be imposed. The first spaces to be defined are the functional spaces of Lebesgue, that can accommodate physical fields of finite energy. They consist in the set of square-integrable functions denoted $L^2(\Omega)$ and $\mathbf{L}^2(\Omega)$ for both scalar and vector spaces:

$$L^2(\Omega) = \left\{ u : \Omega \to \mathbb{R}, \ \int_\Omega |u(\mathbf{x})|^2 \ d\Omega < \infty \right\}, \tag{2.47}$$

$$\mathbf{L}^2(\Omega) = \left\{ \mathbf{u} : \Omega \to \mathbb{R}, \ \int_\Omega |\mathbf{u}(\mathbf{x})|^2 \ d\Omega < \infty \right\}, \tag{2.48}$$

together with their scalar products and associated norms:

$$(u, v)_{L^2(\Omega)} = \int_\Omega u \, v \, d\Omega, \qquad \forall \, u, v \in L^2(\Omega), \tag{2.49}$$

$$\langle u, v \rangle_{L^2(\Gamma)} = \int_\Gamma u \, v \, d\Gamma, \qquad \forall \, u, v \in L^2(\Omega), \tag{2.50}$$

$$(\mathbf{a}, \mathbf{b})_{\mathbf{L}^2(\Omega)} = \int_\Omega \mathbf{a} \cdot \mathbf{b} \, d\Omega, \qquad \forall \, \mathbf{a}, \mathbf{b} \in \mathbf{L}^2(\Omega), \tag{2.51}$$

$$\langle \mathbf{a}, \mathbf{b} \rangle_{\mathbf{L}^2(\Gamma)} = \int_\Gamma \mathbf{a} \cdot \mathbf{b} \, d\Gamma, \qquad \forall \, \mathbf{a}, \mathbf{b} \in \mathbf{L}^2(\Gamma), \tag{2.52}$$

$$\|u\|_{L^2(\Omega)} = \sqrt{(u, u)^2_{L^2(\Omega)}}, \qquad \forall \, u \in L^2(\Omega), \tag{2.53}$$

$$\|\mathbf{a}\|_{\mathbf{L}^2(\Omega)} = \sqrt{(\mathbf{a}, \mathbf{a})^2_{\mathbf{L}^2(\Omega)}}, \qquad \forall \, \mathbf{a} \in \mathbf{L}^2(\Omega). \tag{2.54}$$

Secondly, the Sobolev spaces $H^1(\Omega)$ and $\mathbf{H}^1(\Omega)$ are defined as:

$$H^1(\Omega) = \left\{ u \in L^2(\Omega), \ \frac{\partial u}{\partial x_i} \in L^2(\Omega), \ i = 1, 2, 3. \right\}, \tag{2.55}$$

$$\mathbf{H}^1(\Omega) = \left\{ \mathbf{u} \in \mathbf{L}^2(\Omega), \ \frac{\partial \mathbf{u}}{\partial x_i} \in \mathbf{L}^2(\Omega), \ i = 1, 2, 3. \right\}. \tag{2.56}$$

The functional Hilbert spaces associated with the differential operators **grad**, **rot**, and div, are defined as follows:

$$H(\mathbf{grad}, \ \Omega) = \left\{ u \in L^2(\Omega), \ \mathbf{grad} \ u \in \mathbf{L}^2(\Omega) \right\}, \tag{2.57}$$

$$\mathbf{H}(\mathbf{rot}, \ \Omega) = \left\{ \mathbf{u} \in \mathbf{L}^2(\Omega), \ \mathbf{rot} \ \mathbf{u} \in \mathbf{L}^2(\Omega) \right\}, \tag{2.58}$$

$$\mathbf{H}(\mathrm{div}, \ \Omega) = \left\{ \mathbf{u} \in \mathbf{L}^2(\Omega), \ \mathrm{div} \ \mathbf{u} \in L^2(\Omega) \right\}, \tag{2.59}$$

together with their associated scalar products and norms:

$$(u, v)_{H(\mathbf{grad},\ \Omega)} = (u, v)_{L^2(\Omega)} + (\mathbf{grad}\ u, \mathbf{grad}\ v)_{\mathbf{L}^2(\Omega)},\ \forall\ u, v \in H^1(\Omega), \quad (2.60)$$

$$(\mathbf{a}, \mathbf{b})_{\mathbf{H}(\mathbf{rot},\ \Omega)} = (\mathbf{a}, \mathbf{b})_{\mathbf{L}^2(\Omega)} + (\mathbf{rot}\ \mathbf{a}, \mathbf{rot}\ \mathbf{b})_{\mathbf{L}^2(\Omega)}, \qquad \forall\ \mathbf{a}, \mathbf{b} \in \mathbf{H}^1(\Omega), \quad (2.61)$$

$$(\mathbf{a}, \mathbf{b})_{\mathbf{H}(\mathrm{div},\ \Omega)} = (\mathbf{a}, \mathbf{b})_{\mathbf{L}^2(\Omega)} + (\mathrm{div}\ \mathbf{a}, \mathrm{div}\ \mathbf{b})_{L^2(\Omega)}, \qquad \forall\ \mathbf{a}, \mathbf{b} \in \mathbf{H}^1(\Omega), \quad (2.62)$$

$$\|u\|_{H(\mathbf{grad},\ \Omega)} = \sqrt{\|u\|_{L^2(\Omega)}^2 + \|\mathbf{grad}\ u\|_{\mathbf{L}^2(\Omega)}^2}, \qquad \forall\ u \in H^1(\Omega), \qquad (2.63)$$

$$\|\mathbf{a}\|_{\mathbf{H}(\mathbf{rot},\ \Omega)} = \sqrt{\|\mathbf{a}\|_{\mathbf{L}^2(\Omega)}^2 + \|\mathbf{rot}\ \mathbf{a}\|_{\mathbf{L}^2(\Omega)}^2}, \qquad \forall\ \mathbf{a} \in \mathbf{H}^1(\Omega), \qquad (2.64)$$

$$\|\mathbf{a}\|_{\mathbf{H}(\mathrm{div},\ \Omega)} = \sqrt{\|\mathbf{a}\|_{\mathbf{L}^2(\Omega)}^2 + \|\mathrm{div}\ \mathbf{a}\|_{L^2(\Omega)}^2}, \qquad \forall\ \mathbf{a} \in \mathbf{H}^1(\Omega). \qquad (2.65)$$

An additional norm is introduced to analyze and split the different contributions within the norm on $\mathbf{H}(\mathbf{rot},\ \Omega)$:

$$\|\mathbf{a}\|_{\mathbf{H}_{\mathbf{rot}}} = \sqrt{\|\mathbf{rot}\ \mathbf{a}\|_{\mathbf{L}^2(\Omega)}^2}, \qquad\qquad \forall\ \mathbf{a} \in \mathbf{H}^1(\Omega). \quad (2.66)$$

Finally, the Hilbert sub-spaces denoted with a subscript 0 can be derived from the earlier definition by adding a requirement on the Dirichlet boundary conditions, such that:

$$H_0(\mathbf{grad},\ \Omega) = \left\{ u \in L^2(\Omega),\ \mathbf{grad}\ u \in \mathbf{L}^2(\Omega),\ u|_{\Gamma_D} = 0 \right\}, \qquad (2.67)$$

$$\mathbf{H}_0(\mathbf{rot},\ \Omega) = \left\{ \mathbf{u} \in \mathbf{L}^2(\Omega),\ \mathbf{rot}\ \mathbf{u} \in \mathbf{L}^2(\Omega),\ \mathbf{n} \times\ \mathbf{u}|_{\Gamma_D} = 0 \right\}, \qquad (2.68)$$

$$\mathbf{H}_0(\mathrm{div},\ \Omega) = \left\{ \mathbf{u} \in \mathbf{L}^2(\Omega),\ \mathrm{div}\ \mathbf{u} \in L^2(\Omega),\ \mathbf{n} \cdot\ \mathbf{u}|_{\Gamma_D} = 0 \right\}. \qquad (2.69)$$

The following notations are introduced, where the 0 subscript can be also added to specify the subspaces incorporating the Dirichlet boundary conditions or vanishing traces:

$$X^0 = H^1(\Omega) = H(\mathbf{grad},\ \Omega), \qquad (2.70)$$

$$X^1 = \mathbf{H}(\mathbf{rot},\ \Omega), \qquad (2.71)$$

$$X^2 = \mathbf{H}(\mathrm{div},\ \Omega), \qquad (2.72)$$

$$X^3 = L^2(\Omega). \qquad (2.73)$$

The domain Ω represents the physical domain and $\hat{\Omega}$ corresponds to the parametric domain, both are linked by a continuous differentiable parametrization $\mathbf{F}$ or map, such that $\mathbf{F} : \hat{\Omega} \to \Omega$. Therefore, all the spaces defined on Ω can be sent onto the

parametric domain by *pullbacks* defined as:

$$\iota^0(u) = u \circ \mathbf{F}, \qquad\qquad \forall\, u \in X^0 \qquad (2.74)$$

$$\iota^1(\mathbf{a}) = (D\mathbf{F})^T(\mathbf{a} \circ \mathbf{F}), \qquad\qquad \forall\, \mathbf{a} \in X^1 \qquad (2.75)$$

$$\iota^2(\mathbf{b}) = \det(D\mathbf{F})(D\mathbf{F})^{-1}(\mathbf{b} \circ \mathbf{F}), \qquad\qquad \forall\, \mathbf{b} \in X^2 \qquad (2.76)$$

$$\iota^3(v) = \det(D\mathbf{F})(v \circ \mathbf{F}), \qquad\qquad \forall\, v \in X^3 \qquad (2.77)$$

where, $(D\mathbf{F})$ represents the Jacobian of the parametrization. The commuting de Rham diagram is satisfied:

$$
\begin{array}{ccccccccc}
\mathbb{R} & \longrightarrow & \hat{X}^0 & \xrightarrow{\widehat{\mathbf{grad}}} & \hat{X}^1 & \xrightarrow{\widehat{\mathbf{rot}}} & \hat{X}^2 & \xrightarrow{\widehat{\mathrm{div}}} & \hat{X}^3 & \longrightarrow & 0 \\
& & \uparrow{\iota^0} & & \uparrow{\iota^1} & & \uparrow{\iota^2} & & \uparrow{\iota^3} & & \\
\mathbb{R} & \longrightarrow & X^0 & \xrightarrow{\mathbf{grad}} & X^1 & \xrightarrow{\mathbf{rot}} & X^2 & \xrightarrow{\mathrm{div}} & X^3 & \longrightarrow & 0.
\end{array}
\qquad (2.78)
$$

The structure of the de Rham diagram enables the construction of well-behaved approximation spaces for discretizing physical problems relying on the differential operators. The pullbacks for the approximation spaces are called:

- grad-conforming transformation for ι^0,

- curl-conforming transformation for ι^1,

- div-conforming or *Piola* transformation for ι^2,

- integral-conforming transformation for ι^3.

These transformations can be used to create edge and face elements, known as the Nédélec and Raviart-Thomas elements, respectively. These elements are commonly used in structure-preserving discretization, also called compatible spaces. The Raviart-Thomas elements [95] are used for Navier-Stokes problems in fluid mechanics. The Nédélec elements of the first family [165] are used for the electromagnetic problems resulting from Maxwell's equations [66, 67]. Their construction is detailed in Section 2.4.3.

2.4.2   Approximation spaces

To discretize the partial differential equations that describe the physical phenomena of interest, building suitable approximation spaces is necessary. Tridimensional approximation spline spaces are constructed from the univariate B-splines $N_{i,p}$ on a given knot vector Ξ, such as:

$$S^p(\Xi) = \mathrm{span}\left\{N_{i,p},\ i = 1, 2, 3\right\}. \qquad (2.79)$$

In the full notation $S_{r,h}^p(\Xi)$, designates an univariate space of degree p, of regularity r, and mesh refinement h. When not specified, it is considered that the spaces are formed with maximum regularity, i.e. $r = p - 1$. The derivative of a spline defined on Ξ', is a spline defined on the corresponding $(p - 1)$ open knot vector without the boundary knot repetition:

$$S^p(\Xi) \xrightarrow{\frac{d}{d\xi}} S^{p-1}(\Xi').$$

The knot vector argument Ξ is removed for clarity and compactness. The physics to be simulated evolves in three spatial dimensions, therefore the trivariate spline setting is of interest. Subsequently, the following approximation spaces are constructed and denoted with the subscript h:

$$\hat{X}_h^0 = S^{p_1,p_2,p_3}, \tag{2.80}$$

$$\hat{X}_h^1 = S^{p_1-1,p_2,p_3} \times S^{p_1,p_2-1,p_3} \times S^{p_1,p_2,p_3-1}, \tag{2.81}$$

$$\hat{X}_h^2 = S^{p_1,p_2-1,p_3-1} \times S^{p_1-1,p_2,p_3-1} \times S^{p_1-1,p_2-1,p_3}, \tag{2.82}$$

$$\hat{X}_h^3 = S^{p_1-1,p_2-1,p_3-1}. \tag{2.83}$$

These spaces form the spline approximation of the de Rham complex, or spline complex [18], and are an exact sequence. Moreover, the analogous diagram applies to the approximation spaces incorporating the boundary conditions $\hat{X}_{0,h}^i$, $i = 0, 1, 2, 3$. This spline complex constitutes the spline extension of finite elements discrete differential forms, such as the Whitney forms [24, 229] and k-forms [9, 109]. A periodic table of finite elements exists [8], which is organized following the theory of finite element exterior calculus [10].

When assembling multiple patches, the continuity at the interface between the elements has to be imposed such that the de Rham complex sequence holds. In particular, denoting the trace γ, a basis function $\mathbf{v}$, and the normal to the interface $\mathbf{n}$, the following continuities should be imposed:

- trace continuity, $\gamma \mathbf{v} = \mathbf{v}$, for $\hat{X}_h^0$,

- tangential trace continuity, $\gamma_t \mathbf{v} = \mathbf{n} \times (\mathbf{v} \times \mathbf{n})$, for $\hat{X}_h^1$,

- normal trace continuity, $\gamma_n \mathbf{v} = \mathbf{v} \cdot \mathbf{n}$, for $\hat{X}_h^2$

- no continuity for $\hat{X}_h^3$.

Such a construction is simplified for fully matching conformity between the patches, as long as the same orientation of the boundary spaces between the patches is respected. In case the discontinuous Galerkin method is employed, the interface conditions

have to be added to the formulation, to handle the jump and mean values across the interface [34]. This is detailed in Section 5.3 for the spaces $\hat{X}_h^0$ and $\hat{X}_h^1$, which discretize the two- and three-dimensional electromagnetic problems, respectively.

2.4.3   High-order generalization of mixed spaces

Isogeometric generalizations of mixed finite elements families [82] are suited for a proper discretization of mixed formulations and satisfies the *inf-sup* or *Babuška-Brezzi* condition [13, 28], which guarantees stability of the solution. Such compatible pairs of spaces have originally been developed for the Stokes problem [30] and are div-conforming. The mixed isogeometric spline spaces are:

- Taylor-Hood
  $$\begin{cases} \widehat{\boldsymbol{V}}_h^{\text{TH}} = (S^{p_1,p_2,p_3})^3, \\ \widehat{Q}_h^{\text{TH}} = S^{p_1-1,p_2-1,p_3-1}. \end{cases}$$

- Raviart-Thomas
  $$\begin{cases} \widehat{\boldsymbol{V}}_h^{\text{RT}} = S^{p_1,p_2-1,p_3-1} \times S^{p_1-1,p_2,p_3-1} \times S^{p_1-1,p_2-1,p_3}, \\ \widehat{Q}_h^{\text{RT}} = S^{p_1-1,p_2-1,p_3-1}. \end{cases}$$

- Nédélec of the second family
  $$\begin{cases} \widehat{\boldsymbol{V}}_h^{\text{NDL}} = S_{p_1-1,p_2-2,p_3-2}^{p_1,p_2,p_3} \times S_{p_1-2,p_2-1,p_3-2}^{p_1,p_2,p_3} \times S_{p_1-2,p_2-1,p_3-2}^{p_1,p_2,p_3}, \\ \widehat{Q}_h^{\text{NDL}} = S_{p_1-2,p_2-2,p_3-2}^{p_1-1,p_2-1,p_3-1}. \end{cases}$$

- Sub-grid
  $$\begin{cases} \widehat{\boldsymbol{V}}_h^{\text{SG}} = (S_{h/2}^{p_1,p_2,p_3})^3, \\ \widehat{Q}_h^{\text{SG}} = S_{h/2}^{p_1-1,p_2-1,p_3-1}. \end{cases}$$

All the corresponding isogeometric physical spaces are then defined through the div-preserving and integral-preserving transform, for the vector and scalar spaces, respectively. A numerical comparison of approximation properties of these mixed spaces in the context of the finite cell method can be found in [114]. Nédélec elements of the first family [165] are curl-conforming and they are the preferred discretization for Maxwell's equations. The Raviart-Thomas elements and the Nédélec elements of the second family [165] are the preferred discretizations for the Navier-Stokes equations.

2.4.4   The Lagrange multipliers and saddle point problems

As described in the potential formulation, (2.30), (2.34), (2.38), (2.44) impose a constraint or a gauge on the divergence of the fields. Taking $\mathbf{u} \in \mathbf{H}_0(\mathbf{rot},\ \Omega)$, a common

example of physical constraint is:

$$\operatorname{div} \mathbf{u} = 0. \tag{2.84}$$

One option to impose this constraint strongly and pointwise would be to construct the following functional space:

$$\mathbf{V}_0 = \mathbf{H}_0(\mathbf{rot},\ \Omega) \cap \mathbf{H}_0(\operatorname{div},\ \Omega). \tag{2.85}$$

Finding such a subspace can be a challenging task. An alternative method is to apply the Lagrange multiplier method [28] to remove the strong constraint from the functional space and instead impose it in a weak sense. Indeed, there is the equivalence:

$$(\operatorname{div} \mathbf{u} = 0 \quad \text{in } \Omega) \quad \Leftrightarrow \quad \left(\int_\Omega q \operatorname{div} \mathbf{u} \, \mathrm{d}\Omega = 0, \quad \forall q \in L_0^2(\Omega) \right), \tag{2.86}$$

$$\Leftrightarrow \quad \left(\int_\Omega \mathbf{grad}\ q \cdot \mathbf{u} \, \mathrm{d}\Omega = 0, \quad \forall q \in H_0^1(\Omega) \right). \tag{2.87}$$

Satisfying these constraints through minimization leads to saddle point problems and therefore to mixed variational formulations. This approach is exemplified in Section 3.3.1. As two or more fields coexist in the formulations, the order and continuity of the basis functions need to be chosen carefully to yield compatible discretizations, as described in Section 2.4.3.

2.5   Conclusion

In this chapter, the fundamental elements necessary to conduct an isogeometric analysis of electromagnetic problems have been introduced. First, the construction of the basis functions, such as B-splines, NURBS, and THB-splines have been detailed. Geometry discretization of conforming and nonconforming grids have been briefly introduced. Second, Maxwell's equations and their underlying structure have been described. Nonlinear single-valued and hysteretic constitutive equations for the electromagnetic problems have been presented, moreover, data interpolation structure using splines has been discussed. Finally, the functional spaces and the elements necessary to construct them have been introduced. They guarantee the stability and follow the same structure as the physical fields they discretize. These functional spaces, and especially the Nédélec elements of the first family are used in the discretization of the 3D magnetostatic and eddy current problems for which the variational formulations are detailed in the next chapter.

Chapter 3

Maxwell's solvers for quasi-static electromagnetic problems

IN this chapter, the functional spaces are applied to the discretization of the low-frequency Maxwell's equations and lead to the variational formulation of the static and eddy current problems. This results in different solvers that span both two-dimensional and three-dimensional space discretizations, which require different functional space structures for the electromagnetic potentials. Two methods are detailed for solving magnetostatic problems with nonlinear material characteristics. Linear eddy current problems are discussed in the specific harmonic regime as well as in the more general transient regime.

3.1   2D Cartesian linear magnetostatics

Considering a magnetostatic problem in the (x, y) plane, it follows that $\mathbf{B} = B_x \mathbf{e}_x + B_y \mathbf{e}_y + 0 \mathbf{e}_z$ and the magnetic vector potential $\mathbf{A} = A_z \mathbf{e}_z$ is reduced to a scalar field. In 2D, A_z is obviously independent of z, and therefore div $\mathbf{A} = 0$ falls naturally. Taking J_s the imposed electrical current density in the coil regions and $\mathbf{B}_r$ the remanent magnetic flux density of the permanent magnets, the strong form in 2D is a Laplace problem which reads:

$$\text{div}(\nu(\mathbf{x})\mathbf{grad}\ A) = J_s + \nu(\mathbf{x})\mathbf{rot}\ \mathbf{B}_r, \tag{3.1}$$

$$A|_{\Gamma_D} = 0. \tag{3.2}$$

The discrete solution approximation of the PDE is obtained with the Galerkin method. The isoparametric approach is chosen, meaning that the same approximation space is taken as the scalar space $V_h = X_{0,h}^0$, which is a subset of the bivariate B-spline grad-conforming basis functions that vanish on the Dirichlet boundary Γ_D, as defined in Section 2.4.1, for both the test v_h and trial u_h functions. The *variational formulation* of the boundary value problem reads: *Find $u_h \in V_h$, such that:*

$$a(u_h, v_h) = b(v_h) = (f, v_h), \ \forall\ v_h \in V_h. \tag{3.3}$$

The solution is written as a linear combination of general B-spline basis functions ω_i, which span the approximation space V_h, such that dim $V_h = N_h$:

$$u_h = \sum_{j=1}^{N_h} \alpha_j \omega_j. \tag{3.4}$$

The bilinear operator for assembling the stiffness matrix entries and the inner product for assembling the right-hand side are given by:

$$a_{i,j} = \int_\Omega \nu(\mathbf{x})\ \mathbf{grad}\ \omega_j \cdot \mathbf{grad}\ \omega_i\ d\mathbf{x}, \tag{3.5}$$

$$b_i = \int_\Omega (J_s(\mathbf{x})\ \omega_i + \nu(\mathbf{x})\mathbf{B}_r(\mathbf{x}) \cdot \mathbf{rot}\ \omega_i)\ d\mathbf{x}, \tag{3.6}$$

where, $\mathbf{rot}$ is the 2D curl operator, which corresponds to a 90 degrees clockwise rotation of the gradient. In 2D Cartesian, $\mathbf{B} = \mathbf{rot}(A)$. In practice, for implementation purposes, the curl can be obtained using the product between the Levi-Civita symbol ϵ and the field gradient. In 2D, this antisymmetric matrix reads:

$$\epsilon_{ij} = \begin{pmatrix} 0 & 1 \\ -1 & 0 \end{pmatrix}. \tag{3.7}$$

The entries for the right-hand side given by the integral of a general function f are approximated numerically. The function f is tested against the basis function ω_i and is replaced by a Gaussian quadrature on N_{el} elements partitioning the domain Ω:

$$b_i = \int_\Omega f\ \omega_i\ d\mathbf{x} \simeq \sum_{k=1}^{N_{el}} \sum_{l=1}^{n_k} w_{l,k} f(\mathbf{x}_{l,k}) \omega_i, \tag{3.8}$$

where, for each element $w_{l,k}$ are the weights for the n_k quadrature points of position $\mathbf{x}_{l,k}$. The quadrature is done in the physical domain, using the appropriate mapping $\mathbf{F}$, its Jacobian, and the chain rule for composed functions. The essential boundary conditions are imposed weakly through a lifting and L^2 projection [221].

3.2   2D axisymmetric linear magnetostatics

For a magnetic problem in the (r, z) plane, the magnetic vector potential reduces to $\mathbf{A} = A_\theta \mathbf{e}_\theta$. In the axisymmetric (or cylindrical) coordinate system:

$$\mathbf{B} = \frac{1}{r}\mathbf{rot}(rA). \tag{3.9}$$

It is possible to introduce the change of variable proposed in [105]: $\tilde{A} = rA$, where r, is the radius. The variational formulation remains the same as in (3.3), only the entries for the bilinear operator read instead:

$$a_{i,j} = \int_\Omega \nu(\mathbf{x})\ \mathbf{grad}\ \omega_j \cdot \mathbf{grad}\ \omega_i\ \frac{1}{r}\ d\mathbf{x}. \tag{3.10}$$

where, $d\mathbf{x} = dxdy = drdz$, equivalently. It is clear from (3.10), that the central rotation axis $r = 0$ should be kept outside the considered geometry, by starting with a controllable offset for instance. It possible to avoid the singularity in the stiffness matrix, by first writing the weak form without operating a change of variables and then developing it to the axisymmetric case [132]. However, a singularity persists for the axial component of the magnetic flux density, in case integration points lie on the rotation axis, which is the case with for instance Gauss-Lobatto points in SEM [53].

A simple way of computing the solution of a 2D axisymmetrical systems without removing the central axis and without considering a change of variables is possible if the employed numerical software handles 3D geometries. It can be done by revolving the 2D cross-section around the central axis and assigning constant basis functions which yield a single degree-of freedom along the angular direction. The change of coordinate system is automatically accounted for during the matrix assembly via the Jacobian of the transformation.

3.3   3D linear magnetostatics
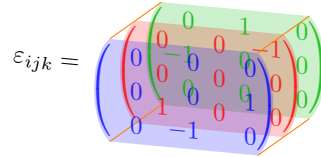
In the three-dimensional setting, all three components of the magnetic vector potential are non-zero. Therefore, a vector space has to be built on the refined geometrical mesh, and the Coulomb gauge condition (3.12) has to be imposed:

$$\mathbf{rot}(\nu(\mathbf{x})\mathbf{rot}\ \mathbf{A}) = \mu_0\left(\mathbf{J}_s + \nu(\mathbf{x})\mathbf{rot}\ \mathbf{B}_r\right), \tag{3.11}$$

$$\mathrm{div}\ \mathbf{A} = 0, \tag{3.12}$$

$$\mathbf{n} \times \mathbf{A}|_{\Gamma_D} = 0. \tag{3.13}$$

In practice, for forming the three-dimensional curl operator, the Levi-Civita symbol is used and is defined by:

$$\varepsilon_{ijk} = \tag{3.14}$$

3.3.1   Mixed formulation

To discretize the strong form (3.11), the *mixed formulation* or more precisely *Kikuchi's formulation* [134] is applied. It incorporates the Coulomb gauge, or *div-free property* defined in (3.12), by introducing an auxiliary Lagrange multipliers space Q_h. Such a mixed formulation reads: *Find $\boldsymbol{u}_h \in \boldsymbol{V}_h$ and $p_h \in Q_h$, such that:*

$$a(\mathbf{u}_h, \mathbf{v}_h) + c(\mathbf{v}_h, p_h) = (f, \mathbf{v}_h),\ \forall\ \mathbf{v}_h \in \mathbf{V}_h, \tag{3.15}$$

$$c(\mathbf{u}_h, q_h) = (0, q_h),\ \forall\ q_h \in Q_h. \tag{3.16}$$

The following pair of approximation spaces, $(\mathbf{V}_h,\ Q_h) = (X_h^1,\ X_h^0)$ is taken, as defined in Section 2.4.1, and the matrix entries of the bilinear operators read:

$$a_{i,j} = \int_\Omega \nu(\mathbf{x})\ \mathbf{rot}\ \boldsymbol{\omega}_j \cdot \mathbf{rot}\ \boldsymbol{\omega}_i\ d\mathbf{x}, \tag{3.17}$$

$$c_{i,j} = \int_\Omega \mathbf{grad}\ w_j \cdot \boldsymbol{\omega}_i\ d\mathbf{x}. \tag{3.18}$$

3.3.2   Regularization

Another way to discretize the strong form (3.11) while incorporating the gauge condition (3.12), is to use the regularization method. This regularization incorporates a
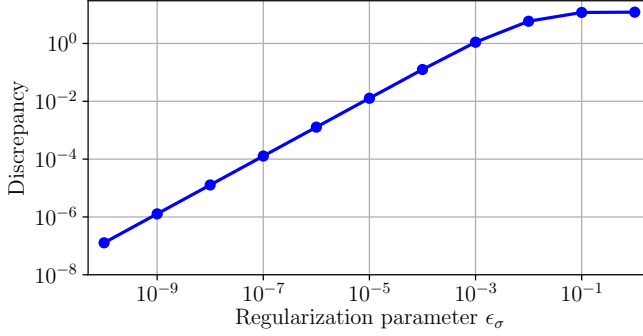
Figure 3.1: Convergence of the regularized solution towards the one obtained with the mixed formulation, in terms of the $\mathbf{H_{rot}}$ norm defined in (2.66).

fictitious conductivity ϵ_σ in the whole domain, and avoids the introduction of the Lagrange multipliers. It is also possible to take a singleton for the Lagrange multiplier space, in order to minimize the computational overhead. The regularized problem reads: *Find $\boldsymbol{u}_h \in \boldsymbol{V}_h$, such that:*

$$a(\mathbf{u}_h, \mathbf{v}_h) = (f, \mathbf{v}_h), \ \forall \ \mathbf{v}_h \in \mathbf{V}_h, \tag{3.19}$$

$$a_{i,j} = \int_\Omega \nu(\mathbf{x}) \ \mathbf{rot} \ \boldsymbol{\omega}_j \cdot \mathbf{rot} \ \boldsymbol{\omega}_i \ d\mathbf{x} + \int_\Omega \epsilon_\sigma \ \boldsymbol{\omega}_j \cdot \ \boldsymbol{\omega}_i \ d\mathbf{x}. \tag{3.20}$$

It can be shown that both formulations are converging towards the same solution, by reducing the value of the regularization parameter ϵ_σ by orders of magnitude. This convergence is illustrated in Fig. 3.1 and shows that both problem formulations are equivalent in magnetostatics. The value $\epsilon_\sigma = 10^{-7}$ is selected in the rest of the numerical experiments.

Although it has not been implemented in this thesis, in some cases, an additional coupling of the magnetic equations with the circuit equations might be required: for instance, to accurately predict the circulating and eddy current losses in windings of an electrical machine [149, 215]. Then, the mixed formulation is the most natural way to realize the circuit coupling, since the Lagrange multipliers $p_h \in Q_h$, therefore correspond with the electric scalar potential V. The electric field in the conductors is obtained using (2.27).

3.4 Global parameters computation

In magnetoquasistatics and throughout this thesis, the computation of global parameters, namely the magnetic force components F_i and the eddy current losses P, is of interest. The magnetic forces are computed from the Maxwell stress tensor (MST) $\sigma_{\text{MST},ij}$ following:

$$\sigma_{\text{MST},ij} = \frac{1}{\mu_0} B_i B_j - \frac{1}{2\mu_0} \delta_{ij} |\mathbf{B}|^2, \tag{3.21}$$

where, δ is the Kronecker symbol. This symmetric tensor of rank 2 in three dimensions is integrated from the viewpoint of the air, on the interface $\mathcal{S}$ enclosing the solid, where the magnetic force components F_i are calculated with:

$$F_i = \oint_{\mathcal{S}} \sigma_{\text{MST},ij} \cdot \mathbf{n}_j \ \mathrm{d}S, \tag{3.22}$$

where, $\mathbf{n}$ is the normal of the enclosing surface $\mathcal{S}$. This expression is further simplified on the Dirichlet and periodic boundaries, where the overall contribution to the forces is equal to zero. As an alternative to the Maxwell stress tensor approach, the virtual work principle is often used in the context of traditional finite elements [52].

The eddy current losses in an electrically conducting domain Ω_C are computed from the integration of the eddy current density, which is, in this thesis, solely obtained from the time-derivative of magnetic vector potential:

$$\mathbf{J} = -\sigma \frac{\partial \mathbf{A}}{\partial t}, \tag{3.23}$$

$$P = \int_{\Omega_C} \frac{|\mathbf{J}|^2}{\sigma} \ \mathrm{d}V, \tag{3.24}$$

where, σ is the electrical conductivity of the material, which can be a function of temperature and therefore, a function of the position, as considered in Chapter 6.

3.5 2D and 3D nonlinear magnetostatics

Many simulations require the ability to model nonlinear material characteristics, for instance the magnetic reluctivity $\nu(\mathbf{x}, \mathbf{B})$. Two techniques are introduced, namely the fixed-point method (FPM), and the Newton-Raphson method (NRM), to deal with the nonlinearity $\nu(\mathbf{x}, \mathbf{B})$. 2D and 3D nonlinear magnetostatic equations are first
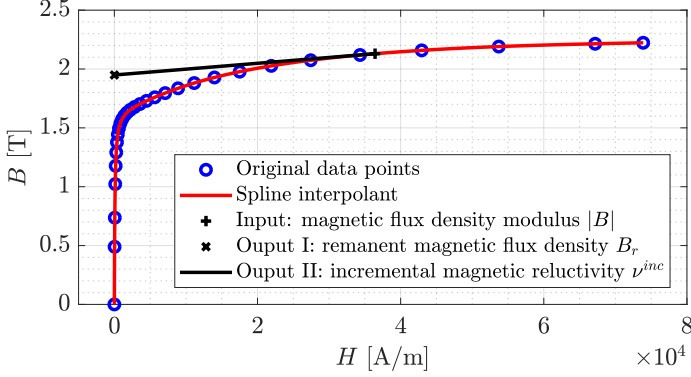
Figure 3.2: Graphical representation of the fixed-point algorithm used for the iterative calculation of the magnetic field distribution in presence of soft-magnetic materials with nonlinear characteristics.

introduced through the general nonlinear algebraic system of equations:

$$S(\mathbf{A})\mathbf{A} = \mathbf{J}, \qquad \text{with,} \qquad (3.25)$$

$$S_{i,j} = \int_\Omega \nu(\mathbf{x}, \mathbf{B}) \ \mathbf{grad} \ \omega_j \cdot \mathbf{grad} \ \omega_i \ d\mathbf{x}, \qquad \text{in 2D,} \qquad (3.26)$$

$$S_{i,j} = \int_\Omega \nu(\mathbf{x}, \mathbf{B}) \ \mathbf{rot} \ \boldsymbol{\omega}_j \cdot \mathbf{rot} \ \boldsymbol{\omega}_i \ d\mathbf{x}, \qquad \text{in 3D,} \qquad (3.27)$$

$$\mathbf{J}_i = \int_\Omega (\mathbf{J}_s \cdot \boldsymbol{\omega}_i + \nu(\mathbf{x})\mathbf{B}_r \cdot \mathbf{rot} \ \boldsymbol{\omega}_i) \ d\mathbf{x}. \qquad (3.28)$$

3.5.1   The fixed-point method

The fixed-point method (FPM) can be related to an application of a Picard iterative process to magnetics, and similar algorithms have been reported as the *B-H* curve linearization in MEC [160, 169, 224], or as the *locally convergent* version of the FPM in finite elements [70, 71]. The reluctivity $\nu(\mathbf{x}, \mathbf{B})$ is successively updated together with an additional source term $\mathbf{J}_{\text{iron}}$ in the right-hand side of (3.28), which consists of an equivalent remanent magnetic flux density, similar to a nonlinear permanent magnet. The version applied in this thesis is somewhat different from the original FPM: it has the advantage to be simpler to implement and can be graphically understood from the *B-H* curve exemplified in Fig. 3.2. Additionally, using a spline interpolation step ensures smooth derivatives that increase the convergence rates.

After an initialization with linear material characteristic, the reluctivity in the iron, is replaced at each quadrature point by the incremental reluctivity defined as:

$$\nu^{\mathrm{inc}}(\mathbf{x}, \mathbf{B}) = \frac{\partial H(B(\mathbf{x}))}{\partial B}, \tag{3.29}$$

where, $B(\mathbf{x}) = |\mathbf{B}(\mathbf{x})|$. This incremental reluctivity term should not be confused with the apparent reluctivity defined as:

$$\nu^{\mathrm{app}}(\mathbf{x}, \mathbf{B}) = \frac{H(B(\mathbf{x}))}{B}. \tag{3.30}$$

A supplementary source term is added with:

$$\mathbf{J}_{\mathrm{iron},i} = (\nu^{\mathrm{inc}}(\mathbf{x}, \mathbf{B})\boldsymbol{\alpha}(\mathbf{x}, \mathbf{B})B_r(\mathbf{x}, \mathbf{B}), \ \mathbf{rot}\ \boldsymbol{\omega}_i), \tag{3.31}$$

where, $\boldsymbol{\alpha} = \mathbf{B}B^{-1}$ represents the direction of the remanent flux density. As shown in Fig. 3.2, B_r is the intercept, which represents the remanent magnetic flux density in the iron, and ν^{inc} is the inverse of the slope of the tangent.

This technique is related to the physical behavior of the material, where the iron is expressed as a nonlinear permanent magnet. Furthermore, the FPM delivers good performance both in terms of local and global indicators [85]. Local accuracy is measured by the maximum error in the L^2, H^1, or H_{curl} norm of the potential solution, depending on the type of functional space used. Global accuracy is measured through the comparison of scalar parameters resulting from an integration, such as the magnetic energy, the magnetic force, or the inductance. Additionally, this method exhibits a linear convergence and certain robustness with respect to the mesh size and B-H characteristics, as demonstrated by Fig. 3.4 in the next subsection.

3.5.2   The Newton-Raphson method

Compared to the fixed-point method, the Newton-Raphson method has more of a mathematical background, which ensures a quadratic convergence of the residual. First, the general idea of the method is derived, before being applied to the magneto-static problem.

Let $\mathbf{f}$ be a vector of nonlinear equations, e.g. a residual, and $\mathbf{x}$ an unknown solution vector. The Newton-Raphson method writes:

$$\mathbf{f}(\mathbf{x}) = 0, \tag{3.32}$$

$$\mathbf{f}(\mathbf{x}_{k+1}) = \mathbf{f}(\mathbf{x}_k + \mathbf{d}_k) = \mathbf{f}(\mathbf{x}_k) + \frac{\partial \mathbf{f}}{\partial \mathbf{x}_k} \mathbf{d}_k + \mathcal{O}(\mathbf{d}_k^2) = 0, \tag{3.33}$$

$$J(\mathbf{x}_k)_{i,j} = \frac{\partial \mathbf{f}_i(\mathbf{x})}{\partial \mathbf{x}_j}. \tag{3.34}$$

The general algebraic system to resolve is:

$$J(\mathbf{x}_k)\mathbf{d}_k = -\mathbf{f}(\mathbf{x}_k), \tag{3.35}$$

where, J is the Jacobian matrix and $\mathbf{d}_k$ is the increment such that $\mathbf{x}_{k+1} = \mathbf{x}_k + \eta_k \mathbf{d}_k$, where $\eta_k \in [0,1]$ is a relaxation parameter chosen such that $|\mathbf{d}_k^\top \mathbf{f}(\mathbf{x}_k + \eta_k \mathbf{d}_k)|$ is minimum. In practice, this is achieved through a *line search* algorithm [181].

There are two main ways to express the Jacobian of the stiffness matrix for magnetic problems. Using the chain rule for derivation, the first way gives:

$$J_{i,j} = \frac{\partial S_{i,k}}{\partial \mathbf{A}_j} = \left(\frac{\partial \nu(\mathbf{B})}{\partial \mathbf{A}_k} \, \mathbf{rot} \, \boldsymbol{\omega_i}, \, \mathbf{rot} \, \boldsymbol{\omega_k} \right), \qquad \text{with} \tag{3.36}$$

$$\frac{\partial \nu(\mathbf{B})}{\partial \mathbf{A}_j} = \frac{\partial \nu(\mathbf{B})}{\partial \mathbf{B}} \frac{\partial \mathbf{B}}{\partial \mathbf{A}_j}, \tag{3.37}$$

where, $\mathbf{A}$ represents the magnetic vector potential. Using (3.29) and (3.30), each of these two terms can be written:

$$\frac{\partial \nu(\mathbf{B})}{\partial \mathbf{B}} = \frac{\partial}{\partial \mathbf{B}} \frac{H(B)}{B} = \frac{H'(B)B - H(B)}{B^2} = \frac{1}{B}(\nu^{\text{inc}} - \nu^{\text{app}})(B), \tag{3.38}$$

$$\frac{\partial \mathbf{B}}{\partial \mathbf{A}_j} = \mathbf{rot} \, \boldsymbol{\omega_j} \cdot \frac{\mathbf{B}}{B}. \tag{3.39}$$

The Jacobian matrix can be written as the sum of the stiffness matrix S_1 plus an additional incremental stiffness S_2:

$$J = S_1 + S_2, \tag{3.40}$$

$$S_{1,i,j} = (\nu^{\text{app}}(B) \, \mathbf{rot} \, \boldsymbol{\omega_i}, \, \mathbf{rot} \, \boldsymbol{\omega_j}), \tag{3.41}$$

$$S_{2,i,j} = \left((\nu^{\text{inc}} - \nu^{\text{app}})(B) \, \mathbf{rot} \, \boldsymbol{\omega_i} \cdot \frac{\mathbf{B}}{B}, \, \mathbf{rot} \, \boldsymbol{\omega_j} \cdot \frac{\mathbf{B}}{B} \right). \tag{3.42}$$

Although they are equivalent [98], the other way of expressing the Jacobian matrix entry is:

$$J_{i,j} = \left(\frac{\partial \mathbf{H}}{\partial \mathbf{B}} \ \mathbf{rot} \ \boldsymbol{\omega_i}, \ \mathbf{rot} \ \boldsymbol{\omega_j} \right), \qquad \text{with} \tag{3.43}$$

$$\frac{\partial \mathbf{H}}{\partial \mathbf{B}} = \nu^{\mathrm{app}}(\mathbf{B}) + \frac{\partial \nu(\mathbf{B})}{\partial \mathbf{B}} = \nu^{\mathrm{app}}(\mathbf{B}) + 2\mathbf{B}^2 \frac{\partial \nu(\mathbf{B})}{\partial \mathbf{B}^2}, \tag{3.44}$$

$$J_{i,j} = (\nu^{\mathrm{app}}(B) \ \mathbf{rot} \ \boldsymbol{\omega_i}, \ \mathbf{rot} \ \boldsymbol{\omega_j}) + \left(2\frac{\partial \nu(B)}{\partial B^2} \ \mathbf{rot} \ \boldsymbol{\omega_i} \cdot \mathbf{B}, \ \mathbf{rot} \ \boldsymbol{\omega_j} \cdot \mathbf{B} \right). \tag{3.45}$$

Finally, the considered isotropic formulation can be written as:

$$J\mathbf{d} = \mathbf{r}, \qquad \text{with} \tag{3.46}$$

$$J = S_1 + S_2, \tag{3.47}$$

$$\mathbf{r} = (f, \ v) - \ S_1 \mathbf{A}, \tag{3.48}$$

$$S_{1,i,j} = (\nu^{\mathrm{app}}(\mathbf{B}) \ \mathbf{rot} \ \boldsymbol{\omega_i}, \ \mathbf{rot} \ \boldsymbol{\omega_j}), \tag{3.49}$$

$$S_{2,i,j} = \left(2\frac{\partial \nu(B^2)}{\partial B^2} \ \mathbf{rot} \ \boldsymbol{\omega_i} \cdot \mathbf{B}, \ \mathbf{rot} \ \boldsymbol{\omega_j} \cdot \mathbf{B} \right). \tag{3.50}$$

and is implemented through its tensor form, reading in 3D:

$$S_{2,i,j} = \left(2\frac{\partial \nu(B^2)}{\partial B^2} \ \mathbf{rot} \ \boldsymbol{\omega_i} \begin{bmatrix} B_x^2 & B_x B_y & B_x B_z \\ B_x B_y & B_y^2 & B_y B_z \\ B_x B_z & B_y B_z & B_z^2 \end{bmatrix} \ \mathbf{rot} \ \boldsymbol{\omega_j} \right), \tag{3.51}$$

and in 2D:

$$S_{2,i,j} = \left(2\frac{\partial \nu(B^2)}{\partial B^2} \ \mathbf{grad} \ \omega_i \begin{bmatrix} B_y^2 & -B_x B_y \\ -B_x B_y & B_x^2 \end{bmatrix} \ \mathbf{grad} \ \omega_j \right). \tag{3.52}$$

The nonlinear magnetostatic problem of [85] is considered as a benchmark, which geometry and simensions are given in Appendix A. It consists of a C-core with a permanent magnet embedded in the magnetic circuit, which attracts a moving bar. The magnetostatic problem is solved with both the fixed-point method and the Newton-Raphson method in the isogeometric framework, and are compared with the NRM implemented in a commercial FEM software [42]. The resulting convergence plot shown in Fig. 3.3 is obtained. The NRM and FPM exhibit a similar linear convergence rate for the first five iterations. However, afterward, the convergence rate becomes quadratic for the NRM. Nonetheless, if a global parameter resulting from domain integration, for instance, the force is calculated, it can be seen in Fig. 3.4 that both methods perform similarly, for different uniform mesh h-refinements $(1/h)$ indicated in the legend. At the coarsest level, i.e. $(1/1)$ however, the NRM does not converge while the FPM does, which demonstrates a certain robustness advantage.
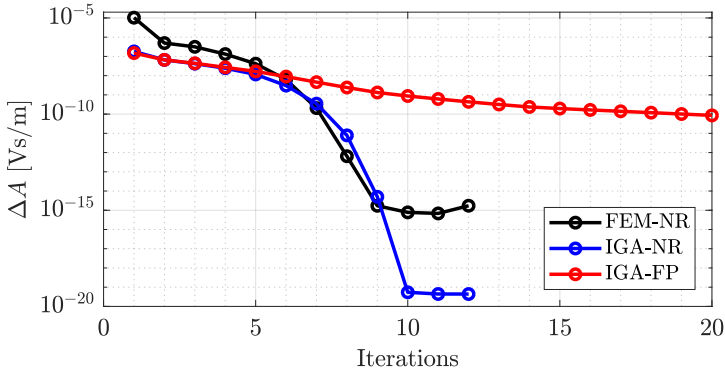
Figure 3.3: Convergence analysis of the fixed-point method and the Newton-Raphson method compared on the norm of the residual.
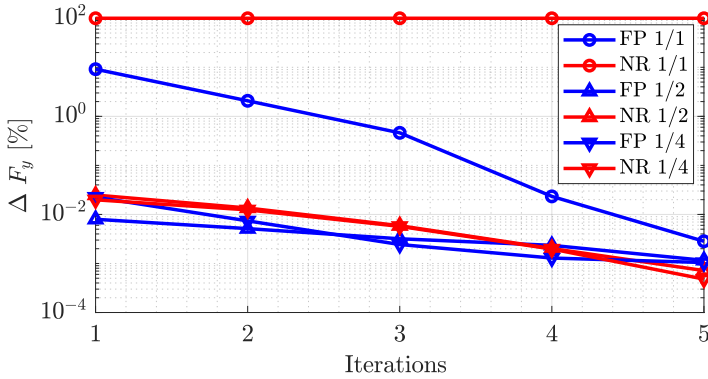
Figure 3.4: Convergence analysis of the fixed-point method and the Newton-Raphson method, for different mesh refinement $1/h$, compared on the computation of the attraction force F_y.

Therefore, one can start to iterate with the FPM and then continue with the NRM. This is similar to a hybrid method combining the Picard iterations for initialization, and the Newton iterations afterward [219]. However, the Picard iterations usually do not use the incremental reluctivity in conjunction with the remanent field density in the iron, as detailed with the FPM of section 3.5.1, but rather use an efficient line search along the increment direction.

As a remark, the derivation of the magnetic reluctivity is different depending on whether isotropic or anisotropic material magnetic properties are considered. Similarly, as derived in the isotropic system of equations (3.40-3.42) for the anisotropic

case, reluctivity tensors, $\bar{\boldsymbol{\nu}}$, are introduced that yield the following expression for the Jacobian:

$$J = S_1 + S_2, \tag{3.53}$$

$$S_{1,i,j} = (\bar{\boldsymbol{\nu}}^{\mathrm{app}}(\mathbf{B}) \, \cdot \, \mathbf{rot} \, \boldsymbol{\omega_i}, \, \mathbf{rot} \, \boldsymbol{\omega_j}), \tag{3.54}$$

$$S_{2,i,j} = ((\bar{\boldsymbol{\nu}}^{\mathrm{inc}} - \bar{\boldsymbol{\nu}}^{\mathrm{app}})(\mathbf{B}) \, \cdot \, \mathbf{rot} \, \boldsymbol{\omega_i}, \, \mathbf{rot} \, \boldsymbol{\omega_j}). \tag{3.55}$$

3.6   Steady-state thermal problems

Electromagnetic fields are often coupled to the thermal field in applications involving design optimization. In most electromechanical applications, the temperature constraints in the windings and permanent magnets constitute the main limiting factor. The thermal model influences the electromagnetic model through the temperature-dependent parameter $\sigma(T)$, where σ is the electrical conductivity, as well as the *B-H* characteristics of the material, although the latter is not considered in this thesis. The temperature influence on the remanent field of the permanent magnet $\mathbf{B}_r(T)$ is however considered in Chapter 6. Both parameters influence the penetration depth, i.e. the skin depth, of the eddy currents, and therefore the eddy current losses distribution. Throughout this thesis, steady-state solutions are of interest. The coupled problem can be either weakly or strongly coupled, meaning that the two (or more) fields are solved sequentially or simultaneously. Heat sources, P, are composed by Joule losses from electrical currents (imposed or eddy), and by the excess and hysteresis losses in the magnetic material if they are considered. These sources are imposed as a volumic density term b. Heat sinks are composed by thermal radiation and convection, both natural and forced. The thermal field, T, is a scalar field in both 2D and 3D spaces, therefore the variational formulation reads *Find $u_h \in V_h = X_h^0$, such that:*

$$a(u_h, v_h) = b(v_h) = (f, v_h), \; \forall \; v_h \in V_h. \tag{3.56}$$

where,

$$a_{i,j} = \int_\Omega \kappa(\mathbf{x}, T) \, \mathbf{grad} \, \omega_j \cdot \mathbf{grad} \, \omega_i \, d\mathbf{x}, \tag{3.57}$$

$$b_{\mathrm{source},i} = \int_{\Omega_{\mathrm{source}}} P \, \omega_i \, \mathrm{d}\mathbf{x}, \tag{3.58}$$

$$b_{\mathrm{conv},i} = \int_{\Gamma_{\mathrm{conv}}} h_{\mathrm{conv}}(T - T_0) \, \omega_i \, \mathrm{d}\mathbf{x}, \tag{3.59}$$

$$b_{\mathrm{rad},i} = \int_{\Gamma_{\mathrm{rad}}} \sigma_{\mathrm{SB}} \epsilon_{\mathrm{rad}}(T^4 - T_0^4) \, \omega_i \, \mathrm{d}\mathbf{x}. \tag{3.60}$$

where, κ is the thermal conductivity, h_{conv} is the convection coefficient or distribution, T_0 is the ambient temperature, σ_{SB} is the Stefan-Boltzmann constant, ϵ_{rad} is the emissivity. If radiation is present, it is crucial to solve in terms of the absolute temperature i.e. in Kelvin. Nonlinearities are present in (3.57) and (3.60), and are resolved using the Newton-Raphson method.

If the thermal model is in a 2D axisymmetric coordinate system, the bilinear operator and the right-hand side entries are adapted according to:

$$a_{i,j} = \int_\Omega \kappa(\mathbf{x}, T)\ \mathbf{grad}\ \omega_j \cdot \mathbf{grad}\ \omega_i\ r\ d\mathbf{x}, \tag{3.61}$$

$$b_i = \int_\Omega f\ \omega_i\ r\ d\mathbf{x}. \tag{3.62}$$

Scalar-valued convection coefficients, as well as emissivity and absorption coefficients, derived analytically for idealized geometries are often considered. However, in reality, these mechanisms are represented by a distribution on a given interface Γ. To identify the distribution of these coefficients for complicated geometries, empirical data can be obtained using thermopiles [106], or additional physics can be resolved using numerical models. For the convection-diffusion problem, computational fluid dynamic (CFD) models solving the Navier-Stokes equations with additional equations for accounting turbulence effects are required to obtain the convection distribution [187, 231]. To resolve the radiation problem, one would normally have to solve Maxwell's wave equation to calculate the emissivity and absorption distributions, which may involve ray tracing algorithms [83].

3.7   Linear magnetoharmonics

In magnetoharmonics, the transient formulation (2.37), is assumed to be time-periodic. Additionally, the linearity assumption allows for the superposition of multiple frequencies for the excitation and response of the system, that therefore can be solved sequentially. In particular, cross-coupling effects are not captured with this solver. Any time signal can be written equivalently in complex or real time-harmonic form.

First, a single frequency time-harmonic physical field u, can be written in complex form:

$$u(\mathbf{x}, t) = \mathrm{Re}(\widehat{u}(\mathbf{x})\ e^{j\omega t}), \tag{3.63}$$

where, $\widehat{u}(\mathbf{x})$ are the complex Fourier coefficients at each physical point. Therefore, by replacing the time derivative by the complex scalar factor $j\omega$, the complex magneto-harmonic formulation solves directly for the harmonic coefficients and reads: *Find*

$\widehat{u}_h \in V_h$, *such that:*

$$a(\widehat{u}_h, \widehat{v}_h) = (f, \widehat{v}_h), \ \forall \ \widehat{v}_h \in V_h, \tag{3.64}$$

$$a_{i,j} = \int_\Omega \nu(\mathbf{x}) \ \mathbf{grad} \ \omega_j \cdot \mathbf{grad} \ \omega_i \ d\mathbf{x} + j\omega \int_\Omega \tilde{\sigma} \ \omega_j \cdot \ \omega_i \ d\mathbf{x}, \tag{3.65}$$

where,

$$\tilde{\sigma} = \begin{cases} \sigma, & \text{if } \Omega_C \\ \epsilon_\sigma, & \text{if } \Omega_{NC} \end{cases} \tag{3.66}$$

depending on whether the region is electrically conducting (Ω_C) or not (Ω_{NC}). The regularization parameter, ϵ_σ, is the same as introduced in (3.20). The algebraic complex system of bilinear form a, is composed by two terms as depicted in (3.65), the first one is the stiffness matrix, S, while the second one is the mass matrix, M, which gives:

$$\left[\ S + M \ \right] \left[\ \widehat{u} \ \right] = \left[\ \widehat{f} \ \right]. \tag{3.67}$$

Alternatively, the complex form can be decoupled into the real and imaginary parts, following Euler's identity:

$$u(\mathbf{x}, t) = \tilde{u}_c(\mathbf{x}) \ \cos(\omega t) + \tilde{u}_s(\mathbf{x}) \ \sin(\omega t). \tag{3.68}$$

The coupled system of equation becomes:

$$\begin{bmatrix} S & M \\ -M & S \end{bmatrix} \begin{bmatrix} \tilde{u}_c \\ \tilde{u}_s \end{bmatrix} = \begin{bmatrix} \tilde{f}_c \\ \tilde{f}_s \end{bmatrix}. \tag{3.69}$$

The real system exhibits inherently twice the amount of degrees of freedom as compared to the complex system.

Some attempts were made to include nonlinearities in magnetoharmonic regime, by incorporating an equivalent B-H curve, which conserves the energy of the system [220]. However, no DC excitation from a static permanent magnet, nor nonlinear magnetic materials and cogging forces can be modeled accurately using only the magnetoharmonic approach. Instead, this can be realized by using the harmonic balance method [234], which is described in the isogeometric framework in Chapter 4.

3.8   Adaptive meshing

The goal of adaptive meshing is to refine the mesh locally based on error estimators. Such refinements are beneficial in regions where the solution field exhibits strong gradients, as well as to resolve singularities, which can originate from the geometry or the physics. In Section 2.2.3, the truncated hierarchical B-spline basis functions (THB) have been introduced. These functions exhibit advantageous properties for flexible local refinements, due to the simple children-parent relationships between basis functions belonging to nested mesh levels.

Residual-based refinement strategies are introduced in this section, and h-refinements are applied to the THB space. However, p-refinements are also possible and attractive for triangular elements or spectral elements for instance. Another strategy, namely *goal-oriented adaptive* refinement has been proposed [108, 145], where a dual basis is selected. This method is considered more powerful than the residual-based strategy, since it can indicate refinements nonlocal to the occurrence of the error, which is particularity relevant for non-elliptic problems. *Feature-based* refinement strategies can be considered, which do not require space enrichment, as opposed to the first two techniques mentioned, and form an indicator from available properties [133], e.g. divergence, gradient or wiggles, but this approach is very much problem-dependent.

Firstly, the two-dimensional quasi-static electromagnetic problems that are detailed in the previous sections of this chapter, can be written as a general elliptic variational problem, which reads: *Find $u_{\tilde{\mathcal{T}}} \in H_0^1$, such that:*

$$a(u_{\tilde{\mathcal{T}}}, v_{\tilde{\mathcal{T}}}) = (f, v), \qquad \forall v_{\tilde{\mathcal{T}}} \in H_0^1, \tag{3.70}$$

where, $a(\cdot, \cdot)$ is a bilinear form and f is a linear operator. Any matrix M^* that composes the bilinear form associated with the elliptic problem, such as stiffness, Jacobian or mass matrices, and the right-hand side f, are assembled per level, using C_l^τ to change of basis while preserving the coefficients:

$$M^* = \sum_{l=0}^{n-1} [C_l^\tau \ \mathbf{0}]^\top M_l^* [C_l^\tau \ \mathbf{0}]. \tag{3.71}$$

The adaptive algorithm consists of four main steps:

- solve the PDE with the current mesh,

- estimate the error distribution in each element,

- mark the elements where the error is larger than a specified threshold,

- refine the marked elements only, and repeat the process.

Secondly, estimators for the error can act on either the elements or the set of basis functions. Reliable and efficient *a posteriori* error indicators have been developed in [32] for the functions, and in [33] for the elements. Function-based error estimates have been selected together with a simplified version of the THB-splines, as they reduce the interaction between different refinement levels, and therefore, lead to sparser matrices and a further reduction of the number of degrees of freedom. The error estimators, ϵ_β, are based on the L^2 norm of the specific problem residuals weighted by the mesh-size h_β:

$$\epsilon_\beta = h_\beta \Big(\int_{\mathbf{F}(\text{supp}\beta)} |f - a(u_{\tilde{\mathcal{T}}}, u_{\tilde{\mathcal{T}}})|^2 (\beta \circ \mathbf{F}^{-1}) \Big)^{\frac{1}{2}}. \tag{3.72}$$

Such estimators are adapted to include the different material properties and are particularized to the bilinear form.

Thirdly, several elementary marking strategies are possible:

- Guaranteed Error Reduction Strategy (GERS),

- Maximum Strategy (MS),

- Global Refinement (GR),

that can act on both elements and basis functions. The GERS is, in fact, equivalent to the marking strategy introduced by Dörfler in [72], where the parameter $\theta = \frac{1}{2}$ is selected, which ensures that the sum of the error contributions of the marked entities represents more than half of the total estimated error:

$$\mathcal{M} = \{\beta, \ \sum_{\beta \in \tilde{\mathcal{T}}} \epsilon_\beta \geq \theta \sum_{\beta' \in \tilde{\mathcal{T}}} \epsilon_{\beta'}\}. \tag{3.73}$$

The MS marking uses the same $\theta = \frac{1}{2}$ parameter, which, in this case, marks the entities exceeding half of the maximum error:

$$\mathcal{M} = \{\beta, \ \epsilon_\beta \geq \theta \max_{\beta' \in \tilde{\mathcal{T}}} \epsilon_{\beta'}\}. \tag{3.74}$$

The GR refines the whole mesh at each iteration, without using the error estimate.

Finally, the h-refinement step uses the advantageous properties of the THB-spline meshes and approximation spaces [90]. At each level, the active cells, which are contained in the support of the marked function, are dyadically refined, creating an enlargement of the subdomains $\mathbf{\Omega^*_{n+1}}$. The marked basis functions are deactivated and replaced by their children. Details on the THB-spline refinement algorithms can be found in [90]. Analysis and proofs of the optimal local approximation properties

and convergence of the error estimates is detailed in [31] using a multi-scale quasi-interpolant operator.

Numerical investigation and results of the convergence of the adaptive isogeometric method for the 2D linear magnetostatic and magnetoharmonic have been published in [87], using the library [221], on the electromagnetic actuator benchmark, which is exemplified in Appendix A. Indeed, adaptive hierarchical refinement strategies enable the selection of an optimum mesh discretization for the considered problem. The hierarchical mesh discretization minimizes the number of degrees of freedom, and therefore, the memory requirements and computational effort, while capturing the local field gradients and losses accurately. For the considered geometry, the adaptive hierarchical refinement using the maximum strategy (MS) decreases the number of degrees of freedom by a factor 100 compared to FEM and by a factor 10 compared to uniform IGA, while maintaining similar accuracy. The hierarchical adaptive method alleviates the need for geometrical model truncation [16], and is advantageous in case of multiscale problems.

The error estimator introduced in (3.72) can be calculated differently following:

$$\epsilon_\beta = h_\beta \Big(\int_{\mathbf{F}(\mathrm{supp}\beta)} |a(u_{\tilde{\mathcal{T}}}, u_{\tilde{\mathcal{T}}}^{\mathrm{ref}}) - \langle f, u_{\tilde{\mathcal{T}}}^{\mathrm{ref}} \rangle|^2 (\beta \circ \mathbf{F}^{-1}) \Big)^{\frac{1}{2}}. \tag{3.75}$$

Indeed, the residual is projected onto a uniformly and dyadically refined THB space on which the basis functions, $u_{\tilde{\mathcal{T}}}^{\mathrm{ref}}$, are constructed. The same marking strategies can be used further on. This definition error estimator has the advantage of being able to refine problems with nonlinear characteristics. Furthermore, to speed up the calculation time, the previous nonlinear solution can be projected onto the newly refined mesh and given as an initial guess to the nonlinear Newton solver.

3.9   Transient problems

The last class of solvers to be covered in this chapter are transient solvers. They follow the evolution of the solution through the time dimension. Different methods exist for discretizing this remaining physical dimension. In Maxwell's equations describing low-frequency eddy current problems, a first-order time derivative is present, which yields a parabolic problem. In high-frequency electromagnetism, a second-order time derivative yields a hyperbolic problem. This thesis focuses on the parabolic problems. To discretize the time gradient, different approaches are possible and are categorized into two classes: discrete and continuous. Continuous methods, such as the space-time Galerkin method, are detailed in Section 5.4. Discrete methods are referred to as *time-stepping* techniques and are the subject of this section.

The most common time-stepping techniques are the so-called θ-*methods* [180]. The general algebraic system is considered:

$$M\frac{\partial u}{\partial t} + Su = b, \tag{3.76}$$

$$u(t=0) = u_0, \tag{3.77}$$

where, M and S are the mass and stiffness matrix respectively, while b is the source term. The discrete time series is introduced:

$$t^{n+1} = t^n + \Delta t, \tag{3.78}$$

with Δt is the time step. The matrix R is introduced as:

$$R(u,t) = M^{-1}[Su - b]. \tag{3.79}$$

So that the first-order ordinary differential equation reads:

$$\frac{\partial u}{\partial t} + R(u,t) = 0, \qquad \text{for } t \in (t^n, t^{n+1}) \tag{3.80}$$

$$u(t^n) = u^n, \qquad \forall n \in \mathbb{N}. \tag{3.81}$$

Finite difference discretization of the time derivative is introduced using two levels, so that the θ-scheme reads:

$$\frac{u^{n+1} - u^n}{\Delta t} + \left[\theta R\left(u^{n+1}, t^{n+1}\right) + (1-\theta)R\left(u^n, t^n\right)\right] = 0, \qquad 0 \leq \theta \leq 1 \tag{3.82}$$

where, θ is the implicitness parameter, which can generate some of the implicit and explicit time-stepping schemes presented in Table 3.1. An explicit scheme is only a function of the previous time steps, while an implicit scheme is a function of previous and current time steps. The precision indicated in Table 3.1 refers to the error made at a specific time t, and is different from the local truncation error, which is defined

Table 3.1: θ-schemes for standard time-stepping approaches

θ	Name	Scheme	Precision
0	Forward Euler	explicit	$\mathcal{O}(\Delta t)$
0.5	Crank-Nicolson	implicit	$\mathcal{O}(\Delta t)^2$
1	Backward Euler	implicit	$\mathcal{O}(\Delta t)$

as the error made in one step, indicated in (3.83)-(3.86):

$$u^{n+1} = u^n + f\left(t^n, u^n\right)\Delta t + \mathcal{O}(\Delta t)^2, \qquad \text{Forward Euler}$$

(3.83)

$$u^{n+1} = u^n + f\left(t^{n+1}, u^{n+1}\right)\Delta t + \mathcal{O}(\Delta t)^2, \qquad \text{Backward Euler}$$

(3.84)

$$u^{n+1} = u^n + \frac{1}{2}\left[f\left(t^n, u^n\right) + f\left(t^{n+1}, u^{n+1}\right)\right]\Delta t + \mathcal{O}(\Delta t)^3, \qquad \text{Crank-Nicolson}$$

(3.85)

$$u^{n+1} = u^n + f\left(t^{n+1/2}, u^{n+1/2}\right)\Delta t + \mathcal{O}(\Delta t)^3, \qquad \text{Leapfrog method}$$

(3.86)
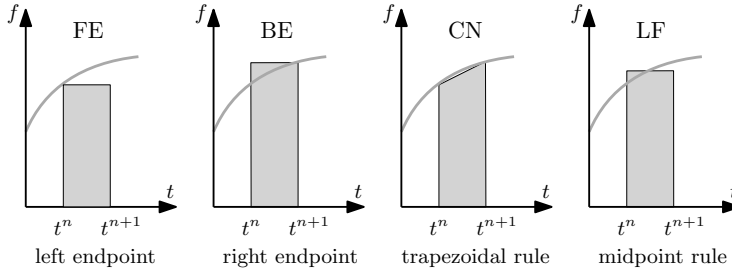
Figure 3.5: Graphical representation of the numerical integration rule on the interval (t^n, t^{n+1}) for the θ-schemes (3.83)-(3.86)).

The θ-schemes introduced in (3.83)-(3.86) use different numerical time-integration quadrature rules, which are graphically exemplified in Fig. 3.5 [146].

Explicit schemes have a low computational cost per time step and are simple to implement as well as to parallelize. However, small time steps are required for stability reasons, especially for high speeds and high mesh-size aspect ratios.

Implicit schemes exhibit stability over a wider range of time steps and do constitute a good iterative solver for steady-state problems. However, they have a higher cost per time step and are more difficult to implement as well as parallelize. They may get insufficiently accurate for unsteady transient problems as the time steps increases, which deteriorates the convergence [146].

More advanced transient solvers have been proposed, such as the three-level explicit leap-frog method, or fractional-step θ-methods. As the two-level methods can only be at most second-order accurate, higher-order time integration methods have been developed, such as the Adams methods and the Runge-Kutta methods [97].

3.10   Conclusion

In this chapter, the variational formulations for two-dimensional, axisymmetric, and three-dimensional topologies have been defined for different electromagnetic regimes. Problems in magnetostatic with linear and nonlinear material characteristics, in magnetoharmonic with linear material characteristics and a single frequency, as well as steady-state thermal problems have been discussed. Two methods for modeling nonlinear characteristics have been introduced and compared, namely the Newton-Raphson and the fixed-point method. Transient solvers using standard time-stepping techniques, such as the θ-methods have been presented.

In the next chapter, motional eddy current problems and alternatives to the time-stepping approach are detailed. In particular, the harmonic balance method is investigated and validated on different benchmark geometries, against a traditional backward Euler transient solver. The gain in efficiency for reaching the steady-state solution is demonstrated. The resulting accuracy and convergence of the proposed approach are both analyzed.

Chapter 4

Harmonic balance method for motional eddy current problems

In this chapter, the harmonic balance method is introduced for two- and three-dimensional nonlinear multiharmonic eddy current problems. The fully coupled approach is validated on two-dimensional slotless and slotted benchmarks. The resulting field distributions and post-processed parameters profiles are compared with the standard backward Euler time-stepping approach, in terms of accuracy, stability, and computational effort.

4.1   Introduction

In this section, several approaches to model motional problems are briefly summarized. The motivation for the concept of harmonic balance as an alternative to the time-stepping approach, to model motional problems occurring in electrical machine applications is given. The harmonic balance (HB) method has been applied to many motion-free applications, however, it has not yet been applied to nonlinear motional eddy current problems in the context of the isogeometric analysis. Additionally, the convergence analysis of the harmonic balance method in terms of the residual has not been demonstrated in the literature. Two motional eddy current benchmarks are considered to establish the accuracy, convergence, and computational efficiency of the proposed approach.

4.1.1   Motional eddy current problems

To model the effects due to relative motion between two or more rigid subsystems, several approaches are possible. The Euler and Lagrange formulations can be distinguished.

The Euler formulation is based on a unique frame of reference, while the Lagrange approach uses as many reference frames as moving parts. The choice of the formulation and the reference frame changes the expression of the total time-derivative and therefore of the eddy-current term [58, 59, 182]. These formulations are compared in Section 5.4.3. In particular, in the Euler formulation, the term $\sigma \mathbf{v} \times \mathbf{B}$ is subtracted from the left-hand side of (2.43). The resulting solution sometimes necessitates a stabilization technique, if the mesh-size cannot resolve the eddy-current penetration depth. Upwind schemes, such as streamline-upwind Petrov-Galerkin (SUPG) can be used [58]. The eddy current penetration depth, or *skin-depth* δ, is defined for eddy current problems with linear material characteristics as:

$$\delta = \frac{1}{\sqrt{\pi f \mu \sigma}},\tag{4.1}$$

where, f is the electrical frequency. However, in the case of eddy currents in a soft-magnetic material, the magnetic permeability μ is a nonlinear function of the magnetic field density. Furthermore, in case a thermal model is considered, the electrical conductivity σ can be a function of temperature. By analogy with fluid mechanics, a dimensionless parameter, the magnetic Reynold number Rm, has been proposed [27, 214]:

$$\mathrm{Rm} = \mu \sigma v L,\tag{4.2}$$

where, v is the relative displacement speed and L is a characteristic length, which can be taken as equal to the skin depth δ. The magnetic Reynolds number represents the ratio of the secondary magnetic fields due to eddy currents to the primary magnetic fields, i.e. for Rm $\gg$ 1, the eddy current phenomenon cannot be neglected, as it expels the magnetic field from the conductor. In the nonlinear case, the skin depth and magnetic Reynolds number both become nonhomogeneous distributions across the geometry. These values can be averaged, although their variations increase as a function of frequency.

Traditionally, Lagrangian approaches have been used for simplicity, symmetry, and stability reasons. In traditional finite elements, the remeshing of the airgap region between subsystems at each time step was used originally. It is by far the most expensive method due to the necessity of interpolation of the previous solution on the new mesh. The locked-step method is very popular and consists of a uniformly spaced mesh on a sliding interface and of a fixed time step, which corresponds to a multiple of the mesh size time divided by the speed. This method can be restrictive and potentially unstable if a certain mismatch occurs. Macro-element methods propose to use other basis functions in the airgap, for instance, the Fourier basis in periodic models, to which stator and rotor can be strongly coupled [22, 53, 230]. Sliding band techniques have been proposed, which couples the stator and rotor degrees of freedom in the frequency domain through Lagrange multipliers [61, 65]. Approaches that couple with the boundary-element method (BEM) are also possible as the air regions do not require meshing, therefore enabling the subsystems to move freely [75]. Most of the mentioned techniques have demonstrated satisfying results for two-dimensional problems, however, their applicability to three-dimensional problems might be limited.

Many general coupling approaches have been applied beyond electrical machine applications. The Lagrange multiplier methods have been proposed, as well as Mortar methods [29, 36, 182], which increase the matrix size as additional variables are introduced. Nitsche methods [166] have been developed that do not add degrees of freedom but introduce a penalty parameter instead. Overlapping methods [238] and Arlequin methods [69] have been researched, as well as overlapping Mortar methods [48] to allow for coupling interfaces, which evolve with time. Schwarz overlapping domain decomposition [19] exists, as well as Schur complement methods and Neuman-to-Dirichlet maps [93]. Master-slave coupling approaches on nonconforming grids [50] have been suggested to reduce the traditional computational overhead due to additional degrees of freedom. Schwarz and Schur complements, balancing domain decomposition by constraint (BDDC) and finite element tearing and interconnecting (FETI) methods are general domain decomposition methods that are also often employed for building preconditioners for iterative solvers and for enabling parallel computing [18, 182].

Using one of the aforementioned methods seems unavoidable if transient time-stepping simulations with localized features in time are required. However, alternative techniques may be considered in the case of periodic motion profiles, which often are reasonable assumptions when designing electrical machines.

4.1.2   Alternative schemes to the time-stepping approach

An alternative to discrete time-stepping approaches consists of using continuous methods instead. After the high-order Galerkin methods have been applied in space, it is only natural to extend these methods to the space-time manifold. For instance, the space-time Galerkin isogeometric methods, which are truly 4D methods, have been presented [115, 155] for single and multiple space-time patches. Both the continuous and discontinuous Galerkin methods can be used in this very general setting, which allows for adaptive refinement in space-time. These approaches are compared in Section 5.3.3.

In practice, each application has different requirements in space and in time. The optimal basis functions are the ones that directly embed the characteristic properties of the signal in their core. In the space domain, this is done with mimetic or structure-preserving basis functions, which have been introduced already for Maxwell's problems [170]. In the time domain, few situations can arise in electrical machines applications with permanent magnet arrays.

On the one hand, steady-state operations often appear in periodical systems evolving at a constant speed, such as rotating machines or long-stroke linear machines with many repeating geometrical periods, which yield fields with a discrete and finite frequency spectrum. The best basis functions in time might, therefore, be trigonometric functions, i.e the Fourier series. Solving the problems in terms of the coefficients of these series is commonly referred to as the harmonic balance (HB) method [234, 235]. Other techniques, such as the time-periodic finite element method [104] can reach the steady-state solution. Improved transient solvers have been developed, such as shooting methods [178] and parallel-in-time simulations using Parareal [196], which can yield the transient and steady-state solutions more efficiently.

On the other hand, some electrical machines, such as short-stroke energy harvesters, may be driven by forces resulting from random motion [141]. A random motion usually involves a continuous spectrum with energy distributed through multiple scales. In these cases, the best basis functions might be wavelet series [139, 140]. Some of these functions have very interesting properties, such as time-frequency localization, efficient multiscale operation, and may even be constructed from given experimental signals. The approach of solving for the time-frequency coefficients of the wavelet

series is referred to as the wavelet balance (WB) method. Steady-state analysis using WB is also possible [78, 153, 164, 201].

Finally, if electrical circuit coupling is of interest, time-integrated potentials have been presented [73]. In order to account for the coils, winding functions have been developed [195]. Several specific methods have been suggested to efficiently deal with separated nonlinearities and frequency spectra, such as the waveform relaxation method (WRM) [40, 151] and the multirate pulse-width modulation (PWM) balance method [99, 171].

4.2   Harmonic balance method

The harmonic balance (HB) method is a powerful alternative to a transient solver, when the time-periodic steady-state solution is sought. Moreover, it yields very good efficiency when the harmonic content is small, i.e. the time signals are reasonably smooth. The application of the HB method is mainly restricted to discrete and small frequency spectrum applications, although the considered frequencies can be widely spaced. Indeed, it is not uncommon that the highest frequency is orders of magnitude higher than the lowest frequency. This would require an enormous amount of time-stepping in practice and lead to prohibitive integration cost [4]. Originally, the HB method was employed for solving nonlinear electrical circuits, analog RF, and microwave problems in the frequency domain. The response and total harmonic distortion (THD) of a system under single or multi-tone excitation can be analyzed efficiently using the HB method. Frequency sweeping can efficiently simulate the performance of a system for a wide range of operating points. Outside of electromagnetic applications, the HB method has been applied to flow problems [55], mechanical vibrations, and deformations [227].

The harmonic balance has been extended to finite element applications, especially transformer problems, where the electric circuit coupling with magnetics is important. It has been applied to both $A-V$ and $T-\Phi$ formulations [174, 175] and compared with time-periodic finite element (TPFEM) approaches. Thanks to this method, the influence of the DC bias [173], due to cosmic radiation [241] for instance, on the losses can be studied more efficiently. The HB method has been applied to shielding and welding problems [14], laminated cores [118], and induction heating [189]. Multiphysics simulations for microelectromechanical systems (MEMS) using the HB method have been proposed [103]. Electrical machines with linear material characteristics have been modeled in 2D [177, 230]. However, the HB method has not yet been applied to nonlinear motional eddy current problems. Furthermore, the convergence of the HB method has not yet been clearly demonstrated.

In the next sections, the concept of the HB method including two variants are detailed. In Section 4.3, the HB method is applied to two benchmarks that mimic slotless and slotted permanent magnet machine topologies, to show that the correct profile for the force ripples and mean values can be obtained efficiently. Additionally, the convergence of the proposed method is analyzed.

4.2.1   Concept

The idea of the harmonic balance method is to expand the time dimension of the fields into truncated time-harmonic series:

$$\mathbf{A}(\mathbf{x}, t) \simeq \sum_{k=0}^{N} [\tilde{\mathbf{u}}_k^c(\mathbf{x})\cos(k\omega t) + \tilde{\mathbf{u}}_k^s(\mathbf{x})\sin(k\omega t)] = \text{Re}\left(\sum_{k=0}^{N} \widehat{\mathbf{u}}_k(\mathbf{x})e^{jk\omega t}\right), \quad (4.3)$$

with the relationship $\widehat{\mathbf{u}}_k = \tilde{\mathbf{u}}_k^c - j\tilde{\mathbf{u}}_k^s$. In the rest of this chapter, the vectorial character of the Fourier coefficients as well as their spatial dependency are frequently omitted from the notation. The Fourier transform $\mathcal{F}$, is applied to the nonlinear diffusion equation:

$$\nabla \times (\nu(A(t))\nabla \times A(t)) - \sigma\frac{\partial A(t)}{\partial t} = J(t) + \nabla \times \nu M(t), \quad (4.4)$$

$$\nabla \times (\mathcal{F}(\nu\nabla \times (A)) - \sigma\frac{\partial\mathcal{F}(A)}{\partial t} = \mathcal{F}(J) + \nabla \times \mathcal{F}(\nu M). \quad (4.5)$$

In between each nonlinear iteration, the time signals are reconstructed from the Fourier coefficients, the nonlinear relationship is applied on the time signal $\nu(t) = f(B(t))$, before being transformed back to the frequency domain. The harmonic balance is therefore an alternating time-frequency scheme, which solves for the Fourier coefficients and alleviates from time-stepping convergence issues.

4.2.2   Fully coupled harmonic balance

For solving the fully coupled scheme, starting from (4.4) and using the real Fourier transform yields:

$$\nabla \times (\mathcal{F}(H(t))) - \sigma D\mathcal{F}(A(t)) = \mathcal{F}(J(t)) + \nabla \times \mathcal{F}(\nu M(t)), \quad (4.6)$$

where the derivative matrix D is given by:

$$D = \begin{bmatrix} 0 & 1 & 0 & 0 & 0 & \cdots \\ -1 & 0 & 0 & 0 & 0 & \cdots \\ 0 & 0 & 0 & 3 & 0 & \ldots \\ 0 & 0 & -3 & 0 & 0 & \cdots \\ 0 & 0 & 0 & 0 & 0 & \cdots \\ \vdots & \vdots & \vdots & \vdots & \vdots & \end{bmatrix}. \tag{4.7}$$

The matrix M only represents the sources due to the permanent magnet array as the system (4.6) is solved using the Newton-Raphson method. The term $H(t)$ is obtained at each node through:

$$\mathbf{H}(\mathbf{x}, t) = \nu(|\mathbf{B}(\mathbf{x}, t)|)\mathbf{B}(\mathbf{x}, t), \qquad \text{where,} \tag{4.8}$$

$$\mathbf{B}(\mathbf{x}, t) = \nabla \times \mathcal{F}^{-1}\left(\tilde{\mathbf{A}}(\mathbf{x})\right), \qquad \text{with,} \tag{4.9}$$

$$\tilde{\mathbf{A}}(\mathbf{x}) = \begin{bmatrix} \tilde{\mathbf{A}}_1^c(\mathbf{x}) & \tilde{\mathbf{A}}_1^s(\mathbf{x}) & \tilde{\mathbf{A}}_3^c(\mathbf{x}) & \tilde{\mathbf{A}}_3^s(\mathbf{x}) & \tilde{\mathbf{A}}_5^c(\mathbf{x}) & \cdots \end{bmatrix}^\top. \tag{4.10}$$

This illustrates the alternating time-frequency approach of the harmonic balance method. In addition to the systems of equations, which have been detailed in this chapter, the boundary conditions have to be added, and if a 3D problem is considered, additional gauging through Lagrange multipliers or regularization has to be applied, as detailed in Sections 3.3.1 and 3.3.2.

4.2.3   Decoupled harmonic balance

The harmonic balance method [74, 235], is employed to obtain the coupled system of equation for solving the nonlinear multiharmonic problem. The complex-valued problem derived from the harmonic balance is linearized using the fixed-point method described in [85, 88] and in Section 3.5.1. The solution in the time-domain is reconstructed from the computed Fourier coefficients. Moreover, the resulting algebraic system is 2N+1 times larger than the original spatial system, where N is the highest harmonic considered in the solution. Therefore, an iterative solver, such as GMRES, might be required to find a solution depending on the size of the system, which in turns necessitates proper preconditioning and smoothing [14]. In order to limit the implementation overhead, a decoupled harmonic system is presented, where each harmonic is solved sequentially, and the inter-harmonic coupling part is expressed through an equivalent source term, and the right-hand side [74]. The derivation of the multiharmonic model comes from the Fourier transform of the diffusion equation (4.11),

which reads:

$$\nabla \times (\nu'(A(\mathbf{x},t))\nabla \times A(\mathbf{x},t)) - \sigma \frac{\partial A(\mathbf{x},t)}{\partial t} = J(\mathbf{x},t) + \nabla \times \nu'(A(\mathbf{x},t))M(\mathbf{x},t),$$

(4.11)

$$\nabla \times (\mathcal{F}(\nu') * \nabla \times \mathcal{F}(A)) - \sigma \frac{\partial \mathcal{F}(A)}{\partial t} = \mathcal{F}(J) + \nabla \times \mathcal{F}(\nu'M), \tag{4.12}$$

$$\nabla \times \left(\sum_{i=-N}^{N} \widehat{\nu'_{k-i}} \nabla \times \widehat{A_i} \right) - kj\omega\sigma\widehat{A}_k = J_k + \nabla \times \widehat{\nu'M}_k, \tag{4.13}$$

where, $*$ is the convolution product, and $\widehat{A}_k$ is the k-th harmonic coefficient of the magnetic vector potential. The reluctivity coefficients $\widehat{\nu'}$, are obtained through the fast Fourier transform (FFT) of the reconstructed time profiles at each node. Similarly, $\widehat{\nu'M}$ represents the magnetization coefficients in the permanent magnets and the equivalent magnetization in the nonlinear iron material. The full stiffness matrix $\boldsymbol{S}$, which cross-couples the harmonic modes is given by blocks:

$$\boldsymbol{S} = \begin{bmatrix} \boldsymbol{S}_{\widehat{\nu'_0}} & \boldsymbol{S}_{\widehat{\nu'_1}} & \boldsymbol{S}_{\widehat{\nu'_{-1}}} & \boldsymbol{S}_{\widehat{\nu'_2}} & \boldsymbol{S}_{\widehat{\nu'_{-2}}} & \cdots \\ \boldsymbol{S}_{\widehat{\nu'_{-1}}} & \boldsymbol{S}_{\widehat{\nu'_0}} & \boldsymbol{S}_{\widehat{\nu'_{-2}}} & \boldsymbol{S}_{\widehat{\nu'_1}} & \boldsymbol{S}_{\widehat{\nu'_{-3}}} & \cdots \\ \boldsymbol{S}_{\widehat{\nu'_1}} & \boldsymbol{S}_{\widehat{\nu'_2}} & \boldsymbol{S}_{\widehat{\nu'_0}} & \boldsymbol{S}_{\widehat{\nu'_3}} & \boldsymbol{S}_{\widehat{\nu'_{-1}}} & \cdots \\ \boldsymbol{S}_{\widehat{\nu'_{-2}}} & \boldsymbol{S}_{\widehat{\nu'_{-1}}} & \boldsymbol{S}_{\widehat{\nu'_{-3}}} & \boldsymbol{S}_{\widehat{\nu'_0}} & \boldsymbol{S}_{\widehat{\nu'_{-4}}} & \cdots \\ \boldsymbol{S}_{\widehat{\nu'_2}} & \boldsymbol{S}_{\widehat{\nu'_3}} & \boldsymbol{S}_{\widehat{\nu'_1}} & \boldsymbol{S}_{\widehat{\nu'_4}} & \boldsymbol{S}_{\widehat{\nu'_0}} & \cdots \\ \vdots & \vdots & \vdots & \vdots & \vdots & \end{bmatrix}, \tag{4.14}$$

$$\widehat{\boldsymbol{A}}(\mathbf{x}) = \begin{bmatrix} \widehat{\mathbf{A}}_0(\mathbf{x}) & \widehat{\mathbf{A}}_{-1}(\mathbf{x}) & \widehat{\mathbf{A}}_1(\mathbf{x}) & \widehat{\mathbf{A}}_{-2}(\mathbf{x}) & \widehat{\mathbf{A}}_2(\mathbf{x}) & \widehat{\mathbf{A}}_{-3}(\mathbf{x}) & \cdots \end{bmatrix}^\top. \tag{4.15}$$

The assembly of each block is computationally expensive. In order to save time for finding the solution using a direct solver, the cross-coupling terms are moved to the right-hand side, so that each harmonic coefficient can be solved sequentially while keeping the same stiffness block, $\boldsymbol{S}_{\widehat{\nu'_0}}$, for the DC incremental reluctivity:

$$\nabla \times (\widehat{\nu'_0}\nabla \times \widehat{A}_k) - kj\omega\sigma\widehat{A}_k = \widehat{J}_k + \nabla \times \widehat{\nu'M}_k \ldots \tag{4.16}$$

$$- \nabla \times \left(\sum_{\substack{i=-N \\ i \neq k}}^{N} \widehat{\nu'_{k-i}} \nabla \times \widehat{A}_i \right),$$

$$[\boldsymbol{S}_{\widehat{\nu'_0}} + k\boldsymbol{M}]\widehat{A}_k^{p+1} = \widehat{J}_k + \nabla \times \widehat{\nu'M}_k - \sum_{\substack{i=-N \\ i \neq k}}^{N} \boldsymbol{S}_{\widehat{\nu'_{k-i}}}\widehat{A}_i^p. \tag{4.17}$$

The decoupled approach is well suited for situations where magnetic cross-coupling is not too critical, such as slotless structures. However, in general, the accuracy and robustness of the decoupled approach can be limited. Therefore, the fully coupled approach should be considered for general cases, in order to observe and analyze the convergence, before simplifying the system further.

4.2.4   Motion incorporation

In order to include the motion within the harmonic balance framework, different techniques can be applied depending on the motion profile and the geometry. Depending on whether the eddy currents are only of interest in the stator or the mover, the Eulerian or Lagrangian approaches can be used, respectively. These representations and their equivalence are discussed in Section 5.4.3. However, if the eddy currents in both mover and stator are important, or if both stator and mover present a complex topology, a coupling strategy in the airgap should be considered [61]. The applications considered in the thesis focus on surface-mounted permanent magnet electrical machines, and the eddy currents are solely of interest in the stator, notably, no electrical conductivity is considered in the mover. The considered motion profiles are exclusively constant displacement speeds in both linear and rotating coordinate systems. Therefore, the geometry and the relative motion of the permanent magnet array can be both approximated by a periodic traveling magnetization wave, without the need for a coupling strategy. In particular, only the fundamental time harmonic can be considered as the basis for the moving spatial-magnetization function:

$$M(\mathbf{x}, t) = M^s(\mathbf{x})\cos(\omega t) \ - M^c(\mathbf{x})\sin(\omega t). \tag{4.18}$$

The square wave representing the spatial distribution of the magnetization in the direction of motion can be approximated by means of Fourier series. However, in practice, only the fundamental spatial-harmonic is considered by employing the following simple source term in the permanent magnet array region:

$$M(\mathbf{x}, t) = \frac{B_{rem}}{\mu_{pm}} \left(\sin\left(\frac{\pi\mathbf{x}}{\tau_p}\right) \cos(\omega t) - \cos\left(\frac{\pi\mathbf{x}}{\tau_p}\right) \sin(\omega t) \right). \tag{4.19}$$

The exact description of the actual magnetization spatial distribution is not crucial if the eddy currents are only of interest in the stator, because the airgap acts as a low-pass filter and tends to exhibit a sinusoidal magnetic flux density distribution. Additionally, using the equivalence between the Eulerian and Lagrangian approaches detailed in Section 5.4.3, it is possible to adapt the magnetization source term in terms of amplitude or distribution, so that the stator eddy current losses predicted by the Eulerian approach with an approximated mover geometry, do match the losses predicted by the Lagrangian approach, where the mover geometry is not approximated.

The proposed approach allows to incorporate easily the motion of a surface-mounted permanent magnet array in the frequency domain without stator-mover coupling. Furthermore, it enables to study efficiently the eddy current phenomena in complex stator core geometries and with nonlinear *B-H* characteristics, as will be demonstrated numerically in the next sections.

4.2.5   Practical considerations

In this section, several practical aspects related to the implementation of the harmonic balance method are discussed.

Complex or real-valued system   The solving scheme has to be adapted depending on whether a complex or real-valued Fourier series expansion is considered. If the Newton iterations are considered, it is beneficial to use the real Fourier transform. Indeed, the bilinear operator is real, and therefore, differentiable. This is not straightforward for the complex-valued operator [14, 60], for which the construction of the Jacobian matrix is cumbersome. Instead, for the complex-valued operator, a fixed-point scheme is often preferred. Both real and complex approaches are described in this section.

Harmonic reduction   A few simplifications of the scheme can be made, depending on the type of excitation and source. If the source is composed of odd harmonics, then only odd harmonics are required for the solution and its derivatives [14]. Therefore, even harmonics are removed from the unknown solution vector (4.15), since they are identically null. In the case of purely complex-valued sinusoidal time excitation, only one frequency is needed to represent the signal, while for a real-valued sinusoidal signal, the spectrum consists of two frequencies, which are conjugate symmetric, i.e. Hermitian. In this case, it is possible to replace the discrete Fourier transform (DFT) by a discrete cosine transform (DCT), thereby reducing the size of the system by a factor 2. Further harmonic reduction can be realized if *a priori* or *a posteriori* knowledge about the harmonic content is available [11].

Solver choice   Depending on the selected scheme and the size of the system, different solvers can be used. For fully coupled harmonic balance, with a large system size and a wide frequency spectrum, iterative solvers [191], such as GMRES [178] or QMR [15], can be employed with appropriate block preconditioners and smoothers. This can also be resolved with multigrid (MG) solvers [14], which propagate the information from a fine mesh to a coarser mesh, where the matrix is inverted directly, and the information is transferred back to the finer space. They can be

algebraic (AMG) [186], geometric (GMG), or geometric agglomerated algebraic multigrid solvers (GAMG) [168]. Geometric multigrid approaches are natural in the context of isogeometric analysis, and can be of type p-MG [209] or h-MG [63]. For the decoupled harmonic balance approach, each harmonic is solved separately and sequentially. The only coupling mechanism present is through the equivalent source terms on the right-hand side. Therefore, a direct solver can be used. Direct solvers can also be used to solve the fully coupled harmonic balance if relatively small systems with limited frequency content are considered, which is the case in the numerical experiments presented in this work.

Meshing constraint It might be necessary to have a certain constraint on the mesh, depending on the number of harmonics considered. In the periodic motional problems considered in Section 4.3, the time dimension is closely related to the first geometrical dimension x, along which the uniform translation is operated. Therefore, it can be beneficial to impose sufficient mesh refinement for resolving the highest frequency component considered in the HB scheme.

4.3   Numerical results

In this section, the numerical results of the harmonic balance methods are presented. They are obtained using the fully coupled method formed with the real Fourier transform. The simulated systems are small and therefore a direct solver is used.

4.3.1   Benchmarks

The two considered 2D benchmark geometries are shown in Fig. 4.1, and their respective dimensions are gathered in Table 4.1. In the first benchmark, the core region is slotless, while the second benchmark is slotted. This is done to demonstrate that both the correct force-ripple profiles and the mean damping force can be accurately predicted. Furthermore, such slotless and slotted geometries constitute the most common topologies in linear permanent magnet machine applications. The Dirichlet boundary conditions are imposed at both the top and bottom boundaries, while periodic conditions link each side. Both the iron and core regions have nonlinear magnetic properties corresponding to the material *M270-50A-50Hz*. The radial magnet array has a relative magnetic permeability of $\mu_r = 1.05$ and a remanent magnetic flux density of $B_r = 1.35$ T. To force the soft-magnetic materials to strongly saturate, the value of the remanent magnetic flux density is artificially increased by 40 % in the benchmarks considered in both Chapters 4 and 5. Only the stator core region is electrically conductive with $\sigma = 1.8182\ 10^6$ S/m. The depth of the domain is taken as

$D_0 = 10$ mm. The permanent magnet array is translated with constant linear speeds $v \in \{0.1, 1, 10\}$ m/s.
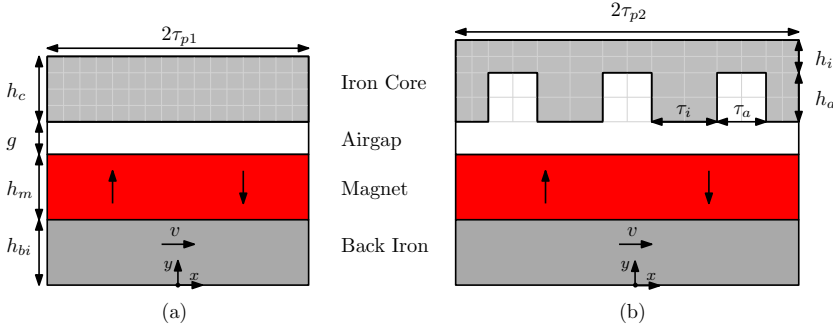
Figure 4.1: a) Slotless and b) slotted 2D benchmark geometries considered for validating the harmonic balance method.

Table 4.1: Geometrical dimensions of the 2D benchmarks

Parameter	Value [mm]	Parameter	Value [mm]
$2\tau_{p1}$	8.0	$2\tau_{p2}$	10.5
h_c	2.0	τ_i	2.0
g	1.0	τ_a	1.5
h_m	2.0	h_i	1.5
h_{bi}	2.0	h_a	2.0

4.3.2   Convergence analysis

Slotless benchmark   For the slotless benchmark, the reference discretization is taken to be 4 elements along the height and 16 elements along the width per region as shown in Fig. 4.1, with bivariates splines of degree 3. Odd harmonics until $H = 7$, which is equivalently denoted as $N = 4$, are simulated for the harmonic balance. Three periods are simulated with 120 time steps per period for the transient time-stepping solver, which is a backward Euler solver with $\theta = 1$. The number of samples of the discrete Fourier transform is selected to be equivalent to the number of time-steps per period for the time-stepping solver, to match the resolution. Reducing the number of time-samples decreases the computational effort, for both the time-stepping approach and the harmonic balance solver.

The magnetic flux density distributions for speeds $v \in \{0.1, 1, 10\}$ m/s are shown for both the harmonic balance (HB) and time-stepping (TS) solvers in Fig. 4.2. The distributions are matching very well at low speeds, while at 10 m/s the time-stepping approach suffers from small instabilities. The absolute value of the difference in

magnetic flux density between both approaches is shown in Fig. 4.4. A maximum discrepancy of 58 mT and 375 mT is found for speeds equal to 1 m/s and 10 m/s, respectively. The profiles of the attraction force, the damping force, and the eddy current losses in the core regions are shown for three different speeds in Fig. 4.3, for an increasing number of considered harmonics. A good agreement is obtained between both solvers, with less than 2 % discrepancy among the mean values of the times profiles, as shown in Table 4.2. This discrepancy can be lowered by increasing the refinement in space and time, but the current discretization represents a trade-off between accuracy and computational effort. However, such a discrepancy is considered sufficiently accurate for the engineering problems considered in this work, where a discrepancy of 5 to 10 % is typically accepted.

In this slotless core example, concerning Fig. 4.3 completely flat profiles are expected, i.e. the amplitude of the ripples should tend to zero. This can be achieved using intensive h-refinements with the time-stepping approach, where the amplitude tends to the computer precision at the cost of an increased computational effort. Alternatively, with the HB method, the correct profiles are directly obtained at a reduced cost. The computational effort can be further reduced by relaxing the h-refinement and restricting the number of harmonics considered. The harmonic balance method has the advantage of being stable disregarding the considered speed, whereas the time-stepping approach gets unstable at high speeds, as shown on the distribution of Fig. 4.2f and the profiles of Figs. 4.3b, 4.3d, 4.3f, where unphysical spurious oscillations appear for $v = 10$ m/s. As shown in Table 4.2, the force discrepancies increase by one order of magnitude for 10 m/s as compared to 1 m/s.

The nonlinear convergence of the solution is shown in Fig. 4.5a for different speeds. The nonlinear convergence at a speed of 10 m/s for different considered harmonic spectra is shown in Fig. 4.5b. The number of nonlinear iterations is reasonable and

Table 4.2: Mean relative discrepancy in percentage, for the damping force ΔF_x, attraction force ΔF_y, and eddy current losses ΔP, between the transient time-stepping solution and the ones obtained with harmonic balance of increasing harmonic content N and upper harmonic order H, for speed $v \in \{1, 10\}$ m/s, for the slotless benchmark.

		ΔF_x [%]		ΔF_y [%]		ΔP [%]	
N	H	1 m/s	10 m/s	1 m/s	10 m/s	1 m/s	10 m/s
1	1	1.88	2.58	4.41 10^{-2}	2.36 10^{-1}	1.84	2.54
2	3	1.68	2.32	9.63 10^{-3}	9.20 10^{-2}	1.64	2.27
3	5	1.54 10^{-1}	2.10	1.04 10^{-3}	8.81 10^{-3}	1.50	2.05
4	7	1.43 10^{-1}	1.76	2.84 10^{-3}	1.73 10^{-2}	1.39	1.72

(a)

(b)

(c)

(d)

(e)

(f)

Figure 4.2: Magnetic flux density modulus distribution B in [T] and flux lines for the slotless benchmark at speed $v \in \{0.1, 1, 10\}$ m/s, using the harmonic balance in a), c), e), and the time-stepping approach in b), d), f).

Figure 4.3: Attraction force F_y, damping force F_x, and eddy current losses P, for the slotless benchmark at speed $v = 1$ m/s in a), c), e) and $v = 10$ m/s in b), d), f), using the harmonic balance method with increasing number of harmonics and the time-stepping approach (TS).

Figure 4.4: Absolute discrepancy in the magnetic flux density distribution ΔB in [T] between the harmonic balance and time-stepping solutions, a) at 1 m/s and b) at 10 m/s.
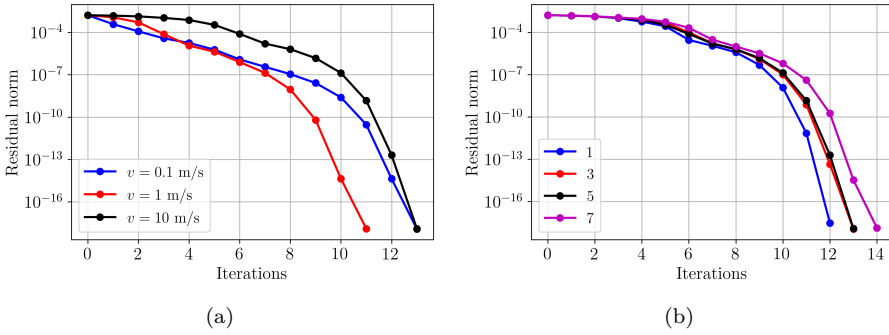
Figure 4.5: a) Nonlinear convergence of the solution including up to the third harmonic, b) nonlinear convergence at 10 m/s, for different harmonic spectra H.
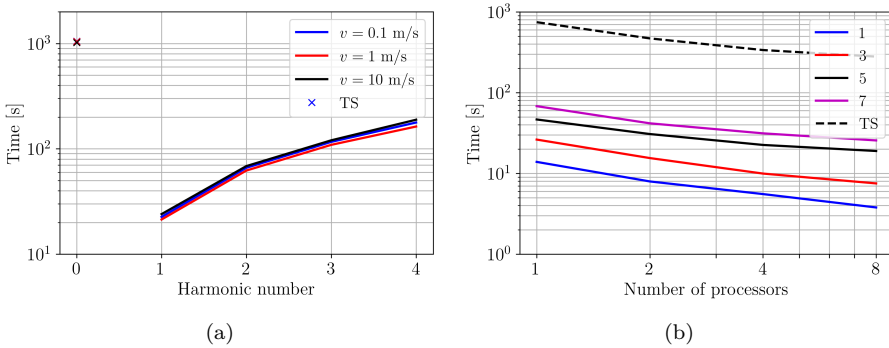
Figure 4.6: a) Computational effort for the time-stepping approach (TS) and harmonic balance method with increasing harmonic content N and different speeds, b) scaling of the computational effort by increasing the number of processors in parallel for the slotless benchmark.

only slightly affected by the additional harmonic content. It indicates that the additional harmonic content has little effects on the final solution, which is also visible in Fig. 4.3. The computational effort as a function of the number of considered harmonics is given in Fig. 4.6a. The computational effort for the time-stepping approach is indicated at harmonic index zero as a reference. Furthermore, the scaling of computational effort is shown in Fig. 4.6b as the number of cores working in parallel for the matrix assembly is increased. It can be seen that the computational effort does not correspond between Fig. 4.5b and Fig. 4.6b for the case with one processor. The reason is that Fig. 4.6b is obtained with a Linux machine, which enables the multithreading of the solving step, and therefore reduces the overall computational time. Depending on the number of considered harmonics, the proposed HB method achieves a speed up of at least a factor 11 compared to the time-stepping approach.

Slotted benchmark   Similarly, for the slotted benchmark, the reference discretization is taken to be 2 elements along the height and 2 elements along the width per region as shown in Fig. 4.1, with bivariates splines of degree 3. Odd harmonics until $H = 9$, or equivalently $N = 5$, are solved for the harmonic balance and 3 periods are simulated with 120 time steps per period for the transient time-stepping solver.

The magnetic flux density distributions are shown in Fig. 4.7 for three different speeds. A very good agreement is observed between the time-stepping approach and the proposed harmonic balance approach. The absolute value of the difference in magnetic flux density between both approaches is shown in Fig. 4.9. A maximum discrepancy of 138 mT and 213 mT is found for speeds equal to 1 m/s and 10 m/s, respectively. The profiles of the attraction force, the damping force, and the eddy current losses in the core regions are shown for two different speeds in Fig. 4.8, for an increasing number of considered harmonics. In the slotted benchmark, the cogging profiles shown in Fig. 4.8 are correctly predicted from $H = 7$. For a speed of 10 m/s, the discrepancy between the mean values of the three post-processed parameters is less than 1 %, as can be seen in Table 4.3. Furthermore, the mean deviation, calculated as the normalized root-mean-square (rms) error, is less than 2 % for all profiles.

The nonlinear convergence of the solution is shown in Fig. 4.10a for different speeds. It is observed that the number of iterations increases significantly for increasing speeds in the slotted example, as compared to the slotless example 4.5a. Indeed, the higher-order harmonics are truly excited by the slotting effect. Furthermore, for a speed of 10 m/s, the nonlinear convergence for different harmonic spectra considered in the HB method is given in Fig. 4.10b, which demonstrates a large increase in iterations as compared to the slotless case in Fig. 4.5b. The computational effort as a function of the number of considered harmonics is given in Fig. 4.11a. The computational effort for the time-stepping approach is indicated at harmonic index zero as a reference. The scaling of computational effort is shown in Fig. 4.11b as the number of cores
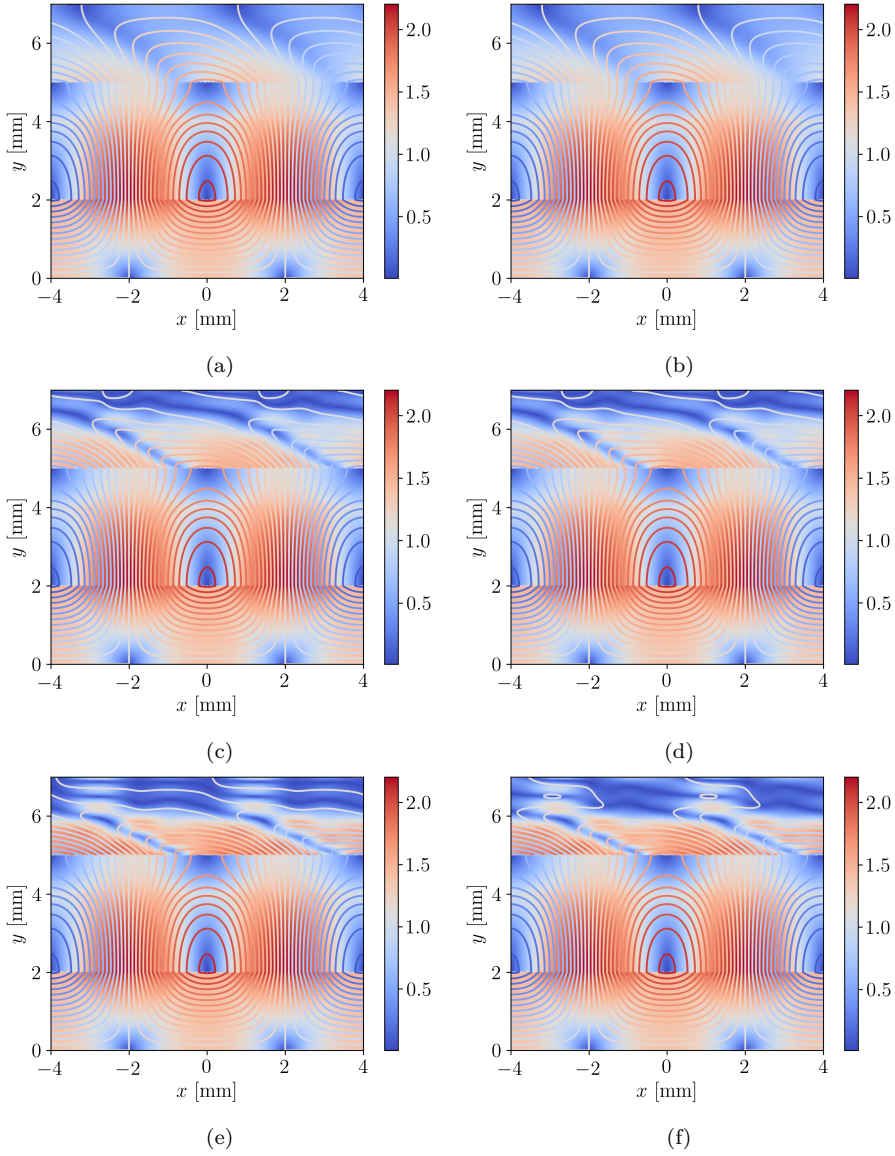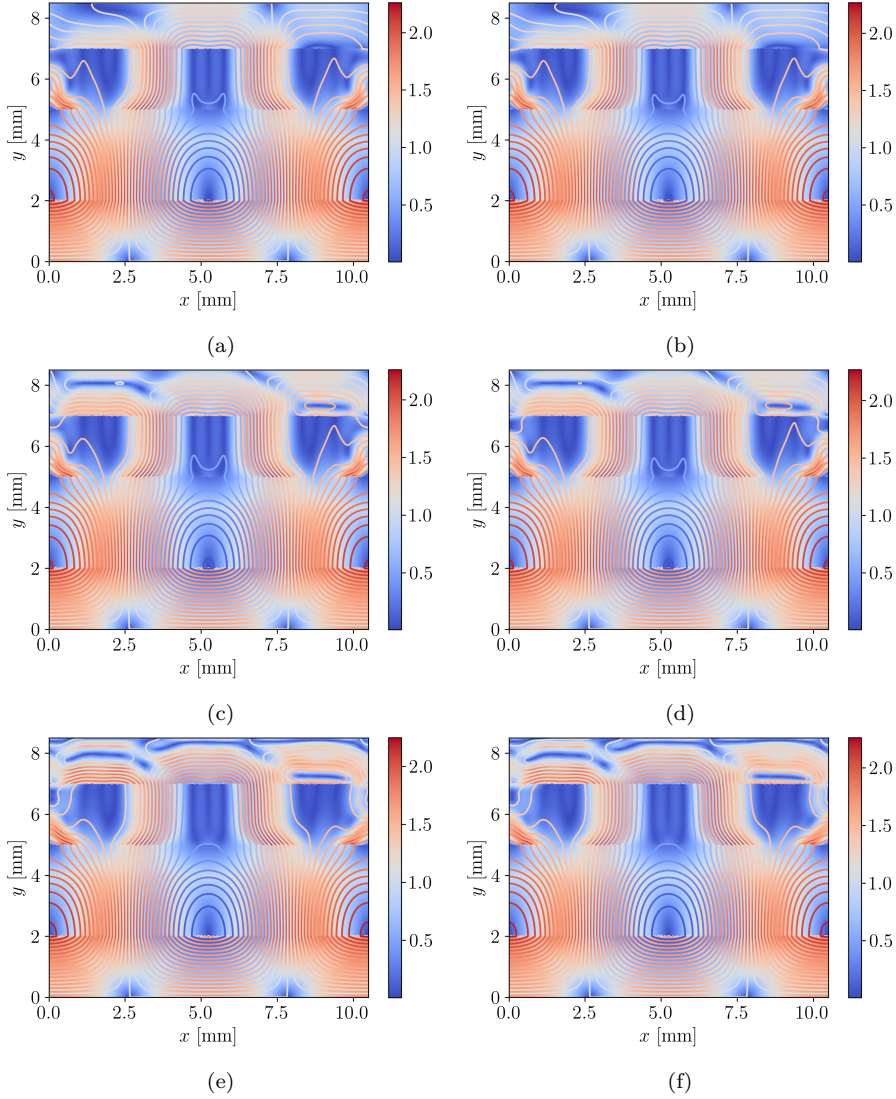
Figure 4.7: Magnetic flux density modulus distribution B in [T] and flux lines for the slotted benchmark at speed $v \in \{0.1, 1, 10\}$ m/s, using the harmonic balance in a), c), e), and the time-stepping approach in b), d), f).
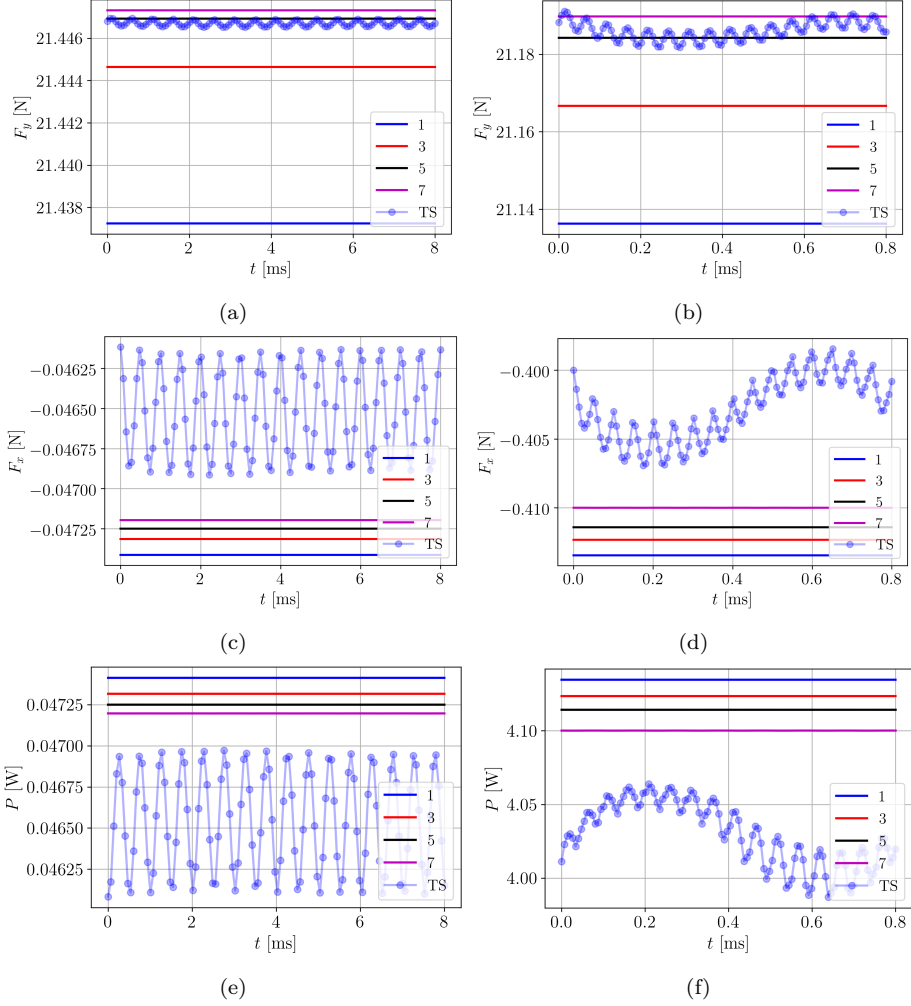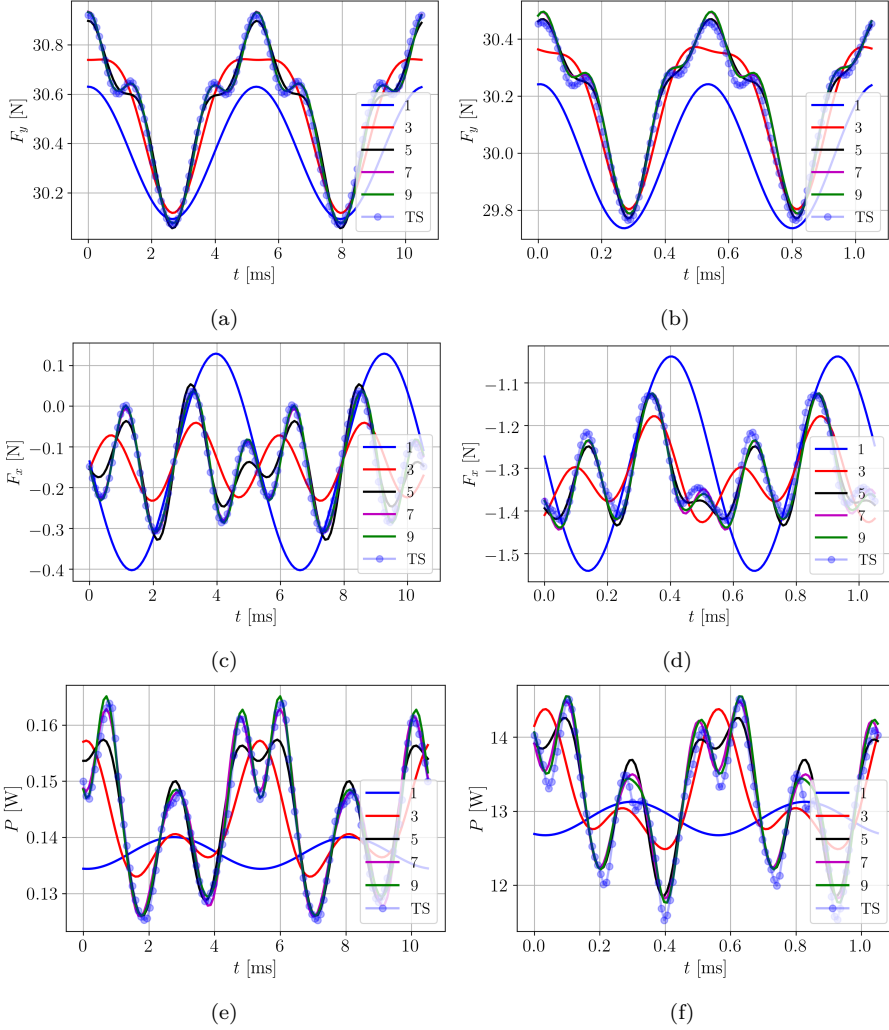
Figure 4.8: Attraction force F_y, damping force F_x, and eddy current losses P, for the slotted benchmark at speed $v = 1$ m/s in a), c), e) and $v = 10$ m/s in b), d), f), using the harmonic balance method with increasing number of harmonics and the transient approach.
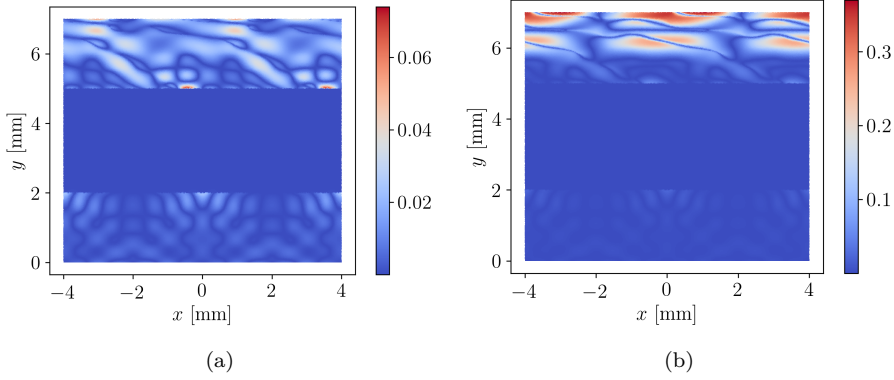
(a)   (b)
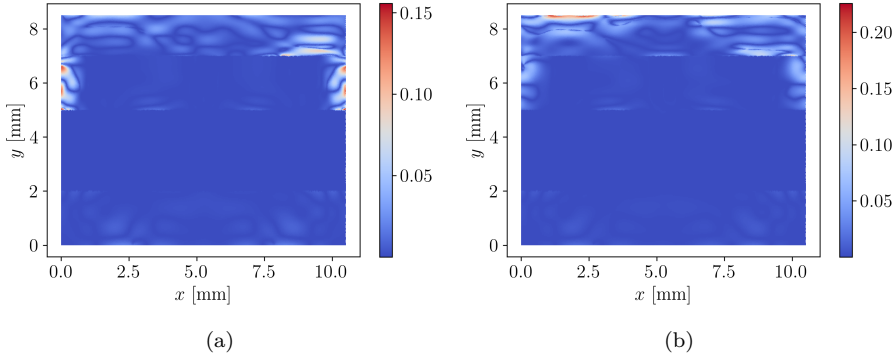
Figure 4.9: Absolute discrepancy in the magnetic flux density distribution ΔB in [T] between the harmonic balance and time-stepping solutions, a) at 1 m/s and b) at 10 m/s.

(a)   (b)
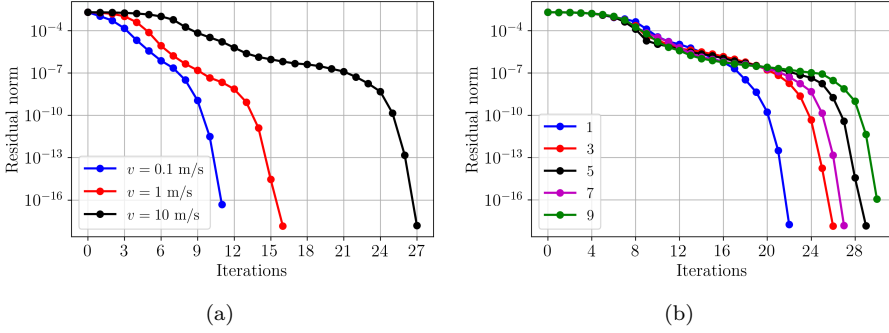
Figure 4.10: a) Nonlinear convergence of the solution including up to the seventh harmonic, b) nonlinear convergence at 10 m/s, for different harmonic spectra H.

(a)   (b)
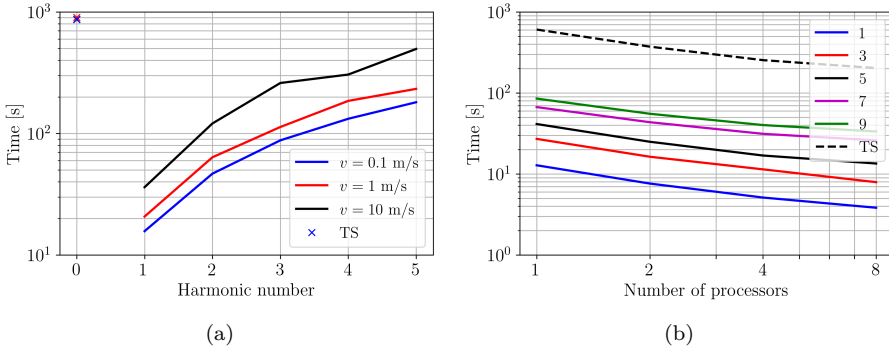
Figure 4.11: a) Computational effort for the time-stepping approach (TS) and harmonic balance method with increasing harmonic content N and different speeds, b) scaling of the computational effort by increasing the number of processors in parallel for the slotted benchmark.

working in parallel for the matrix assembly is increased. Depending on the number of considered harmonics, the proposed HB method achieves a speed up of at least a factor 7 compared to the time-stepping approach.

4.4   Conclusion

The harmonic balance approach for simulating nonlinear motional eddy current problems is developed in this chapter. It is demonstrated that the proposed approach is well suited for the simulation of nonlinear motional eddy current problems. Furthermore, it is more computationally efficient than the backward Euler time-stepping approach for reaching the steady-state solution. In addition, it prevents from having to choose a time step value, which influences the convergence and final values by introducing numerical oscillations.

Slotless and slotted benchmarks are simulated to establish the accuracy of the time profiles of post-processed parameters, as well as to verify that the cogging waveform is correctly predicted. The mean discrepancies and average deviations are less than 2 % for all cases. The magnetic flux density modulus distributions are compared between both approaches. A good agreement is obtained on the field distributions. Maximum discrepancies of 58 mT and 375 mT for the slotless benchmark, as well as 138 mT and 213 mT for the slotted benchmark, at speeds of 1 m/s and 10 m/s, respectively, are registered. These discrepancies occur in regions away of the main field and may be attributed in majority to the time-stepping solver instabilities. For the considered refinements at high speeds, e.g. 10 m/s, the harmonic balance solver has demonstrated a better stability and an absence of numerical oscillations on the time profiles, compared to the time-steeping approach. Moreover, the convergence of

Table 4.3: Mean and rms relative discrepancy in percentage, for the damping force ΔF_x, attraction force ΔF_y, and eddy current losses ΔP, between the transient time-stepping solution and the ones obtained with harmonic balance of increasing harmonic content N and upper harmonic order H, for speed $v = 10$ m/s, for the slotted benchmark.

| N	H	ΔF_x [%]		ΔF_y [%]		ΔP [%]	
		mean	rms	mean	rms	mean	rms
1	1	1.64	$1.40 \ 10^1$	$6.25 \ 10^{-1}$	$6.74 \ 10^{-1}$	1.71	6.97
2	3	$5.40 \ 10^{-1}$	4.27	$5.22 \ 10^{-2}$	$1.87 \ 10^{-1}$	$4.86 \ 10^{-1}$	4.01
3	5	$7.85 \ 10^{-1}$	1.67	$3.77 \ 10^{-2}$	$7.85 \ 10^{-2}$	$7.29 \ 10^{-1}$	1.83
4	7	$8.60 \ 10^{-1}$	1.60	$6.46 \ 10^{-2}$	$9.26 \ 10^{-2}$	$8.05 \ 10^{-1}$	1.51
5	9	$8.90 \ 10^{-1}$	1.58	$6.85 \ 10^{-2}$	$9.45 \ 10^{-2}$	$8.36 \ 10^{-1}$	1.27

the norm of the residual is demonstrated for the proposed harmonic balance method. Depending on the number of considered harmonics, the computational time is reduced by at least a factor 7 and 11 compared to the time-stepping approach, for the slotted and slotless benchmark, respectively.

In the next chapter, the developed harmonic balance scheme is extended to the adaptive setting using THB-splines and residual-based h-refinements. Furthermore, a space-time Galerkin approach is introduced, so that a spline space can be used to discretize the time dimension. Additionally, the discontinuous Galerkin method is introduced for nonlinear eddy current problems to deal with trimmed regions and motional problems. Numerical results are presented on the slotless benchmark with a trimmed core, on which the space-time Galerkin solution is compared to both the time-stepping and the harmonic balance solutions.

Chapter 5

Adaptive isogeometric analysis on trimmed domains

I N this chapter, the numerical scheme researched for handling trimming operations is explained. The space-time Galerkin framework is detailed for both continuous and discontinuous methods. Adaptive refinements are implemented for the harmonic balance and are tested on the slotless benchmark with different trimmed regions. This benchmark represents the problem of detecting defects in steel through motional eddy current testing.

5.1   Introduction

This chapter aims at building more advanced concepts upon the proposed harmonic balance solver and demonstrating the robustness and flexibility of this approach. First, two methods for realizing the trimming operations are introduced, one in the framework of conforming mesh discretization, the other utilizing the concepts of truncated hierarchical splines, level-set, and discontinuous Galerkin method.

Second, to further investigate the advantages of the harmonic balance, the space-time Galerkin method is discussed. Using this method, the equivalence between Lagrange and Euler formulations for modeling motional eddy currents in the stator is studied numerically on both the slotless and slotted benchmarks.

Third, numerical experiments are conducted on the slotless benchmark, where a buried defect is trimmed away. The impact of the size and depth of the defect on the forces and eddy current losses is quantified and compared to the time-stepping approach. The impact of the time-discretization is quantified and the robustness of the harmonic balance solver is demonstrated.

Fourth, the framework of truncated hierarchical B-splines is used to create adaptive mesh refinements using the harmonic balance solver. Initially, on the untrimmed slotless domain, where a technique to speed up repetitive calculations is presented: the previous solution is projected on the refined domain and is used as an initial guess for the next Newton-Raphson iteration. Subsequently, the adaptive meshing algorithm is applied to the trimmed problem and the resulting hierarchically refined meshes are presented.

5.2   Trimming operation

To model realistic geometries, it is often necessary to include the presence of holes, slits, cavities, or other complex features. Two methods for creating these features have been investigated during the research: the multipatch continuous Galerkin (CG) approach and the hierarchical discontinuous Galerkin (DG) approach, which are illustrated in Fig. 5.1.

First, the multipatch CG approach is shown in Fig. 5.1a. It shows that the trimming operation is handled by preparing a conforming structure, deforming the interfaces to realize the desired shape, and assigning different properties to the trimmed region. However, the complexity increases with the number of trimming regions. Indeed, the main drawback of this multipatch approach is that the conformity of the mesh requires propagating the mesh structure to all geometrical dimensions, which can
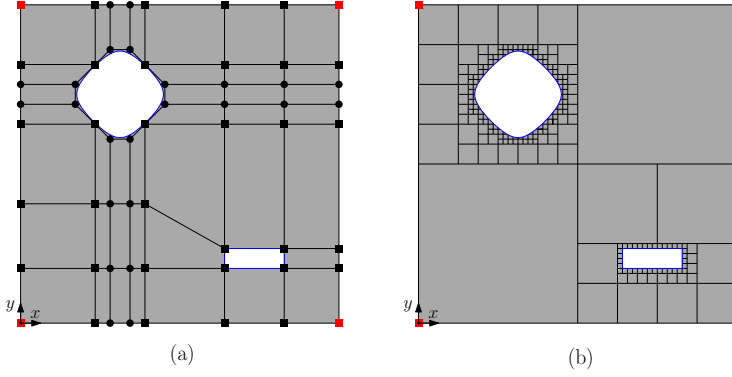
Figure 5.1: a) Multipatch contiuous Galerkin approach: original domain delimited by red squares, additional patches delimited by black squares, knot refinements are shown in black circles, and the interfaces of the trimmed domain are represented in blue, b) hierarchical discontinuous Galerkin approach: the meshes at different levels are shown in black in the untrimmed domain.

become rapidly a computational bottleneck. The intersection of two trimmed features cannot be realized easily. Furthermore, for the trimming of some shapes, such as a circle, it might be difficult to obtain corners guaranteeing angles close to 90 degrees, therefore decreasing the accuracy.

Second, the hierarchical DG approach, shown in Fig. 5.1b, treats the trimming problem more generally. The flexibility is improved as any number of slits can be trimmed without having to manually define the underlying complex conforming multipatch structure. In this case, the trimming operation is done by defining a level set function. It is a scalar-valued function defined on the whole computational domain, which takes positive values in the untrimmed domain, 0 at the interfaces, and negative values in the trimmed domain. The mesh is hierarchically refined up to a desired mesh level towards the interface before a triangulation algorithm is called. THB-spline spaces are then built upon the resulting mesh.

The level set concept is able to efficiently handle arbitrary complex shapes and boolean operations. Furthermore, it is widely used in other contexts. In fluid mechanics, it is used for boundary tracking in the context of immersogeometric analysis [63]. In structural mechanics, it is widely used for topology optimization [125].

In electromagnetics the air region is an integral part of the domain, and the trimmed regions have to be embedded back into the computational domain, contrary to fluid or solid mechanics models that keep only the air or solid regions, respectively. Therefore, two sets of basis functions are defined: one for the untrimmed domain and one for the trimmed parts. A partition is created between both discontinuous basis functions at the trimmed interface. The interface continuity between the basis functions is

handled using the discontinuous Galerkin approach, which is discussed for the two- and three-dimensional settings in the next section.

5.3   The discontinuous Galerkin method

To handle the interface continuity between the two pairs of basis functions, defined on the untrimmed and the trimmed domain, the discontinuous Galerkin (DG) approach is considered [34, 180]. In addition to the magnetic formulations inside the domains, which have been detailed throughout Chapter 3, boundary conditions at the interface Γ_T between the different basis functions have to be defined. The interface conditions for two-dimensional scalar-valued magnetic vector potential and three-dimensional vector-valued magnetic vector potential are described separately.

5.3.1   2D formulation

For the test and trial functions, u and v, respectively, the following quantities are defined:

$$\{v\} = \frac{v^+ + v^-}{2}, \tag{5.1}$$

$$[v] = v^+ \mathbf{n}^+ + v^- \mathbf{n}^-, \tag{5.2}$$

where, v is a scalar-valued function, "+" and "-" denote the two possible values across the interface, $\mathbf{n}$ is the normal to the interface, $\{\cdot\}$ and $[\cdot]$ represent the mean values and jumps on the edges of the elements, respectively. Similarly, the mean values and jumps for a vectorial gradient field ∇v are given by:

$$\{\!\{\nabla v\}\!\} = \frac{(\nabla v)^+ + (\nabla v)^-}{2}, \tag{5.3}$$

$$[\![\nabla v]\!] = (\nabla v)^+ \cdot \mathbf{n}^+ + (\nabla v)^- \cdot \mathbf{n}^-. \tag{5.4}$$

The bilinear operator $c(u_h, v_h)$, which acts on the basis functions restricted to the trimmed/untrimmed interface, and complements the magneto-quasistatic formulations, is given by:

$$c_{i,j} = \int_{\Gamma_T} \left([\omega_i] \cdot \{\!\{\nu(\mathbf{x})\nabla\omega_j\}\!\} + \tau\,[\nabla\omega_j] \cdot \{\!\{\nu(\mathbf{x})\nabla\omega_i\}\!\} - \gamma h_\beta^{-1}(\mathbf{x})\,[\omega_j] \cdot [\omega_i] \right) d\mathbf{x}, \tag{5.5}$$

where the values for the stabilization parameter $\gamma = \{10^5, 10^6\}$ are selected. The choice of these values is motivated in Sections 5.3.3 and 5.5.3 for the untrimmed and trimmed problem, respectively. The characteristic length of each element is denoted

$h_\beta(\mathbf{x})$, and $\tau = 1$ is taken so that it yields the so-called Symmetric Interior Penalty Galerkin (SIPG) method. Several other variants of this DG formulation exist for different values of the parameter τ [180].

5.3.2   3D formulation

In three-dimensional curl-conforming spaces, only the tangential continuity of the vectorial fields at the interface has to be imposed [34]. Mean and jump operators are redefined:

$$\{\!\{\mathbf{v}\}\!\} = \frac{\mathbf{v}^+ + \mathbf{v}^-}{2}, \tag{5.6}$$

$$[\![\mathbf{v}]\!]_T = \mathbf{n}^+ \times \mathbf{v}^+ + \mathbf{n}^- \times \mathbf{v}^-. \tag{5.7}$$

The bilinear operator for the interface continuity is therefore given by:

$$c_{i,j} = \int_{\Gamma_T} \left([\![\boldsymbol{\omega}_i]\!]_T \cdot \{\!\{\nu(\mathbf{x})\nabla \times \boldsymbol{\omega}_j\}\!\} + \tau [\![\boldsymbol{\omega}_j]\!]_T \cdot \{\!\{\nu(\mathbf{x})\nabla \times \boldsymbol{\omega}_i\}\!\} \right) d\mathbf{x}$$

$$- \int_{\Gamma_T} \gamma h_\beta^{-1}(\mathbf{x}) [\![\boldsymbol{\omega}_j]\!]_T \cdot [\![\boldsymbol{\omega}_i]\!]_T \, d\mathbf{x}. \tag{5.8}$$

The same values of parameters as described in the 2D case are chosen to yield the SIPG method.

5.3.3   Validation

In order to verify the convergence of the SIPG method used for trimming, the slotless benchmark is considered. The solution obtained with the continuous Galerkin approach is used as a reference. A defect of size null, i.e. a point, is trimmed at the interface between the airgap and the core. The value of the stabilization parameter γ is varied, such that different solutions using the discontinuous Galerkin SIPG method are obtained. The harmonic balance solver is selected with a solution that contains the first and third time harmonics. The convergence of the magnetic vector potential and the magnetic flux density is shown in Fig. 5.2a. The convergence of post-processed parameters is given in Fig. 5.2b. It should be indicated that the Newton-Raphson tolerance was 10^{-12} during this numerical experiment and had to be relaxed to 10^{-10} for the last two values $\gamma = \{10^7, 10^8\}$ to converge. This can be attributed to the condition number of the system matrix, which increases with the stabilization parameter, as depicted in Fig. 5.2a and as observed in [131, 188]
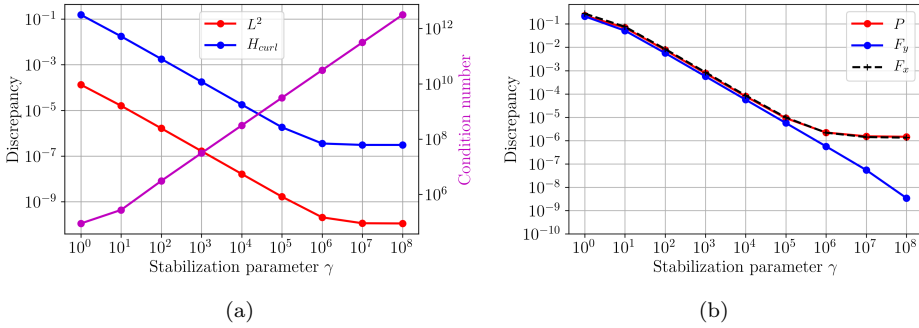
Figure 5.2: a) Convergence of the harmonic balance solution using the discontinuous Galerkin approach on the slotless benchamrk, containing the first and third time harmonics, in terms of both L^2 and H_{curl} norms defined in (2.54) and (2.66), respectively, together with the evolution of the condition number, indicated on the right axis, as a function of the stabilization parameter. b) Convergence of the post-processed parameters i.e. the attraction force F_y, damping force F_x, and eddy current losses P, for an increasing value of the stabilization parameter, γ, in the SIPG method.

for nodal and edge elements. However, no dependency on the degree of the polynomial has been observed. The value of the stabilization parameter for the untrimmed benchmark is selected as $\gamma = 10^6$.

5.4   The space-time Galerkin method

5.4.1   2D and 3D space-time Galerkin method

In this section, the space-time Galerkin approach is introduced and compared with the harmonic balance solver. The space-time Galerkin approach consists of extruding the geometrical model along the additional time dimension. The spline basis functions are built on the entire domain. Specific augmented Levi-Civita symbols are used to assemble the curl and time-derivative operators, from the overall gradient. For a 2D geometrical model, discretized with a scalar-valued magnetic vector potential:

$$\epsilon_{i'j'}^x = \left\{ \begin{array}{ll} \epsilon_{ij} & \text{if } (i',j') = (i,j), \\ 0 & \text{otherwise,} \end{array} \right. \tag{5.9}$$

$$\epsilon_{i'j'}^t = \delta_{i'3}. \tag{5.10}$$

where, $(i',j') \in [1,3]^2$ and $(i,j) \in [1,2]^2$, ϵ_{ij} is the 2D Levi-Civita symbol defined in (3.7), and δ is the Kronecker symbol. Similarly, for a 3D geometrical model,

discretized with a vector-valued magnetic vector potential:

$$\epsilon^{x}_{i'j'k'} = \begin{cases} \epsilon_{ijk} & \text{if } (i',j',k') = (i,j,k), \\ 0 & \text{otherwise,} \end{cases} \tag{5.11}$$

$$\epsilon^{t}_{i'j'k'} = \delta_{i'j'4}. \tag{5.12}$$

where, $(i',j',k') \in [1,4]^3$ and $(i,j,k) \in [1,3]^3$, ϵ_{ijk} is the 3D Levi-Civita symbol defined in (3.14).

Similar expansion and contraction operations are necessary to accommodate the curl-conforming transform given in (2.75). Alternatively, it is possible to construct a spatial topology and a time topology and build an overall domain through the tensor product of space and time topologies.

The approach described above is a particular case of space-time solver that is valid for the considered nonlinear eddy current problems. However, in the general space-time framework used in relativity, the electromagnetic four-potential should be considered [81]. The potential $\boldsymbol{A} = (V, \mathbf{A})$, combines the electric scalar potential along the time dimension and the magnetic vector potential along the spatial dimensions, as introduced in Section 2.3.1. The components of the magnetic and electric fields are gathered in the antisymmetric electromagnetic tensor $F_{\mu\nu}$ of rank 2 in four dimensions, which is obtained as:

$$F_{\mu\nu} = \nabla_\mu \boldsymbol{A}_\nu - \nabla_\nu \boldsymbol{A}_\mu. \tag{5.13}$$

5.4.2 Comparison with the harmonic balance method

In case a motion-free or a periodic motional problem is considered, a time-varying source is defined similarly to the harmonic balance method, and a continuous Galerkin (CG) approach is used. This case is illustrated in Fig. 5.3a, and is used throughout this chapter.

As an alternative to the time-varying source approximation, the rotor geometry could also be extruded along the time direction and skewed to the next stator period. This is illustrated in Fig. 5.3b. The airgap interface continuity is then handled through a space-time DG approach. In this case, not only the basis functions are discontinuous but the topology as well. Therefore, additional treatments, that have not been implemented in this work, are required in the airgap for coupling both domains. This approach is the most general, as no assumptions on the source or geometry of the mover are necessary. In particular, the slotting of the magnet array can be modeled exactly, and the eddy currents in the moving parts could be modeled easily.
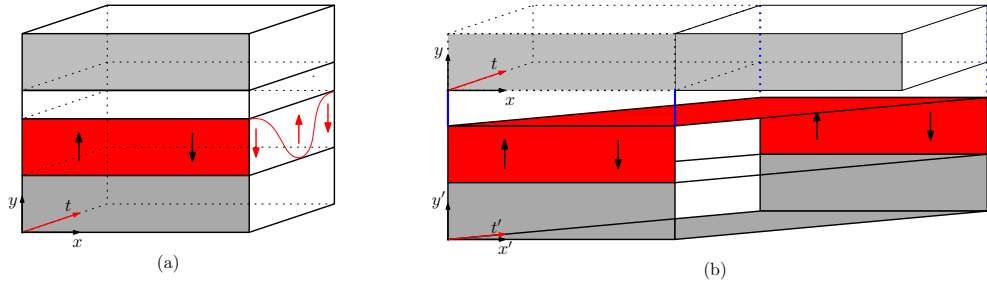
Figure 5.3: Space-time domains with a) the continuous and b) discontinuous Galerkin methods.

In Table 5.1, the computational effort for the slotless and slotted benchmarks are given, for the space-time CG approach illustrated in Fig. 5.3a, and compared to the harmonic balance method, and the time-stepping technique. The temporal and spatial discretizations described in Sections 4.3.2 are reused for both the slotless and slotted benchmarks. The only difference is that only eight elements along the periodic x-direction are used for the slotless benchmark. Because of the correlation between the x and time t dimensions due to the motion, eight elements are taken along the periodic time dimension as well. A Newton-Raphson tolerance of 10^{-8} is specified for all solvers, and a speed of 1 m/s is considered.

Table 5.1: Computational effort comparison among the three nonlinear transient approaches for the 2D benchmarks, harmonic balance method with up to the third (HB(2)) or seventh (HB(4)) time harmonic, space-time (ST), and time-stepping (TS) methods, without adaptivity, and with a single core.

	Slotless			Slotted		
	HB(2)	ST	TS	HB(4)	ST	TS
Time [s]	24	119	821	138	236	1470
Ratio [-]	-	5.0	34.4	-	1.72	10.6

The results of Table 5.1 demonstrate that the space-time approach is advantageous compared to the time-stepping technique, with a speedup factor of 6. Furthermore, they show that the harmonic balance method is the most efficient solution overall, with a speedup factor of 34 and 10 compared to the time-stepping technique for the slotless and slotted benchmarks, respectively. However, as the solution gets more complex in terms of local features and as the time-harmonic content is increased, i.e. from solution including up to the third and seventh time harmonics, the advantages of the harmonic balance method are lessened.

When solving large problems using the harmonic balance solver, for instance with significant harmonic spectra and/or in three dimensions, the computational efficiency
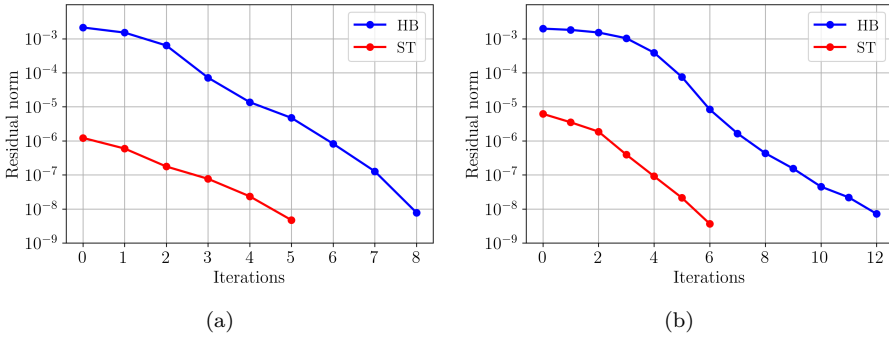
Figure 5.4: a) Nonlinear convergence of the space-time approach and harmonic balance method with the third time harmonic for the slotless benchmark of Fig. 4.1a , b) nonlinear convergence of the space-time approach and harmonic balance method with the seventh time harmonic for the slotted benchmark of Fig. 4.1b.

can be impaired. One way to speed up the overall solving time is to adopt a *progressive* harmonic refinement strategy. This strategy is called progressive as opposed to adaptive, since the refinement is not based on error estimators. Instead, the system is first solved using the fundamental harmonic alone and this intermediate solution is then used as an initial guess for the next Newton-Raphson iteration, which solves the system for incrementally richer harmonic content. For instance, applying this strategy to the slotted benchmark can save up to 37 % of the computational time reported in Table 5.1.

Fig. 5.4 shows the nonlinear convergence of the space-time and harmonic balance approaches. Since the harmonic balance is based on trigonometric basis functions, as the time signals get more complex, more harmonics are necessary, which degrades the convergence due to cross-coupling effects. For the slotless benchmark, 5 and 8 iterations are necessary to reach convergence for the space-time and harmonic balance approaches, respectively, while it takes 6 and 12 iterations for the slotted problem to converge. As expected, the number of iterations needed for the space-time solver is much less sensitive to the complexity of the solution in time than for the HB solver. However, since an HB iteration is typically faster than an ST iteration due to reduced dimensionality, the harmonic balance approach is still competitive overall.

The solutions obtained with the space-time Galerkin approach are given as the distribution of the modulus of the magnetic flux density in Fig. 5.5 for both the slotted and slotless benchmarks. The direction of motion can be seen from the top plane in the slotless example.
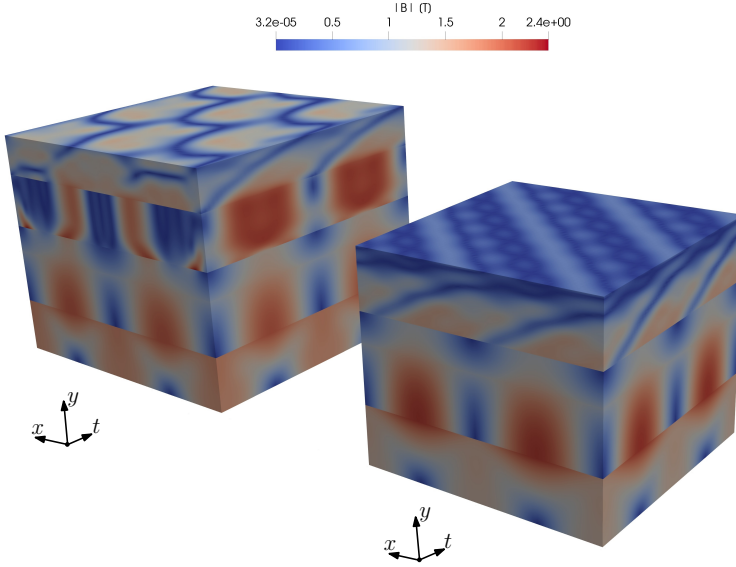
Figure 5.5: Space-time solutions for the slotted and slotless benchmarks of Fig. 4.1, on the left and right, respectively.

5.4.3   Euler and Lagrange formulations

As introduced in Section 4.1.1, several situations can arise in motional eddy current problems that can be described following either the Lagrange or Euler formulations. In the Euler formulation, a single reference frame is considered and therefore the total derivative applies:

$$\frac{\mathrm{D}A(\mathbf{x},t)}{\mathrm{D}t} = \frac{\partial A(\mathbf{x},t)}{\partial t} + \boldsymbol{v} \cdot \nabla_{\mathbf{x}}(A(\mathbf{x},t)), \tag{5.14}$$

where, $\boldsymbol{v}$ is the displacement speed. For the slotless benchmark, the speed is equal to $\boldsymbol{v} = -v\mathbf{x}_0$ in the stator and $v = 0$ in the mover. Considering solely eddy currents in the stator core, the formulation reads:

$$\nabla \times (\nu'(A(t))\nabla \times A(t)) - \sigma \frac{\mathrm{D}A(t)}{\mathrm{D}t} = J(t) + \nabla \times \nu'M(t), \tag{5.15}$$

$$\nabla \times (\nu'(A(t))\nabla \times A(t)) - \sigma \boldsymbol{v} \cdot \nabla_{\mathbf{x}}(A(t)) = J(t) + \nabla \times \nu'M(t). \tag{5.16}$$

This approach is equivalent to the Lagrange formulation with the moving material approach, where the source term $M(t)$ in the permanent magnet array is moving at
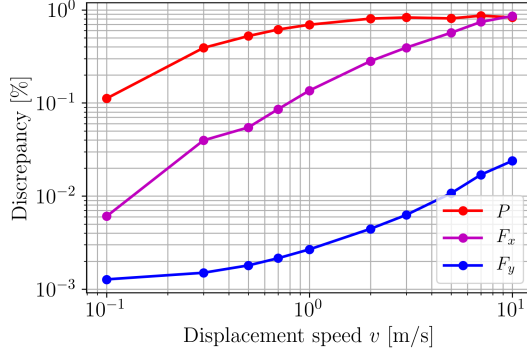
Figure 5.6: Comparison of the discrepancy of the post-processed parameters, i.e. the eddy current losses P, damping force F_x, and attraction force F_y, between the Euler and Lagrange formulations on the slotless benchmark of Fig. 4.1a.

a speed v along the x-direction:

$$\nabla \times (\nu'(A(t))\nabla \times A(t)) - \sigma \frac{\partial A(t)}{\partial t} = J(t) + \nabla \times \nu' M(t). \tag{5.17}$$

The equivalence is demonstrated numerically in Fig. 5.6, based on the slotless benchmark, where the discrepancy between the post-processed parameters, such as the force and eddy current losses, is smaller than 1 %. However, a better accuracy would be expected and possible remedies are given at the end of the section.

Additionally, there is the case where the eddy currents are of interest in the mover. The Euler formulation works well for the slotless benchmark, where the eddy currents in the mover are identically zero. However, for the slotted benchmark, the Euler formulation does not directly allow for the relative motion of the slotted core. The Lagrange formulation with moving material approach is able to consider the slotting effect, and can be adapted to include the eddy currents in the mover. To do so, a new normalized time vector **t** is introduced, such that:

$$\mathbf{t} = \begin{cases} \mathbf{t} & \text{in the stator,} \\ (\mathbf{t} + v\mathbf{x})\left(1 + v^2\right)^{-0.5} & \text{in the mover.} \end{cases} \tag{5.18}$$

In this case, the eddy current term in the space-time topology is obtained as:

$$\sigma \frac{\partial A}{\partial t} = \sigma \nabla A \cdot \mathbf{t}. \tag{5.19}$$

The eddy current losses in the slotless benchmark, in both the stator and mover are shown in Figure 5.7 for the same benchmark. It can be seen that the eddy current losses in the mover tend to zero as the number of elements is increased. This can be
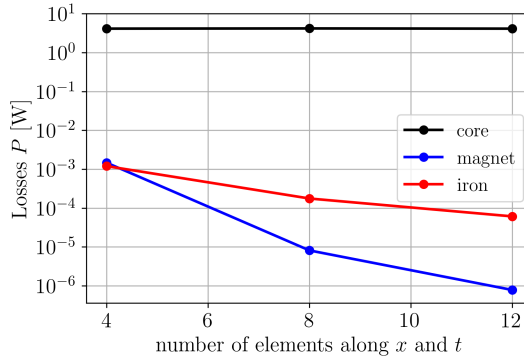
Figure 5.7: Eddy current losses in the stator and mover at $v = 10\text{m/s}$ in the slotless benchmark of Fig. 4.1a, for an increasing number of elements along the periodic dimensions.

explained as the fields are skewed with respect to the underlying mesh, and it is more difficult to obtain an identically zero derivative along the new time vector $\mathbf{t}$.

To ensure the eddy currents in the mover are identically zero with computer precision, the discontinuous space-time topology of Fig. 5.3b should be used to have the time direction collinear with the direction of motion. The sliding band approach could be applied to realize the coupling as well [61, 65]. Alternatively, the B-spline basis functions could be enriched with trigonometric functions (cos, sin) to enable an exact approximation of the sinusoidal derivatives independently of the mesh refinements. These generalized B-spline (GB) basis functions have been applied to isogeometric analysis in the context of collocation and boundary-element methods [5, 159].

5.5   Adaptive harmonic balance method

5.5.1   Motional eddy current testing benchmark

To research trimming, a new geometrical model is considered in this section. It is constructed from the 2D slotless benchmark. A rectangle of height h and width w is trimmed from the core, at a depth d from the airgap-core interface, as shown in Fig. 5.8a. Additionally, in Fig. 5.8b several variations of the trimmed shapes are illustrated, a few of these variations will be considered in the numerical experiments of this section.
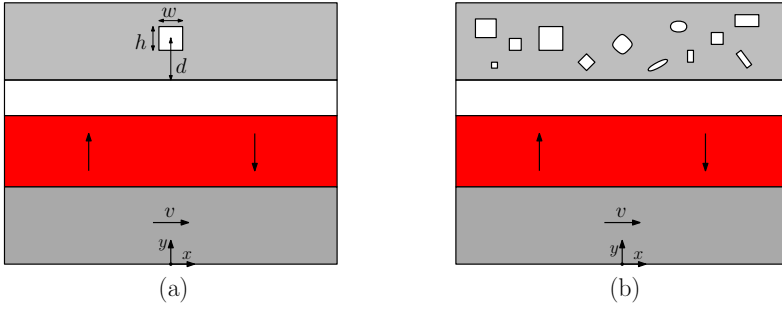
Figure 5.8: a) 2D slotless benchmark with trimmed core and b) variations of the trimmed shapes.

This benchmark can represent the problem of the detection of defects in a conductive material through electromagnetic nondestructive testing (NDT). Electromagnetic detection methods include: eddy current testing (ECT) and Lorentz force eddy current testing (LET) [27]. ECT relies on a time-harmonic excitation coil, which induces eddy currents in the material sheet, and a pick-up coil from which the voltage is analyzed. LET relies on a moving magnet array, to which a force sensor is attached. The presence of a defect modifies the sensed signal compared to the background signal, as a result enabling the defect detection. A further analysis aims at quantifying the size, shape, and depth of the potential defects. The LET system benefits from stronger magnetic fields due to the permanent magnets, and therefore yields a faster detection of deeper defects. Most of the research available in the literature focuses on defect detection in non-ferromagnetic metal sheets, such as aluminum or copper. Detection of defects in aluminum is widely researched because of the absence of the endurance limit, as opposed to steel. Indeed in aluminum, the fatigue crack will always occur independently of the stress magnitude, if a sufficiently long stress cycle is applied. Furthermore, the modeling of the aluminum crack detection is relatively simple, since it belongs to the class of linear eddy current problems, which can be solved efficiently by analytical models [46, 79, 214, 228]. However, the eddy current testing of steel sheets, which are both electrically conducting and magnetically permeable with a nonlinear material characteristic are much less discussed, as it requires a nonlinear transient numerical model. In this case, not only the Lorentz force is acting, but also the reluctance force. The harmonic balance method constitutes a novel and efficient approach for solving the motional eddy current testing (MET) problem in steel sheets.

5.5.2   Numerical experiments

First, the harmonic balance method is compared to the backward-Euler time-stepping technique on the trimmed square benchmark of Fig. 5.8a. This aims at characterizing

the evolution of the force signals under changes of the defect size and depth, as well as the accuracy of the harmonic balance solver on trimmed domains. The depth of the defect is varied from 0.1 to 0.9 mm, while the size of the trimmed square is varied from 0.1 to 0.4 mm. The mover speed is equal to 1 m/s.

The attraction and damping force profiles shown in Fig. 5.9, demonstrate that the results obtained from the time-stepping and harmonic balance methods are in good agreement, although for the attraction force an offset of 0.1 % is present between both methods. For the detection of smaller signals, such as depicted in Fig. 5.9e, where the defect is buried at a depth of 0.9 mm, the harmonic balance method gives smoother signals, while the time-stepping technique contains a higher frequency ripple. By construction, the harmonic balance method provides an efficient way of avoiding the nonphysical high-frequency component from the solution and derivatives. In Fig. 5.10, the computational effort is compared between both methods, and the harmonic balance method demonstrates an important computational time reduction with respect to the time-stepping technique. It can be seen that the computational effort is mostly independent of the depth of the defect, while larger defects are more expensive, since the problem exhibits a higher number of degrees of freedom.

Second, a trimmed rectangular slit topology with a fixed height of 2 mm, a depth of 0.9 mm and a varying width is considered. The number of time steps per period for the transient approach and similarly the number of time samples for the discrete Fourier transform for the harmonic balance approach are varied. In Fig. 5.11a, the different time profiles for the attraction and damping forces are given for different time discretization for a width of 0.1 mm. The time-stepping approach yields different results depending on the number of time steps considered per period. On the contrary, the results obtained with the harmonic balance are much less dependent on the number of time samples considered in the discrete Fourier transform. With the time-stepping approach, the mean variation between the solution using 15 and 120 time steps is $1.8 \ 10^{-2}$ % and 12.6 %, for the attraction and damping force respectively, while being only $5.4 \ 10^{-6}$ % and $2.4 \ 10^{-4}$ % with the harmonic balance method. While the offset persists between both methods for the attraction force, the damping force from the time-stepping approach converges towards the same value as obtained with the harmonic balance method. In Fig. 5.11b the influence of the time discretization on the computational effort is depicted for both the time-stepping and harmonic balance approaches. It is clear that the harmonic balance method is more efficient than the time-stepping counterpart, especially given the fact that the harmonic balance is more accurate for the same time-discretization.
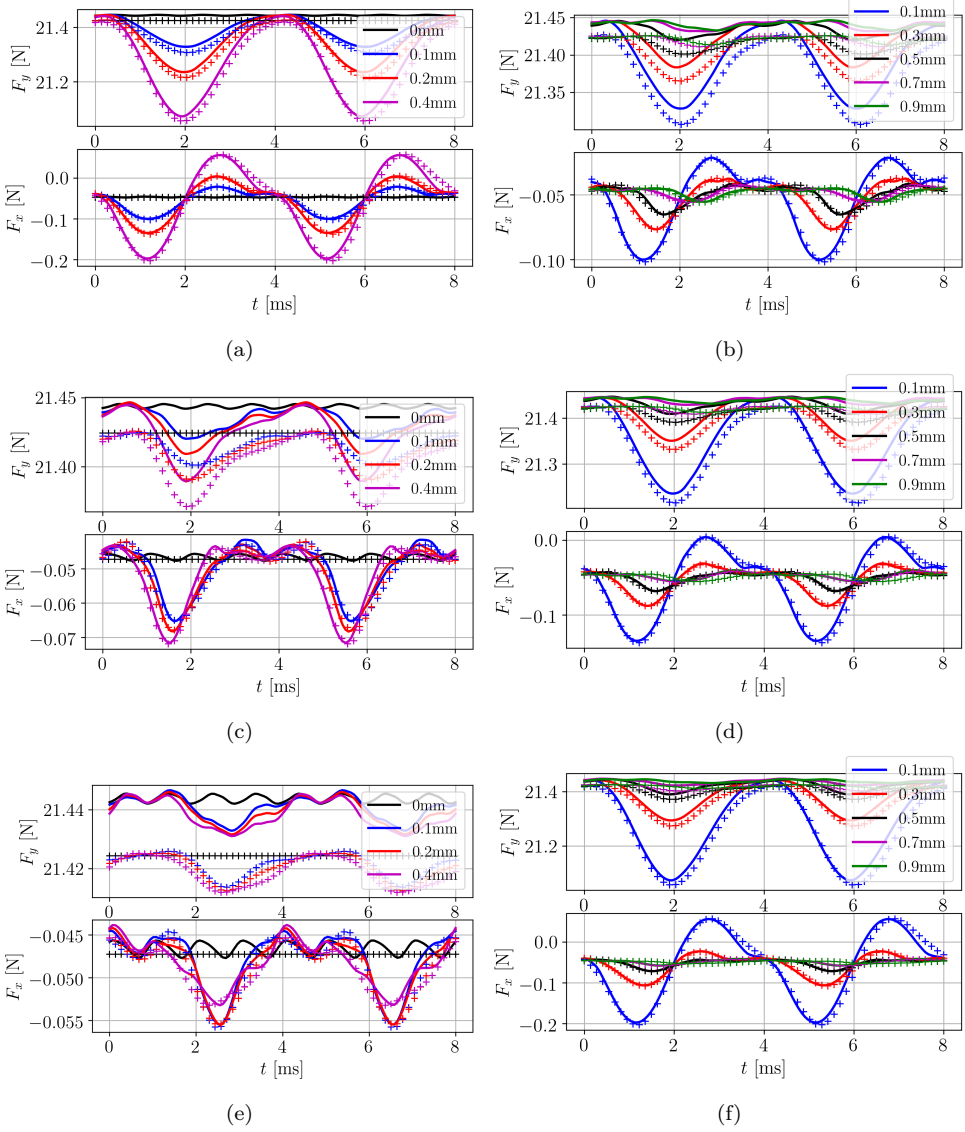
Figure 5.9: Attraction force F_y and damping force F_x profiles for different defect sizes indicated in the legends, at depths 0.1, 0.5, and 0.9 mm in subfigures a), c), and e), respectively. Attraction force F_y and damping force F_x profiles at differents defect depths indicated in the legends, for defect sizes of 0.1, 0.2, and 0.4mm in subfigures b), d), and f), respectively. The results obtained with time-stepping approach are plotted with continuous lines while the results from harmonic balance method are represented with plus markers.
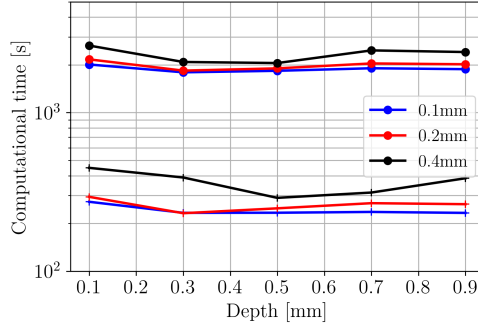
Figure 5.10: Comparison of the computational effort between the results obtained with the time-stepping approach and the harmonic balance method, given with dot and plus markers, respectively.

(a)

(b)
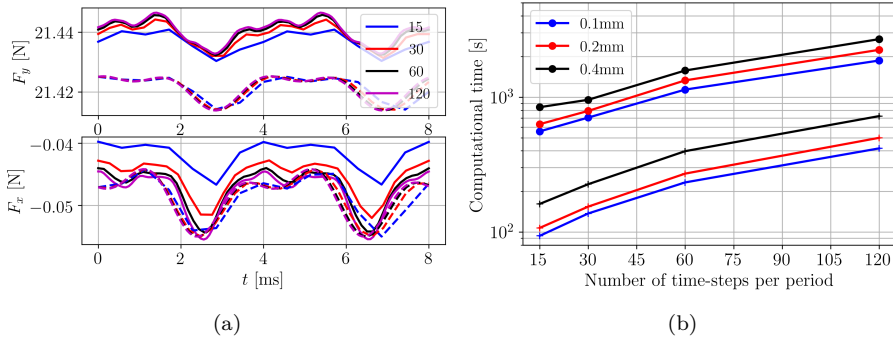
Figure 5.11: a) Comparison of the attraction force F_y and damping force F_x time-profiles generated with different time discretizations, the time-stepping results are given with continuous lines and the results from the harmonic balance method are given with dashed lines. b) Comparison of the computational time as a function of the number of time steps per period, between the results obtained with both the time-stepping approach and the harmonic balance method, shown in dot and plus markers, respectively.

5.5.3 Adaptive refinements

As mentioned in Section 4.4, it is possible to implement spatial adaptive refinements for the harmonic balance method. Refinements in time are already handled through the selection of the harmonic content of the solution. However, these refinements are operated *a priori* or *a posteriori*, and not in a truly adaptive manner. The harmonic balance method can be seen as a pseudo-spectral method because of the Fourier basis functions in time. The time-harmonic refinements are therefore not localized. However, for complex systems, progressive harmonic refinements can be considered to speed up the computational time of the harmonic balance solver, as explained in

Figure 5.12: Residual norm at successive Newton-Raphson iterations for the untrimmed problem, increasing the refinement levels without initial guess a) and with an initial guess obtained from the solution at the previous level b). c) Evolution of the number of degrees of freedom and corresponding computational time. d) Convergence of the mean value of the eddy current losses for increasing refinement level.

Section 5.4.2. In this section, numerical results are presented that characterize the accuracy and computational cost of the spatial adaptive harmonic balance method for solving the trimmed benchmark problem.

Some preliminary results are first established on the untrimmed slotless benchmark, and additional results are given on a trimmed core benchmark, consisting of a 2 mm square with rounded edges rotated by 45 degrees at a depth of 3 mm, as illustrated with the top-left defect in Fig. 5.1 and the central defect in Fig. 5.8b. The speed of the mover is equal to 10 m/s.

The preliminary results on the untrimmed problem aim at demonstrating the increase in computational efficiency for solving the adaptive refinement problem using the solution at the previous level as an initial guess for the first Newton-Raphson iteration at the new mesh level. This is realized by L^2 projection. Figs. 5.12a and 5.12b show that the number of nonlinear iterations is greatly reduced. Moreover, the potential convergence plateau is avoided. Altogether, it reduces the computational effort as

shown in Fig. 5.12c. The reduction is such that the cumulative time of the proposed strategy can get smaller than the original time at one level, as seen at levels 1 and 5. Furthermore, Fig. 5.12d demonstrates that both strategies converge to the same value, which verifies that the initial guess strategy does not stir towards a wrong solution.

The strategy of using the solution from the previous level as an initial guess is more important for the trimmed problem. Because the trimmed problem is ill-conditioned, reaching a tolerance of 10^{-12} in the Newton-Raphson solver for an arbitrary trimmed shape is not guaranteed. Even when using the previous solution as an initial guess, the value of the stabilization parameter has to be reduced to $\gamma = 10^5$ to decrease the condition number of the trimmed problem and to enable convergence to the prescribed tolerance.

In Fig. 5.13a, the convergence of the residual for the trimmed problem is presented, using the solution from the previous level as an initial guess for the Newton-Raphson solver. In Fig. 5.13b, the evolution of the condition number with the number of degrees of freedom following the adaptive mesh refinement is given. It shows that the trimmed problem is very ill-conditioned, but has a tendency to improve as the refinements increase and thus decrease the ratio of mesh sizes. The untrimmed problem is well-conditioned but slowly degrades as the refinements progress. The ill-conditioning of the trimmed problem can be explained because of the small intersection between the trimmed domain and the background grid. Direct solvers can still find a solution to the resulting matrix however it can become a bottleneck for larger systems. In this case, preconditioned iterative solution techniques should be considered [62].

The convergence of the eddy current losses is shown in Fig. 5.13d, which indicates that the converged value is reached at the fourth refinement. Additionally, one can notice that the trimmed topology exhibits higher losses although there is less conductive volume, which is due to the higher value of the time gradient of the magnetic flux density as the magnetic field goes around the hole. In Fig. 5.13e and Fig. 5.13f, the magnetic flux density distribution and the hierarchically refined mesh of level four are given for the untrimmed and trimmed topology, respectively. The refinements are concentrated in the core region, where the complex physical behavior occurs due to the interaction between the eddy currents and the trimmed defect. To obtain more refinements along the gap interface, as in the untrimmed topology, the value of the parameter θ should be decreased. The untrimmed problem exhibits faster growth than the trimmed problem in terms of the number of degrees of freedom, as shown in Fig. 5.13c, since the error is less localized, i.e. has larger support.
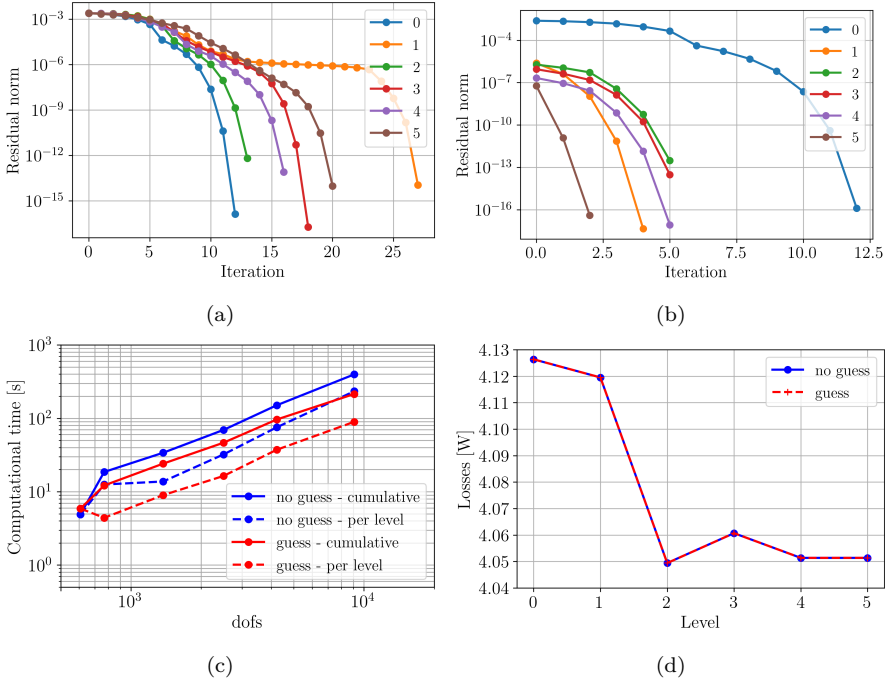
(a)

(b)

(c)

(d)

(e)

(f)
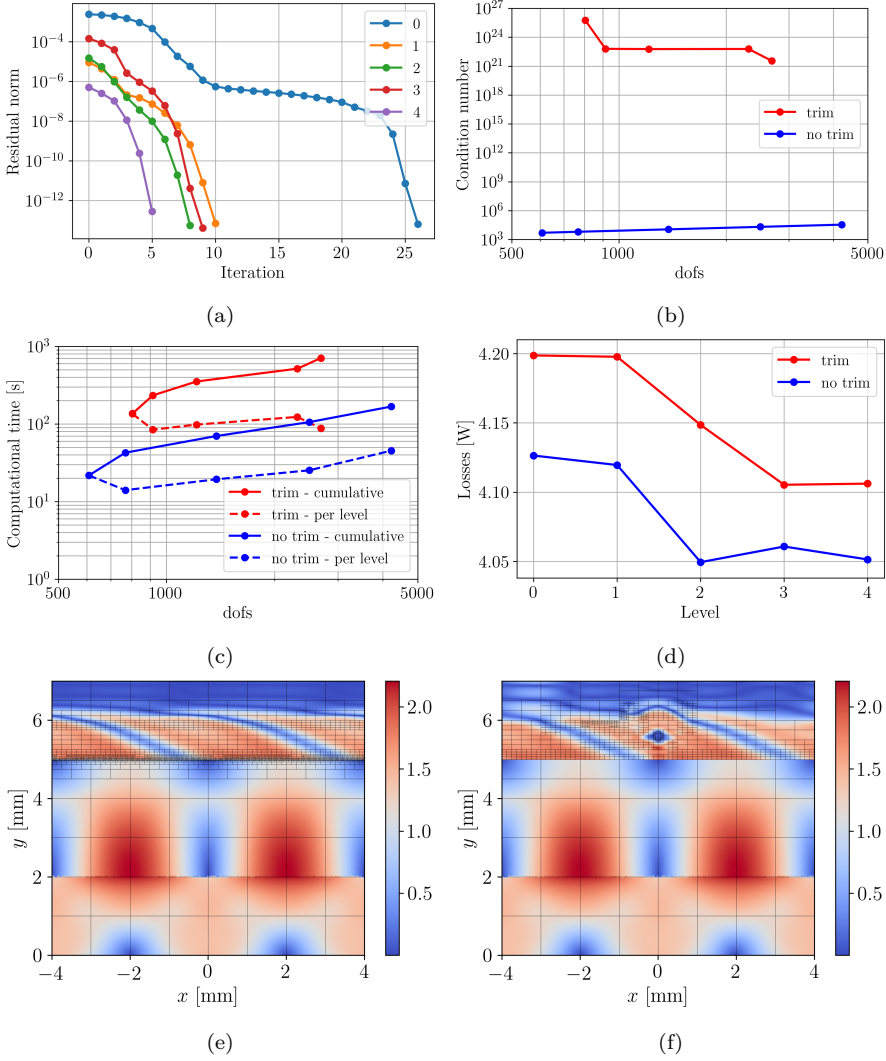
Figure 5.13: a) Residual norm at successive Newton-Raphson iterations for the trimmed slotless problem, for increasing refinement level with initial guess from the solution at the previous level. b) Condition number of the trimmed and untrimmed problems as a function of the number of degrees-of-freedom with increasing refinement level. c) Evolution of the number of degrees of freedom and the corresponding computational time. d) Convergence of the mean value of the eddy current losses for an increasing refinement level. Magnetic flux density distribution B in [T] and mesh at the last level for e) the untrimmed problem and f) the trimmed problem.

5.6   Conclusion

In this chapter, the framework for performing isogeometric analysis on trimmed domains is detailed. In particular, the concepts of the level set and discontinuous Galerkin approach have been discussed. The interface boundary conditions have been detailed for the scalar- and vector-valued magnetic vector potential. The convergence of the discontinuous Galerkin approach has been demonstrated as a function of the stabilization parameter. It is shown that a trade-off on the value of this parameter has to be found, since it deteriorates the condition number of the system matrix. Furthermore, this trade-off is different for trimmed and untrimmed problems. The DG scheme is not needed for the untrimmed case and was mainly considered as a means for preliminary validation.

The space-time Galerkin approach has been detailed and compared to the harmonic balance and time-stepping approaches on both the slotless and slotted benchmarks. It is shown that the harmonic balance is the most advantageous method for the considered problems. The space-time solver is further investigated to quantify the numerical difference arising between the Euler and Lagrange formulations of the motional eddy current problem. The eddy currents in the mover are found to be inaccurate using the Euler formulation. The eddy current effects in the mover could be modeled in the space-time Galerkin framework by employing a discontinuous stator topology, a skewed mover topology, and an adequate coupling in the airgap.

The harmonic balance method is compared to the time-stepping approach and demonstrates a certain independence on the time-discretization, which is advantageous for further computational time reduction. Finally, spatial adaptive refinements are implemented for the harmonic balance together with an initial guess for the Newton-Raphson iterations based on the solution at the previous level, which enables faster convergence. It results in a decrease in the computational effort by a factor 2 and 5, for the untrimmed and trimmed benchmark, respectively. The proposed approach constitutes a novel and efficient way of solving the motional eddy current testing problem in steel sheets and laminations.

In the next chapter, the framework developed to solve the motional eddy current problem on trimmed domains is applied to a three-dimensional problem consisting of a single-sided axial-flux permanent magnet machine with slitted core. The nonlinear eddy current model is coupled with a thermal model. A prototype is realized to validate the multi-physical numerical model by conducting measurements on the global friction torque, local electromagnetic spectra, temperatures, and airflow velocity.

Chapter 6

Motional eddy currents in the slitted core of an AFPM machine

THE different models introduced in previous chapters are combined in order to resolve an academic problem with industrial relevance. The challenge is to simulate the steady-state multi-physical behavior of a single-sided axial-flux permanent magnet (AFPM) machine. The curved geometry is a complex three-dimensional trimmed domain. The multi-physical model, which couples electromagnetic and thermal solutions, is implemented in the developed isogeometric framework. A sensitivity analysis is conducted to characterize the influence of the time-harmonic spectra, material characteristics, and geometrical parameters. The proposed numerical model is validated with experiments, which spans a large range of rotational speeds and airgap lengths. Global quantities, such as the losses in the slitted core, as well as local quantities, such as the temperature and electromagnetic field spectra, are measured and compared to the simulated quantities.

6.1   Introduction

Permanent magnet machines fall into three main categories, depending on the motion they enable: linear, planar, or rotational movement. A linear machine segment, stacked along the z-direction and periodic along the x-direction, can generate the so-called tubular, radial, or axial machines, by wrapping the geometry around the x, y, or z axis, respectively. The latter is of interest in this chapter.

The axial-flux permanent magnet (AFPM) topology can exhibit higher power density and efficiency than traditional radial-flux permanent magnet (RFPM) machines [12, 39, 41, 94, 120, 137, 199]. A compact structure, better cooling capabilities, and an adjustable airgap make the AFPM technology an attractive alternative to conventional RFPM topologies [130]. Owing to their beneficial characteristics, AFPM machines have become increasingly popular in numerous applications, such as transportation with in-wheel automotive motors [84], ship propulsion [167], aircraft propulsion [240], medical use with CT-scanner drives [194, 200], and energy generation with wind turbines [129]. The AFPM topology spans all sizes and arrangements: single-sided, double-sided, and multi-stack topologies are possible depending on the application requirements [130].

A slotless single-sided topology is considered for conducting the experiments. To validate the different modeling features, the single-sided topology is advantageous because the airgap length can be more easily adapted. This enables to increase the magnetic saturation in the stator core, together with the eddy current losses and the temperature. The topology of the single-sided AFPM machine is illustrated in Fig. 6.1. In the experiments, however, the windings are not considered as the machine is externally driven. In the industry, the single-sided topology choice is motivated by a simpler design and manufacturing solution, and easier stator and rotor removal process. However, single-sided designs suffer from unbalanced axial forces, which can lead to more complex bearing systems and thicker dimensions to avoid deflection.

The stator core of the AFPM machine is made of soft-magnetic material that exhibits nonlinear B-H characteristics and leads to hysteresis losses, eddy current losses, and additional excess losses under rotating magnetic fields. In general, two main design methods are used to reduce these losses in electrical machines, either lamination of the core is performed employing electrical steel, or soft-magnetic composite materials (SMC) are used. However, in axial-flux topologies, the lamination technique is not possible as the stator core would consist of a large set of concentric iron rings with incrementally increasing diameter, or of a spiral sheet winding. Both are difficult to manufacture especially for large machines. The use of SMC core is often preferred with smaller AFPM machines, and the development of such materials has been greatly reducing the core losses [92]. However, SMC does exhibit a lower permeability
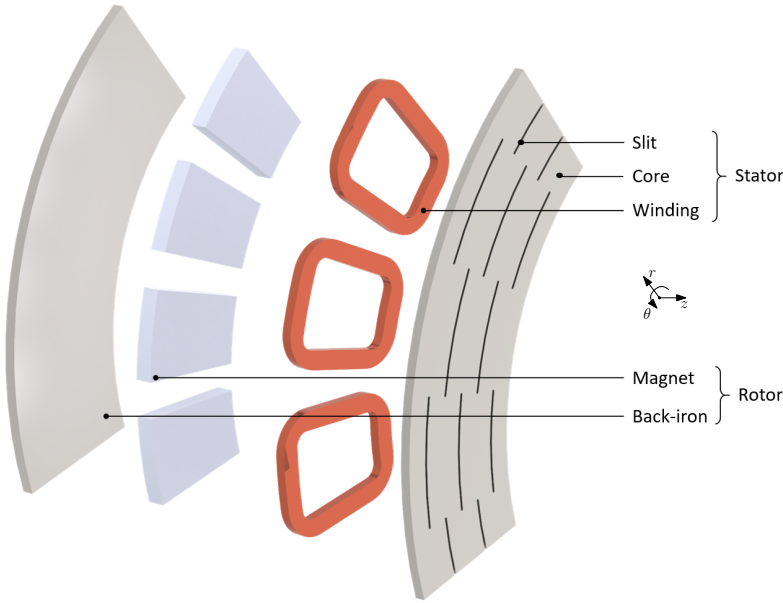
Figure 6.1: Exploded view of a periodic section of a single-sided AFPM topology with slitted stator core.

and saturation level than more common types of steel [137]. Furthermore, it has a much higher cost and necessitates complex molds and large presses which limit the scalability towards larger diameter AFPM machines [94].

Slitted cores partially replace the laminations in their role of eddy current barriers, while guaranteeing better structural properties and ease of manufacturing. They provide a cheaper alternative to the use of SMC material. In this chapter, an economical solution for the manufacturing of the AFPM machine stator core is investigated. It consists of the trimming through laser cutting of elongated holes, or slits, in the azimuthal direction of the core, which is made out of soft-magnetic material like electrical steel. The resulting topology is illustrated in Fig. 6.1.

A geometrically accurate and time-efficient model is required to assess the performances of the machine. AFPM topologies are inherently 3D problems, but 2D simplifications are often proposed to reduce the computational effort [7, 128, 138, 211]. However, quasi-3D models lack accuracy and robustness with respect to dimension changes, especially when nonlinear characteristics are present and when the eddy current loss estimation is of interest. Therefore, the discretization in three spatial dimensions is conducted in the isogeometric analysis framework.

Including motional eddy current effects in the simulation can be done using either time-stepping linearization or time discretization with the Galerkin method, resulting in 4D models. Both methods lead to large systems of equations and require the development of additional techniques to represent accurately the airgap sliding interface. Moreover, since nonlinear material characteristics are included, several iterations per time step are needed. If the steady-state solution is of interest, it is necessary to step through several periods, which makes such a method unusable for optimization problems. By assuming harmonic excitation corresponding to a constant rotational speed, and taking advantage of both time and space periodicity of the solution, the complexity can be reduced to a spatial problem in the frequency domain. Moreover, since the soft-magnetic material characteristic is nonlinear, higher-order field harmonics are excited. Therefore, the resulting electrodynamic solution is well approximated by means of a multiharmonic time series, using the harmonic balance method introduced in Chapter 4.

To simulate the three-dimensional motional eddy-current problem with nonlinear magnetic properties, a modeling approach is proposed, which combines the isogeometric framework with the harmonic balance method. The isogeometric analysis enables the exact representation of three-dimensional curved geometries and slits. Furthermore, IGA provides the accurate solution of electromagnetic fields on such a complex geometrical structure, at a reduced cost with regard to the number of degrees of freedom, when compared to the traditional FEM. The multiharmonic system is significantly smaller than its transient counterpart and enables fast and accurate extraction of the machine parameters, such as torque ripples and time-averaged eddy current losses.

In addition to the nonlinearities of the magnetic reluctivity originating from the *B-H* characteristics of the iron core, the electrical conductivity and the magnetic remanence are temperature dependent. These two parameters influence the penetration and amplitude of the eddy currents in the material. The resulting eddy currents represent a major heat source, and therefore the electromagnetic and thermal models are coupled. Different types of models are possible, such as, with increasing complexity, analytical lumped parameters, thermal finite elements analysis (FEA) with empirical coefficients for convective heat transfer, and coupled CFD-FEA with iterations across the physics [3, 192]. The empirical convection coefficient approach is implemented in the framework of isogeometric analysis in Section 6.4, while the conjugate heat transfer coupling with laminar and turbulent flow models is investigated in [231].

In this chapter, the experimental setup and all the composing elements are first detailed. The three-dimensional coupled model is then introduced, starting from the electromagnetics. Some parameters composing the nonlinear model, such as the *B-H* characteristics and the number of time harmonics, are selected from the experimental data presented afterwards. Using the measured dissipated power, core temperatures

and airflow velocity, an empirical convection law is determined to build the thermal model, which includes conduction and radiation heat transfer mechanisms as well. Both the electromagnetic and thermal models are then coupled and validated against the experimental measurements. A sensitivity analysis is conducted to characterize the impact of the *B-H* characteristics and number of time harmonics in the model, on the predicted losses. Furthermore, the influence of the dimensions and number of slits is explored in terms of losses reduction. The temperature distribution is illustrated together with its effect on the electrical conductivity. Different mesh discretization strategies are discussed for both conforming and nonconforming topologies.

6.2   Experimental setup

The experimental setup manufactured to validate the numerical model is presented in Fig. 6.2. It is built to verify that the modeling aspects of interest, such as the three-dimensional complex trimmed geometry with nonlinear material characteristics including eddy currents and temperature-dependent properties, are correctly captured by the proposed modeling approach. The rotor of the AFPM machine with surface-mounted permanent magnets is attached to an externally driven motor, which rotates between 500 rpm and 1500 rpm. The slitted stator core is attached to a support, which is axially translated using a spindle mechanism, and, as a result the airgap length can be adapted. Reducing the airgap increases the magnetic flux density in the slitted core, which excites higher-order time harmonics, due to an increased level of magnetic saturation. This effect is captured with current probes that are utilized as flux sensors. Furthermore, more eddy currents are induced in the core and higher temperatures are reached, which locally modify the material properties. The temperature is measured at several locations using thermocouples. The electromagnetic damping torque resulting from the eddy currents and the rotational speed are both measured using a dynamometer.

The prototype setup is realized with parts from different sources. The rotor used in the prototype was originally designed as part of the new electric motor present in the *Stella Era* solar-powered electric vehicle. The *Solar Team Eindhoven* participates in the Cruiser Class biennial race of the *World Solar Challenge*. They already have been victorious during the 2013, 2015, 2017, and 2019 editions. For the next edition in 2021, they are expecting to compete with a new twin-rotor AFPM motor, manufactured by *Prodrive Technologies B.V.*, from which a single rotor is used for realizing the prototype. The 16 pole-pairs magnet array is composed of a solid steel back-iron and NdFeB N50M permanent magnets with black epoxy over nickel coating. The geometrical dimensions are summarized in Table 6.3 and the physical parameters are given in Table 6.4 and Table 6.5, for the electromagnetic and thermal quantities, respectively. The back-iron is mounted onto a rotor support made of aluminum,
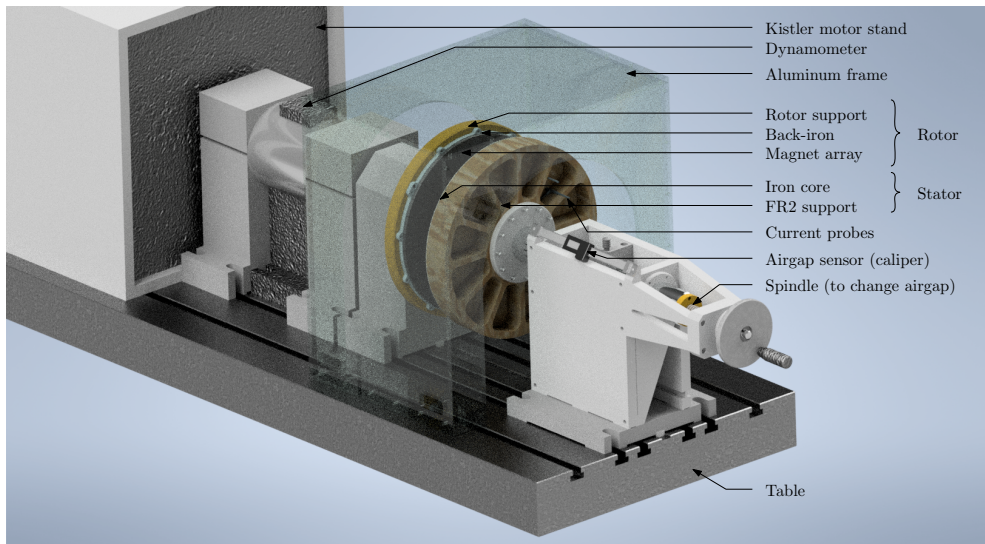
Figure 6.2: Rendered schematic of the experimental setup.

which is attached to the shaft of the driving motor through a torque meter, as shown in Fig 6.2.

For the stator core, two slitted electrical steel disks are investigated, one is made of M270-50A and the other M800-50A. Both disks are made of a single steel lamination with a thickness of 0.5 mm. This thickness is selected for the sake of experiments, i.e. lower attraction forces as well as lower eddy current losses and temperatures are present. This enables to build a safer setup with a wider range of operating points. Furthermore, this thin stator core leads to faster magnetic saturation, such that the effects of the nonlinear properties are amplified. For a realistic motor application, a thicker core should be realized. The disks are trimmed with four slits along the radial direction per pole-pair, as exemplified in Fig 6.3 with associated dimensions indicated in Table 6.1. The slitting is performed by CO_2 laser-cutting through the company *LCD LaserCut AG*. The slits are 2 mm wide. In addition to the slitted cores, ring-shaped and bar-shaped samples are manufactured in order to characterize the *B-H* relationship of both materials with a soft-magnetic steel tester, as detailed in Section 6.3.2.

The stator core is attached to an aluminum mechanical support, which is designed and realized by the *Equipment & Prototype Center* (EPC) of the Eindhoven University of Technology. As an intermediary between the soft-magnetic core and the aluminum mechanical support, a thick cylinder of phenolic resin of type FR2 is placed, because this resin is easy to mill and is both a thermal and electrical insulator. The latter
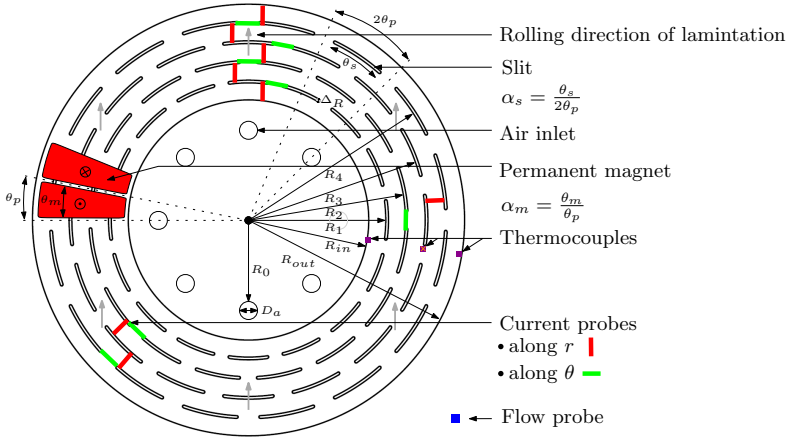
Figure 6.3: Schematic of the slitted stator core geometry.

Table 6.1: Parameter values of the slitted core

Parameter	Symbol	Value	Unit
Inner radius	R_{in}	88.0	mm
First slit radius	R_1	101.4	mm
Second slit radius	R_2	115.8	mm
Third slit radius	R_3	130.2	mm
Fourth slit radius	R_4	144.6	mm
Outer radius	R_{out}	158.0	mm
Slit width	ΔR	2.0	mm
Slit opening to pole-pitch ratio	α_s	0.70	
Pole-arc to pole-pitch ratio	α_m	0.95	
Air inlet position radius	R_0	43.0	mm
Air inlet opening diameter	D_a	9.0	mm

is the most important property to be able to measure the electromagnetic damping of the core, while ensuring no eddy currents are induced in the aluminum support. To measure the currents in the slitted core, current sensors are attached around the slits. However, due to the large cross-coupling with the magnetic field in the airgap produced by the permanent magnets, the currents in the core could not be obtained. For this reason, the sensors have been used to determine the spectra of the magnetic flux density. The current sensors are Rogowski coils type CWT6 Ultra-mini, which are 1.7 mm in diameter. Since the coil length is limited to 80 mm, eight pockets are milled in the FR2 support to be able to access and close the current probes, as shown in Fig 6.3. In addition to the pockets, small holes are machined to pass the current probes through the FR2 support in both radial and angular direction. The current probes are wrapped with Kapton tape and are attached in both radial and
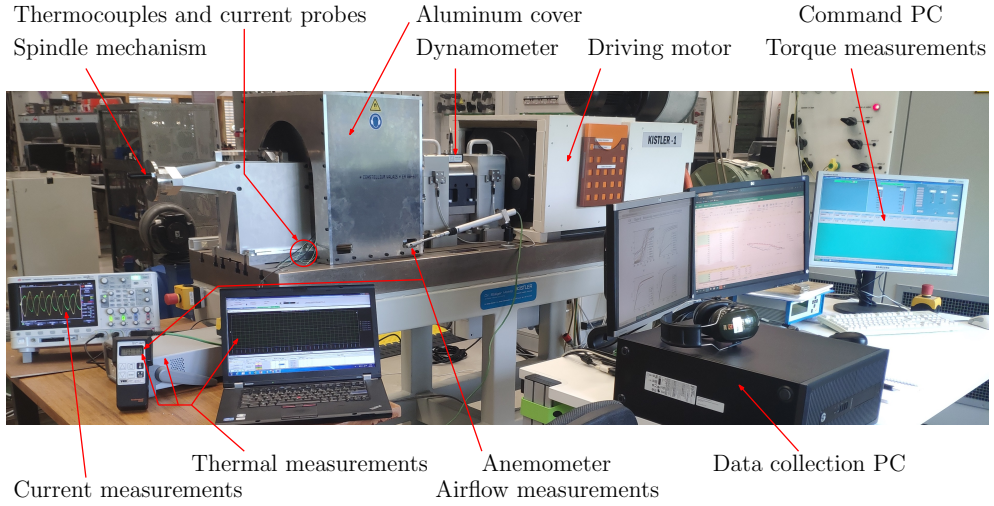
Figure 6.4: Photo of the experimental setup with measurement apparatus.

Table 6.2: Conversion between the considered speeds and frequencies.

ω_n	[rpm]	500	800	1000	1200	1500
ω_m	[rad/s]	52.36	83.77	104.7	125.7	157.1
$v_{R_{in}}$	[m/s]	4.60	7.37	9.21	13.82	13.82
$v_{R_{mid}}$	[m/s]	6.39	10.22	12.77	15.33	19.16
$v_{R_{out}}$	[m/s]	8.17	13.07	16.34	19.60	24.50
f_m	[Hz]	8.33	13.33	16.66	20.00	25.00
f_e^1	[Hz]	133	213	266	320	400
f_e^5	[kHz]	0.66	1.66	1.33	1.60	2.00
Rm	[-] (10^3)	0.56	0.90	1.12	1.34	1.68
Re	[-] (10^5)	0.55	0.88	1.10	1.32	1.65

angular directions around the slits. The pockets are made to enable the measurements of the local magnetic flux density in regions with an angle of 0 degree, 45 degrees, and 90 degrees with respect to the rolling direction of the non-oriented electrical steel. Furthermore, eight circular holes are milled around the spindle axis, all the way through the stator support in order to create air inlets and enable a natural throughflow. In addition to the current probes, three thermocouples are attached to the iron core, at the positions indicated in Fig 6.3, in order to monitor the temperature distribution.

The stator core and the FR2 support are glued together. The temperature is expected to rise to 120 °C, which could cause the glue to fail. To avoid a situation where the core would collapse into the magnet array due to the high temperatures and strong attraction forces, Kevlar strings are tightly woven around the slits, attaching the core

to the FR2 support. To enable a variable airgap length, the stator support is attached to a spindle mechanism, as shown in Fig 6.2, which is fixed to the table of the setup. An aluminum cover is placed around the prototype to avoid the risk of flying objects.

The Kistler motor stand consists of a three-phase inverter and an induction machine which can operate at the desired rotational speed. The rotor of the prototype is mechanically connected to the induction motor through a flexible shaft coupling. For safety reasons, the rotational speed is kept below or equal to 1500 rpm. Table 6.2 lists the speeds considered during the experiments and characterizations, where ω_n is the rotational speed, $v_{R_{in}}$, $v_{R_{mid}}$, $v_{R_{out}}$ are the tangential velocities at inner, middle and outer radii, f_m is the mechanical frequency, and, f_e^1 and f_e^5 are the fundamental and fifth time-harmonic electrical frequencies. Additionally, the magnetic Reynolds number, Rm, and the rotational Reynolds number, Re, are indicated in the table. The Reynolds number characterize the type of fluid flow, which spans laminar, transition, and turbulent flow regimes [231]. A photo of the experimental setup is given in Fig. 6.4, which shows the different measurement systems.

6.3   Electromagnetic model and measurements

6.3.1   Electromagnetic model

A periodic section of the three-dimensional electromagnetic model of the AFPM machine is obtained from a single-patch cuboid, which is partially wrapped around the z axis. By controlling the knot vector multiplicity, the different regions are created. A two-dimensional axisymmetric schematic of the AFPM machine is given in Fig. 6.5, where the corresponding dimensions are given in Table 6.3. To perform the slitting operations, two trimming techniques are investigated, namely the conforming and nonconforming approaches described in Section 5.2.

The vectorial basis functions consist of the high-order Nédélec edge-elements, introduced in (2.71), since only the tangential component of the magnetic vector potential is continuous at the interfaces. Truncated hierarchical B-splines (THB) functions, periodic along the θ-direction are considered, to handle the trimming of the slits and the adaptive refinements. The basis functions are mapped through a curl-conforming transformation, introduced in (2.75). A divergence-free solution is ensured by gauging the magnetic vector potential. This is done by regularization, i.e. the introduction of an infinitesimal conductivity in the non-conducting regions, as detailed in Section 3.3.2. Concerning the nonlinear solver, the harmonic balance method described in Section 4.2.2 is used.
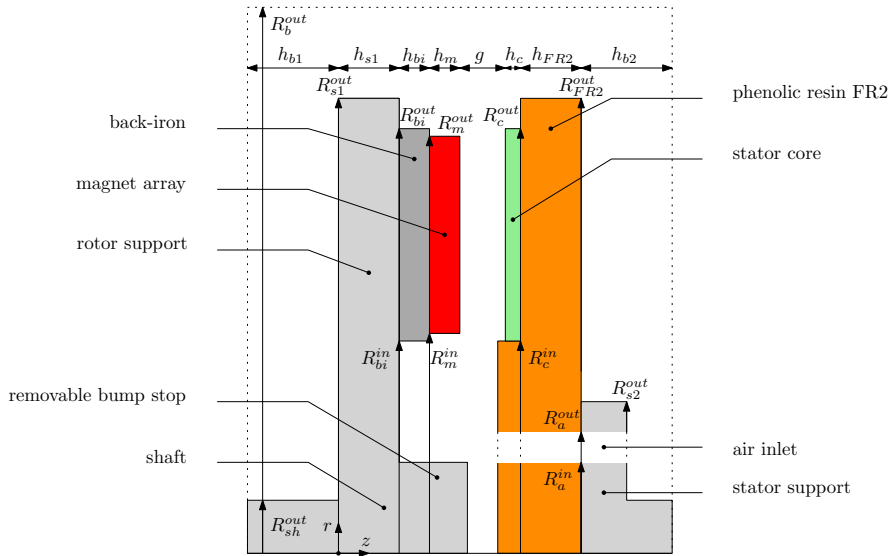
Figure 6.5: Axisymmetric cross-section of the considered AFPM topology.

Table 6.3: Geometrical parameter values of the considered AFPM topology

Parameter	Symbol	Value [mm]
Rotor box height	h_{b1}	90
Rotor support height	h_{s1}	25
Back-iron height	h_{bi}	7
Magnet height	h_m	8
Airgap and coil height	g	[5, 20]
Core height	h_c	0.5
Phenolic resin height	h_{FR2}	49
Stator box height	h_{b2}	95
Outer air inlet radius	R_a^{out}	47.5
Inner air inlet radius	R_a^{in}	38.5
Outer box radius	R_b^{out}	250
Shaft radius	R_{sh}^{out}	40
Outer support radius	R_{s1}^{out}	170
Outer support radius	R_{s2}^{out}	70
Outer back-iron radius	R_{bi}^{out}	158
Inner back-iron radius	R_{bi}^{in}	88
Outer magnet array radius	R_m^{out}	156
Inner magnet array radius	R_m^{in}	90
Outer core radius	R_c^{out}	156
Inner core radius	R_c^{in}	88
Outer phenolic resin radius	R_{FR2}^{out}	156

The eddy current losses, P, are calculated with (3.24). The torque, T_z, is obtained through the integration of the cross product between the Maxwell stress tensor and the radius, r, at the axial interface, $\mathcal{S}$, between the airgap and the core, from the viewpoint of the air:

$$T_z = \frac{1}{2\mu_0} \oint_{\mathcal{S}} r B_\theta B_z \, \mathrm{d}S. \tag{6.1}$$

The magnetic shielding effectiveness is considered as an indication of the shielding performance of the core, that is, the capability to decouple the region behind the stator from the field of the permanent magnets. This figure may be important in moving-coil applications where sensitive measurement apparatus can be attached to the core [200], and should not be disturbed by the changing magnetic fields. The magnetic shielding effectiveness, measured in decibel, is computed using the following expression:

$$S_E = 20 \log \left(\frac{\Phi_{B_0}}{\Phi_B} \right), \tag{6.2}$$

$$\Phi_B = \int_{\mathcal{S}} |\mathbf{B}| \, \mathrm{d}S, \tag{6.3}$$

where, Φ_B and Φ_{B_0} are the magnetic fluxes integrated for the configuration of interest and a reference configuration without core, respectively. The surface of integration is an axial slice, which covers the entirety of the domain and is positioned behind of the core at 0.5 mm distance.

Following Bertotti and Steinmetz loss separation [20, 203], the losses contributions exhibit a power-law growth as a function of speed with exponent values of 1, 1.5, and 2 for the hysteresis, excess losses, and eddy current losses, respectively. In the electromagnetic model, the reaction due to both the nonlinear material characteristics and the eddy currents is implemented. The excess losses could be implemented in the developed framework, however available formulations, such as [185], only exist for a 1D magnetic flux path normal to the lamination cross-section. Unfortunately, the 1D model cannot be extended straightforwardly in 3D, and therefore has not been considered. The excess losses do not exceed 5 to 10 % of the total losses in lamination steels [49], so their omission is reasonable. The hysteresis model requires considerable implementation overhead and, for that reason, has not been considered. Correspondingly, the hysteresis losses are omitted.

The values of the material properties used in the model are given in Table 6.4. In the next section, the nonlinear B-H characteristics to be included in the nonlinear numerical model are obtained experimentally. In addition, the number of time harmonics considered in the harmonic balance method is selected from the measured electromagnetic spectra.

Table 6.4: Steel conductivity and permanent magnet properties at ambient temperature

Property	Symbol	Value	Unit
Electrical conductivity of the core M270-50A	σ_c^1	1.81 10^6	S/m
Electrical conductivity of the core M800-50A	σ_c^2	2.77 10^6	S/m
Nominal remanence of the magnet at ambient	$B_{r,0}$	1.415	T
Permeability of the magnet	μ_{pm}	1.05	

6.3.2   Magnetic measurements

Ring-shaped and bar-shaped samples are manufactured to characterize both materials in a ring-core tester and an Epstein frame, respectively. The bar-shaped samples have dimensions 30×320 mm, while the ring-shaped samples have an inner and outer diameter of 100 and 110 mm, respectively. The thickness is 0.5 mm for all samples. Both magnetic measurements are performed using the same soft-magnetic steel tester, a Brockhaus GmbH MPG 200. Furthermore, the three different bars are selected, with angles of 0 degree, 45 degrees, and 90 degrees compared to the rolling direction of the material, in order to characterize the anisotropy of the materials. In both ring and sheet measurements, the principle is the same: a primary magnetic field strength is generated through a controlled oscillating current in the primary windings, and the magnetic flux density is measured via the voltage of the secondary windings. The current is controlled such that the magnetic flux density in the material is sinusoidal, thus characterizing the losses for a specific electrical frequency.

In order to obtain the correct shape of steel sheets in electrical machine applications, different manufacturing processes can be employed. For small series and prototypes, laser cutting, water jet cutting or wire-cut electrical discharge machining are possible. Those methods are known to have the most impact on the magnetic properties [68]. In particular, laser cutting induces large thermal stresses that locally modify the microstructure and degrade both mechanical and magnetic properties of the material near the cut edge. For large series, punching is preferred for economical reasons, although it requires expensive tooling for appropriate punches and dies. This method is known to have the least impact on the magnetic properties of the material, even though it still generates mechanical stresses in the steel sheets [68]. The influence of the cutting technique, including mechanical punching and laser cutting, on the magnetic properties of electrical steels has been quantified in amongst others [26, 68, 204, 223], and they show that the quasi-static hysteresis losses and the magnetic permeability are the most impacted. In particular, the influence of different material width, i.e. the cut edge length to mass ratio, is characterized in [223] and a linear relationship with regard to the hysteresis losses coefficient is demonstrated. Furthermore, it is shown in [26] that compared to a reference without degradation, mechanical cutting increases the iron losses by 15 %, while laser cutting increases the losses by 31 %

to 51 % depending on the power and speed of the laser, the faster being beneficial. Additionally, strong deformations of the *B-H* hysteresis loops around the origin are observed.

Similar deformation effects are observed on the measured *B-H* hysteresis loops via the bar and ring samples, as shown in Fig. 6.6a for M270 material. In particular, Figs. 6.6a and 6.6b shows the hysteresis and major loops for both M270 and M800 materials, with measurements made on the Epstein frame using the bar samples with 0 degree, 45 degrees, and 90 degrees rotation with respect to the rolling direction, as well as the measurement made on the ring sample. The M800 exhibits higher permeability and higher saturation values than the M270 material. Furthermore, both of these values deteriorate gradually as the angle to the rolling direction is increased. For the ring samples, the measured properties are extremely degraded with respect to the bar samples. This is due to the anisotropy of the material, and the large influence of the laser cutting due to a larger cutting edge length to surface ratio. The distance between cut edges is 30 mm and 10 mm for the bar and ring sample, respectively. When comparing the cut edge proportion [223], the bar and ring samples give 18.7 m/kg and 25.6 m/kg, respectively. For the slitted core, the inter-slit distance along the radial direction is 12.4 mm, while along the angular direction it ranges from 12 mm to 17 mm, and the cut edge proportion is 16.8 m/kg. Therefore, the impact of laser cutting on the slitted core is expected to be less than for the ring and bar samples based on the cut edge proportion. The *B-H* characteristics of the bar samples are chosen for the electromagnetic model of the slitted core.

Figures 6.6c and 6.6d, show the *B-H* curves for the M270 material aligned with the rolling direction using the Epstein frame, and the ring sample, respectively, for increasing frequencies. Figs. 6.6e and 6.6f, show the same characteristics for the M800 material. Magnetic permeability and saturation levels both decrease with the increase in frequency. In particular, the strongest changes in magnetic behavior occur in the same region for both materials, namely between 500 rpm and 1500 rpm, or equivalently between 133 Hz and 400 Hz, as indicated on Table 6.2. The characteristics change at high-speeds because of the eddy currents. If the *B-H* characteristics would be adapted as a function speed in the model, the losses prediction would be underestimated at higher speeds, since the eddy currents are influencing the measured characteristics. Therefore, as the bulk eddy currents reaction is already included in the model, the *B-H* characteristics for the material are taken at 133 Hz, for all speeds.

Figure 6.7a shows the iron losses for M270 and M800 materials measured using the Epstein frame and the ring sample for increasing frequencies. Figure 6.7b shows a close-up of the iron loss characteristics around a frequency 60 Hz at a magnetic flux density of 1.5 T, for which the typical and maximum loss values are extracted from the Cogent electrical steel datasheet [49]. Comparing the Epstein measurement with
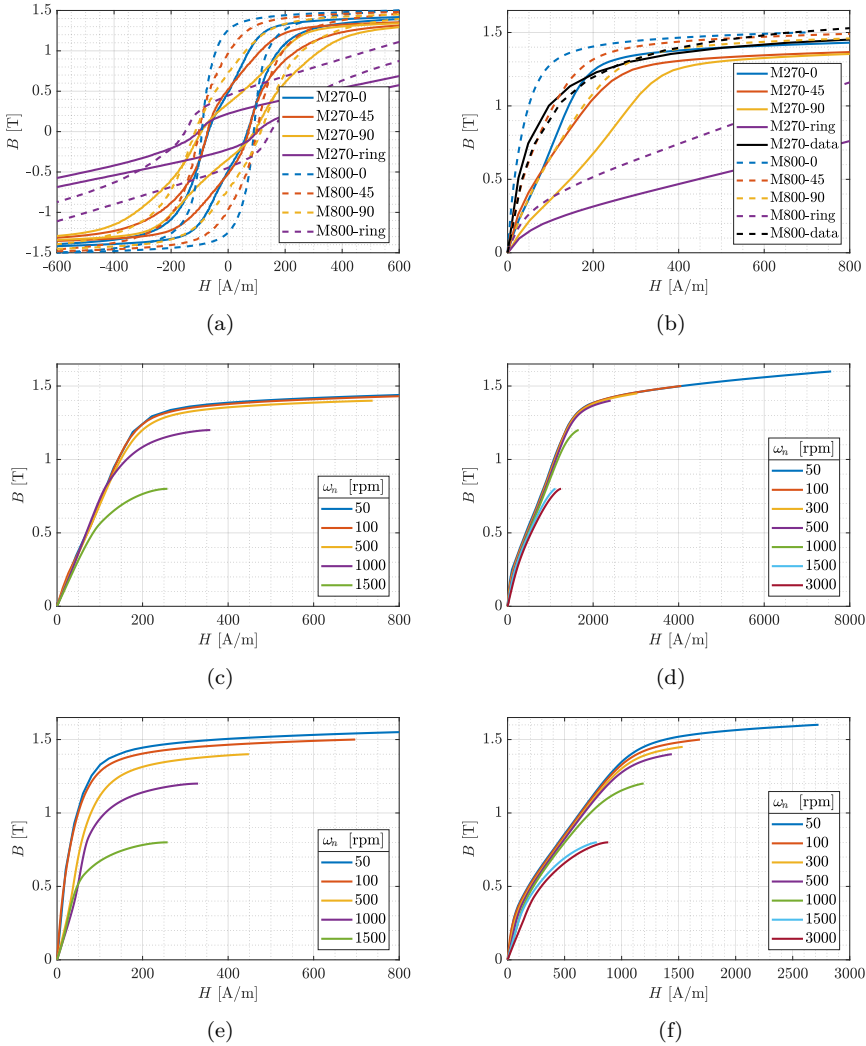
Figure 6.6: a) Major hysteresis loops at 26.66 Hz corresponding to 100 rpm, for Epstein measurement at 0, 45, 90 degrees to the rolling direction, as well as ring samples, for both M270 and M800 materials. b) Branches of the major loops at 26.66 Hz for Epstein measurement at 0, 45, 90 degrees to the rolling direction, as well as ring samples, for both M270 and M800 materials, and the characteristics from the Cogent datasheet. c) Branches of the major loops at different speeds for Epstein measurement at 0 degree to the rolling direction for M270 material. d) Branches of the major loops at different speeds for Epstein measurement with the ring sample for M270 material. e) Branches of the major loops at different speeds for Epstein measurement at 0 degree to the rolling direction for M800 material. f) Branches of the major loops at different speeds for Epstein measurement with the ring sample for M800 material.

Figure 6.7: (a) Iron losses for increasing frequency, measured for both M270 and M800 materials, using the Epstein frame and the bar samples with an angle of 0, 45, and 90 degrees with respect to the rolling direction, as well as ring samples, in addition the losses from the dataheet for M270 material are indicated. b) Close up of the iron characteristics at 60 Hz, for which the typical and maximum losses obtained from the Cogent electrical steel datasheet are indicated.
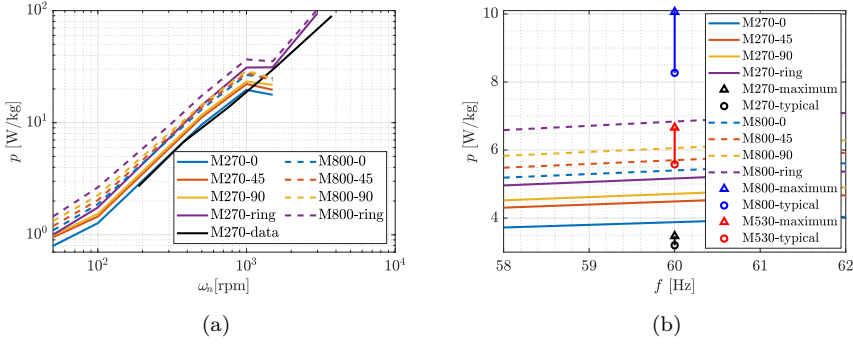
the orientation aligned with the rolling direction, M270 exhibits 11 % more losses than the maximum value reported by the manufacturer, while M800 has 34 % fewer losses than the typical value. As shown in Fig. 6.7a, M800 exhibits on average 30 % more losses than M270 across the considered range of speeds. Such differences of values demonstrate the importance of measuring the magnetic characteristics of the steel, especially when additional processes, such as laser cutting, are performed. On Fig. 6.7a, the losses given by the datasheet are indicated for the M270 material. The values correspond with the measured ones with a material orientation aligned with the rolling direction of the steel. Therefore, in the model, the *B-H* characteristics with zero degree with respect to the rolling direction are selected for the simulations. A sensitivity analysis of the losses predicted by the model with respect to the *B-H* curves with other orientation is given in Section 6.6.1.

6.3.3   Electromagnetic spectra measurements

To characterize the time harmonics present in the vicinity of the slitted core, electromagnetic spectra measurements are performed using two current probes CWT6 Ultra-mini. The signals are measured around four locations for the angular slits, and five locations for the radial slits, as indicated in Fig. 6.3. In particular, for the angular slits, two measurements are performed simultaneously: one probe encircling the air, which acts as a reference, the other encircling the core, which is of interest as the eddy currents flow through it. Both signals show strong similarity, although the first probe does not encircle any current flow. This is because the Rogowski coil senses the induced electromotive force (emf) following Faraday's law of induction. The current

probe is calibrated for detecting an alternating magnetic field in the air, generated solely from the current-carrying wire being encircled. In the test setup configuration, the magnetic flux is dominated by the field produced by the permanent magnet array, and the eddy current contribution is much smaller. Therefore, the eddy currents flowing in the core cannot be directly detected by the probe. The Rogowski coils are used as flux probes in the experiments to determine which time harmonics are present in the airgap and the vicinity of the core.

As the airgap value is decreased, the magnetic saturation increases in the core. Additional harmonics, especially the third and fifth, are excited and observed on the measured signal. This is shown in Fig. 6.8, where the probe encircles radially the core between the third (R_3) and fourth slit (R_4). Although the absolute amplitude value of the signal cannot be directly compared to the magnetic flux density data, the frequency spectrum and relative amplitudes between harmonics can be interpreted. The frequency spectra are represented in Fig. 6.9, for decreasing airgap values as well as different materials and orientations with respect to the rolling direction of the steel. As the airgap value is decreased, the amplitude of the first harmonic decreases, while the amplitude of the third harmonic increases continuously. This is especially the case for airgap values 8 and 6 mm, which manifests a fifth harmonic component. The orientation of the material seems to have some minor effects on the harmonic content, although a general rule cannot be clearly derived. For example, as shown in Figs 6.9e and 6.9f, the 90 degrees orientation exhibits both the lowest and highest fifth harmonic component for the 6 mm airgap with M270 and M800 materials, respectively. In all cases, however, the higher-order time harmonics are gradually excited as the airgap length is decreased.
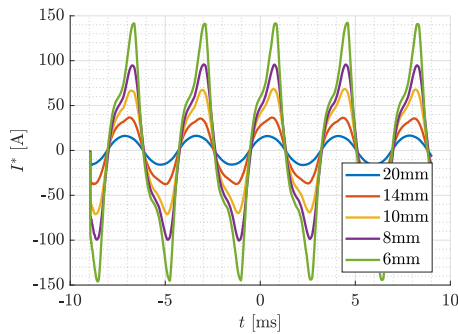
Figure 6.8: Denoized signal acquired through the current probe at a rotational speed equal to 1000 rpm for the M800 material and for decreasing airgap values. The probe is along the rolling direction of the electrical steel.
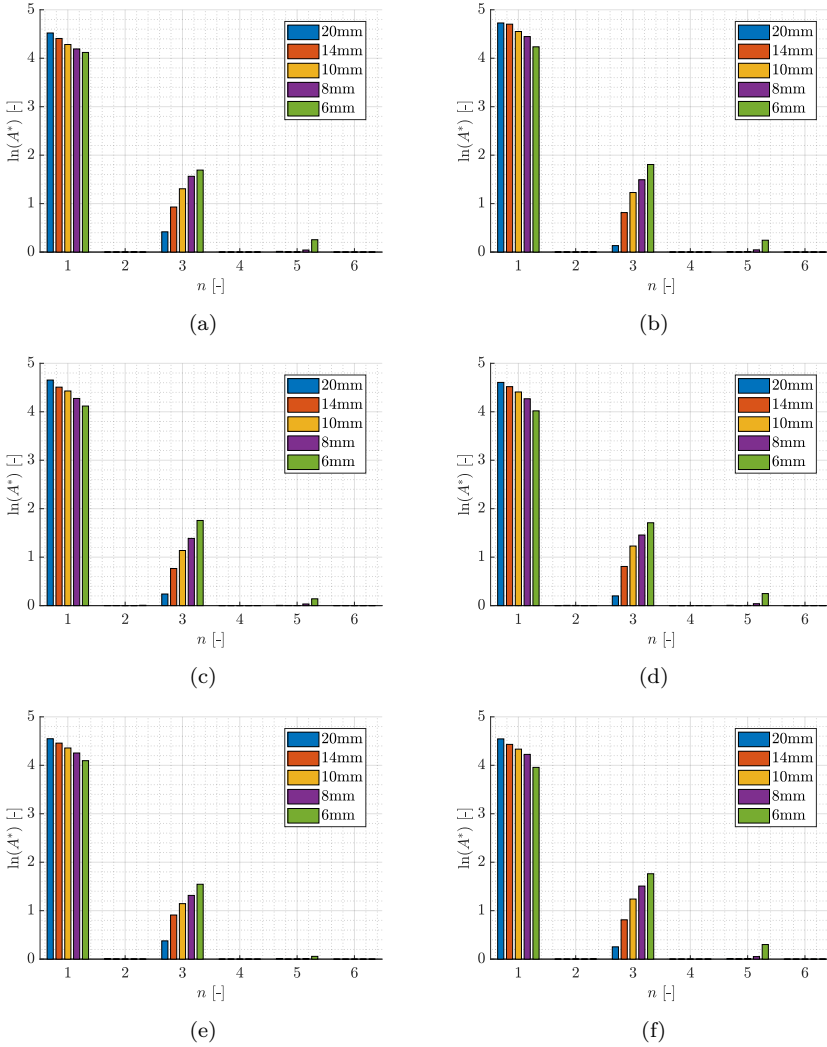
Figure 6.9: Frequency spectrum logarithmic amplitudes for the magnetic induction signals measured by the current probes for different airgap values at a rotational speed equal to 1000 rpm in the following materials: a) M270 material 0 degree, b) M800 material 0 degree, c) M270 material 45 degrees, d) M800 material 45 degrees, e) M270 material 90 degrees, f) M800 material 90 degrees.
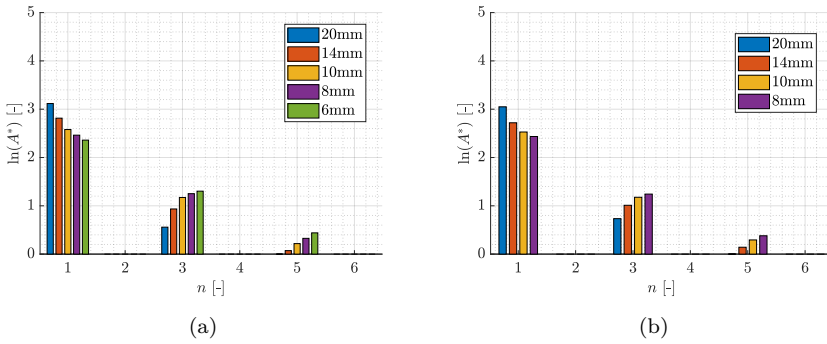
Figure 6.10: Frequency spectrum normalized logarithmic of the simulated magnetic flux density in the core for different airgap values at a rotational speed equal to 1000 rpm in the following materials: a) M270 and b) M800 materials, both with an orientation aligned with the rolling direction of the steel.

Using the harmonic balance method described in Chapter 4, these higher-order time-harmonic components are naturally captured. To improve the computational efficiency of the numerical scheme, the electromagnetic model uses a progressive harmonic refinement strategy, as explained in Sections 5.4.2 and 5.5.3. In the beginning, only the first harmonic is used. This initial solution is then projected onto a basis, which includes the third harmonic as well. The same process is repeated to include the fifth time-harmonic component in the solution.

In Fig. 6.10 the simulated electromagnetic induction spectra are computed by integrating the magnetic flux density over a surface mimicking the probe location in the core. The spectra for both materials are given for different airgap lengths and can be compared with the measured ones given in Fig. 6.9. Although the amplitudes differ, the same behavior is observed, i.e. the smaller the airgap the more magnetic saturation in the material, which leads to increasing time-harmonic content in the electromagnetic fields.

6.3.4   Electromagnetic damping torque measurements

The torque is measured with a torque sensor Kistler 4503A5H. Due to a low sampling rate of the data-acquisition system, the torque ripple cannot be captured accurately, and therefore, only the mean value of the torque is measured. The damping torque of the setup is obtained by subtracting the friction torque, measured without the core present, from the measured torque. The friction torque is modeled as a linear function of speed, which is composed of Coulomb and viscous friction terms. Different damping torque measurements are performed for both materials at various airgap lengths and increasing speeds, which are shown in Fig. 6.11. Correspondingly, the
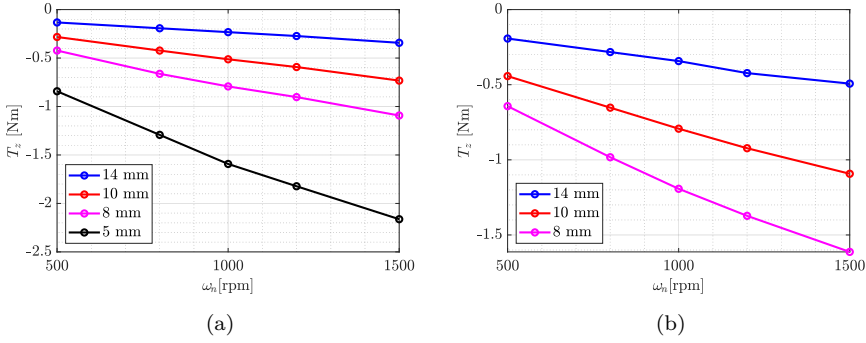
Figure 6.11: Damping torque measured for different airgap values and increasing rotational speeds a) in M270 and b) in M800 materials.
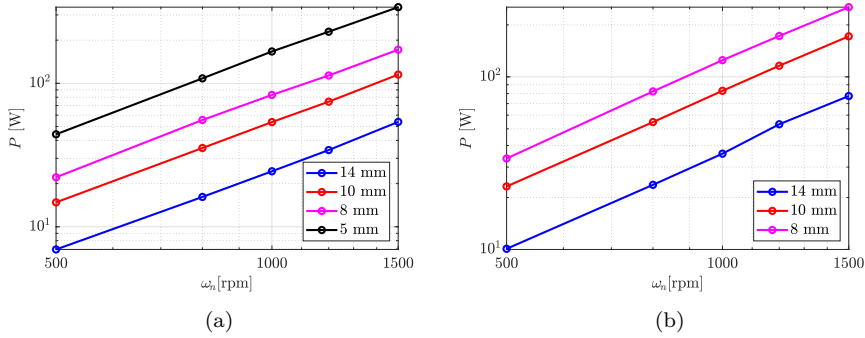
Figure 6.12: Dissipated power measured for different airgap values and increasing rotational speeds a) in M270 and b) in M800 materials.

mechanical power is shown in Fig. 6.12. The measurements exhibit a clear quadratic trend. Since the electrical conductivity of M270 is smaller than the one of M800, an additional airgap value of 5 mm can be measured, while still satisfying the maximum temperature constraint of 120 °C, as shown in the next section. The loss comparison with the simulation results, obtained with the coupled model are given in Section 6.5, since the thermal model is required for their computation.

6.4   Thermal model and measurements

6.4.1   Thermal model

In the AFPM machine, the heat transfer is dominated by convection. Heat conduction operates inside solids as well as in the air if stationary. At the interface between solid

Table 6.5: Values of the physical parameters composing the thermal model

Parameter	Material	Symbol	Value	Unit
Thermal conductivity	aluminum	κ_{al}	237.0	Wm^{-1}K^{-1}
	back-iron	κ_{bi}	40.0	Wm^{-1}K^{-1}
	magnet	κ_{pm}	7.6	Wm^{-1}K^{-1}
	M270-50A core	κ_c^1	25.0	Wm^{-1}K^{-1}
	M800-50A core	κ_c^2	36.0	Wm^{-1}K^{-1}
	phenolic resin	κ_{FR2}	0.2	Wm^{-1}K^{-1}
Thermal emissivity	shinny surface	ϵ_{shi}	0.3	
	mat surface	ϵ_{mat}	0.9	
	Kapton tape	ϵ_{Kap}	0.95	
	Kevlar string	ϵ_{Kev}	0.50	
Stefan-Boltzmann constant		σ_{SB}	5.67 10^{-8}	Wm^{-2}K^{-4}
Ambient temperature		T_0	293.15	K
Thermal dependency	core	α_ρ	3.93 10^{-3}	K^{-1}
	magnet	α_B	1.20 10^{-3}	K^{-1}

and air regions, thermal radiation occurs and is taken into account as detailed in Section 3.6. The parameters values for conduction and radiation are given in Table 6.5 for the solids.

Several coefficients of the coupled model are temperature-dependent. For the air, the variation of the conductivity κ is given by the Sutherland identity:

$$\kappa(T) = \kappa_0 \frac{T_0 + S_\kappa}{T + S_\kappa} \left(\frac{T}{T_0} \right)^{n_\kappa}, \tag{6.4}$$

where, $T_0 = 293.15$ K is the ambient reference temperature, $S_\kappa = 250$ K is the Sutherland constant, $\kappa_0 = 2.816 \ 10^{-2}$ Wm^{-1}K^{-1}, and $n_\kappa = 1.45$ [106]. Concerning the solids, the evolution of the electrical resistivity $\rho = \sigma^{-1}$ of the iron and the remanent magnetic flux density of the permanent magnets B_r, are given by:

$$\rho(T) = \rho_0 \left(1 + \alpha_\rho(T - T_0)\right), \tag{6.5}$$
$$B_r(T) = B_{r,0} \left(1 - \alpha_B(T - T_0)\right), \tag{6.6}$$

where, ρ_0 is the inverse of the electrical conductivity given in Table 6.4 and the other parameters are given in Table. 6.5. For metals, the Wiedemann-Franz law indicates the proportionality between the electrical conductivity σ and the thermal conductivity κ through:

$$\kappa(T) = \sigma(T)LT, \tag{6.7}$$

where, $L = 2.8 \ 10^{-8}$ WΩK^{-2} is the Lorenz ratio for soft-magnetic materials [123].

The modeling of the interaction and coupling between the solid and fluid domains can be realized with the so-called conjugate convective heat transfer, which solves for pressure, velocity, and temperature among others. Depending on a range of speeds either a laminar or turbulent flow is achieved. While the laminar model can be more easily implemented, its applicability to realistic geometries and heat transfer conditions is limited. A turbulent model should be considered, which solves an additional pair of strongly nonlinear coupled equations, i.e. the turbulent kinetic energy and turbulent viscosity. The implementation and validation within the isogeometric framework of a Lam-Bremhorst turbulent model and a laminar model applied to the AFPM machine two-dimensional flow and coupled to a conjugate heat transfer model are thoroughly discussed in [231].

However, a three-dimensional turbulent model is relatively expensive to implement on complex geometries, such as the AFPM machine, as a very fine mesh is required near all solid wall interfaces. Even a 2D turbulent model is challenging in the developed environment and requires a step-by-step validation process with gradually increasing the geometrical complexity. Such a model would be necessary to perform an in-depth study of the convective transfer mechanism and the influence of the alteration of the geometry to enhance the cooling capabilities by using air inlets with forced throughflow, shrouds, or impeller. However, for an estimation of the temperature in the core and permanent magnets materials, a steady-state thermal model with empirical convection coefficients is considered to be sufficient.

In the next sections, the airflow velocities and temperatures are measured for different airgap and rotational speed values, respectively. These results are used to propose an empirical convection law, which yields simulated temperature values close to the one measured experimentally. The results are based on the measured losses shown in Fig. 6.12, which are used as input to the model.

6.4.2   Airflow measurements

Airflow measurements are performed with an anemometer Testovent 4000, which uses a rotating turbine. The sensor is placed facing the opening in the aluminum cover, as seen from Fig. 6.4, which is slightly behind the rotor support. Little variations of the airflow are observed as a function of the airgap value. However, the experiments are repeated with the flow sensor at an other location, for which the airgap variations are absent. Nonetheless, the linear trend as a function of speed is identified from Fig. 6.13, which confirms the linear empirical convection law chosen in (6.8).
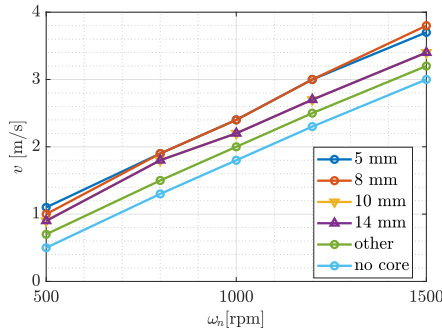
Figure 6.13: Airflow velocity measurements for different gap configurations.

6.4.3   Thermal measurements

To perform local thermal measurements during operation, thermocouples are placed on the stator core at three different locations as indicated in Fig. 6.3. The steady-state temperatures recorded for the different locations at various airgap values and for increasing rotational speeds are given in Fig. 6.14. The higher electrical conductivity of M800 leads to higher losses and temperatures. The temperature is maximum at the middle thermocouple location, and minimum at the inner radius of the core, where the conduction path to the phenolic resin support is the largest.

To get a global picture of the thermal distribution, a FLIR E40 thermal camera is used to capture shots right after the operation, which are shown in Fig. 6.15. This infrared camera measures radiation and the resulting temperature is then a function of the selected emissivity. The different features can be identified on these shots, such as the FR2 support, which is the coolest spot, the slits, and the glued Kevlar strings, which appear as a hot spot probably because of a different emissivity value as given by Table 6.5. A Kapton tape is placed in the middle to obtain a uniform emissivity across the radial direction, where a radial temperature gradient is also visible.

6.4.4   Convection law

A linear empirical convection law is chosen, since a similar law is observed for the airflow velocity in Fig 6.13:

$$h_{\text{conv}}(\omega_m) = h_{\text{conv},0} + h_{\text{conv},1}\omega_m, \tag{6.8}$$
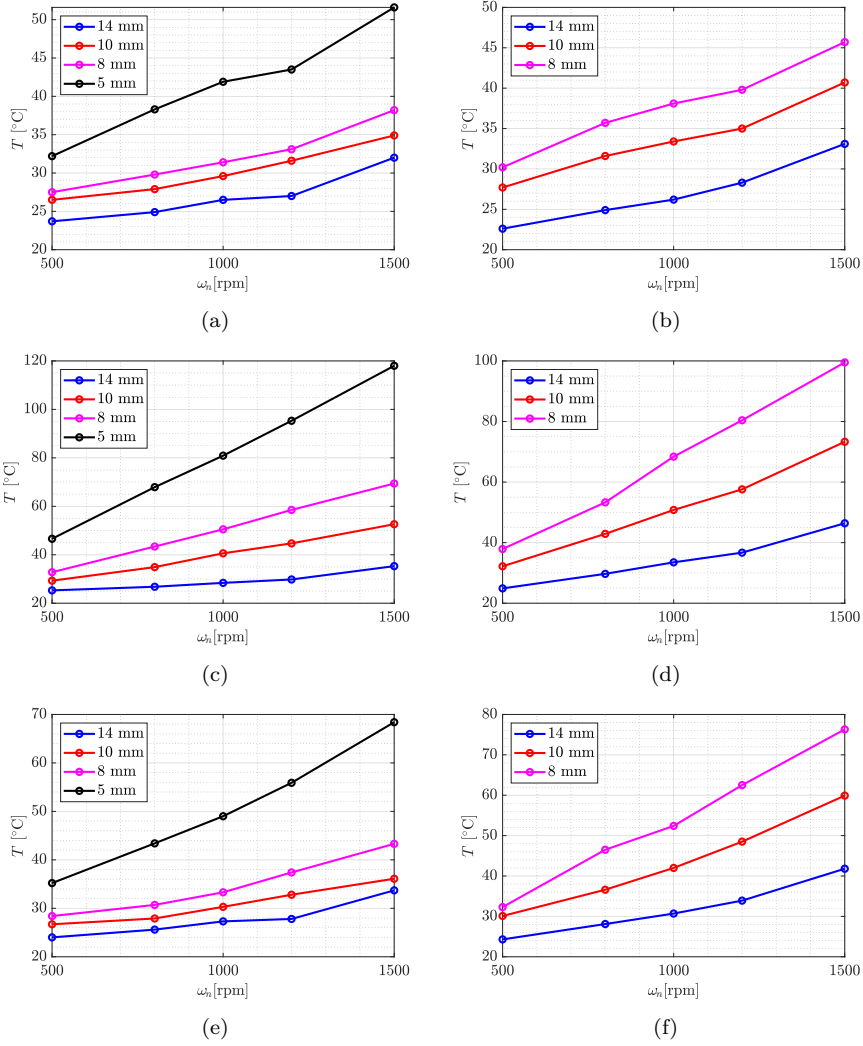
Figure 6.14: Temperature evolution for different airgap values with increasing rotational speeds at the following material locations: a) M270 material inner radius, b) M800 material inner radius, c) M270 material middle radius, d) M800 material middle radius, e) M270 material outer radius, f) M800 material outer radius.
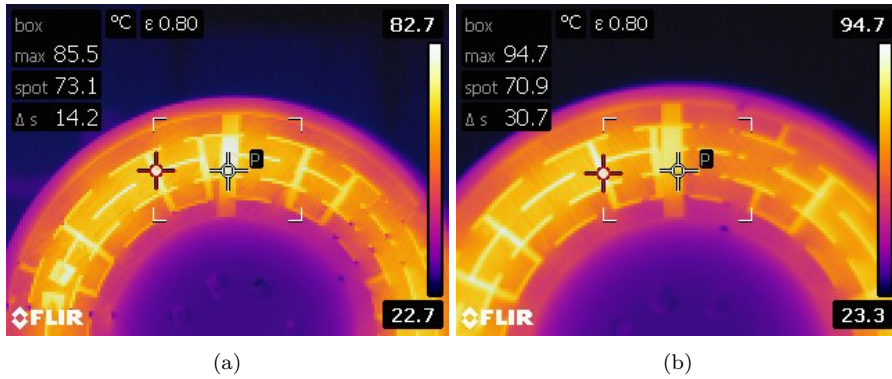
Figure 6.15: Thermal camera shots for a) M270 and b) M800 stator cores.

where, $h_{\mathrm{conv},0}$ is taken as 2.27 $\mathrm{Wm^{-2}K^{-1}}$ and 3.87 $\mathrm{Wm^{-2}K^{-1}}$ for the rotor and stator, respectively. The convection is considered to increase linearly with the rotational speed ω_m through a coefficient $h_{\mathrm{conv},1}$ equal to 0.4462 $\mathrm{W\,s\,rad^{-1}m^{-2}K^{-1}}$ and 0.3622 $\mathrm{W\,s\,rad^{-1}m^{-2}K^{-1}}$ for the rotor and stator, respectively. These values have been advantageously chosen to yield simulated temperatures close to the measurement values. While a linear law has been chosen due to the range of speeds, a square-root evolution law can also be considered for much wider ranges [198]. For simplicity, the convection coefficient is not adapted as a function of the airgap length, although it conditions the cooling performance [231].

6.5   Model validation

In this section, the multi-physical coupled model is validated against the measurements. The essential point consists in verifying that the eddy current losses and the corresponding temperatures are correctly estimated for different rotational speeds and airgap values. The *B-H* characteristics are the ones aligned with the rolling direction of the steel, and the characteristics measured for 500 rpm are used for all speeds, as explained in Section 6.3.2.

In Fig. 6.16, the temperature measured by the central thermocouple indicated on Fig. 6.4 is given. It can be seen that all of the experimental values are contained within the mean and maximum simulated temperature over the radius of the core, which are indicated in Fig. 6.16 as well. As the temperature increases, so does the range of the thermal distribution in the core. The discrepancies between the measurements and the average between the mean and maximum values of the model are gathered in Fig. 6.17. The simulated temperatures are within 10 % for both materials and the whole range of rotational speed and airgap lengths.

In Fig. 6.18, both the simulation results are given for the eddy current losses together with the experimental values obtained from the torque measurements. A good agreement is observed for both materials. The discrepancies between the measurements and the model are gathered in Fig. 6.19. The simulated losses are within 10 % of the measured values, for both materials and the whole range of rotational speed and airgap lengths, which is considered a good agreement.

6.6 Sensitivity analysis

In this section, a sensitivity analysis is conducted to characterize the influence of the number of time harmonics on the solution, as well as the orientation of the material

(a)

(b)
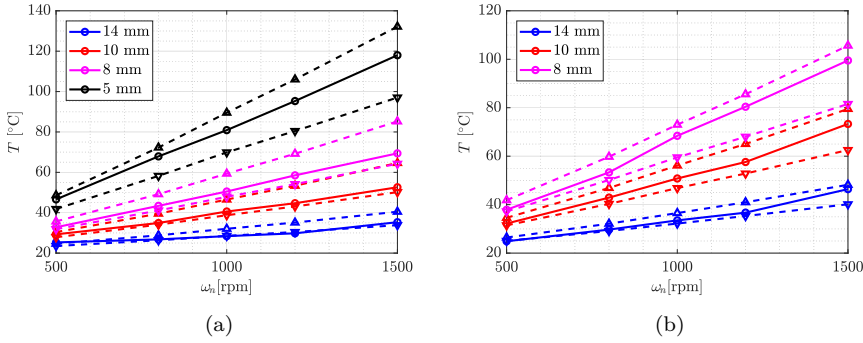
Figure 6.16: Temperatures for a) M270 and b) M800 materials. The experimental results are given with a circular marker, while the maximum and mean simulated temperatures are indicated with dashed lines and an upper and lower triangular markers, respectively.

(a)

(b)
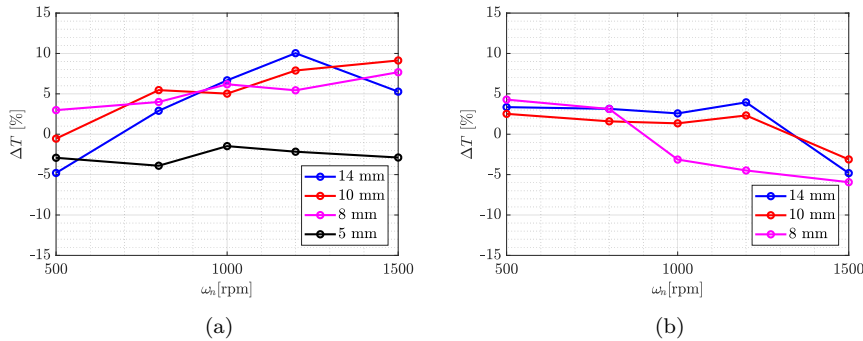
Figure 6.17: Discrepancy on the temperatures between simulation and experimental results for a) M270 and b) M800 materials.
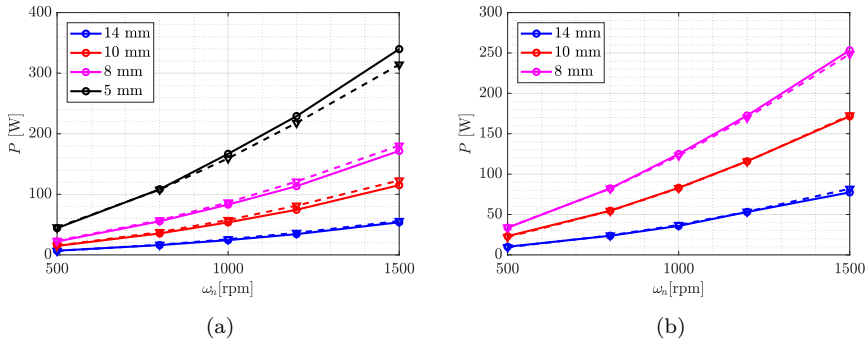
Figure 6.18: Damping losses for a) M270 and b) M800 materials. The experimental results are indicated with a circular marker, while the simulation results are given with dashed lines and triangular markers.
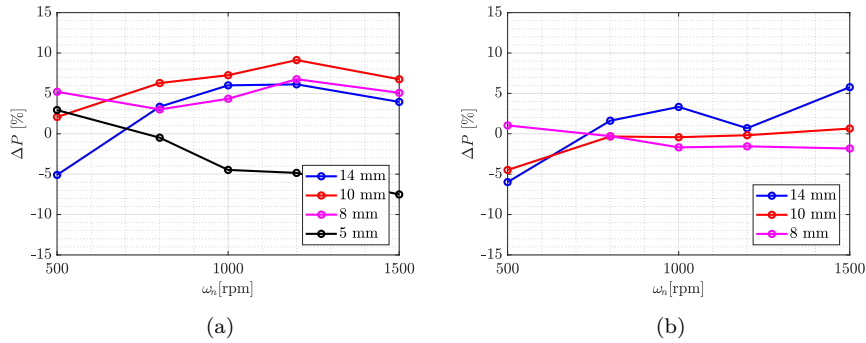
Figure 6.19: Discrepancy on the losses between simulation and experimental results for a) M270 and b) M800 materials.

with respect to the rolling direction of the steel. The impact of the dimensions of the slits in the core is detailed, in terms of the angular opening, width, and number of radial slits. Visualizations of the eddy currents and temperature distribution are presented, as well as different mesh discretizations of the trimmed stator core.

6.6.1   Model sensitivity

The sensitivity of the eddy current losses with the number of considered harmonics is given in Fig. 6.20. It shows that compared to a reference solution, which includes up to the fifth harmonic, taking a solution with up to the third harmonic will decrease the accuracy between 1 % and 2 % for all considered airgap values, rotation speeds, and materials. Similarly, taking a solution that includes only the fundamental harmonic will decrease the accuracy between 3 % and 5 % for the whole range of considered

airgap values, rotation speeds, and materials. This discrepancy is created by the higher-order harmonic losses in the material due to the magnetic saturation. This phenomenon is well captured by the harmonic balance solver. Furthermore, as the discrepancy is still relatively low, using the solution containing solely the fundamental harmonic constitutes a computationally efficient way of exploring the design space and understanding quickly the different parameter sensitivities.

The sensitivity of the model with respect to the angle to the rolling direction of the steel is presented in Fig. 6.21. The material is modeled as isotropic, which yields to losses variations within 1 % to 2 % depending on the airgap length for M270 and up to 3 % for M800. The most representative angles, which exhibit the lowest discrepancy, are 0 degree and 45 degrees, for M800 and M270 materials, respectively. The simulated values show less sensitivity to the angle than identified in Fig. 6.7a using the Epstein measurements, where the losses were continuously increasing with respect to the angle to the rolling direction. Therefore, using an anisotropic material model can improve the accuracy of the predicted losses shown in Fig. 6.19.

6.6.2   Slit influence

The influence of the dimensions of the slits on the reduction of the eddy current losses is investigated. When not specified, the dimensions considered corresponds to the ones from the experimental setup, which are gathered in Table 6.1. In Fig. 6.22, the impact of the slit opening in the circumferential is shown. It can be seen that for both minimum and maximum slit opening, the generated ripple is minimized. The maximum slit opening exhibit the strongest reduction in eddy currents, with a four-fold decrease in losses, as it mimics the effect of laminations the best. However, for
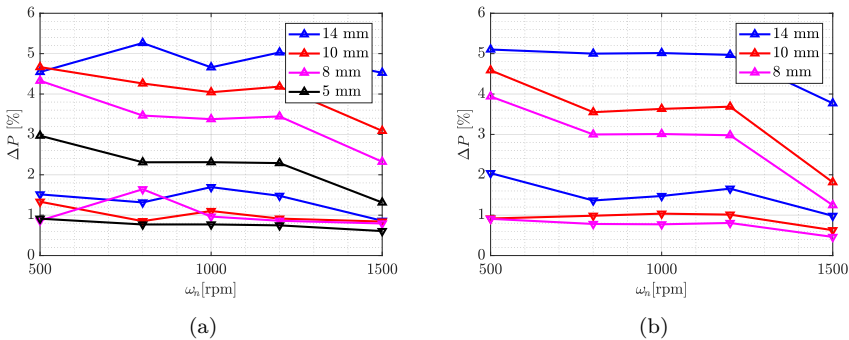
Figure 6.20: Discrepancy on the simulated losses between the solutions including up to the first and third time harmonics indicated with an upper and lower triangular marker, respectively, compared to the reference solution including up to the fifth time harmonic, for a) M270 and b) M800 materials.
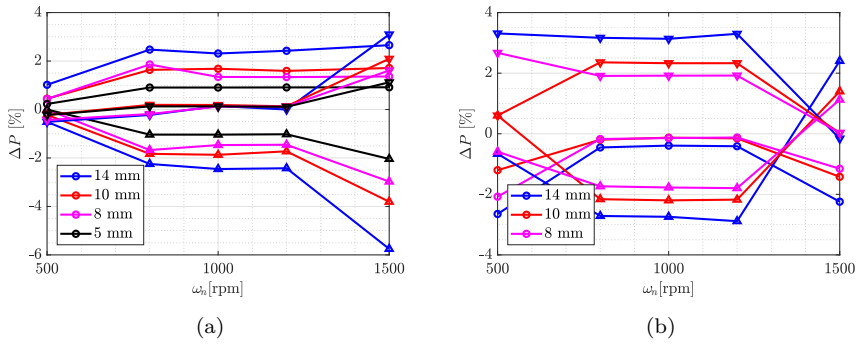
Figure 6.21: Variations of the calculated losses for a) M270 and b) M800 stator cores, with respect to the material orientation: 0, 45, and 90 degrees, represented with circular, upper triangular and lower triangular markers, respectively.

such a large value of the slit opening, it might be more difficult to guarantee the structural integrity of the structure. Furthermore, it can be seen that intermediate values increase the ripple. In order to minimize the ripple, the slits could be continuously rotated or skewed with respect to each other.

The influence of the slit width in the radial direction is given in Fig. 6.23. Fig. 6.23a shows that a smaller width increases the losses, as there is more conductive material present. However, Fig. 6.23b shows that reducing the slit width strongly reduces the torque ripple, and thus the slit width should be minimized. In practice, the slit width should be minimized down to the kerf width of a laser cutting machine, which can be as small as 0.1 mm, depending on the type, speed, and focal length of the laser. This guarantees a smaller torque ripple as well as larger torque production capability.
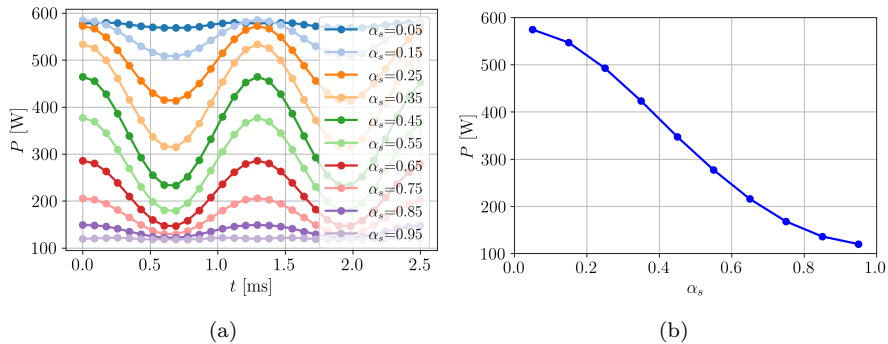
Figure 6.22: Influence of the slit opening on a) the eddy current losses time profiles and b) mean values, at a rotational speed equal to 1500 rpm and an airgap length of 8 mm for the M270 material.

(a)

(b)
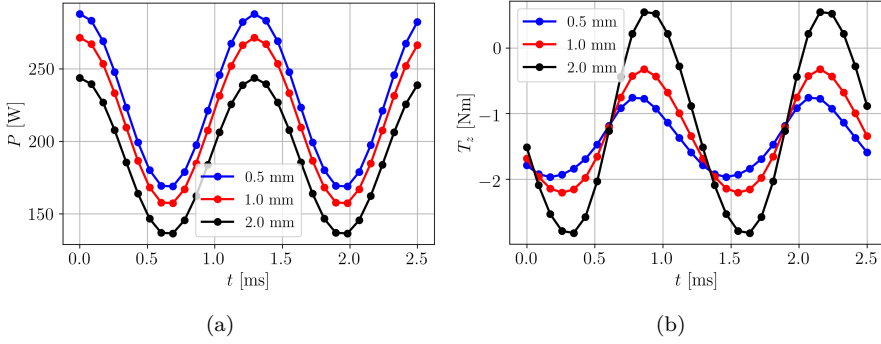
Figure 6.23: Influence of the slit thickness on a) the eddy current losses and b) damping torque, with an airgap length of 8 mm for the M270 material.

(a)

(b)
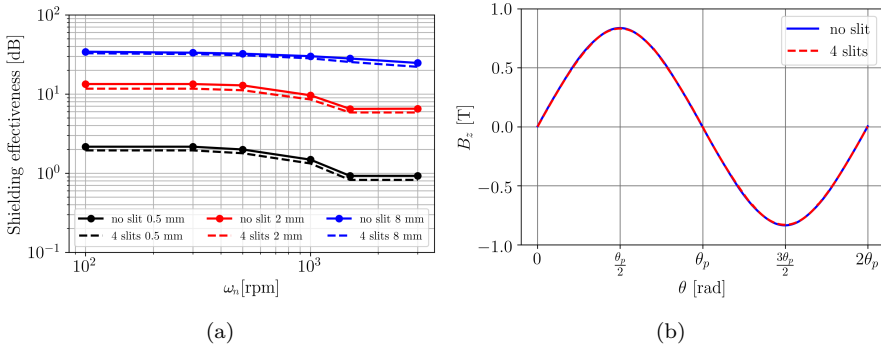
Figure 6.24: a) Magnetic shielding effectiveness for different stator core thicknesses and b) flux density in the middle of the airgap, for different core configurations, at a rotational speed equal to 1500 rpm and an airgap length of 8 mm for the M270 material.

In Fig. 6.24a, the magnetic shielding effectiveness of the core, computed following (6.2), is presented for different core configurations. It can be seen that the shielding effectiveness decreases with the slitted topology compared to a non-slitted topology. As the width of the slit decreases, the magnetic shielding effectiveness increases. Furthermore, the magnetic shielding effectiveness increases quickly with the thickness of the core, which reduces the magnetic saturation. In Fig. 6.24b, the magnetic flux density in the middle of the airgap is represented for different core configurations. It shows that the magnetic flux density in the airgap is only slightly impacted by the presence of the slits. Therefore, the slit core topology should not have much influence on the capability of the AFPM motor to produce torque at the rated performances compared to a slitless topology, given that the slit width is sufficiently small.

(a)   (b)
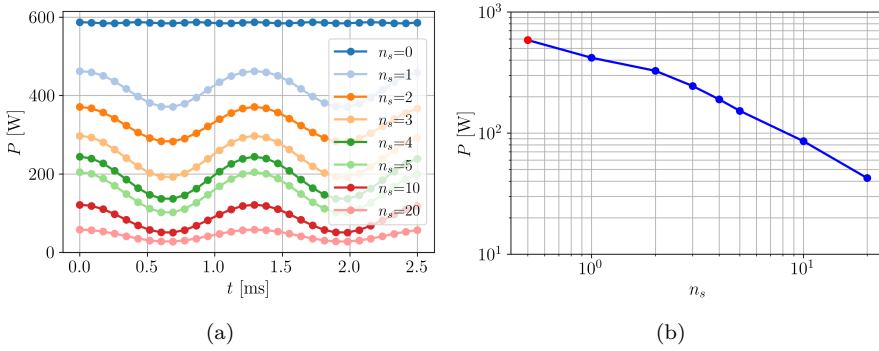
Figure 6.25: Influence of the number of slits on a) the eddy current losses profiles and b) mean values, at a rotational speed equal to 1500 rpm and an airgap length of 8 mm for the M270 material. The value in red indicates the configuration without slit.

In Fig. 6.25, the influence of the number of slits on the eddy current losses is presented. In addition to the configuration with no slits, configurations with one to five slits are considered with a thickness of 2 mm. Configurations with 10 and 20 slits are studied as well, for which the slit thickness is adapted to 1 mm and 0.5 mm, respectively. Between the configuration without slits and with four slits, a factor 3 reduction in terms eddy current losses is obtained. Following the simulated trend, 15 slits would be necessary for a factor 10 reduction, and 95 slits for a factor 100 reduction. The latter reduction is significant and would bring the eddy current losses back to a level close to high-performance soft-magnetic materials, such as Somaloy 1000-3P [117], but at a reduced cost. Additional research would be required to perform the comparison between both materials in motor mode, using a realistic core thickness and commutated currents in the different windings.

In Fig. 6.26, the distributions of the eddy current density, J, are visualized on each face of the core, using the surface line integral convolution plugin in Paraview [156, 157], for both the slitless and slitted topologies. The nature of the eddy currents can be seen the most clearly on the front face of the slitless topology, where the currents encircle the shape of the magnets in order to oppose the field that created them. Different patterns can be observed on both faces of the same topology. The strongest currents flow closest to the magnets, i.e. the front face. The local current density around the slits might be overestimated by the conforming topology, due to the coarse discretization and the right angle of the slit corners. The different mesh discretizations are discussed in Section 6.6.4.
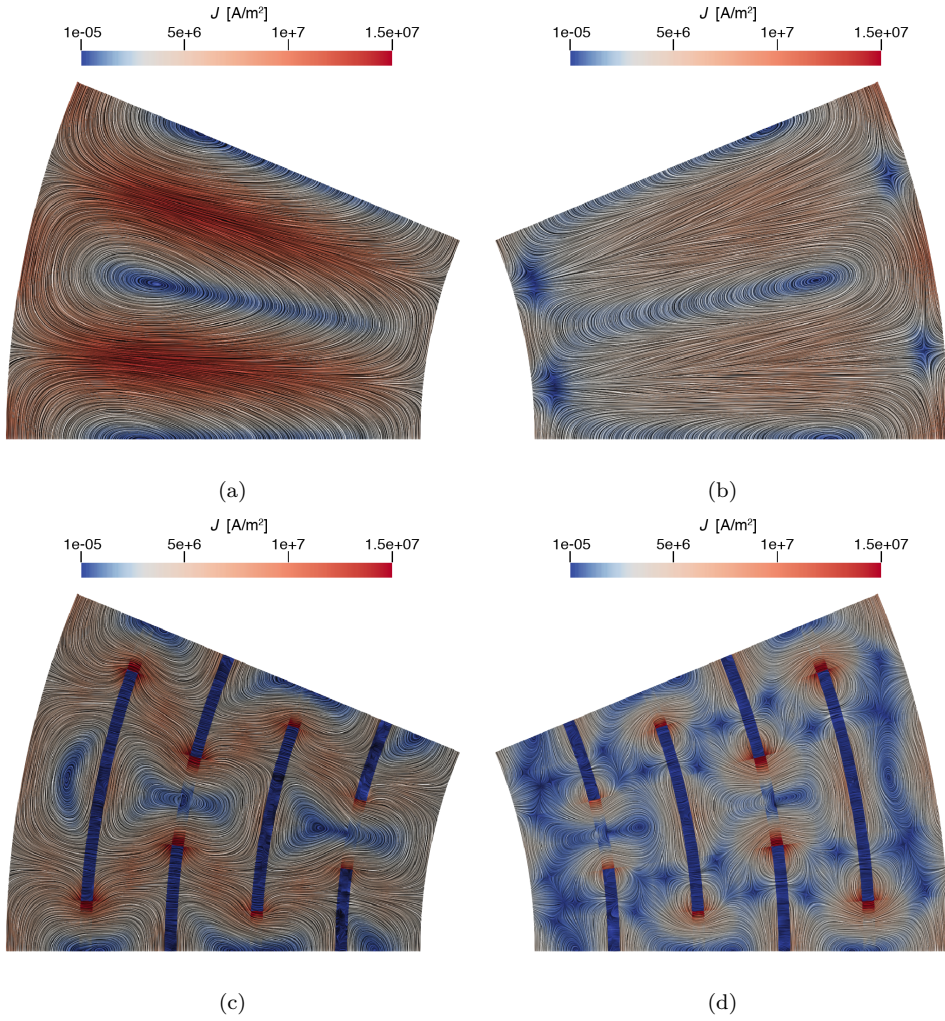
Figure 6.26: Eddy current density distribution on a) the front and b) back faces of the slitless core, as well as c) the front and b) back faces of the slitted core, at a rotational speed equal to 1500 rpm and an airgap length of 5 mm for the M270 material.

(a)   (b)
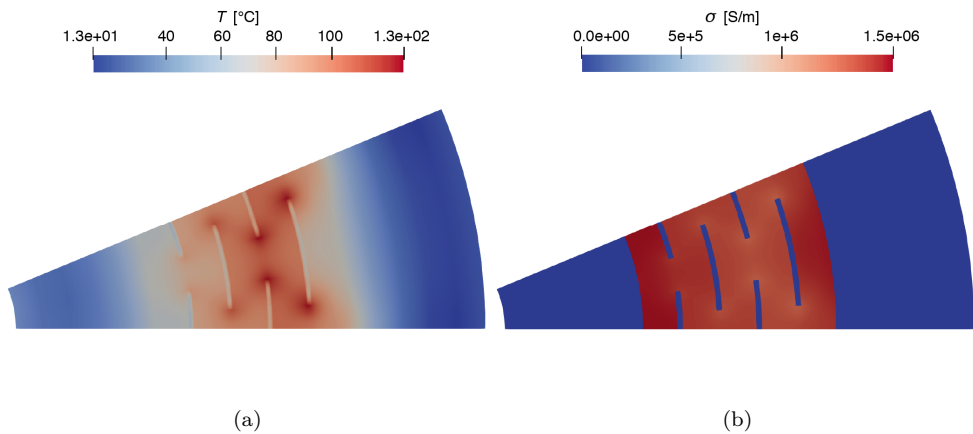
Figure 6.27: a) Temperature distribution in the core and b) electrical conductivity variations due to temperature profile in M270 material, at a rotational speed equal to 1500 rpm and an airgap length of 5 mm.

6.6.3   Thermal influence

Using the thermal model provided in Section 6.4, the losses resulting from the eddy current distributions shown in Figs. 6.26c and 6.26d, yields the thermal distribution given in Fig. 6.27a on the front face of the core. It can be seen that large temperature variations are obtained, with differences between the mean and maximum values equal to 35 °C. It was also shown by the experimental values given in Fig. 6.14. This leads to variations up to 25 % in the core material properties, as exemplified in Fig. 6.27b, where the electrical conductivity is linked to the thermal conductivity through the Lorenz ratio (6.7). In particular, the hottest region is between the second and fourth slit, which decreases the effective conductivity and therefore the losses.

6.6.4   Mesh discretization and trimming

In Fig. 6.28, three different mesh discretizations are represented for the slitted core region. Note that the mesh is quadrilateral and that the triangulation effect is artificially produced due to the visualization workflow. The conforming topology is shown in Fig. 6.28a, where all the slits are assigned on a suitably chosen mesh. Changing the number of slits necessitates altering the background mesh. A conforming topology is therefore, the least flexible approach. However, due to the structured mesh, it is the fastest approach, and it computes the steady-state temperature distribution in 60 s. In Fig. 6.28b, the mesh corresponding to three-dimensional tensor product topology is shown, which results from the multiplication of the r-θ topology with the z topology that stacks the different materials. The slits are trimmed on the two-dimensional r-θ
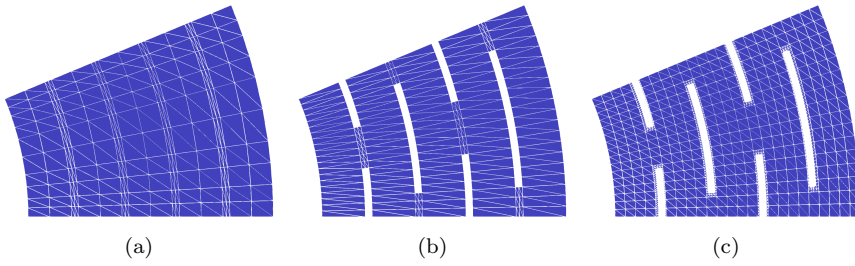
Figure 6.28: a) Mesh structure of the stator core for a) conforming CG, b) 2D trimmed tensor product DG, and c) 3D trimmed DG topologies.
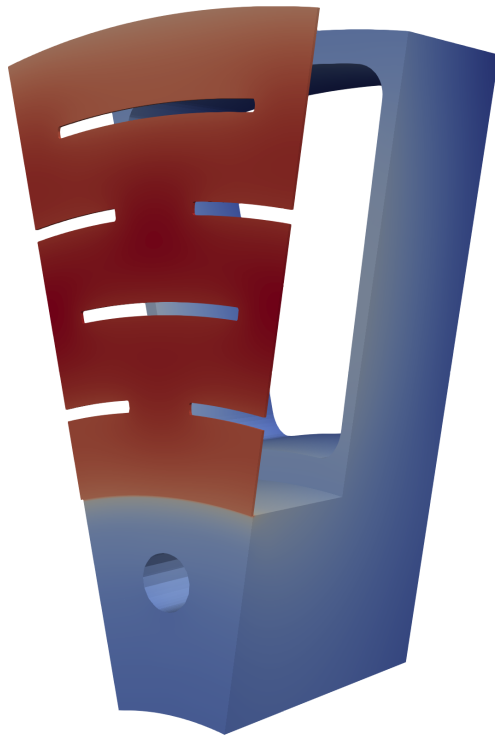
Figure 6.29: Trimmed topology with the slitted stator core in red, and the phenolic resin support in blue including air pocket and air inlet.

topology in an efficient manner. The discretization is then propagated to the whole structure along the z direction. This approach is relatively flexible and solves the thermal problem in 320 s. In Fig. 6.28c, the slits are trimmed directly on the 3D topology. This is the most expensive approach at the moment, with computational efforts of 1100 s and 2200 s, depending on whether one or two mesh refinements are performed to accommodate the trimmed regions. However, this is also the most flexible approach, as topology modifications can be performed at any time during the design stage. This is demonstrated in Fig. 6.29, where, in addition to the slits in the stator core, an air pocket is trimmed at the back of the phenolic resin support and an air inlet is trimmed all the way through. A part of the phenolic resin support is cut away in post-processing to enable the visualization of the air pocket.

6.7   Conclusion

In this chapter, the axial-flux permanent magnet machine is introduced as a three-dimensional academic problem with complex geometry and industrial relevance. An electromagnetic model of the machine is presented based on the content of the previous chapters. It enables to simulate the eddy current damping in the slitted core of the machine, which exhibits nonlinear material characteristics. The simulation is performed in the frequency domain utilizing the developed harmonic balance solver, which includes the fundamental, third, and fifth time harmonics in the solution. A thermal model is created and coupled to the electromagnetic model to take into account the thermal loading which deteriorates locally the electrical conductivity of the core.

To validate the multi-physical coupled model, an experimental test setup is realized. The setup is used to characterize the different physical phenomena occurring in the machine, as a function of the rotational speed and airgap length, which can be adjusted. In particular, the core temperature is monitored and exhibits less than 10 % discrepancy with the simulated values. The losses are measured and demonstrate a good agreement compared to the prediction from the model, with less than 10 % discrepancy across the whole range of measurements. This is possible since the model parameters have been carefully calibrated based on the performed measurements. This close correspondence between experimental and numerical results validates the developed approach based on the isogeometric analysis for an accurate spatial discretization combined with the harmonic balance solver for the efficient electrodynamic modeling of nonlinear motional eddy currents phenomena.

A sensitivity analysis is conducted on the electromagnetic model. It shows that compared to the reference solution including up to the fifth harmonic, 1 % to 2 % discrepancy on the losses is generated by removing the fifth harmonic and 3 % to

5 % discrepancy by only considering the first harmonic. In terms of the orientation with respect to the rolling direction of the steel, the influence on the losses is up to 3 %. The impact of the dimensions of the slits in the core has shown that the angular opening has a a large influence on the amplitude and ripple of the electromagnetic damping. It has been demonstrated that the losses can be reduced proportionally with the number of slits.

Chapter 7

Conclusions and recommendations

T HE final chapter of this thesis summarizes the outcomes of the research into the numerical modeling of the steady-state solution for nonlinear motional eddy current problems in the isogeometric analysis framework. Furthermore, conclusions are given about the multi-physical modeling of the axial-flux permanent magnet machine and its experimental verification. The scientific contributions of the work are listed and recommendations for future research are given.

7.1   Conclusions

In this thesis, a hierarchical isogeometric analysis modeling framework is researched in conjunction with a harmonic balance solver. The goal is to compute efficiently the eddy current distribution, due to the motion of a permanent magnet array, in soft-magnetic structures with nonlinear material characteristics and complex geometrical features, such as slits. The convergence of the proposed method is demonstrated on different benchmarks.

7.1.1   Numerical modeling

The isogeometric analysis (IGA) constitutes an extension of the finite-element method (FEM) using high-order polynomials or splines basis functions. The function properties are endowed with the same structure as the physical fields that should be simulated. IGA uses the same basis functions for the discretization of the partial differential equations and for the exact description of the complex geometrical features that arise in computer-aided design (CAD) models.

The framework enabling the isogeometric analysis of two- and three-dimensional structures is detailed. Based on the functional approximation spaces, different magnetostatic formulations are introduced and implemented. Two different methods for simulating the behavior of soft-magnetic materials that exhibit nonlinear characteristics have been investigated, namely the Newton-Raphson method and a variation of the fixed-point method. While the latter has proved its robustness with respect to the mesh size and its convenient applicability to various modeling methods, the former remains the most general method and is used to resolve other nonlinearities, such as the thermal radiation.

A harmonic balance solver is researched and implemented in the isogeometric analysis framework to enable the steady-state modeling of the nonlinear eddy currents induced by the motion of a permanent magnet array. The harmonic balance method constitutes an alternating time-frequency solver that exhibits a cross-coupling between the different time harmonics. The applicability of this method to motional problems is established against transient solvers, such as the time-stepping backward Euler technique and the space-time Galerkin approach.

The harmonic balance method has demonstrated its accuracy and computational efficiency on a pair of two-dimensional actuator benchmarks. The discrepancy between the mean values of all post-processed parameters, such as attraction force, damping force, and eddy current losses, is less than 1 % and 2 % for the slotted and slotless benchmarks, respectively. The ripples in the profiles are correctly predicted with less

than 2 % discrepancy, at a reduced computational cost. Depending on the number of considered harmonics, the speedup factor is at least 7 and 11 compared to time-stepping technique for the slotted and slotless benchmarks.

The space-time Galerkin approach is applied to two- and three-dimensional geometries. It is more computationally efficient than the time-stepping technique with a speedup factor of 6, although it is less efficient than the harmonic balance method. Furthermore, it is used to investigate the possibility of modeling eddy currents in the moving permanent magnet regions due to the slotting of the stator. However, the applicability of the current method is limited and several alternatives, such as using a discontinuous space-time topology, sliding-band approach, or generalized B-spline functions, are proposed to enable the efficient modeling of eddy currents in moving regions.

To further improve on the harmonic balance method, adaptive mesh refinements are adopted in the framework of hierarchical isogeometric analysis, using truncated hierarchical splines. To speed up computations, an acceleration method for the nonlinear harmonic balance solver is presented, using the projection of the solution at a previous level onto the adaptively refined grid, as an initial guess for the Newton-Raphson solver. It results in a decrease of the computational effort by a factor 2 and 5, for the untrimmed and trimmed benchmark, respectively. The proposed approach constitutes a novel and efficient way of solving the motional eddy current testing problem in steel sheets and laminations. This method is also applied to increase the computational efficiency of parametric studies. In addition, a progressive time-harmonic refinement strategy is proposed that enables the convergence of larger problems and improves the convergence speed.

The discontinuous Galerkin method is employed to perform trimming operations using topological partitions generated by the level set method. The resulting trimming approach is flexible with respect to the shape and number of parts. It allows to modify the topology easily by boolean operations at any point during the design stage and is employed to create local features, such as holes, slits, and channels. In addition, this approach can be used to add new solid parts and features to the existing topology. It is shown that the discontinuous Galerkin method deteriorates the condition number, limiting the range of the applicable penalty parameter for imposing the tangential continuity in the formulation. Although the technique is fast in two dimensions, the refinements necessary for trimming worsen the solving time in three dimensions. As an alternative, a tensorial approach is explored to perform the trimming in two dimensions and extend the resulting mesh along the third dimension. This approach reduces the computational effort by having spaces with tensor product structures, although they are inherently overly rich in terms of degrees of freedom. Another alternative remains using conforming discretizations,

which yields the cheapest solution although it lacks flexibly with regard to topology modifications.

7.1.2   Experimental verification

To demonstrate the applicability of the proposed method to a wider class of industrially relevant problems, a coupled, three-dimensional, transient, multiphysics problem with complex geometry is considered. More particularly, the eddy current damping in the slitted stator core of a single-sided axial-flux permanent magnet (AFPM) machine has been studied. The soft-magnetic material characteristic of the core is nonlinear due to magnetic saturation. Further nonlinearities are induced by the thermal model and temperature-dependent material properties.

To validate the coupled multi-physical numerical model, an experimental test setup has been manufactured. It consists of a prototype of an AFPM machine without windings. The permanent magnet array of the AFPM machine is rotated at a wide range of speeds, i.e. between 500 rpm and 1500 rpm, using an external driving motor. Facing the rotor, a solid steel disk is positioned and acts as the stator core. The disk, which consists of a single lamination, is slit along the angular direction with a pattern of four radial slits repeating periodically, where the slits act as eddy current barriers. Two different core materials, *M270-50A* and *M800-50A*, have been chosen that exhibit different electromagnetic behaviors. Employing a spindle mechanism, the airgap length between the rotating permanent magnet array and the slitted stator core is adapted from 5 mm to 14 mm. This affects the level of magnetic saturation in the core, and therefore the amount of eddy currents and the temperature.

Global quantities, such as the losses, have been measured and compared to the simulated quantities for different airgap values and rotational speed. Over the whole range of airgap lengths and speeds, a discrepancy between the measured and simulated values lower than 10 % has been obtained for both materials. Local quantities, such as the temperature, have been measured using thermocouples with less than 10 % difference compared to the predicted values from numerical simulations. Finally, local electromagnetic induction spectra have been measured via Rogowski coils that act as flux probes. The amplitudes of the different time harmonics exhibit a similar behavior as observed with the model, i.e. higher-order time harmonics, such as the third and fifth harmonics, are increasingly excited by the stronger magnetic fields resulting from smaller airgap lengths. This nonlinear dynamic behavior is efficiently captured by the harmonic balance method, which enables the accurate modeling of eddy current phenomena in complex geometries when coupled to the isogeometric analysis framework.

7.2 Thesis contribution

In this thesis, the framework of adaptive isogeometric analysis is explored as a promising direction to enhance the numerical modeling of permanent magnet electrical machines. To this purpose, several numerical methods are investigated to simulate the motional eddy current phenomena in the presence of nonlinear material characteristics. The scientific contributions of the research are summarized as:

- The implementation of two-dimensional and three-dimensional magnetostatic formulations, with structure-preserving functional spaces in the framework of the isogeometric analysis, including two different methods for simulating nonlinear B-H characteristics.

- The investigation into frequency-domain and time-domain hierarchical isogeometric solvers for simulating eddy currents due to the motion of a permanent magnet array. These solvers allow for trimmed regions and nonlinear soft-magnetic material characteristics.

- The creation of a three-dimensional multi-physical model to simulate the steady-state nonlinear behavior of a single-sided axial-flux permanent magnet machine with a slitted stator core, which includes a coupling between electromagnetic and thermal fields.

- The experimental validation of the multi-physical model, for a wide range of rotational speeds, airgap lengths, and magnetic flux densities, based on the measurement of local electromagnetic spectra, airflow velocities, temperatures, and the global electromagnetic damping torque.

7.3 Recommendations

Based on the modeling approaches developed in this thesis for the solution of nonlinear electromagnetic problems, recommendations are given for future research towards a general purpose, geometrically flexible, and computationally efficient multi-physical framework built upon the isogeometric paradigm.

7.3.1 Coupling with a turbulent flow model

The isogeometric analysis provides a natural framework for solving the Navier-Stokes equations using for example the Raviart-Thomas elements. In electrical machines applications, a turbulent flow, which can be computed for instance with the Lam

Bremhorst model, constitues a far more realistic description than given by a laminar model. Further development of the numerical work presented in [231] should be pursued to realize the coupling between electromagnetic and turbulent flow modeling through a conjugate heat transfer model. Fundamental understanding of the flow is necessary to optimize the topology of electrical machines by improving the electromagnetic performances through the convective cooling, using air or other fluids. The flow model complexity should be increased gradually from a simplified 2D model to full 3D trimmed geometries, while performing successive validations of the finite element code using recognized finite volume solutions. Maintaining the robustness and computational efficiency of the isogeometric scheme might be challenging.

7.3.2   Extension of the trimming and partition framework

Trimming a region away from the original topology, or embedding it back in, using the partition framework, increases the flexibility in building complex geometries and simulations, compared to the deformation of compatible conforming topologies. In addition to the existing level set method, it would be advantageous to extend the partition framework to enable the trimming of non-uniform rational B-splines (NURBS) objects to create a novel way to embed complex-shaped geometrical regions. For instance, realizing a flexible embedding of the accurate geometry of the coils inside a larger domain for physical analysis using the discontinuous Galerkin framework in three-dimensions could be researched. In electrostatic simulations, it is is crucial to have an accurate description of the shape of the conductor, insulation, protrusions, and other cavities, in order to realize designs that mitigate local electric field enhancements thereby preventing partial discharges in high-voltage electrical machines [217].

7.3.3   Topology optimization

After a model has been developed, its accuracy validated, its convergence analyzed, and its computational effort reduced, the design optimization procedure can start. Materials, dimensions, shapes, and topologies can be optimized. An advantage of the isogeometric analysis framework over FEM consists of the availability of the high-order shape derivatives. This enables to perform accurate sensitivity analysis and fast optimization. Furthermore, the isogeometric analysis is well suited for volumetric representations. It can be utilized to model non-homogeneous distributions of materials that are realized with, for example, additive manufacturing processes. Dimensions and shapes can be easily handled through the control points of the splines, while the topology can be adapted through the level method. It would be beneficial to perform a topology optimization in the context of multiphysics problems, such as the

AFPM machine, where simultaneous optimization of the electromagnetic perform-
ances and convective heat transfer could lead to specific local features that improve
the overall design.

7.3.4 Improvement on the space-time modeling

Concerning motional problems, additional research is needed to create a general and
robust space-time framework. Further experimentation with the trimming and par-
tition frameworks can be performed in the space-time setting. This enables the mod-
eling of moving systems with changing interfaces in time, which are of importance
in many multiphysics applications, such as vibroacoustics or ferrofluids. A general
setting for low-frequency electromagnetism with four-vector formalism and Galilean
transformations could be implemented [183, 184]. Further development in the coup-
ling of nonconforming space-time topologies is advantageous to model arbitrary mo-
tion between two or more bodies and their induced effects while minimizing the as-
sumptions on the regularity of time-signals and other geometrical simplifications.

7.3.5 Implementation of iterative solvers

Solving large-scale, three-dimensional, time-dependent, nonlinear problems, formu-
lated either in frequency or time domain, can become a very computationally intens-
ive task, especially when coupled multi-physical models are considered. Reducing
the computational cost of such complex simulations is of paramount importance and
requires both efficient system assembly and inversion. The assembly of the finite
element system can be performed across many cores in parallel. The inversion of
the resulting matrix should be done using iterative solvers, instead of direct solvers,
which are mostly recommended for two-dimensional problems. Iterative solvers rely
on problem-specific preconditioners and smoothers [62]. In the context of hierarchical
isogeometric analysis, the use of h-multigrid appears as a natural and efficient solu-
tion for developing high-performance iterative solvers [63]. Furthermore, monolithic
solvers can be employed to yield the solution directly, instead of sequentially solving
one physical problem at a time.

7.3.6 Extension towards application-specific basis functions

To improve the efficiency of the solvers, it is of utmost importance to reduce the num-
ber of basis functions to its minimum for a specific application. This has been demon-
strated with the harmonic balance method for smooth periodic excitation, which en-
ables faster computations. The wavelet balance can be implemented for simulating

efficiently the complex and highly dynamic motion profiles arising in linear, tubular, and planar motor technologies. To take into account the impact of the power electronics switching frequency, through voltage-driven, circuit-coupled electromechanics, the PWM-balance can be implemented. Finally, the generalized B-spline basis functions can be enriched with specific pairs of functions, such as trigonometric or hyperbolic functions, which enable salient profiles and special features to be represented exactly [159].

7.4   Publications

7.4.1   Journal publications

- D. Ceylan, L. A. J. Friedrich, K. O. Boynov, and E. A. Lomonova, "Effects of DC-field excitation on the incremental inductance of a variable flux reluctance machine," *IEEE Transactions on Magnetics (Early access)*, 2020, pp. 1-5.

- D. Ceylan, L. A. J. Friedrich, K. O. Boynov, and E. A. Lomonova, "Convergence analysis of the fixed-point method with the hybrid analytical modeling for 2-D nonlinear magnetostatic problems," *IEEE Transactions on Magnetics (Early access)*, 2020, pp. 1-5.

- M. Kleijer, L. A. J. Friedrich, B. L. J. Gysen, and E. A. Lomonova, "Framework for efficient dynamic analysis applied to a tubular generator for suspension applications," *(Under review)*, 2020, pp. 1-8.

- L. A. J. Friedrich, B. L. J. Gysen, J. W. Jansen, and E. A. Lomonova, "Analysis of motional eddy currents in the slitted stator core of an axial-flux permanent magnet machine," *IEEE Transactions on Magnetics*, vol. 56, no. 02, 2020, pp. 1-4.

- L. A. J. Friedrich, B. L. J. Gysen, M. G. L. Roes, and E. A. Lomonova, "Adaptive isogeometric analysis applied to an electromagnetic actuator," *IEEE Transactions on Magnetics*, vol. 55, no. 05, 2019, pp. 1-4.

- L. A. J. Friedrich, M. Curti, B. L. J. Gysen, and E. A. Lomonova, "High-order methods applied to nonlinear magnetostatic problems," *Mathematical and Computational Applications*, vol. 24, no. 19, 2019, pp. 1-15.

- L. A. J. Friedrich, J. J. H. Paulides, and E. A. Lomonova,"Modeling and optimization of a tubular generator for vibration energy harvesting application," *IEEE Transactions on Magnetics*, vol. 53, no. 11, 2017, pp. 1-4.

7.4.2 Conferences publications

- L. A. J. Friedrich, B. L. J. Gysen, and E. A. Lomonova, "Analysis of motional eddy currents in the slitted stator core of an axial-flux permanent magnet machine," *Proceedings of the 22nd International Conference on the Computation of Electromagnetic Fields (COMPUMAG)*, Paris, France, 2019, pp. 1-4.

- L. A. J. Friedrich, B. L. J. Gysen, and E. A. Lomonova, "Modeling of integrated eddy current damping rings for a tubular electromagnetic suspension system," *Proceedings of the 12th International Symposium on Linear Drives for Industry Applications (LDIA)*, Neuchâtel, Switzerland, 2019, pp. 1-4.

- M. Kleijer, L. A. J. Friedrich, B. L. J. Gysen, and E. A. Lomonova, "Dynamic analysis of a tubular generator for automotive suspension applications," *Proceedings of the 12th International Symposium on Linear Drives for Industry Applications (LDIA)*, Neuchâtel, Switzerland, 2019, pp. 1-5.

- L. A. J. Friedrich, B. L. J. Gysen, M. G. L. Roes, and E. A. Lomonova, "Adaptive isogeometric analysis applied to an electromagnetic actuator," *Proceedings of the 18th Biennial IEEE Conference on Electromagnetic Field Computation (CEFC)*, Hangzhou, China, 2018, pp. 1-4.

- L. A. J. Friedrich, M. Curti, B. L. J. Gysen, J. W. Jansen, and E. A. Lomonova, "High-order methods applied to electrical machine modeling," *Proceedings of the IEEE International Magnetics Conference (INTERMAG)*, Singapore, 2018, pp. 1-4.

- L. A. J. Friedrich, M. Curti, B. L. J. Gysen, J. W. Jansen, and E. A. Lomonova, "High-order methods applied to electrical machine modeling with non-linear material characteristics," *Proceedings of the IEEE Young Researchers Symposium in Electrical Power Engineering (YRS)*, Bruxelles, Belgium, 2018, pp. 1-4.

- L. A. J. Friedrich, K. Bastiaens, B. L. J. Gysen, D. C. J. Krop, and E. A. Lomonova, "Design of an axial-flux permanent magnet machine for a solar-powered electric vehicle," *Proceedings of the 13th International Conference on Ecological Vehicles and Renewable Energies (EVER)*, Monaco, 2018, pp. 1-5.

- L. A. J. Friedrich, J. J. H. Paulides, and E. A. Lomonova,"Modeling and optimization of a tubular generator for vibration energy harvesting application," *Proceedings of the IEEE International Magnetics Conference (INTERMAG)*, Dublin, Ireland, 2017, pp. 1-4.

Appendix A

Benchmark

In Section 3.5 the C-core benchmark from [85] is considered. The benchmark is given in Fig. A.1a.

Similarly, in Section 3.8 the C-core benchmark from [86] is considered. The benchmark is given in Fig. A.1b.
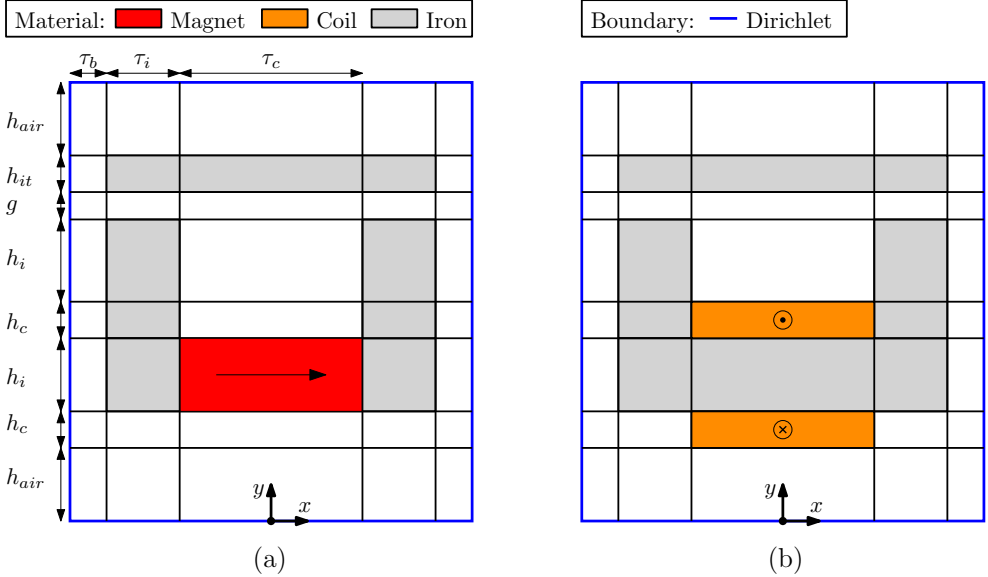
Figure A.1: C-core benchmarks for a) nonlinear magnetostatic, and b) adaptive linear magnetoharmonic simulations.

The dimensions of the C-core benchmark, indicated on Fig. A.1 are gathered in Table A.1.

Table A.1: Geometrical parameter values of the C-core benchmark

Parameter	Symbol	Value [mm]
Air box width	τ_b	5
Side width	τ_i	2
Central width	τ_c	5
Air box height	h_{air}	5
Coil height	h_c	2
Central height	h_i	3
Side height	h_{it}	2
Airgap	g	1

Appendix B

Definitions

Abbreviations

Abbreviation	Description
1D, 2D, 3D, 4D	One-, two-, three-, four-dimensional
AFPM	Axial-flux permanent magnet
AMG	Algebraic multigrid
BDDC	Balancing domain decomposition by constraint
BE	Backward Euler
BEM	Boundary element method
B-spline	Basis spline
CAD	Computer-aided design
CEM	Computational electromagnetism
CFD	Computational fluid dynamic
CG	Continuous Galerkin
CN	Crank-Nicolson
CPU	Central processing unit
CT	Computed tomography
DC	Direct current
DCT	Discrete cosine transform
DFT	Discrete Fourier transform
DG	Discontinuous Galerkin
dofs	Degrees of freedom
EM	Electromechanical
EMC	Electromagnetic compatibility
FE	Forward Euler
FEA	Finite element analysis
FEM	Finite element method
FETI	Finite element tearing and interconnecting

FFT	Fast Fourier transform
FORC	First-order reversal curves
FPM	Fixed-point method
FR2	Flame-retardant type 2 (phenolic resin paper laminate)
GAMG	Geometric algebraic multigrid
GB	Generalized B-spline
GERS	Guaranteed error reduction strategy
GMRES	Generalized minimal residual
GMG	Geometric multigrid
GPU	Graphics processing unit
GR	Global refinement
HAM	Hybrid analytical modeling
HB	Harmonic balance
IGA	Isogeometric analysis
LET	Lorentz force eddy current testing
LF	Leapfrog
MAGLEV	Magnetic levitation
MEC	Magnetic equivalent circuit
MEMS	Microelectromechanical systems
MET	Motional eddy current testing
MG	Multigrid
ML	Major loop
MoM	Method of moments
MNA	Modal nodal analysis
MQS	Magnetoquasistatic
MRI	Magnetic resonance imaging
MS	Maximum strategy
MST	Maxwell stress tensor
NDT	Nondestructive testing
NRM	Newton-Raphson method
NURBS	Non-uniform rational B-spline
PDEs	Partial differential equations
PEEC	Partial electrical equivalent circuit
PWM	Pulse-width modulation
QMR	Quasi-minimal residual
RF	Radio frequency
RFPM	Radial-flux permanent magnet
rms	Root mean square
SEM	Spectral element method
SIPG	Symmetric interior penalty Galerkin
SMC	Soft-magnetic composite
SORC	Second-order reversal curves

SUPG	Streamline-upwind Petrov-Galerkin
ST	Space-time
THB-spline	Truncated hierarchical B-spline
THD	Total harmonic distortion
TPFEM	Time-periodic finite element method
TS	Time-stepping
WB	Wavelet balance
WRM	Waveform relaxation method

Coordinate systems

Notation	Description
r	Polar radial coordinate
θ	Polar angular coordinate
x	Cartesian x-coordinate
y	Cartesian y-coordinate
z	Cartesian and polar z-coordinate
t	Time coordinate
ξ	Computational ξ-coordinate
η	Computational η-coordinate
ζ	Computational ζ-coordinate

Notations

Notation	Description
a	Scalar, tensor, operator
$\mathbf{a}$	Vector
A	Scalar field, matrix
$\mathbf{A}$	Vector field
$\tilde{A}$	Real Fourier coefficient
$\hat{A}$	Complex Fourier coefficient

Operators

Notation	Description
det	Determinant operator
max	Maximum operator
Re	Real part
span	Span operator
supp	Support operator

trunc	Truncation operator
γ	Trace operator
div, $\nabla\cdot$	Divergence operator
grad, ∇	Gradient operator
rot, **curl**, $\nabla\times$	Rotational or curl operator

Physical constants

Symbol	Description	Value	Unit
ϵ_0	Electrical permittivity of vacuum	$8.85 \ 10^{-12}$	F/m
μ_0	Magnetic permeability of vacuum	$4\pi \ 10^{-7}$	H/m
σ_{SB}	Stefan-Boltzmann constant	$5.67 \ 10^{-8}$	$\mathrm{Wm}^{-2}\mathrm{K}^{-4}$

Symbols

Symbol	Description	Unit
α_j	Unknown coefficients	
α_s, α_m	Geometrical ratios	
α_ρ, α_B	Thermal dependency	K^{-1}
$\boldsymbol{\alpha}$	Direction of the remanent flux density	
a	Bilinear form	
A	Magnetic vector potential	Wb/m
b	Right-hand side	
$B_{i,p}$	B-spline basis functions of order p	
B	Magnetic flux density	T
$\mathbf{B}_r$	Remanent magnetic flux density	T
$\beta_{i,l}$	B-spline basis functions of mesh level l	
C	Electric capacitance	F
$\mathbf{C}_i$	Control points	
C^0, C^1	Order of the continuity	
d	Number of physical dimensions	
d	Increment vector	
D	Diameter	m
D	Derivative matrix	
D	Electric displacement field	$\mathrm{C/m}^2$
δ	Kronecker symbol	
Δt	Time-step value	s
e	Unit vector	
E	Electric field strength	V/m
ϵ	Electric permittivity	F/m
ϵ	Levi-Civita symbol	

ϵ_β	Error estimator	
ϵ_σ	Regularization parameter	
ϵ_{rad}	Thermal emissivity	
f	Frequency	Hz
F_x	Force	N
$\mathbf{F}$	Mapping function	
$\mathcal{F}$	Fourier transform	
g	Airgap length	m
γ	Stabilization parameter	
Γ	Interface	
Γ_D	Dirichlet boundary	
Γ_N	Neumann boundary	
h	Height (axial)	m
h_β	Mesh size	m
h_{conv}	Convection coefficient	$\mathrm{Wm^{-2}K^{-1}}$
H	Upper time-harmonic order	
$\mathbf{H}$	Magnetic field strength	A/m
$\mathcal{H}$	Hierarchical spline space	
$H^1(\Omega), \mathbf{H}^1(\Omega)$	Scalar and vectorial Sobolev spaces on Ω	
θ	Implicitness parameter	
θ_p	Half the angular opening of a periodic section	rad
I	Electric current	A
$\iota^0, \iota^1, \iota^2, \iota^3$	Pullbacks	
J	Jacobian matrix	
$\mathbf{J}$	Electric current density	$\mathrm{A/m^2}$
$\mathbf{J}_s$	Imposed electric current density	$\mathrm{A/m^2}$
κ	Thermal conductivity	$\mathrm{Wm^{-1}K^{-1}}$
L	Electric inductance	H
$L^2(\Omega), \mathbf{L}^2(\Omega)$	Scalar and vectorial Lebesgue spaces on Ω	
M	Mass matrix	
M	Magnetization function	A/m
$\mathbf{M}_r$	Remanent magnetization	A/m
μ	Magnetic permeability	H/m
μ_r	Relative magnetic permeability	
n	Harmonic number	
n_k	Number of quadrature points	
n_s	Number of slits	
$\mathbf{n}$	Normal vector to an interface	
N	Number of time harmonics	
N_{el}	Number of elements	
$N_{i,p}$	NURBS basis functions of order p	
ν^{app}, ν	Apparent magnetic reluctivity	m/H

ν^{inc}, ν'	Incremental magnetic reluctivity	m/H
ξ_i	Knot	
Ξ	Knot vector	
$\mathcal{O}$	Asymptotic comparison	
P	Power	W
Q	Electric charge	C
$\mathbf{r}$	Residual vector	
R	Radius	m
R	Electric resistance	Ω
R_i	Reversal point	
Re	Reynolds number	
Rm	Magnetic Reynolds number	
ρ	Electric resistivity	Ω/m
ρ_q	Electric charge density	A/m^3
S	Stiffness matrix	
S_E	Shielding effectiveness	dB
S^p	Spline space of degree p	
$\mathcal{S}$	Enclosed surface	m^2
σ	Electric conductivity	S/m
σ_{MST}	Maxwell stress tensor	N/m^2
t^n	Time at instant n	s
T	Temperature	K
T_0	Ambient temperature	K
T_z	Torque	Nm
$\mathbf{T}$	Electric vector potential	A/m
$\mathcal{T}$	Truncated hierarchical spline space	
τ_p	Half the angular width of a periodic section	m
u_h	Trial functions	
v	Displacement speed	m/s
v_h	Test functions	
V	Electric scalar potential	V
Φ	Magnetic scalar potential	A
Φ_B	Magnetic flux	Wb
X^0, X^1, X^2, X^3	Functional Hilbert spaces	
w_i	NURBS weights	
$w_{l,k}$	Quadrature weights	
ω	Angular velocity	rad/s
ω_i, $\boldsymbol{\omega}_i$	Scalar and vectorial basis functions	
ω_n	Rotation speed	rpm
Ω	Physical domain	
$\hat{\Omega}$	Computational domain	
Ω_C	Electrically conducting domain	

Ω_{NC}	Non electrically-conducting domain
Ω_k	Patch
Ω_l	Domain at mesh level l
$\boldsymbol{\Omega_n}$	Hierarchy of subdomains of depth n

Bibliography

[1] T. Åström, "Use of non destructive testing in engineering insurance," in *IMIA Conference*, 2002.

[2] B. Ackermann and R. Sottek, "Analytical modeling of the cogging torque in permanent magnet motors," *Electrical Engineering*, vol. 78, no. 2, pp. 117–125, 1995.

[3] A. Acquaviva, O. Wallmark, E. A. Grunditz, S. T. Lundmark, and T. Thiringer, "Computationally efficient modeling of electrical machines with cooling jacket," *IEEE Transactions on Transportation Electrification*, vol. 5, no. 3, pp. 618–629, 2019.

[4] Agilent Technologies, Advanced Design System, *Harmonic Balance Simulation, User Guide*.

[5] A. Aimi, M. Diligenti, M. L. Sampoli, and A. Sestini, "Non-polynomial spline alternatives in isogeometric symmetric Galerkin BEM," *Applied Numerical Mathematics*, vol. 116, pp. 10–23, 2017.

[6] A.-M. Ampère, *Théorie des phénomènes électro-dynamiques, uniquement déduite de l'expérience*. Méquignon-Marvis, 1826.

[7] A. Arkadan, T. Hijazi, and B. Masri, "Design evaluation of conventional and toothless stator wind power axial-flux PM generator," *IEEE Transactions on Magnetics*, vol. 53, no. 6, pp. 1–4, 2017.

[8] D. N. Arnold and A. Logg, "Periodic table of the finite elements," *SIAM News*, vol. 47, no. 9, p. 212, 2014. [Online]. Available: http://www-users.math.umn.edu/~arnold/femtable/

[9] D. N. Arnold, R. S. Falk, and R. Winther, "Finite element exterior calculus, homological techniques, and applications," *Acta numerica*, vol. 15, pp. 1–155, 2006.

[10] D. N. Arnold, R. S. Falk, and R. Winther, "Finite element exterior calculus: from Hodge theory to numerical stability," *Bulletin of the American mathematical society*, vol. 47, no. 2, pp. 281–354, 2010.

[11] S. Außerhofer, O. Bíró, and K. Preis, "An efficient harmonic balance method for nonlinear eddy-current problems," *IEEE Transactions on Magnetics*, vol. 43, no. 4, pp. 1229–1232, 2007.

[12] M. Aydin, S. Huang, and T. A. Lipo, "Axial flux permanent magnet disc machines: A review," in *Conf. Record of SPEEDAM*, vol. 8, 2004, pp. 61–71.

[13] I. Babuška, "The finite element method with Lagrangian multipliers," *Numerische Mathematik*, vol. 20, no. 3, pp. 179–192, 1973.

[14] F. Bachinger, "Multigrid solvers for 3D multiharmonic nonlinear magnetic field computations," Ph.D. thesis, Johannes Kepler Universitat Linz, 2003.

[15] F. Bachinger, U. Langer, and J. Schöberl, "Efficient solvers for nonlinear time-periodic eddy current problems," *Computing and Visualization in Science*, vol. 9, no. 4, pp. 197–207, 2006.

[16] K. Bastiaens, M. Curti, D. C. J. Krop, S. Jumayev, and E. A. Lomonova, "Spectral element method modeling of eddy current losses in high-frequency transformers," *Mathematical and Computational Applications*, vol. 24, no. 1, p. 28, 2019.

[17] K. Bastiaens, D. C. J. Krop, S. Jumayev, and E. A. Lomonova, "Optimal design and comparison of high-frequency resonant and non-resonant rotary transformers," *Energies*, vol. 13, no. 4, p. 929, 2020.

[18] L. Beirao da Veiga, A. Buffa, G. Sangalli, and R. Vázquez, "Mathematical analysis of variational isogeometric methods," *Acta Numerica*, vol. 23, pp. 157–287, 2014.

[19] M. Bercovier and I. Soloveichik, "Overlapping non matching meshes domain decomposition method in isogeometric analysis," *arXiv preprint arXiv:1502.03756*, 2015.

[20] G. Bertotti, "General properties of power losses in soft ferromagnetic materials," *IEEE Transactions on magnetics*, vol. 24, no. 1, pp. 621–630, 1988.

[21] O. Bíró and K. Preis, "On the use of the magnetic vector potential in the finite-element analysis of three-dimensional eddy currents," *IEEE Transactions on Magnetics*, vol. 25, no. 4, pp. 3145–3159, 1989.

[22] Z. Bontinck, J. Corno, S. Schöps, and H. De Gersem, "Isogeometric analysis and harmonic stator–rotor coupling for simulating electric machines," *Computer Methods in Applied Mechanics and Engineering*, vol. 334, pp. 40–55, 2018.

[23] M. Bonvalot, P. Courtois, P. Gillon, and R. Tournier, "Magnetic levitation stabilized by eddy currents," *Journal of magnetism and magnetic materials*, vol. 151, no. 1-2, pp. 283–289, 1995.

[24] A. Bossavit, "Whitney forms: A class of finite elements for three-dimensional computations in electromagnetism," *IEE Proceedings A (Physical Science, Measurement and Instrumentation, Management and Education, Reviews)*, vol. 135, no. 8, pp. 493–500, 1988.

[25] A. Bossavit, "Differential geometry for the student of numerical methods in electromagnetism," *Lecture notes*, 1990.

[26] K. Bourchas, A. Stening, J. Soulard, A. Broddefalk, M. Lindenmo, M. Dahlén, and F. Gyllensten, "Influence of cutting and welding on magnetic properties of electrical steels," in *2016 XXII International Conference on Electrical Machines (ICEM)*.   IEEE, 2016, pp. 1815–1821.

[27] H. Brauer, M. Ziolkowski, K. Weise, M. Carlstedt, R. P. Uhlig, and M. Zec, *Motion-induced Eddy Current Techniques for Non-destructive Testing and Evaluation.*   Institution of Engineering and Technology, 2018.

[28] F. Brezzi, "On the existence, uniqueness and approximation of saddle-point problems arising from Lagrangian multipliers," *Publications mathématiques et informatique de Rennes*, no. S4, pp. 1–26, 1974.

[29] E. Brivadis, A. Buffa, B. Wohlmuth, and L. Wunderlich, "Isogeometric mortar methods," *Computer Methods in Applied Mechanics and Engineering*, vol. 284, pp. 292–319, 2015.

[30] A. Buffa, C. de Falco, and G. Sangalli, "Isogeometric analysis: new stable elements for the Stokes equation," *J. Numer. Meth. Fluids*, vol. 10, 2010.

[31] A. Buffa and E. M. Garau, "Refinable spaces and local approximation estimates for hierarchical splines," *IMA Journal of Numerical Analysis*, vol. 37, no. 3, pp. 1125–1149, 2017.

[32] A. Buffa and E. M. Garau, "A posteriori error estimators for hierarchical B-spline discretizations," *Mathematical Models and Methods in Applied Sciences*, vol. 28, no. 08, pp. 1453–1480, 2018.

[33] A. Buffa and C. Giannelli, "Adaptive isogeometric methods with hierarchical splines: error estimator and convergence," *Mathematical Models and Methods in Applied Sciences*, vol. 26, no. 01, pp. 1–25, 2016.

[34] A. Buffa and I. Perugia, "Discontinuous Galerkin approximation of the Maxwell eigenproblem," *SIAM Journal on Numerical Analysis*, vol. 44, no. 5, pp. 2198–2226, 2006.

[35] A. Buffa, G. Sangalli, and R. Vázquez, "Isogeometric methods for computational electromagnetics: B-spline and T-spline discretizations," *Journal of Computational Physics*, vol. 257, pp. 1291–1320, 2014.

[36] A. Buffa, J. Corno, C. de Falco, S. Schöps, and R. Vázquez, "Isogeometric Mortar coupling for electromagnetic problems," *SIAM Journal on Scientific Computing*, vol. 42, no. 1, pp. B80–B104, 2020.

[37] C. Canuto, M. Y. Hussaini, A. Quarteroni, and T. A. Zang, *Spectral methods: fundamentals in single domains.* Springer Science & Business Media, 2007.

[38] C. Canuto, M. Y. Hussaini, A. Quarteroni, and T. A. Zang, *Spectral methods: evolution to complex geometries and applications to fluid dynamics.* Springer Science & Business Media, 2007.

[39] F. G. Capponi, G. De Donato, and F. Caricchi, "Recent advances in axial-flux permanent-magnet machine technology," *IEEE Transactions on Industry Applications*, vol. 48, no. 6, pp. 2190–2205, 2012.

[40] G. Caron, "Modélisation numérique par la méthode des éléments finis des systèmes électrotechniques: recherche du régime permanent," Ph.D. thesis, Université Lille 1, 2017.

[41] A. Cavagnino, M. Lazzari, F. Profumo, and A. Tenconi, "A comparison between the axial flux and the radial flux structures for PM synchronous motors," *IEEE transactions on industry applications*, vol. 38, no. 6, pp. 1517–1524, 2002.

[42] F. Cedrat Corporation, Grenoble, "Flux 12.2 user's guide," 2016. [Online]. Available: www.altair.com/flux/

[43] D. Ceylan, L. A. J. Friedrich, K. O. Boynov, and E. A. Lomonova, "Convergence analysis of the fixed-point method with the hybrid analytical modeling for 2-D nonlinear magnetostatic problems," *IEEE Transactions on Magnetics*, pp. 1–5, (Early Access), 2020.

[44] D. Ceylan, L. A. J. Friedrich, K. O. Boynov, and E. A. Lomonova, "Effects of DC-field excitation on the incremental inductance of a variable flux reluctance machine," *IEEE Transactions on Magnetics*, pp. 1–5, (Early Access), 2020.

[45] O. Chadebec, J.-L. Coulomb, and F. Janet, "A review of magnetostatic moment method," *IEEE Transactions on Magnetics*, vol. 42, no. 4, pp. 515–520, 2006.

[46] T. Chady and J. M. Grochowalski, "Eddy current transducer with rotating permanent magnets to test planar conducting plates," *Sensors*, vol. 19, no. 6, p. 1408, 2019.

[47] F. Chauvicourt, "Vibro-acoustics of rotating electric machines: Prediction, validation and solution," Ph.D. thesis, KU Leuven, 2018.

[48] A. Christophe-Argenvillier, "Méthode des éléments finis avec joints en recouvrement non-conforme de maillages: application au contrôle non destructif par courants de Foucault," Ph.D. thesis, Université Paris Sud - Paris XI, 2014.

[49] Cogent. Non-oriented electrical steel datasheets. [Online]. Available: https://cogent-power.com/downloads

[50] L. Coox, F. Greco, O. Atak, D. Vandepitte, and W. Desmet, "A robust patch coupling method for NURBS-based isogeometric analysis of non-conforming multipatch surfaces," *Computer Methods in Applied Mechanics and Engineering*, vol. 316, pp. 235–260, 2017.

[51] I. Cortes Garcia, S. Schöps, H. De Gersem, and S. Baumanns, "Systems of differential algebraic equations in computational electromagnetics," *Applications of Differential-Algebraic Equations: Examples and Benchmarks*, pp. 123–169, 2019.

[52] J.-L. Coulomb and G. Meunier, "Finite element implementation of virtual work principle for magnetic or electric force and torque computation," *IEEE Transactions on Magnetics*, vol. 20, no. 5, pp. 1894–1896, 1984.

[53] M. Curti, "A spectral element based framework for efficient computation of electromechanical problems: applied to magnetic, electric, thermal and eddy current field modelling in electrical machines," Ph.D. thesis, Eindhoven University of Technology, Department of Electrical Engineering, 2019.

[54] C. H. M. Custers, "Overactuated magnetically levitated systems: flexible modes and eddy current phenomena in high-precision bearingless planar motors," Ph.D. thesis, Eindhoven University of Technology, Department of Electrical Engineering, 2019.

[55] G. Cvijetić, I. Gatin, V. Vukčević, and H. Jasak, "Harmonic balance developments in OpenFOAM," *Computers & Fluids*, vol. 172, pp. 632–643, 2018.

[56] L. Daniel, L. Bernard, and O. Hubert, "Multiscale Modeling of Magnetic Materials," in *Reference Module in Materials Science and Materials Engineering*. Elsevier, 2020. [Online]. Available: https://hal.archives-ouvertes.fr/hal-02777610

[57] C. De Boor, *A practical guide to splines*, ser. Applied Mathematical Sciences. Springer-Verlag New York, 1978, vol. 27.

[58] H. De Gersem, "Combined spectral-element, finite-element discretization for magnetic-brake simulation," *IEEE Transactions on Magnetics*, vol. 46, no. 8, pp. 3520–3523, 2010.

[59] H. De Gersem, "Spectral-element method for high-speed rotating cylinders," *COMPEL-The international journal for computation and mathematics in electrical and electronic engineering*, 2009.

[60] H. De Gersem, H. Vande Sande, and K. Hameyer, "Strong coupled multi-harmonic finite element simulation package," *COMPEL-The international journal for computation and mathematics in electrical and electronic engineering*, 2001.

[61] H. De Gersem, J. Gyselinck, P. Dular, K. Hameyer, and T. Weiland, "Comparison of sliding-surface and moving-band techniques in frequency-domain finite-element models of rotating machines," *COMPEL-The international journal for computation and mathematics in electrical and electronic engineering*, 2004.

[62] F. de Prenter, "Preconditioned iterative solution techniques for immersed finite element methods: with applications in immersed isogeometric analysis for solid and fluid mechanics," Ph.D. thesis, Eindhoven University of Technology, Department of Mechanical Engineering, 2019.

[63] F. de Prenter, C. V. Verhoosel, E. H. van Brummelen, J. A. Evans, C. Messe, J. Benzaken, and K. Maute, "Scalable multigrid methods for immersed finite element methods and immersed isogeometric analysis," *arXiv preprint arXiv:1903.10977*, 2019.

[64] G. De Rham, *Sur l'analysis situs des variétés à n dimensions*. Gauthier-Villars, 1931, vol. 1305.

[65] A. Demenko, K. Hameyer, L. Nowak, K. Zawirski, H. De Gersem, M. Ion, M. Wilke, and T. Weiland, "Trigonometric interpolation at sliding surfaces and in moving bands of electrical machine models," *COMPEL-The international journal for computation and mathematics in electrical and electronic engineering*, 2006.

[66] L. Demkowicz, *Computing with hp-Adaptive Finite Elements, Vol. 2, Frontiers: Three Dimensional Elliptic and Maxwell Problems with Applications*. Chapman & Hall/CRC Applied Mathematics & Nonlinear Science, 2008.

[67] L. Demkowicz, P. Monk, L. Vardapetyan, and W. Rachowicz, "De Rham diagram for hp finite element spaces," *Computers & Mathematics with Applications*, vol. 39, no. 7-8, pp. 29–38, 2000.

[68] M. Dems, K. Komeza, W. Kubiak, and J. Szulakowski, "Impact of core sheet cutting method on parameters of induction motors," *Energies*, vol. 13, no. 8, p. 1960, 2020.

[69] H. B. Dhia and G. Rateau, "The Arlequin method as a flexible engineering design tool," *International journal for numerical methods in engineering*, vol. 62, no. 11, pp. 1442–1462, 2005.

[70] E. Dlala and A. Arkkio, "Analysis of the convergence of the fixed-point method used for solving nonlinear rotational magnetic field problems," *IEEE Transactions on Magnetics*, vol. 44, no. 4, pp. 473–478, 2008.

[71] E. Dlala, A. Belahcen, and A. Arkkio, "Locally convergent fixed-point method for solving time-stepping nonlinear field problems," *IEEE transactions on magnetics*, vol. 43, no. 11, pp. 3969–3975, 2007.

[72] W. Dörfler, "A convergent adaptive algorithm for Poissons' equation," *SIAM Journal on Numerical Analysis*, vol. 33, no. 3, pp. 1106–1124, 1996.

[73] T. Dreher, R. Perrin-Bit, G. Meunier, and J.-L. Coulomb, "A three dimensional finite element modelling of rotating machines involving movement and external circuit," *IEEE Transactions on Magnetics*, vol. 32, no. 3, pp. 1070–1073, 1996.

[74] J. Driesen, G. D. T. Van Craenenbroeck, and K. Hameyer, "Implementation of the harmonic balance FEM method for large-scale saturated electromagnetic devices," *WIT Transactions on Engineering Sciences*, vol. 22, 1999.

[75] M. Elasmi, C. Erath, and S. Kurz, "Non-symmetric isogeometric FEM-BEM couplings," *arXiv preprint arXiv:2007.09057*, 2020.

[76] G. Farin and D. Hansford, "Discrete Coons patches," *Computer aided geometric design*, vol. 16, no. 7, pp. 691–700, 1999.

[77] A. Fasolo, L. Alberti, and N. Bianchi, "Performance comparison between switching-flux and IPM machines with rare-earth and ferrite PMs," *IEEE Transactions on Industry Applications*, vol. 50, no. 6, pp. 3708–3716, 2014.

[78] K. Fedick and C. Christoffersen, "Effect of wavelet selection on periodic steady-state analysis," *IEEE Access*, vol. 8, pp. 70 784–70 796, 2020.

[79] B. Feng, A. L. Ribeiro, T. J. Rocha, and H. G. Ramos, "Comparison of inspecting non-ferromagnetic and ferromagnetic metals using velocity induced eddy current probe," *Sensors*, vol. 18, no. 10, p. 3199, 2018.

[80] P. Ferrouillat, "Développement de formulations éléments finis 3D en potentiel vecteur magnétique: application aux machines asynchrones en mouvement," Ph.D. thesis, Université Grenoble Alpes, 2015.

[81] R. P. Feynman, R. B. Leighton, and M. L. Sands, "The Feynman Lectures on Physics vol. 2," 1989. [Online]. Available: feynmanlectures.caltech.edu

[82] M. Fortin, "An analysis of the convergence of mixed finite element methods," *RAIRO. Analyse numérique*, vol. 11, no. 4, pp. 341–354, 1977.

[83] M. Francoeur and M. P. Mengüç, "Role of fluctuational electrodynamics in near-field radiative heat transfer," *Journal of Quantitative Spectroscopy and Radiative Transfer*, vol. 109, no. 2, pp. 280–293, 2008.

[84] L. A. J. Friedrich, K. Bastiaens, B. L. J. Gysen, D. C. J. Krop, and E. A. Lomonova, "Design of an axial-flux permanent magnet machine for a solar-powered electric vehicle," in *2018 Thirteenth International Conference on Ecological Vehicles and Renewable Energies (EVER)*.   IEEE, 2018, pp. 1–5.

[85] L. A. J. Friedrich, M. Curti, B. L. J. Gysen, and E. A. Lomonova, "High-order methods applied to nonlinear magnetostatic problems," *Mathematical and Computational Applications*, vol. 24, no. 19, pp. 1–15, 2019.

[86] L. A. J. Friedrich, B. L. J. Gysen, and E. A. Lomonova, "Modeling of integrated eddy current damping rings for a tubular electromagnetic suspension system," in *12th International Symposium on Linear Drives for Industry Applications (LDIA)*, 2019, pp. 1–4.

[87] L. A. J. Friedrich, M. G. L. Roes, B. L. J. Gysen, and E. A. Lomonova, "Adaptive isogeometric analysis applied to an electromagnetic actuator," *IEEE Transactions on Magnetics*, vol. 55, no. 6, pp. 1–4, 2019.

[88] L. A. J. Friedrich, B. L. J. Gysen, J. W. Jansen, and E. A. Lomonova, "Analysis of motional eddy currents in the slitted stator core of an axial-flux permanent-magnet machine," *IEEE Transactions on Magnetics*, vol. 56, no. 2, pp. 1–4, 2020.

[89] Y. Gao, G. Y. Tian, P. Wang, H. Wang, B. Gao, W. L. Woo, and K. Li, "Electromagnetic pulsed thermography for natural cracks inspection," *Scientific reports*, vol. 7, no. 1, pp. 1–9, 2017.

[90] E. M. Garau and R. Vázquez, "Algorithms for the implementation of adaptive isogeometric methods using hierarchical B-splines," *Applied Numerical Mathematics*, vol. 123, pp. 58 – 87, 2018.

[91] I. C. Garcia, S. Schöps, H. De Gersem, and S. Baumanns, "Systems of differential algebraic equations in computational electromagnetics," *Applications of Differential-Algebraic Equations: Examples and Benchmarks*, pp. 123–169, 2019.

[92] W. Geng, Z. Zhang, and Q. Li, "High torque density fractional-slot concentrated-winding axial-flux permanent-magnet machine with modular SMC stator," in *2019 IEEE Energy Conversion Congress and Exposition (ECCE)*. IEEE, 2019, pp. 2991–2995.

[93] P. Gervasio and A. Quarteroni, "The INTERNODES method for non-conforming discretizations of PDEs," *Communications on Applied Mathematics and Computation*, vol. 1, no. 3, pp. 361–401, 2019.

[94] J. F. Gieras, R.-J. Wang, and M. J. Kamper, *Axial flux permanent magnet brushless machines.* Springer Science & Business Media, 2008.

[95] V. Girault and P.-A. Raviart, "Finite element approximation of the Navier-Stokes equations," *Lecture Notes in Mathematics, Berlin Springer Verlag*, vol. 749, 1979.

[96] F. Gires and E. Fourteau, *L'Empire de la physique: cabinet de physique du lycée Guez de Balzac d'Angoulême.* ASEISTE, 2006.

[97] N. Gödel, S. Schomann, T. Warburton, and M. Clemens, "GPU accelerated Adams–Bashforth multirate discontinuous Galerkin FEM simulation of high-frequency electromagnetic fields," *IEEE Transactions on magnetics*, vol. 46, no. 8, pp. 2735–2738, 2010.

[98] J. Gyselinck, P. Dular, N. Sadowski, J. Leite, and J. P. A. Bastos, "Incorporation of a Jiles-Atherton vector hysteresis model in 2D FE magnetic field computations," *COMPEL-The international journal for computation and mathematics in electrical and electronic engineering*, 2004.

[99] J. Gyselinck, C. Martis, and R. V. Sabariego, "Using dedicated time-domain basis functions for the simulation of pulse-width-modulation controlled devices–application to the steady-state regime of a buck converter," in *International Symposium on Advanced Electromechanical Motion Systems*, 2013.

[100] B. L. J. Gysen, K. J. Meessen, J. J. H. Paulides, and E. A. Lomonova, "General formulation of the electromagnetic field distribution in machines and devices using Fourier analysis," *IEEE Transactions on Magnetics*, vol. 46, no. 1, pp. 39–52, 2009.

[101] B. L. J. Gysen, J. J. H. Paulides, and E. A. Lomonova, "Direct-drive electromagnetic active suspension system with integrated eddy current damping for automotive applications," in *Proceedings of the 8th International Symposium on Linear Drives for Industry Applications (LDIA)*, 2011.

[102] B. Hague, *Electromagnetic problems in electrical engineering: an elementary treatise on the application of the principles of electromagnetism to the theory*

of the magnetic field and of the mechanical forces in electrical machinery and apparatus. H. Milford, 1929.

[103] A. Halbach, "Domain decomposition techniques for the nonlinear, steady state, finite element simulation of MEMS ultrasonic transducer arrays," Ph.D. thesis, Université de Liège, Belgique, 2017.

[104] T. Hara, T. Naito, and J. Umoto, "Time-periodic finite element method for nonlinear diffusion equations," *IEEE Transactions on Magnetics*, vol. 21, no. 6, pp. 2261–2264, 1985.

[105] F. Henrotte, H. Hedia, N. Bamps, A. Genon, A. Nicolet, and W. Legros, "A new method for axisymmetrical linear and nonlinear problems," *IEEE Transactions on Magnetics*, vol. 29, no. 2, pp. 1352–1355, 1993.

[106] M. Hettegger, B. Streibl, O. Bíró, and H. Neudorfer, "Identifying the heat transfer coefficients on the end-windings of an electrical machine by measurements and simulations," in *The XIX International Conference on Electrical Machines (ICEM)*, 2010, pp. 1–5.

[107] J. Hinz, M. Möller, and C. Vuik, "Elliptic grid generation techniques in the framework of isogeometric analysis applications," *Computer Aided Geometric Design*, vol. 65, pp. 48–75, 2018.

[108] J. Hinz, M. Abdelmalik, and M. Möller, "Goal-oriented adaptive THB-spline schemes for PDE-based planar parameterization," *arXiv preprint arXiv:2001.08874*, 2020.

[109] R. Hiptmair, "Finite elements in computational electromagnetism," *Acta Numerica*, vol. 11, pp. 237–339, 2002.

[110] R. Hiptmair, R. H. Hoppe, and U. Langer, "Computational electromagnetism," *Oberwolfach Reports*, vol. 1, no. 1, pp. 545–632, 2004.

[111] R. Hiptmair, R. H. Hoppe, P. Joly, and U. Langer, "Computational electromagnetism and acoustics," *Oberwolfach Reports*, vol. 4, no. 1, pp. 273–370, 2007.

[112] R. Hiptmair, R. H. Hoppe, P. Joly, and U. Langer, "Computational electromagnetism and acoustics," *Oberwolfach Reports*, vol. 7, no. 1, pp. 415–519, 2010.

[113] R. Hiptmair, R. H. Hoppe, P. Joly, and U. Langer, "Computational electromagnetism and acoustics," *Oberwolfach Reports*, vol. 10, no. 1, pp. 129–237, 2013.

[114] T. Hoang, "Isogeometric and immersogeometric analysis of incompressible flow problems," Ph.D. thesis, Eindhoven University of Technology, Department of Mechanical Engineering, 2018.

[115] C. Hofer, U. Langer, M. Neumüller, and I. Toulopoulos, "Time-multipatch discontinuous Galerkin space-time isogeometric analysis of parabolic evolution problems," 2018.

[116] C. Hofreither, B. Jüttler, G. Kiss, and W. Zulehner, "Multigrid methods for isogeometric analysis with THB-splines," *Computer Methods in Applied Mechanics and Engineering*, vol. 308, pp. 96–112, 2016.

[117] Höganäs. Somaloy 3P material data. [Online]. Available: www.hoganas.com/globalassets/download-media/sharepoint/brochures-and-datasheets---all-documents/somaloy-3p_material-data_june_2018_2273hog.pdf

[118] K. Hollaus, "A MSFEM to simulate the eddy current problem in laminated iron cores in 3D," *COMPEL-The international journal for computation and mathematics in electrical and electronic engineering*, 2019.

[119] S. F. Hosseini and B. Moetakef-Imani, "Improved B-spline skinning approach for design of hawt blade mold surfaces," *Journal of Mechanics*, vol. 33, no. 4, pp. 427–433, 2017.

[120] S. Huang, J. Luo, F. Leonardi, and T. A. Lipo, "A comparison of power density for axial flux machines based on general purpose sizing equations," *IEEE Transactions on energy conversion*, vol. 14, no. 2, pp. 185–192, 1999.

[121] T. J. R. Hughes, *The finite element method: linear static and dynamic finite element analysis.* Courier Corporation, 2012.

[122] T. J. R. Hughes, J. A. Cottrell, and Y. Bazilevs, "Isogeometric analysis: CAD, finite elements, NURBS, exact geometry and mesh refinement," *Computer methods in applied mechanics and engineering*, vol. 194, no. 39-41, pp. 4135–4195, 2005.

[123] J. G. Hust and L. L. Sparks, *Lorenz ratios of technically important metals and alloys.* US Department of Commerce, National Bureau of Standards, 1973, vol. 634.

[124] L. H. Ichinose, Y. Kohno, T. Kitada, and M. Matsumura, "Applications of eddy current test to fatigue crack inspection of steel bridges," *Memoirs-Faculty of engineering Osaka city municipality*, vol. 48, p. 57, 2007.

[125] L. Jiang and S. Chen, "Parametric structural shape & topology optimization with a variational distance-regularized level set method," *Computer Methods in Applied Mechanics and Engineering*, vol. 321, pp. 316–336, 2017.

[126] S. Jumayev, J. J. H. Paulides, K. O. Boynov, J. Pyrhönen, and E. A. Lomonova, "3-D analytical model of helical winding PM machines including rotor eddy currents," *IEEE Transactions on Magnetics*, vol. 52, no. 5, pp. 1–8, 2015.

[127] J.-W. Jung, B.-H. Lee, D.-J. Kim, J.-P. Hong, J.-Y. Kim, S.-M. Jeon, and D.-H. Song, "Mechanical stress reduction of rotor core of interior permanent magnet synchronous motor," *IEEE Transactions on Magnetics*, vol. 48, no. 2, pp. 911–914, 2012.

[128] J.-W. Jung, H.-I. Park, J.-P. Hong, and B.-H. Lee, "A novel approach for 2-D electromagnetic field analysis of surface mounted permanent magnet synchronous motor taking into account axial end leakage flux," *IEEE Transactions on Magnetics*, vol. 53, no. 11, pp. 1–4, 2017.

[129] T.-U. Jung and J.-S. Cho, "Electromagnetic structural design analysis and performance improvement of AFPM generator for small wind turbine," *Journal of Magnetics*, vol. 16, no. 4, pp. 374–378, 2011.

[130] S. Kahourzade, A. Mahmoudi, H. W. Ping, and M. N. Uddin, "A comprehensive review of axial-flux permanent-magnet machines," *Canadian journal of electrical and computer engineering*, vol. 37, no. 1, pp. 19–33, 2014.

[131] M. Kaltenbacher, *Numerical Simulation of Mechatronic Sensors and Actuators: Finite Elements for Computational Multiphysics.* Springer, Berlin, 2015.

[132] M. Kaltenbacher, "Numerische Simulation magnetomechanischer Transducer mit Fluidankopplung," Ph.D. thesis, Johannes Kepler Universität Linz, 1996.

[133] S. Kamkar, A. Wissink, V. Sankaran, and A. Jameson, "Combined feature-driven richardson-based adaptive mesh refinement for unsteady vortical flows," *AIAA journal*, vol. 50, no. 12, pp. 2834–2847, 2012.

[134] H. Kanayama, D. Tagami, M. Saito, and F. Kikuchi, "A numerical method for 3-D eddy current problems," *Japan journal of industrial and applied mathematics*, vol. 18, no. 2, p. 603, 2001.

[135] H. Karl, J. Fetzer, S. Kurz, G. Lehner, and W. M. Rucker, "Description of team workshop problem 28: An electrodynamic levitation device," in *Proc. of the TEAM Workshop, Graz, Austria*, 1997, pp. 48–51.

[136] A. Khebir, P. Dłotko, B. Kapidani, A. Kouki, and R. Specogna, "Formulation with higher-order hierarchical basis functions for nonsimply connected conductors," *Mathematical Problems in Engineering*, 2018.

[137] C.-W. Kim, G.-H. Jang, J.-M. Kim, J.-H. Ahn, C.-H. Baek, and J.-Y. Choi, "Comparison of axial flux permanent magnet synchronous machines with electrical steel core and soft magnetic composite core," *IEEE Transactions on Magnetics*, vol. 53, no. 11, pp. 1–4, 2017.

[138] J. S. Kim, J. H. Lee, J.-Y. Song, D.-W. Kim, Y.-J. Kim, and S.-Y. Jung, "Characteristics analysis method of axial flux permanent magnet motor based on 2-D finite element analysis," *IEEE Transactions on Magnetics*, vol. 53, no. 6, pp. 1–4, 2017.

[139] M. Kleijer, L. A. J. Friedrich, B. L. J. Gysen, and E. A. Lomonova, "Framework for efficient dynamic analysis applied to a tubular generator for suspension applications," (Under review), 2020.

[140] M. Kleijer, "Framework for efficient dynamic analysis applied to a tubular generator for suspension applications," Master's thesis, Eindhoven University of Technology, Department of Electrical Engineering, 2019.

[141] M. Kleijer, L. A. J. Friedrich, B. L. J. Gysen, and E. A. Lomonova, "Dynamic analysis of a tubular generator for automotive suspension applications," in *12th International Symposium on Linear Drives for Industry Applications (LDIA)*, 2019, pp. 1–5.

[142] D. C. J. Krop, J. W. Jansen, and E. A. Lomonova, "Decoupled modeling in a multifrequency domain: Integration of actuation and power transfer in one device," *IEEE Transactions on Magnetics*, vol. 49, no. 6, pp. 3009–3019, 2012.

[143] M. Kuczmann, "Potential formulations in magnetics applying the finite element method," *Lecture Notes, Hungary*, 2009.

[144] M. Kuczmann, "Nodal and edge finite element analysis of eddy current field problems," *Przeglad Elektrotechniczny*, vol. 84, no. 12, pp. 194–197, 2008.

[145] G. Kuru, C. V. Verhoosel, K. G. Van der Zee, and E. H. van Brummelen, "Goal-adaptive isogeometric analysis with hierarchical splines," *Computer Methods in Applied Mechanics and Engineering*, vol. 270, pp. 270–292, 2014.

[146] D. Kuzmin, "A guide to numerical methods for transport equations," *University Erlangen-Nuremberg*, 2010.

[147] J. Le Besnerais, "Reduction of magnetic noise in PWM-supplied induction machines-low-noise design rules and multi-objective optimization," Ph.D. thesis, 2008.

[148] Y. Le Floch, "Développement de formulations 3D éléments finis $T\phi$ pour la prise en compte de conducteurs massifs et bobinés avec un couplage ciruit," Ph.D. thesis, Université Grenoble Alpes, 2002.

[149] A. Lehikoinen, "Circulating and eddy-current losses in random-wound electrical machines," Ph.D. thesis, Aalto University, 2017.

[150] L. F. Leindinger, "Explicit isogeometric B-Rep analysis for nonlinear dynamic crash simulations: integrating design and analysis by means of trimmed multipatch shell structures," Ph.D. thesis, Technical University of Munich, Department of Mechanical Engineering, 2020.

[151] E. Lelarasmee, A. E. Ruehli, and A. L. Sangiovanni-Vincentelli, "The waveform relaxation method for time-domain analysis of large scale integrated circuits," *IEEE Transactions on Computer-Aided Design of Integrated Circuits and Systems*, vol. 1, no. 3, pp. 131–145, 1982.

[152] J. Lequeux, *François Arago, un savant généreux.* EDP sciences, 2012.

[153] X. Li, B. Hu, X. Ling, and X. Zeng, "A wavelet-balance approach for steady-state analysis of nonlinear circuits," *IEEE Transactions on Circuits and Systems I: Fundamental Theory and Applications*, vol. 49, no. 5, pp. 689–694, 2002.

[154] Z. J. Liu and J. T. Li, "Analytical solution of air-gap field in permanent-magnet motors taking into account the effect of pole transition over slots," *IEEE Transactions on Magnetics*, vol. 43, no. 10, pp. 3872–3883, 2007.

[155] G. Loli, M. Montardini, G. Sangalli, and M. Tani, "Space-time Galerkin isogeometric method and efficient solver for parabolic problem," *arXiv preprint arXiv:1909.07309*, 2019.

[156] B. Loring, H. Karimabadi, and V. Rortershteyn. Line integral convolution plugin in paraview. [Online]. Available: www.paraview.org/Wiki/ParaView/Line_Integral_Convolution

[157] B. Loring, H. Karimabadi, and V. Rortershteyn, "A screen space GPGPU surface LIC algorithm for distributed memory data parallel sort last rendering infrastructures," Lawrence Berkeley National Laboratory, Berkeley, California, USA, Tech. Rep., 2014.

[158] A. Mahmoudi, N. Rahim, and W. Hew, "Axial-flux permanent-magnet machine modeling, design, simulation, and analysis," *Scientific Research and Essays*, vol. 6, no. 12, pp. 2525–2549, 2011.

[159] C. Manni, A. Reali, and H. Speleers, "Isogeometric collocation methods with generalized B-splines," *Computers & Mathematics with Applications*, vol. 70, no. 7, pp. 1659–1675, 2015.

[160] D. Martínez-Muñoz, "Design, modelling and control of electrical machines-with applications to iron-powder machines and acoustic noise," Ph.D. thesis, Lund University, 2005.

[161] M. Merdzan, J. J. H. Paulides, and E. A. Lomonova, "Comparative analysis of rotor losses in high-speed permanent magnet machines with different winding configurations considering the influence of the inverter PWM," in *2015 Tenth International Conference on Ecological Vehicles and Renewable Energies (EVER)*. IEEE, 2015, pp. 1–8.

[162] G. Meunier, J.-M. Guichon, O. Chadebec, B. Bannwarth, L. Krähenbühl, and C. Guérin, "Unstructured–PEEC method for thin electromagnetic media," *IEEE Transactions on Magnetics*, vol. 56, no. 1, pp. 1–5, 2019.

[163] C. Münger, "Dielectric breakdown prediction with GPU-accelerated BEM," Master's thesis, Swiss Federal Institute of Technology Zurich, Department of Mathematics, 2020.

[164] O. Nastov, R. Telichevesky, K. Kundert, and J. White, "Fundamentals of fast simulation algorithms for RF circuits," *Proceedings of the IEEE*, vol. 95, no. 3, pp. 600–621, 2007.

[165] J.-C. Nédélec, "Mixed finite elements in $\mathbb{R}^3$," *Numerische Mathematik*, vol. 35, no. 3, pp. 315–341, 1980.

[166] V. P. Nguyen, P. Kerfriden, M. Brino, S. P. Bordas, and E. Bonisoli, "Nitsche's method for two and three dimensional NURBS patch coupling," *Computational Mechanics*, vol. 53, no. 6, pp. 1163–1182, 2014.

[167] P. Ojaghlu and A. Vahedi, "Specification and design of ring winding axial flux motor for rim-driven thruster of ship electric propulsion," *IEEE Transactions on Vehicular Technology*, vol. 68, no. 2, pp. 1318–1326, 2018.

[168] OpenCFD Ltd. OpenFOAM: API Guide. [Online]. Available: www.openfoam.com

[169] V. Ostović, *Dynamics of saturated electric machines*. Springer Science & Business Media, 1989.

[170] A. Palha, B. Koren, and F. Felici, "A mimetic spectral element solver for the Grad–Shafranov equation," *Journal of Computational Physics*, vol. 316, pp. 63–93, 2016.

[171] A. Pels, H. De Gersem, R. V. Sabariego, and S. Schöps, "Multirate PWM balance method for the efficient field-circuit coupled simulation of power converters," *Journal of Mathematics in Industry*, vol. 9, no. 1, pp. 1–12, 2019.

[172] L. Piegl and W. Tiller, *The NURBS book*. Springer Science & Business Media, 2012.

[173] R. Plasser, G. Koczka, and O. Bíró, "Improvement of the finite-element analysis of 3-D, nonlinear, periodic eddy current problems involving voltage-driven coils under DC bias," *IEEE Transactions on Magnetics*, vol. 54, no. 3, pp. 1–4, 2017.

[174] R. Plasser, G. Koczka, and O. Bíró, "A nonlinear magnetic circuit model for periodic eddy current problems using $T, \phi - \phi$ formulation," *COMPEL-The international journal for computation and mathematics in electrical and electronic engineering*, 2017.

[175] R. Plasser, Y. Takahashi, G. Koczka, and O. Bíró, "Comparison of two methods for the finite element steady-state analysis of nonlinear 3D periodic eddy-current problems using the $A, V-$ formulation," *International Journal of Numerical Modelling: Electronic Networks, Devices and Fields*, vol. 31, no. 2, p. e2279, 2018.

[176] K. J. W. Pluk, "Hybrid 3-D electromagnetic modeling: the challenge of magnetic shielding of a planar actuator," Ph.D. thesis, Eindhoven University of Technology, Department of Electrical Engineering, 2015.

[177] J. Pries, "Computationally efficient steady–state simulation algorithms for finite-element models of electric machines." Ph.D. thesis, University of Michigan, 2015.

[178] J. Pries and H. Hofmann, "Steady-state algorithms for nonlinear time-periodic magnetic diffusion problems using diagonally implicit Runge–Kutta methods," *IEEE Transactions on Magnetics*, vol. 51, no. 4, pp. 1–12, 2014.

[179] J. Pyrhönen and P. Kurronen, "Increasing the efficiency of high-speed solid-rotor induction machines," *European Transactions on Electrical Power*, vol. 4, no. 2, pp. 101–107, 1994.

[180] A. Quarteroni and S. Quarteroni, *Numerical models for differential problems.* Springer, 2009.

[181] I. Ramière and T. Helfer, "Iterative residual-based vector methods to accelerate fixed point iterations," *Computers & Mathematics with Applications*, vol. 70, no. 9, pp. 2210–2226, 2015.

[182] F. Rapetti, "Approximation des équations de la magnétodynamique en domaine tournant par la méthode des éléments avec joints," Ph.D. thesis, Université Paris 6, 2000.

[183] F. Rapetti and G. Rousseaux, "Implications of Galilean electromagnetism in numerical modeling," 2011.

[184] F. Rapetti and G. Rousseaux, "On quasi-static models hidden in Maxwell's equations," *Applied Numerical Mathematics*, vol. 79, pp. 92–106, 2014.

[185] P. Rasilo, E. Dlala, K. Fonteyn, J. Pippuri, A. Belahcen, and A. Arkkio, "Model of laminated ferromagnetic cores for loss prediction in electrical machines," *IET electric power applications*, vol. 5, no. 7, pp. 580–588, 2011.

[186] S. Reitzinger and J. Schöberl, "An algebraic multigrid method for finite element discretizations with edge elements," *Numerical linear algebra with applications*, vol. 9, no. 3, pp. 223–238, 2002.

[187] P. Renze and K. Akermann, "Simulation of conjugate heat transfer in thermal processes with open source CFD," *ChemEngineering*, vol. 3, no. 2, p. 59, 2019.

[188] K. Roppert, S. Schoder, F. Toth, and M. Kaltenbacher, "Non-conforming Nitsche interfaces for edge elements in curl-curl type problems," *IEEE Transactions on Magnetics*, vol. 56, no. 3, pp. 1–7, 2020.

[189] K. Roppert, F. Toth, and M. Kaltenbacher, "Simulating induction heating processes using harmonic balance FEM," *COMPEL-The international journal for computation and mathematics in electrical and electronic engineering*, 2019.

[190] A. Ruehli, G. Antonini, and L. Jiang, "Circuit oriented electromagnetic modeling using the PEEC techniques," 2017.

[191] Y. Saad, *Iterative methods for sparse linear systems*.   SIAM, 2003.

[192] B. Sanderse, S. P. Van der Pijl, and B. Koren, "Review of computational fluid dynamics for wind turbine wake aerodynamics," *Wind energy*, vol. 14, no. 7, pp. 799–819, 2011.

[193] G. Sangalli and M. Tani, "Matrix-free weighted quadrature for a computationally efficient isogeometric k-method," *Computer Methods in Applied Mechanics and Engineering*, vol. 338, pp. 117–133, 2018.

[194] J. Sapp, R. Sheridan, C. L. Cattell Jr, T. Nemenz, S. Dong, and T. A. Bremenour, "Drive with curved linear induction motor," Feb. 9 2012, US Patent App. US20120032084A1.

[195] S. Schöps, H. De Gersem, and T. Weiland, "Winding functions in transient magnetoquasistatic field-circuit coupled simulations," *COMPEL: The international journal for computation and mathematics in electrical and electronic engineering*, 2013.

[196] S. Schöps, I. Niyonzima, and M. Clemens, "Parallel-in-time simulation of eddy current problems using parareal," *IEEE Transactions on Magnetics*, vol. 54, no. 3, pp. 1–4, 2017.

[197] S. M. Shamsuddin, M. Ahmed, and Y. Smian, "NURBS skinning surface for ship hull design based on new parameterization method," *The International Journal of Advanced Manufacturing Technology*, vol. 28, no. 9-10, pp. 936–941, 2006.

[198] A. Shitzer, "Wind-chill-equivalent temperatures: regarding the impact due to the variability of the environmental convective heat transfer coefficient," *International journal of biometeorology*, vol. 50, no. 4, pp. 224–232, 2006.

[199] K. Sitapati and R. Krishnan, "Performance comparisons of radial and axial field, permanent-magnet, brushless machines," *IEEE Transactions on industry applications*, vol. 37, no. 5, pp. 1219–1226, 2001.

[200] C. A. Smith and J. C. Bartelsen, "Segmented direct drive motor for use in a computed tomography system," Dec. 4 2018, US Patent US10143427B2.

[201] N. Soveiko and M. Nakhla, "Wavelet harmonic balance," *IEEE microwave and wireless components letters*, vol. 13, no. 6, pp. 232–234, 2003.

[202] M. Spink, D. Claxton, C. de Falco, and R. Vázquez, "The NURBS toolbox," octave.sourceforge.net/nurbs/index.html.

[203] C. P. Steinmetz, "On the law of hysteresis," *Proceedings of the IEEE*, vol. 72, no. 2, pp. 197–221, 1984.

[204] R. Sundaria, A. Lehikoinen, A. Arkkio, and A. Belahcen, "Effects of manufacturing processes on core losses of electrical machines," *IEEE Transactions on Energy Conversion*, pp. 1–1, 2020.

[205] J. K. Sykulski, "Computational electromagnetics for design optimisation: the state of the art and conjectures for the future," *Bulletin of the Polish Academy of Sciences: Technical Sciences*, vol. 57, no. 2, pp. 123–131, 2009.

[206] J. A. Tegopoulos and E. E. Kriezis, "Eddy currents in linear conducting media," *Studies in electrical and electronic engineering*, vol. 16, 1985.

[207] N. Tesla, "Magnetic motor," 25 1889, US Patent US405858A.

[208] P. Testoni and P. Sonato, "Implementation in the ANSYS finite element code of the electric vector potential $T - \Omega, \Omega$ formulation," 2004.

[209] R. Tielen, M. Möller, D. Göddeke, and C. Vuik, "Efficient p-multigrid methods for isogeometric analysis," *arXiv preprint arXiv:1901.01685*, 2019.

[210] W. Tobin, *Léon Foucault*. EDP sciences, 2012.

[211] W. Tong, S. Wang, S. Dai, S. Wu, and R. Tang, "A quasi-three-dimensional magnetic equivalent circuit model of a double-sided axial flux permanent magnet machine considering local saturation," *IEEE Transactions on Energy Conversion*, vol. 33, no. 4, pp. 2163–2173, 2018.

[212] E. Tonti, *On the formal structure of physical theories*.   Istituto di matematica del Politecnico di Milano, 1975.

[213] E. Tonti, "Finite formulation of the electromagnetic field," *Progress in electromagnetics research*, vol. 32, pp. 1–44, 2001.

[214] R. P. Uhlig, M. Zec, H. Brauer, and A. Thess, "Lorentz force eddy current testing: a prototype model," *Journal of Nondestructive Evaluation*, vol. 31, no. 4, pp. 357–372, 2012.

[215] C. A. Valdivieso, G. Meunier, B. Ramdane, J. Gyselinck, C. Guerin, and R. V. Sabariego, "Time-domain homogenization of foil windings in 2-D axisymmetric finite-element models," *IEEE Transactions on Power Delivery*, pp. 1–1, 2020.

[216] T. A. van Beek, "Towards high voltage in coreless linear motors: solutions to thermal and electric-field problems in high force-density applications," Ph.D. thesis, Eindhoven University of Technology, Department of Electrical Engineering, 2018.

[217] T. A. van Beek, J. W. Jansen, and E. A. Lomonova, "Analysis of electric field control methods for foil coils in high-voltage linear actuators," *Archives of Electrical Engineering*, vol. 64, no. 4, 2015.

[218] G. van Zwieten, J. van Zwieten, C. V. Verhoosel, E. Fonn, T. van Opstal, and W. Hoitinga, "Nutils (version 7.0)," 2020. [Online]. Available: www.nutils.org

[219] H. Vande Sande, T. Boonen, H. De Gersem, F. Henrotte, and K. Hameyer, "Accelerating non-linear time-harmonic problems by a hybrid Picard-Newton approach," in *Proceedings of the 10th International IGTE Symposium on Numerical Field Calculation in Electrical Engineering*, 2002, pp. 342–347.

[220] E. Vassent, G. Meunier, and J.-C. Sabonnadiere, "Simulation of induction machine operation using complex magnetodynamic finite elements," *IEEE Transactions on Magnetics*, vol. 25, no. 4, pp. 3064–3066, 1989.

[221] R. Vázquez, "A new design for the implementation of isogeometric analysis in Octave and Matlab: GeoPDEs 3.0," *Computers & Mathematics with Applications*, vol. 72, no. 3, pp. 523–554, 2016.

[222] E. Vieil, "Introduction to Formal Graphs, a new approach to the classical formalism," *Phys. Chem. Chem. Phys.*, vol. 9, pp. 3877–3896, 2007.

[223] G. Von Pfingsten, S. Steentjes, A. Thul, T. Herold, and K. Hameyer, "Soft magnetic material degradation due to manufacturing process: A comparison of measurements and numerical simulations," in *2014 17th International Conference on Electrical Machines and Systems (ICEMS)*. IEEE, 2014, pp. 2018–2024.

[224] N. H. Vrijsen, "Magnetic hysteresis phenomena in electromagnetic actuation systems," Ph.D. thesis, Eindhoven University of Technology, Department of Electrical Engineering, 2014.

[225] A. Waser, "On the notation of Maxwell's field equations," 2000.

[226] C. H. P. Wassink, "Innovation in non destructive testing," Ph.D. thesis, Delft University of Technology, Department of Technology, Policy and Entrepreneurship, 2012.

[227] O. Weeger, "Isogeometric finite element analysis of nonlinear structural vibrations," Ph.D. thesis, Technische Universität Kaiserlautern, 2015.

[228] K. Weise, "Advanced modeling in Lorentz force eddy current testing," Ph.D. thesis, Technische Universität Ilmenau, 2016.

[229] H. Whitney, *Geometric integration theory*. Courier Corporation, 2012.

[230] M. Wick, S. Grabmaier, M. Juettner, and W. Rucker, "Motion in frequency domain for harmonic balance simulation of electrical machines," *COMPEL-The international journal for computation and mathematics in electrical and electronic engineering*, 2018.

[231] R. Willems, "Numerical analysis of turbulent heat transfert within an axial-flux permanent magnet machine," Master's thesis, Eindhoven University of Technology, Department of Mechanical Engineering, 2020.

[232] R. M. Wojciechowski, A. Demenko, and J. K. Sykulski, "Comparative analysis of $A-V$ and $A-T-T_0$ calculations of induced currents in multiply connected regions," *IET Science, Measurement & Technology*, vol. 6, no. 5, pp. 312–318, 2012.

[233] W. Wu, Q. Chen, X. Zhu, F. Zhao, and Z. Xiang, "Electromagnetic–mechanical coupling optimization of an IPM synchronous machine with multi flux barriers," *Energies*, vol. 13, no. 7, p. 1819, 2020.

[234] S. Yamada, K. Bessho, and J. Lu, "Harmonic balance finite element method applied to nonlinear AC magnetic analysis," *IEEE Transactions on Magnetics*, vol. 25, no. 4, pp. 2971–2973, 1989.

[235] S. Yamada, P. Biringer, and K. Bessho, "Calculation of nonlinear eddy-current problems by the harmonic balance finite element method," *IEEE Transactions on Magnetics*, vol. 27, no. 5, pp. 4122–4125, 1991.

[236] R. Yazdanpanah and M. Mirsalim, "Axial-flux wound-excitation eddy-current brakes: Analytical study and parametric modeling," *IEEE Transactions on Magnetics*, vol. 50, no. 6, pp. 1–10, 2014.

[237] K. Yoon and B. Kwon, "Optimal design of a new interior permanent magnet motor using a flared-shape arrangement of ferrite magnets," *IEEE Transactions on Magnetics*, vol. 52, no. 7, pp. 1–4, 2016.

[238] H. Zaidi, "Méthodologies pour la modélisation des couches fines et du déplacement en contrôle non destructif par courants de Foucault: application aux capteurs souples," Ph.D. thesis, Université Paris Sud - Paris XI, 2012.

[239] R. Zeinali, D. C. J. Krop, and E. A. Lomonova, "Comparison of Preisach and congruency-based static hysteresis models applied to non-oriented steels," *IEEE Transactions on Magnetics*, vol. 56, no. 1, pp. 1–4, 2020.

[240] Z. Zhang, W. Geng, Y. Liu, and C. Wang, "Feasibility of a new ironless-stator axial flux permanent magnet machine for aircraft electric propulsion application," *CES Transactions on Electrical Machines and Systems*, vol. 3, no. 1, pp. 30–38, 2019.

[241] X. Zhao, D. Guan, F. Meng, Y. Zhong, and Z. Cheng, "Computation and analysis of the DC-biasing magnetic field by the harmonic-balanced finite-element method," *International Journal of Energy and Power Engineering*, vol. 5, no. 1, p. 31, 2015.

[242] Z. Q. Zhu, D. Howe, E. Bolte, and B. Ackermann, "Instantaneous magnetic field distribution in brushless permanent magnet DC motors. I. Open-circuit field," *IEEE Transactions on Magnetics*, vol. 29, no. 1, pp. 124–135, 1993.

Acknowledgments

First of all, I would like to express my sincere gratitude to prof. Elena Lomonova for giving me the opportunity to work as a PhD candidate within her group. Thank you for always demonstrating your support in my enterprises.

Moreover, I want to thank the independent committee members: prof. Analisa Buffa, prof. Manfred Kaltenbacher and prof. Bary Koren for accepting the invitation, reading the manuscript, and giving me extensive reviews and comments that contributed greatly to improve the quality of the final result.

Additionally, I wish to acknowledge all the supervisors I had during this journey. Johan, thank you for being responsive and quickly enrolling me for a Master's graduation project that led me to the start of this PhD research. I would like to thank Miguel and all the persons involved with the Tenneco (DRiV) project, for supporting me since the beginning of this adventure in Eindhoven. Henk and Maurice, many thanks for helping me demystify some power electronics concepts, I always enjoy our casual discussions. Then, I want to thank Bart: your motivating personality has shed new light on many modeling and design aspects, first with your lectures and later with your supervision. Your efficiency and accomplishments continue to be a source of inspiration for me and the colleagues in the EPE Group. Helm, thank you very much for taking me under your wing during the last year. You helped me a great deal to organize and shape my thoughts as well as my thesis. Thank you so much for your reactivity, availability, and all the nice technical exchanges we had.

Many thanks to all my Flux 2.122 officemates: Koen, Sam, Andrea, Matthijs, Siamak, and Doğa for the nice atmosphere in the room and the borrels. Thank you Mitrofan for our recurrent collaborations and conversations on high-order methods. Many thanks to the EM mates in the other office: Jeroen, Bram, and Reza for the many interesting discussions we have had on a wide variety of topics. Furthermore, I am very much obliged to all my colleagues from the EPE group for bringing out such a thriving character to our working place.

Curriculum Vitae

Léo Friedrich was born on October 6, 1993, in Courbevoie, France. In 2013, he finished the intensive two-year curriculum *classes préparatoires* in Mathematics, Physics, and Engineering Sciences (MPSI/PSI) at Lycée Marcelin Berthelot, Saint-Maur-des-Fossés, France. In 2016, he received his *diplôme d'ingénieur* specialized in Physics and Nanosciences, from the *Grande École* Grenoble INP - Phelma, Université Grenoble Alpes, France. During his master, he performed an internship at the National Chiao Tung University in Hsinchu, Taiwan, where he conducted his research on three-dimensional transport simulation and shape optimization of nanowire gate-all-around MOSFET arrays. He followed the Master in Physics, Optics and Condensed Matter Physics as an exchange student for one semester, at the Norwegian University of Science and Technology in Trondheim.

As of February 2016, Léo joined the Eindhoven University of Technology, where he conducted his Master's graduation project, researching and modeling piezoelectric and electromagnetic solutions for harvesting surrounding vibrational energy. In September 2016, he started a PhD study in the Electromechanics and Power Electronics group at Eindhoven University of Technology, where his research focused on the numerical modeling of low-frequency electromagnetic problems, in particular involving eddy currents and nonlinear phenomena, in the context of design and optimization of magnetic devices and electrical machines. He developed frequency-domain finite-element solvers in the framework of isogeometric analysis, which enables the fast and accurate computation of steady-state nonlinear solutions of electromagnetic and thermal field distributions on computer-aided design models of electrical machines.